Antimony-119 for Radiopharmaceutical Therapy

By

Aeli P. Olson

A dissertation submitted in partial fulfillment of

the requirements for the degree of

Doctor of Philosophy

(Medical Physics)

at the

UNIVERSITY OF WISCONSIN-MADISON

2024

Date of final oral examination: 12th of November, 2024

The dissertation is approved by the following members of the Final Oral Committee:
Jonathan W. Engle, Professor, Medical Physics
Beth E. Meyerand, Professor, Medical Physics and Vice Provost for Faculty and Staff Affairs
Bradley T. Christian, Professor, Medical Physics
Paul A. Ellison, Assistant Professor, Medical Physics
Silvia S. Jurisson, Professor, Chemistry

Acknowledgments

When writing dissertation acknowledgments, it is customary to first thank your advisor. Though many may choose such an order out of tradition, thanking my advisor (Dr. Jonathan Engle) first represents the truest and most genuine expression of gratitude I could make. Thank you, Jon, for your tireless effort, thoughtful attention, gentle correction, outpouring of encouragement, patience amongst my confusion and tears, and wise guidance and mentorship. Joining your lab is one of the best decisions that I have made, and thank you for investing your time, energy, and resources into my education. You care deeply about your students, and under your mentorship, the formation I have received as both a scientist and person is unparalleled. Throughout my PhD, I have received education in an unimaginably wide breadth of scientific skills and knowledge, and I enter the next phase of my career with unmatched competence and confidence because of your instruction. Additionally, your leadership continues to make the cyclotron lab both prominent in medical radionuclide production research and a wonderful and enjoyable place to work.

Thank you to my committee members for their contribution to my research formation and degree progression. To Dr. Paul Ellison, thank you for tirelessly, meticulously, and steadfastly investing your time, attention, and energy into my research. Thank you for correcting and expanding my knowledge of chemistry and nuclear medicine, and thank you for the detailed analysis you always enthusiastically supplied regarding my research and manuscript drafting. To Dr. Silvia Jurisson, thank you for lending not only your pnictogen inorganic chemistry expertise but also continual support, generous research resources, and earnest encouragement. To Dr. Brad Christian, thank you for your thoughtful assessments and objectivity, encouraging me to make hard but practical decisions with my research project and degree progression. Finally, thank you to Dr. Beth Meyerand for your enthusiastic encouragement and honest advice on topics beyond science.

It takes a village to raise a scientist, and my cyclotron village is truly one of the best. I am incredibly thankful to the scientists within the cyclotron lab for educating me out of their gifts and talents. Thank you to distinguished scientist Dr. Todd Barnhart. You were patient with every question regarding cyclotron operation and theoretical maintenance scenario, thorough in teaching me about cyclotron maintenance, gracious in allowing me to be involved in repairs (even if alone you could have done it significantly faster), supportive in allowing me to run the cyclotron independently, and generous in making yourself available to answer questions, troubleshoot error messages from afar, or drive into work at 5 am if I was having difficulty getting beam. I genuinely could not have completed my PhD work nor received the unmatched cyclotron operations education and experience without your mentorship.

Thank you to our emeritus professor Dr. Jerry Nickels for allowing me to tag along to the RDS every Monday for a year, learning about cyclotron function and ^{64}Cu chemistry. Helping you maintain and fix the RDS taught me so much about low energy cyclotron function and grew my physical intuition, curiosity, and awe for these small yet mighty machines. A very special thank you to Dr. Eduardo Aluicio-Sarduy. Your early research advice encouraging me to focus on the big picture, understand practical limitations, and to think about speciation, significantly influenced my research and contributed to my formation as a scientist. You were always quick to drop what you were doing or move your schedule to prioritize helping us students, and you and Liuda welcomed me for family dinners and made me feel so loved.

Thank you, Dr. Jason Mixdorf, for how thoughtfully you listened to research problems and attentively tried to help find answers and solutions. Your advice and expertise regarding organic synthesis and molecular design was greatly appreciated. Your sass also kept the lab fun. Thank you to the other trainees I overlapped with: Chris Kutyreff, Kaelyn Becker, Kendall Barrett, Margarita Chernysheva, Wilson Lin, Molly DeLuca, Morgan Dierolf, and Megan Salek. You all made the PhD experience more fun. Late night research in the target lab is way more enjoyable with good people. To Kaelyn, Kendall, and Molly, extra thanks is warranted. Your friendships provided invaluable support through listening to research frustrations, sharing laughs, and being the best conference travel buddies. I treasure the time we spent working through our PhD's together. Thank you to Owen Glaser. Your chemistry help and friendship this last year was unexpected but delightful. Thank you to my undergraduate student, Francesca Verich for continual enthusiastic willingness to help collect experimental data which helped me graduate faster.

Thank you to my wonderful collaborators: Dr. Valery Radchenko, Aivija Grundmane, Dr. Paul Ellison, Dr. Silvia Jurisson, Dr. Heather Hennkens, Dr. Li Ma, Dr. Yutian Feng, Chathurya Munindradasa, Justin Jeffery, Dr. Eszter Boros, Dr. Axia Marlin, Owen Glaser, Emma Phuong Tran, Dr. Nikki Thiele, Dr. Briana Schrage, and Dr. Faizul Islam. Together, we got a lot done, and I have learned so much from you all.

Thank you to my family for your continued and unconditional love and support. To my parents (Mollie and Stephen), siblings (Amy, Bjorn, and Signe), in-laws (Hannah and Tyler), Auntie Gertie, Aunt Karen, Uncle Corey, and cousins (Ellie and Annika), you always checked in about my research and patiently listened to me chatter about it, even if you didn't understand. To my mom, Signe, and Bjorn, in particular, I have felt so loved and seen hearing about how enthusiastically you share and describe (in your own wonderful words) what I research with other people. A huge thank you to my mom for patiently fielding calls when I was upset and offering encouragement and steadfast prayers. Thank you to my Aunt Karen and Uncle Corey for your support and bimonthly dinner outings. Thank you to the littles (Sophie, Soren, Svea, Mia, Teddy, and Walter) for enthusiastically bragging about your ‘Auntie the scientist!’ Thank you to my fiancé Robbie for this last year and our future to come. Thank you for doting on me while I wrote this dissertation. Your unwavering confidence, admiration, and pride in my abilities and accomplishments means the world to me. I love you dearly and am so thankful for you.

Finally, a huge thank you to my friends. The DVM’s (Kayla Miller, Gretja Otten, and Makayla Evans) really helped me get through graduate school. Their friendships are dear blessings from my time here in Madison, and I am so incredibly thankful for their love and support. Thank you to my roommate, Dr. Melinda Chen, whose friendship and community this last year has been a blessing and support. I’m thankful for past roommates, Jen Salvo and Jocelyn English, for their encouragement, love, support, and friendship. I’m incredibly thankful for the support I received from all of the friends that I met through my church community: Diane Brown, Laura Kane, Taylor Nibbe, Rachel Smith, Katie Bier, Kristen Kaltenthaler, Patrick and Kristy, Ryan Hess, Micah Latty, Tyler Stump, Mitchell Paukner, Miguel, Jeff Salvo, and so many others. I’m thankful for the support and prayers provided from bible study members Jim and Coleen and Eve and Guy.

As a person of Christian faith, I’m above all thankful to my God for the gifts, talents, opportunities, resources, purpose, and people He’s surrounded me with. In her essay ‘Why Work,’ Dorothy L. Sayers wrote that “work should, in fact, be thought of as a creative activity undertaken for the love of the work itself; and that man, made in God’s image, should make things, as God makes them, for the sake of doing well a thing that is well worth doing.” Dorothy’s words inscribe my feelings towards my dissertation. I am thankful to have worked hard at this work—work which I believe is very worth doing.

Abstract

This dissertation investigates production, chemical isolation, and radiopharmaceutical incorporation of the therapeutic radionuclide ^{119}Sb (^{119}Sb, $t_{1/2}$ = 38.19 *22* h, EC=100%) and its radioisotopic imaging analogue ^{117}Sb ($t_{1/2}$ = 2.80 *1* h, EC = 100%, E_γ = 158.562 *15* keV, I_γ = 85.9%, $E_{\beta+}$ = 262.4 *4* keV, $I_{\beta+}$ = 1.81 *11 %*). For decades, researchers have predicted ^{119}Sb to be one of the most promising Auger electron-emitting radionuclides for therapeutic application because of its high electron yield (~24 electrons per decay), optimal emitted internal conversion electron energies (20 – 30 keV), and low co-emission of photons (E_{max} = 29.1 keV, I_γ = 2.18 *7 %*). Barriers in ^{119}Sb production, chemical isolation from target material, and stable radiometal complexation with a bifunctional chelator have limited exploration of ^{119}Sb's therapeutic potential to *in silico* studies. This work begins by developing production and chemical isolation techniques, electroplating tin targets suitable for low energy proton and deuteron irradiation and separating Sb from Sn using column chromatography and liquid extraction. We discovered target recycling techniques compatible with our column-based Sn(II)/Sb(III) separation, allowing us to sustainably irradiate 96.3% isotopically enriched ^{119}Sn to make radionuclidically pure ^{119}Sb. With collaborators in inorganic chemistry, we found two chelators capable of bifunctionalization for complexing radioantimony—a trithiol chelator for complexing Sb(III) and a tris-catechol chelator (TREN-CAM) for Sb(V). Using spectroscopy, *in vitro, in vivo,* and *ex vivo* techniques, we characterized [$^{nat/1XX}$Sb]Sb-trithiol-diacid and [$^{nat/1XX}$Sb]Sb-TREN-CAM complexes, reported X-ray crystal structures, and analyzed complex stability. [$^{nat/1XX}$Sb]Sb-trithiol-diacid was stable in serum, but upon conjugation to a targeting moiety, the complexes decomposed in PBS. We collected the first *in vivo* PET and SPECT images of a chelator complexed radioactive antimony to prove [$^{nat/1XX}$Sb]Sb-TREN-CAM complex's stability.

Table of Contents

List of Figures

List of Tables

List of Abbreviations and Symbols

RPT – Radiopharmaceutical Therapy
LET – linear energy transfer
RNS – reactive nitrogen species
ROS – reactive oxygen species
DNA – deoxyribonucleic acid
DSB – double strand DNA breaks
SSB – single strand DNA breaks
MDS – multiple damage sites
DMSO – dimethyl sulfoxide
ATP – adenosine triphosphate
RBE – relative biological effectiveness
AE – Auger electron
EC – electron capture
IC – internal conversion
CE – conversion electron
α - Alpha (helium nucleus)
β^+ – Beta plus (Positron)
β^- – Beta minus (Electron)
γ – Gamma
$t_{1/2}$ – half-life
TND – tumor-to-normal tissue mean absorbed dose rate ratio
SPECT – single photon emission computed tomography

PET – positron emission tomography
LOR – line of response
TOF – time of flight
CPS – counts per second
NMR – nuclear magnetic resonance
XAS – X-ray absorbance spectroscopy
H_2SO_4 – sulfuric acid
MilliQ water – 18 MΩ*cm deionized water
c.HCl – concentrated hydrochloric acid
NaOH – sodium hydroxide
EtOH – ethanol
MeOH – methanol
TLC – thin layer chromatography
NH_4OAc – ammonium acetate
$SnSO_4$ – stannous (tin) sulfate
$Sn(OH)_2$ – tin hydroxide
H_2O_2 – hydrogen peroxide
EOB – end of bombardment
n.c.a – no carrier added
HPGe – high purity germanium
CdTe – cadmium telluride
ICP-OES – inductively coupled plasma optical emission spectrometer
ICP-MS - Inductively coupled plasma mass

spectrometry

ID – inner diameter

IAEA – international atomic energy agency

TENDL – TALYS evaluated nuclear data library

LOD – limit of detection

DBE – dibutyl ether

LLE – liquid-liquid extraction

RP-HPLC – reversed phase high performance liquid chromatography

TFA – trifluoroacetic acid

TCEP – tris(2-carboxyethyl)phosphine hydrochloride

PBS – phosphate buffered saline

BFC – bifunctional chelator

CN – coordination number

HSAB – hard-soft acid-base theory

MeCN - acetonitrile

FBS – fetal bovine serum

$SbCl_3$ – antimony trichloride

HRMS – high resolution mass spectrometry

RCY – radiochemical yield

XANES – X-ray absorption near edge spectroscopy

EXAFS – extended X-ray absorption fine structure

LCMS – liquid chromatography mass spectroscopy

AMA – apparent molar activity

p.i. – post injection

RBC – red blood cells

GSH – glutathione

c.a. – carrier added

TREN-CAM - tris(2-aminoethyl)amine (TREN) catecholamide (CAM)

NH_4OH – ammonium hydroxide

NH_4OAc – ammonium acetate

ppm – parts per million

ppb – parts per billion

CD_3OD – deuterated methanol

$(CD_3)_2SO$ – deuterated dimethyl sulfoxide

DMF – dimethylformamide

VOI – volume of interest

FWHM – full width half maximum

ORNL – oak ridge national laboratory

PVE – partial volume effect

SPS – spark plasma sinter

PSMA – prostate specific membrane antigen

PARP – poly(ADP-ribose) polymerase

DUPA – 2-[3-(1,3-dicarboxypropyl) ureido]pentanedioic acid

Chapter 1: Introduction

1. Overview of Radiopharmaceutical Therapy (RPT) in Cancer Applications

In 2024 within the United States, an estimated 600,000 individuals will die of cancer, and two million new cancer cases will be diagnosed. Among men and women, prostate and breast cancer include the greatest diagnosis of new cases, 29% and 32%, respectively. Treatment of both cancers achieve incredible five-year survival rates, >99% prostate and 99% breast, with therapeutic intervention upon localized disease. However, survival rates decrease significantly for metastatic disease, to 34% and 31%, respectively [1]. Primary treatments for non-metastatic breast and prostate cancer include surgery and radiation therapy (external beam and brachytherapy) [2,3], and though successful in controlling early-stage, local disease, these treatment options are generally ineffective for metastatic disease.

RPT uses biological targeting vectors (e.g., hormones, signaling molecules, antibodies, peptides, antigens) tuned to cellular disease markers (e.g., receptors and proteins overexpressed in cancers) to deliver radionuclides that emit short range, highly damaging radioactivity inside diseased cells [4], offering radiation therapy cancer treatment options in pathologies that are inoperable or refractory to other forms of radiotherapy [5]. RPT can treat metastatic disease [5], reduce dose to healthy tissue, and be applied in combination with other cancer therapy options [6]. RPT agent efficacy depends on delivering sufficient therapeutic dose to diseased cells—a combination of the physiological targeting method and radionuclide decay properties. Radionuclides effective in RPT application cause complex and varied cellular responses, and to choose radionuclides that maximize therapeutic response, researchers must understand radiation biology.

1.1. Radiation Biology

Linear energy transfer (LET) is the measure of energy absorbed by matter per unit pathlength the radiation traverses. With high LET (>1 keV/μm) radiation (alpha particles and low energy electrons), energy is being absorbed in a short range around the decay site. In contrast, low LET (<1 keV/μm) radiation travels longer distances and includes gamma emissions, X-ray photons, and high energy electrons. Because of the extensive application of low LET particle radiation on clinical cancer treatments, biological responses to low LET, external beam radiation form the basis of radiation biology. Knowledge regarding low LET radiation response is generally considered transferrable to high LET RPT. Increased focus on high LET and RPT-specific radiation biology is motivated by differences between low and high LET radiation and external beam versus RPT-induced biological response [7]. RPT causes both targeted and non-targeted radiation effects. Targeted effects include radiation damage to cellular structures that in turn cause decreased cell function. Non-target effects involve cellular response to radiation through activation of complex stress signaling pathways, which can lead to cell death for both irradiated cells and their surrounding non-irradiated counterparts (bystander effect) [7–9]. Both effects are dependent upon dose, dose rate, and LET. Cell killing efficacy from both targeted and non-targeted effects increases with increased LET, motivating high LET RPT agent development.

1.1.1. Targeted Radiation Biology Effects

Particles emitted during decay can deposit energy to DNA or cellular structures via two main mechanisms—direct and indirect. Direct mechanisms involve energy deposition from radiation to cellular structures, causing ejection of single electrons from atoms within those structures. Subsequent ionizations caused by these electrons can disrupt critical structures and important cellular functions. Indirect mechanisms involve energy deposition from radiation to radicalizeable species (commonly water), creating a chemically reactive intermediary. The ionization of water forms hydroxy free radicals, hydrogen peroxide (H_2O_2), reactive oxygen species (ROS), and reactive nitrogen species (RNS), which react with sensitive cellular structures. These radiation-generated free radicals, RNS, and ROS are chemically indistinguishable from species generated endogenously through cellular metabolism and oxidative stress. Indirect mechanisms act at longer distances within the cell than direct mechanism, but indirect mechanisms are more susceptible to electron recombination or neutralization through endogenous ROS cellular protection and antioxidant mechanisms [4,7,9]. DNA within the cell nucleus is the most radiation sensitive subcellular structure, and generally, effective cell killing is achieved when maximizing dose to the cell nucleus [4,10] with lipid and protein oxidation offering additional routes to cell death [7].

Double strand DNA breaks (DSB), single strand breaks (SSB), base modification, deletion, crosslinking, and multiple damage sites (MDS) are all forms of DNA damage observed after exposure to radiation. The extent of DNA damage is dependent upon dose, dose rate, and LET of radiation administered. MDS, sometimes referred to as clustered DNA lesions, occur when at least two DNA lesions (e.g., SSB, base modification) caused by the same radiation decay event are located within two DNA helix turns. With low endogenous production, MDS are indicative of ionizing radiation and increased in quantity and complexity when caused by higher LET radiation. DSB are the lowest form of MDS complexity [11,12]. High LET-induced MDS are repaired primarily through homologous recombination pathways [11], and their increased toxicity is attributed to an increased repair difficulty [7]. Additionally, reduced ability to repair MDS increases the lesion lifetime and, depending upon cell replication phase, increases mutation rate. Increased mutation rates, translocations, chromosomal aberrations, and sister chromatid exchanges result from the increased MDS complexity caused by high LET radiation exposure [11].

High LET radiation causes significant DNA damage through both direct and indirect mechanisms, whereas low LET is limited to primarily indirect mechanisms, generating lower complexity DNA damage. Contribution of direct versus indirect damage to DNA, measured by culturing cells with the antioxidant dimethyl sulfoxide (DMSO), established that low LET radiation primarily causes SSB [13] via indirect mechanisms (70%) [7,11]. The proportion of direct versus indirect contribution increases with LET [7,11]. High LET radiation acts with significant direct contribution upon DNA to cause greater DSB and MDS [13]. Complex DNA damage results in more efficient cell death, which prioritizes applying high LET radiation over low LET radiation in RPT.

Lipid peroxides and protein hydroperoxides formed through chemical reactions with free radicals and cell membrane lipids or cytoplasmic proteins can both initiate oxidative chain reactions, multiplying the destructive effects of the initial radical [7,9]. Direct interactions with lipids and resultant lipid peroxidation increase membrane permeability, which in turn disrupts transmembrane processes and ion gradients, changes membrane fluidity, and damages transmembrane protein function [9]. Mitochondrial DNA is also affected by radiation; however, the effect of the damage caused is not well understood [9]. Carbon-ion and alpha particle micro-beams cause mitochondrial depolarization and fracture, affecting mitochondrial function and initiating pro-apoptosis signaling through cytochrome C release [14].

1.1.2. Non-targeted Radiation Biology Effects

Non-targeted radiation biology effects encompass observed cytotoxic cellular response not caused by radiation damage to cellular structures, which also results in DNA damage, cell death, apoptosis, chromosomal aberrations, and mutations [7,9]. These effects, dependent upon dose,

dose rate, and LET [9], are attributed to activation of oxidative stress and pro-apoptotic cell signaling pathways. They transmit to neighboring cells through secondary molecular messengers including ROS, RNS, ATP, cytokines, and Ca^{2+} ions [7–9,14], leading to ROS production in non-irradiated cells [9]. Many experiments have illustrated these curious bystander effects by dosing cells with RPT agents, removing and washing RPT media, incubating irradiated cells in fresh media, and transferring media to un-irradiated cells. Researchers have observed significant cytotoxicity in non-irradiated cells [8,15–25], including the induction of DNA lesions [8,16,20,23,25] following initial RPT localization to either nuclei or cellular membranes [8].

Irradiation of cell membranes with high LET particles triggers ceramide production, a secondary messenger of cellular apoptosis, and promotes cell death through lipid raft-formation, changing membrane structure and fluidity [9]. In addition to adjusted membrane fluidity, lipid-rafts activate MAPK, AKT, ERK1/2, p38 kinase, and JNK pathways, contributing to nuclear DNA damage and compensating for less effective non-nuclear targeting [8]. Cytoplasmic irradiation alters mitochondrial oxidative phosphorylation and protein synthesis, promoting oxidative stress [9]. When targeting the cell membrane, cytoplasm, and nucleus with high LET Auger electrons from ^{125}I labeled compounds, targeted effects accounted for 13.2%, 12.8%, and 50.7% of cell death for each respective location. Researchers measured comparable non-targeted cell death between nuclear and cell membrane targeting [8], illustrating the significant contribution of non-targeted effects to cell death independent upon nuclear targeting. This observation promotes the consideration of non-targeted strategies in RPT agent development. *Ex vivo* studies showed peripheral tumor accumulation of an ^{125}I RPT agent yet uniform, homogenous distribution of DNA DSB due to bystander effects from high LET radiation [8].

To account for observed differences in efficacy from differing LET radiation, relative biological effectiveness (RBE) is determined for each particle type emitted. Traditionally, experimental RBE measurement occurs by irradiating a cell line with various radiation dosages and normalizing the measured radiation dose (commonly that which achieves 37 percent cell survival) to that of a photon emitter (e.g., cesium-137) [4,10,26,27]. High RBE is desired to deliver high radiation dose to the tumor. Pharmacokinetically-targeted, high LET, high RBE radionuclides for RPT have immense potential to eliminate micrometastases [27–29], as short-range high LET radiation provides specificity in cell killing, sparing nearby, adjacent cells and decreasing radiation therapy side effects. When designing RPT agents, special attention needs to be given to radionuclide choice.

1.2. Therapeutic Radionuclides

Three radioactive decay processes are studied for their RPT potential: β^- emission, α emission, and Internal Conversion and Electron Capture (IC/EC). IC/EC decay frequently stimulates a cascade of low energy conversion electrons (CE) and Auger electrons (AE). Emitted particle energies, ranges, LET, and approximate RBE are summarized in **Table 1**.

Table 1: Decay properties and energy deposition in tissue for common RPT radionuclides. Adapted from [13] with RBE values from [10,30–32].

Emission	Particles	Multiplicity	$E_{(min)}$-$E_{(max)}$	Range	LET	RBE
α particle	Helium nuclei	1	5 – 9 MeV	40 – 100 μm	~80 keV/μm	~20
β^- particle	Energetic electron	1	50 – 2,300 keV	0.05 – 12 mm	~0.2 keV/μm	~1
IC/EC & AE	Low energy electrons	5-30	eV – 400 keV	2 nm – 1 mm	~2–26 keV/μm	~5-20

Clinically approved β^--emitting radionuclides (e.g., ^{177}Lu, ^{90}Y) with low LET, low RBE, and pathlengths as long as 4.4 mm in tissue [33] suffer from dose range effects and deposit lower dose than high LET particles [34]. Despite these dose rate limitations, β^--emitting radionuclides are front runners in RPT agent construction and application due to convenient and scalable production via reactor neutron bombardments [35]. Alpha (α) particles achieve the highest RBE of any decay radiation but often decay to unstable daughter radionuclides, providing uncertain dose distributions as decay recoil energy decouples daughters from molecular constructs [36]. A majority of α-emitter productions require the use of high intensity, heavy ion beams, extremely high energy particle accelerators, or generators constructed from rare, controlled reactor products or feedstock target materials. Currently, these barriers limit global production capacity and inhibit availability [6,37–40].

Within IC/EC decay, an inner atomic orbital electron is removed, creating an inner shell electron hole and subsequent excited state. In internal conversion, dynamic electromagnetic multipoles in the excited nucleus interact with an inner-shell orbital electron, transferring energy that ejects it from the atom [41]. The resultant internal conversion electron (CE) will have the highest energy of any electron emitted by IC/EC. In electron capture, an inner-shell orbital electron is absorbed by the nucleus. After the electron hole is created by either decay method, higher energy shell electrons will de-excite, and the energy difference is either emitted as a characteristic X-ray or reinvested to kick out an electron from the atom. In the latter instance, more electron holes are created, resulting in more electron emissions, and a cascade of emitted low energy electrons results [42]. Secondary and higher-level electrons in the electron cascade are commonly referred to as Coster-Kronig or super Coster-Kronig electrons [43]. Low energy electrons emitted in a cascade effect after IC/CE decay are referred to as AEs, after the French physicist Pierre Auger whose 1923 PhD dissertation work focused on describing and explaining the observation, resulting in a Nobel Prize [44]. The effect was additionally predicted and published by the Austrian-Swedish nuclear physicist Lise Meitner in 1922 [45]. Evidence suggests the data Meitner used to support the radiative emission from electron transmission model were CEs sourced from the nucleus and not originating from electron shells [46]. AEs and some CEs have high LET, high RBE, and short path lengths, providing high radiation dose deposition in small, localized volumes, shredding DNA with demonstrated therapeutic effect [47,48] and resulting in apoptotic cell death [49–52]. Theoretically, AEs allow effective dose delivery and disease management in metastatic disease with significant mitigation of side effects, an advantage over β^--emitters. Production of AE-emitters' is scalable on small cyclotrons already distributed across the world [53], and AE-emitters primarily decay to stable daughters [27,54].

1.3. Auger Electron Specific Radiation Biology

The therapeutic effectiveness of AE-based radiopharmaceuticals is heavily dependent on the emitted electron spectra and subcellular distribution and localization [4,10,26,27,42]. Desirable factors include high AE yields, high AE energies, and half-lives ($t_{1/2}$) on the order of hours or days. An ideal therapeutic radionuclide has low emission of high energy photons, which would increase off target radiation dose and decrease tumor-to-normal tissue mean absorbed dose rate ratio (TND).

Researchers created a mathematical model to evaluate the relationship between TND and electron energy and surveyed low energy electron emitters suitable for small tumor radionuclide therapy. Based on this model, they determined that a radionuclide ideal for small tumor radionuclide therapy, as seen by high TND, would have the following qualities: (1) emitted electron energy less than 40 keV, (2) a photon-to-electron energy ratio below 2, (3) half-life between 30 min and 10 days, (4) stable daughter nuclide or half-life no longer than 60 days, (5) production via neutron capture or proton-, deuteron-, alpha particle-induced reactions, and (6) exclusion of nobel gases due to unsuitable labelling chemistries. From this criteria, five nuclides

(^{119}Sb, ^{103m}Rh, ^{161}Ho, ^{58m}Co, and ^{189m}Os) were determined suitable for small tumor radiotherapy application, contingent on the development of selective targeting vectors for cellular internalization [28]. Additional analysis estimated 100 GBq ^{119}Sb activity would be necessary for 2 Gy whole-body dose, requiring high molar activities to avoid target saturation [28].

AE-emitters' greatest cytotoxic effect occurs when they are incorporated into cellular DNA (e.g., via nucleosides like deoxyuridine and deoxycytidine) [10,55–57]. Increasing the distance between cellular DNA and the AE-emitter decreases cytotoxicity [57–60] due to AEs' short pathlength. When localized at the cell membrane, selenium-75's (^{75}Se, $t_{1/2}$ = 119.78 *5* d, EC = 100%) [61] emitted CE and AEs have RBE equivalent to β^--emitters [62]. CEs emitted by most AE-emitters have longer path lengths (0.05-12.00 mm) and do not require internalization into the cell to yield a therapeutic effect [50]. For small cell clusters, electrons of 20-30 keV provide optimal self-absorbed dose from the targeted cell, maintaining localized energy deposition [29]. AEs not located within the nucleus can cause damage via indirect mechanism or non-targeted effects, creating damage outside the range of the emitter [63]. Using DMSO to supress indirect mechanisms, researchers have observed that up to 90% of dose deposited from select AE-emitters results from indirect mechanisms [64], suggesting that nuclear targeting may not be unequivocally necessary.

Almost half of all medical radionuclides are AE-emitters. Historically, the most common radionuclides investigated for AE RPT are ^{125}I, ^{75}Se, ^{51}Cr, ^{77}Br, ^{201}Tl, ^{111}In, ^{67}Ga, ^{99m}Tc, and ^{123}I [43,55,62,65]. Influential studies have used ^{125}I, ^{111}In, and ^{99m}Tc despite being unideal for AE RPT. Illustrated in **Figure 1**, these radionuclides emit electrons with unsuitable energies (greatest proportion CE/AE outside 20-40 keV), provide additional accompanying emissions (e.g., photons for ^{111}In and ^{99m}Tc), and/or have half-lives incompatible for radiopharmaceutical production and administration (e.g., ^{125}I). Practical issues of production accessibility and easy chemical incorporation motivated choice of these unideal AE-emitters for RPT research. Their induced radiation responses contributed to a belief that effective AE RPT radiotoxicity is achieved exclusively through nuclear targeting. Aforementioned, researchers have observed cell toxicity when targeting CE and AE-emitting radionuclides to cellular locations besides the nucleus, including targeting iodine-125 (^{125}I, $t_{1/2}$ = 59.4 d, EC = 100%) to the cell membrane [66,67] and indium-111 (^{111}In, $t_{1/2}$ = 2.80 d, EC = 100%) to the cytoplasm [68]. These bystander and non-targeted effects illustrate complex AE radiobiological systems, which, though incompletely understood, can be leveraged to increase therapeutic efficacy [4,15,27,64].

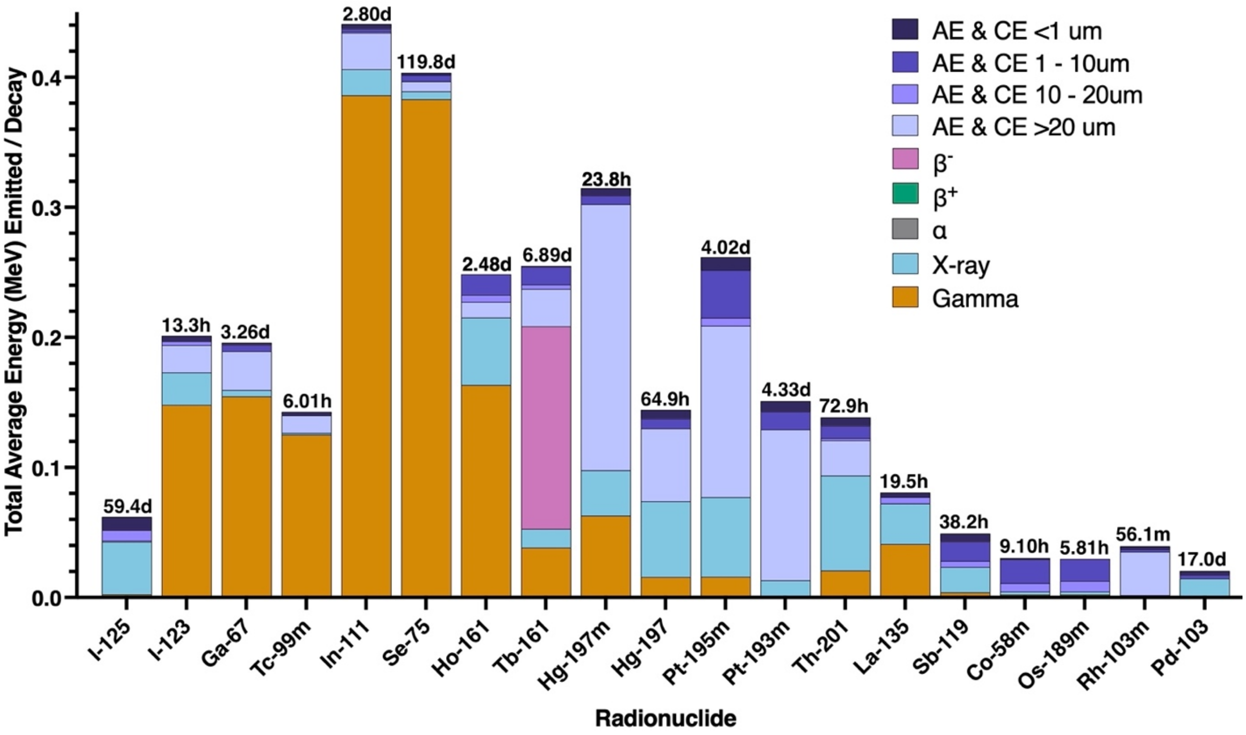

Figure 1: Comparison of total average energy (MeV) emitted from each radionuclide per decay stratified by emission type and AE and CE range with annotated half-life. Nuclear decay properties are from [69,70].

1.4. Antimony-119

Antimony-119 (^{119}Sb, $t_{1/2}$ = 38.19 *22* h, EC = 100%) [71] decays with CE and AE emission of multiple electrons with energies up to 25 keV, providing high RBE and densely ionizing pathlengths up to 15 μm length in tissue [70], long enough to provide nuclear dose when targeted from the cell surface [48]. With a radiological half-life of 38.19 *22* h and low energy electron decay emissions [69], ^{119}Sb is well suited for RPT. It forms a theranostic pair with ^{117}Sb ($t_{1/2}$ = 2.80 *1* h, E_γ = 158.562 *15* keV, I_γ = 85.9%, $E_{\beta+}$ = 262.4 *39* keV, $I_{\beta+}$ = 1.81 *11* %) [72], which emits a 158.6 keV photon ideal for single photon emission computed tomography (SPECT) imaging [48,69] and positrons. The identical chemical properties of isotopes result in identical pharmacokinetic behavior. Two stable isotopes of antimony (^{121}Sb, ^{123}Sb) exist, with many radioisotopes being identified. **Table 2** summarizes half-lives, decay modes, and primary or medically relevant emissions for radioisotopes of antimony produced via proton or deuteron bombardment of tin with half-lives greater than 1 h.

Table 2: Radioantimony isotopes produced via proton and deuteron bombardment of natural tin with primary or medically useful emissions and relevant half-lives [71–76].

Radioantimony	Half-live (h)	Decay	Emission (*I_B*)
^{117}Sb	2.80 *1*	EC/β^+ = 100%	γ = 158.561 *15* keV (85.9 *4* %) β^+ = 262.4 *39* keV (1.81 *11* %)
^{118m}Sb	5.00 *2*	EC/β^+ = 100%	γ = 253.678 *10* keV (99 *6* %) β^+ = 146.8 *14* keV (0.160 *7* %)
^{119}Sb	38.19 *22*	EC = 100%	γ = 23.870 *8* keV (16.5 *2* %)
^{120m}Sb	138.24 *48*	EC = 100%	γ = 197.3 *3* keV (87.0 *11* %) γ = 1171.7 *3* keV (100 %)
^{122}Sb	65.37 *48*	β^- = 97.59% EC/β^+ = 2.41%	β^- = 523.6 *8* keV (66.73 *22* %) γ = 564.24 *4* keV (70.68 *18* %) β^+ = 290.0 *13* keV (0.0061 *5* %)
^{124}Sb	1444.8 *72*	β^- = 100%	β^- = 193.8 *6* keV (51.24 *19* %) γ = 602.7260 *23* keV (97.8 *3* %)

The AE-emitting radioisotope ^{119}Sb provides high LET deposition and a clean dose profile because its highest energy photon emission is 29.1 keV [69,71], and it emits an average of 24 CEs and AEs per decay [70].

1.4.1. *In silico* Cellular Dosimetry Applications of Antimony-119

Yet to be introduced into living systems, ^{119}Sb dosimetry has exclusively been studied via computational modeling. In 2008, [48] calculated MIRD S-values and theoretical dose distributions for ^{119}Sb in various intercellular locations. Dose distributions from various radionuclides (^{67}Ga, ^{193m}Pt, ^{111}In, ^{165}Er, ^{123}I, ^{125}I, ^{119}Sb, and ^{201}Tl) in a spherical 8 μm radius cell with 6 μm nuclear radius were compared against one another. Of the compared AE-emitters, ^{119}Sb delivered the highest dose to the nucleus when activity was uniformly distributed along the cell surface [48]. Other researchers used the Monte Carlo PENELOPE code and Monte Carlo damage simulation [77] to calculate cellular S-values and biological effectiveness for AE-emitting radionuclides (^{119}Sb, ^{67}Ga, ^{80m}Br, ^{89}Zr, ^{90}Nb, ^{99m}Tc, ^{111}In, ^{117m}Sn, ^{123}I, ^{125}I, ^{195m}Pt, and ^{201}Tl). More than 75% of DNA SSB and DSB occurred in regions within 2.5 μm of the center of the nucleus with ^{119}Sb providing the second highest number DNA DSB and SSB of the radionuclides tested (**Table 3**) [47].

Table 3: Comparison of simulated DNA SSB and DSB yields generated from select AE-emitting radionuclides [77].

	^{125}I	**^{119}Sb**	**^{123}I**	**^{111}In**	**^{99m}Tc**
Total SSB (Gbp^{-1} decay^{-1})	4.6	3.6	2.5	2.3	1.4
Total DSB (Gbp^{-1} decay^{-1})	0.38	0.31	0.21	0.20	0.013

In living systems, cellular geometry is irregular, so [47] explored the impact of off-centered nuclei on subsequent cellular S-value calculations for 12 relevant radionuclides. For ^{119}Sb, eccentricity had an extremely large effect on subsequent S-value calculation as seen by an increase in S-value (N→CS) when the off-centered nucleus is closer to the cell surface and lower energy electrons can reach the nucleus to add dose. Reasonably, [47] also shows a decrease in cellular S-value (N→Cy) when the nucleus is off-centered as cytoplasm is displaced and activity located further from the nucleus. For IC/AE radionuclides such as ^{119}Sb, it is imperative to use Monte Carlo methods with event-by-event simulation to have adequate spatial resolution or else suffer an underestimation of secondary electrons created by higher energy CEs, which greatly underestimates energy deposition [47]. **Table 4** compares ^{119}Sb nucleus-to-nucleus S-value reported within literature for various cell and nuclear radius. The lack of high energy gamma emissions from ^{119}Sb makes it difficult to quantify *in vivo* distribution and dosimetry using common lab instrumentation. Theranostics (therapy/diagnostics) helps solve this problem.

Table 4: Comparison of ^{119}Sb S-value calculations (Gy/Bqs) reported within literature.

r_c	r_N	**S(N→N)** [48]	**S(N→N)** [77]	**S(N→N)** [47]
5	2	0.0372	0.0309	0.0394
5	3	0.0128	0.00953	0.0142
5	4	0.00616	0.00418	0.00716
8	6	0.00234	0.00132	0.00272
9	7	0.00162	0.000853	0.00186
10	9	0.000874	0.000415	0.00097

1.5. Theranostics and RPT Imaging Congeners

Theranostics entails pairing therapeutic radionuclides with diagnostic congeners, enabling imaging and therapeutic treatment capabilities. Matched chemical families or properties can be exploited when radioisotopic imaging analogues are not available. Theranostic pairs allow measurement and quantification of *in vivo* biological distributions of therapeutic analogues for radiopharmaceutical development and dosimetry [78]. Positron emission tomography (PET) or SPECT techniques perform physiological imaging and need to be registered to additional modalities (CT, MR) for anatomical identification [79].

1.5.1. PET

Proton rich nuclei decay by either IC, EC, or positron (β^+) emission. Following emission, the β^+ will travel through surrounding matter, losing energy through collisions until annihilating with its antimatter counterpart—the electron. Annihilation results in the conversion of rest mass into two antiparallel photons each with energy 511 keV [79,80]. In PET imaging, rings of detectors windowed for energy (350-650 keV) and time (3-6 ns) identify coincidental annihilation photons [80], indicating (β^+) annihilation events along a line of response (LOR) drawn between the two detectors. Filtered back projection or statistical reconstruction of the coincidence data provides the PET image [80]. Time-of-flight (TOF) PET measures the timing difference between the detection of the two annihilation photons to determine annihilation event location more precisely along the LOR [80]. A PET image is the distribution of annihilation events (not β^+ decay sites) measured by the scanner, considering noise from scatter (coincidence detection post Compton scattering of at least one annihilation photon) and random (simultaneous detection of two 350 – 650 keV photons not associated with the same annihilation) events [80]. The β^+-emitter decays at the radiopharmaceutical site, and the distance the β^+ travels before annihilation is a fundamental limit to spatial resolution achievable through PET imaging. Higher energy β^+ emission results in poorer spatial resolution on the order of millimeters. To maintain conservation of momentum, annihilation photons are not emitted perfectly antiparallel, resulting in angles slightly smaller than 180°. LOR are assumed by scanners to be perfectly antiparallel, resulting in additional uncertainty in placement of annihilation events with greater non-collinearity impacts on larger diameter ring detector sizes. Non-collinearity and innate detector spatial resolution limit PET image resolution [79]. With proper characterization and calibration, PET is a quantitative molecular imaging technique with sensitivity 2-10% (0.02-0.1 CPS/Bq) [81], providing valuable information regarding subject physiology [80].

1.5.2. SPECT

In SPECT imaging, a multihole collimator mounted to the gamma detector provides 2D spatial correlation of detected photons for emission location. The collection of projections of these superimposed data sets allows 3D differentiation [82]. Preclinical SPECT scanners can provide sub-millimeter spatial resolution [83] with the choice of SPECT collimator significantly impacting scanner capabilities. Images collected with pinhole collimators achieve greater resolution at the cost of decreased detector efficiency [83]. Problems associated with pinhole collimation have largely been solved using iterative reconstruction techniques, correcting for scatter, attenuation, and response function [82,83]. Most SPECT scanner components are tuned to maximize accurate detection of technetium-99m's 142 keV emission [82] and have sensitivity 1/200th that of PET systems [81].

2. Motivation

As shown, development of effective RPT agents for cancer radiation therapy require implementation of high LET radionuclides. AE-emitters provide high LET emissions, scalable production routes, and stable daughters. Additionally, an ideal AE-emitter includes the following features: high AE yield, high AE energy, half-life between hours to days, low photon co-emission, and 20-30 keV internal CE energy for optimal self-absorbed dose.

Shown in **Figure 1**, many AE-emitters historically used in Auger radiation biology have high photon dose burden, lack optimal 20-30 keV (9-17 μm in water) range CE/AE-emissions, and have extremely short, emitted AE ranges. Many ideal AE-emitters exist with underdeveloped production, separation, and chelation chemistry technologies. This work aims to develop and study RPT capabilities of one of the most promising AE-emitters, ^{119}Sb, which has previously been limited to *in silico* computational investigation due to underdeveloped production, chemical separation, and chelation strategies. Because of high disease incidences, breast and prostate cancers have multiple well understood molecular targeting strategies (RM2 for gastrin-releasing peptide receptors, Olaparib for PARP inhibition, DUPA for PSMA targeting) which, when conjugated to radioantimony chelators, will be tested as first proof of concept ^{119}Sb RPT agent constructs.

3. Dissertation Organization

Chapter 2 surveys available literature regarding ^{119}Sb production and chemical separation, specifically focusing on the ^{119}Sn(p,n)^{119}Sb nuclear reaction. New methods for tin target fabrication are reported with beam tolerance and physical production yield characterization for ^{nat}Sn and isotopically enriched ^{119}Sn targets irradiated with low energy protons or deuterons. A novel two column chromatography separation is described which retains radioantimony, provides high Sn separation factor, contains low trace metal contamination, and pairs with high efficiency tin target recovery and recycling techniques. We developed low energy detection techniques of ^{119}Sb's unique 23.87 keV gamma emission.

Chapter 3 explores radioantimony(III) labeling using a trithiol chelator, which selectively binds radioantimony in the presence of macroscopic tin target material. We studied Sb-trithiol-diacid complex formation from purified and unpurified solutions and monitored stability in serum. Trithiol-Olaparib and trithiol-RM2 conjugated compounds were radiolabeled, purified, and tested for stability in PBS.

Chapter 4 describes extensive work characterizing the complexation of ^{1XX}Sb(V) with the tris-catechol chelator, TREN-CAM. Fast partial complexation of radioantimony with TREN-CAM in a hydroxy species was found to convert to fully complexed [$^{nat/1XX}$Sb]Sb-TREN-CAM. Complex stability was explored *in vitro* in human serum, *in vivo* through ^{117}Sb SPECT and PET imaging in healthy mice, and *ex vivo* through biodistribution measurements. We characterized and compared ^{117}Sb SPECT and PET imaging using contrast and resolution metrics measured from Derenzo phantom imaging.

Appendix A is a collection of additional data relevant to Chapter 3, including nuclear magnetic resonance (NMR) spectra, high resolution mass spectrometry (HRMS), and X-ray crystallography parameters. Appendix B includes methods, results, and data analysis for X-ray absorption spectroscopy (XAS) and X-ray crystallography experiments conducted by collaborators relevant to Sb-TREN-CAM characterization from Chapter 4. Additional NMR data supporting Chapter 4 conclusions are included.

Chapter 2: Production and Isolation of Radioantimony from Tin

1. Introduction

1.1. Contributors

Most of the content in this chapter was published in EJNMMI Radiopharmacy and Chemistry. Section 1.2 is modified from [Randhawa, P.; Olson, A. P.; et. al. *Curr Radiopharm* **2021**, *14* (4), 394–419.] Section 2.7 and 3.6 are reprinted in part from a co-first authored manuscript with collaborators from TRIUMF, University of British Columbia (UBC), and Simon Fraser University (SFU), specifically Dr. Valery Radchenko, Dr. Thomas Kostlenik, and Aivija Grundmane. [Kostelnik, T. I.; Olson, A. P.; et. al. *Nucl Med Biol* **2023**, *108352*, 122–123.]

1.2. Literature Review

1.2.1. Production of ^{119}Sb

Researchers have explored production of ^{119}Sb for medical application through two main routes: directly via (p,n) and (d,n) nuclear reactions on tin or indirectly via production of ^{119}Sb's parent radionuclide ^{119}Te and subsequent ^{119}Te/^{119}Sb generator development. Possible nuclear reactions, reaction Q values [84], and location of cross section measurements are summarized in **Table 5**.

1.2.1.1. Direct Production of ^{119}Sb via Proton or Deuteron Bombardment of Tin

The feasibility of each nuclear reaction for ^{119}Sb production depends on reaction cross sections, target design, co-produced radionuclidic impurities, and suitable accelerator access. The broad distribution of cyclotrons capable of accelerating 7-16 MeV protons, lack of radionuclidic impurities, and high relative yield favor the ^{119}Sn(p,n)^{119}Sb reaction, which is no-carrier-added (n.c.a.) upon ^{119}Sb separation from bulk target material.

Table 5: Summary of literature-reported ^{119}Sb production methods and radionuclidic impurities. Side reactions with energy thresholds below that of the desired reaction and half-lives < 1 h are excluded [72–75,85,86].

	Incident Particle	Nuclear Reaction	Q (MeV)	Side Reactions / Residual $t_{1/2}$	Ref.
Direct	p	^{119}Sn(p,n)^{119}Sb	-1.37		[87–90]
		^{120}Sn(p,2n)^{119}Sb	-10.48	^{120}Sn(p,n)^{120m}Sb / 5.76 *2* d	
	d	^{118}Sn(d,n)^{119}Sb	2.89		
		^{119}Sn(d,2n)^{119}Sb	-3.60	^{119}Sn(d,n)^{120m}Sb / 5.76 *2* d	[91,92]
Indirect	p	^{121}Sb(p,3n)^{119}Te	-19.34	^{121}Sb(p,n)^{121m,g}Te / 164.2 *8* d, 19.17 *4* d ^{121}Sb(p,pn)^{120m}Sb / 5.76 *2* d	[93–100]
		^{123}Sb(p,5n)^{119}Te	-35.11	^{123}Sb(p,3n)^{121m,g}Te / 164.2 *8* d, 19.17 *4* d ^{123}Sb(p,n)^{123m}Te / 119.2 *3* d ^{123}Sb(p,pn)^{122}Sb / 2.72 *2* d	-
		^{nat}Sb(p,x)^{119}Te		^{121}Sb(p,5n)^{117}Te / 62 *2* m, ^{17}Sb, 2.80 *1* h ^{121}Sb(p,4n)^{118}Te / 6.00 *2* d, ^{118m}Sb, 5.00 *2* h ^{121}Sb(p,n)^{121m,g}Te / 164.2 *8* d, 19.17 *4* d ^{123}Sb(p,3n)^{121m,g}Te / 164.2 *8* d, 19.17 *4* d ^{123}Sb(p,n)^{123}Te / 119.2 *3* d ^{121}Sb(p,pn)^{120m}Sb / 5.76 *2* d ^{123}Sb(p,pn)^{122}Sb / 2.72 *2* d	-
	d	^{121}Sb(d,4n)^{119}Te	-21.57	^{121}Sb(d,2n)^{121m,g}Te / 164.2 *8* d, 19.17 *4* d	[101]
		^{123}Sb(d,x)^{119}Te		^{123}Sb(d,4n)^{121m,g}Te / 164.2 *8* d, 19.17 *4* d ^{123}Sb(d,2n)^{123}Te / 119.2 *3* d	-
	α	^{116}Sn(α,n)^{119}Te	-9.99		[98,102–104]
		^{117}Sn(α,2n)^{119}Te	-16.93		[102]
		^{nat}Sn(α,x)^{119}Te		see footnote	[105]

Alpha-induced reactions involving knockout of more than two neutrons are not included because of the unavoidable creation of ^{121m,g}Te. The number of reactions initiated by irradiation of ^{nat}Sn, which has 10 stable isotopes, is so large as to make this material impractical for production of radioisotopically pure ^{119}Sb.

The Danish Technical University Hevesy Laboratory first reported thin target (5.5 mg/cm^2) ^{119}Sb end of bombardment (EOB) yields from electroplated, 97.4% enriched ^{119}Sn of 1.85 ± 0.12 MBq/μAh [48,53,90]. Tin targets were electroplated from 0.25 M potassium hydroxide (KOH) solutions at 65-70 °C with current densities of 4-6 mA/cm^2 for 6-8 h [48] and recycled at 75% efficiency [90]. Slanted target geometries increased yields, spreading beam current power over a larger water-cooled surface area as compared to perpendicular target geometries. For slanted Sn targets, they report a maximum 16 MeV proton beam current tolerance of 180 μA, giving a thermal power density 1.02 kW/cm^2 on a 15 mg/cm^2 ^{nat}Sn target, and they extrapolate measured ^{nat}Sn bombardment yields to a hypothetical 46 GBq of ^{119}Sb from a 30 mg/cm^2 6° slant, enriched ^{119}Sn target irradiated with 150 μA 16 MeV protons for 3 h [53].

Sadeghi et. al. focused on Sn target development, optimizing electroplating variables and developing a Sn sedimentation process. Sedimentation created 39.3 μm thick targets though thermal shock testing caused losses in target integrity prior to irradiation experiments. Again, KOH alkaline based electrolytic solutions out-perform acidic electrolytic solutions. Authors report best adhesion upon copper target backings at an electrolyte concentration of 40 g/L Sn, 75 °C, and 50 mA/cm^2 current density, resulting in targets with unreported thickness. To increase physical production yields without increasing target thickness, researchers employed inclined targets (6°), and a ^{nat}Sn target of unreported thickness withstood 160 μA 16 MeV beam current intensities for 10 min with no observed degradation. ^{119}Sb yields were not reported; however, some of the anticipated radionuclidic impurities ^{122}Sb, ^{120m}Sb, ^{118m}Sb, and ^{117}Sb were observed. All reported measured EOB corrected physical yields are equal to or greater than thick target (>580 mg/cm^2) physical yield predictions using the IAEA medical isotope browser [106] and TENDL database cross sections [107]. These researchers report EOB corrected physical yields (without uncertainties) for the following radioantimony isotopes with our predicted radioisotopic purity in parenthesis: 2.19 MBq/μAh ^{122}Sb (0.4%), 807 kBq/μAh ^{120m}Sb (0.2%), 46.1 MBq/μAh ^{118m}Sb (8.8%), and 430 MBq/μAh ^{117}Sb (82.5%) [108]. A thick, ^{nat}Sn target irradiated with 16 MeV protons would theoretically provide an ^{119}Sb physical yield of 42.4 MBq/μAh at 8.1% expected radioisotopic purity. Isotopically enriched targets were not tested, perhaps because of the high cost of this material.

1.2.1.2. Indirect Production of ^{119}Sb via ^{119}Te/^{119}Sb Generator

The two isomers of ^{119}Te (^{119m}Te, $t_{1/2}$ = 4.7 *4* d, EC = 100%, E_γ = 153.59 *3* keV, I_γ = 66 *3* %, E_γ = 1212.73 *7* keV, I_γ = 66.1%, ^{119g}Te, $t_{1/2}$ = 16.0 *5* h, EC = 100%, E_γ = 644.01 *4* keV, I_γ = 84.1%) [71] are the radioactive parents of ^{119}Sb—a potential feedstock in a transient equilibrium generator system, allowing ^{119}Sb access to clinics without cyclotron production capabilities [109]. Production of ^{119}Te begins with proton irradiation of ^{nat}Sb via (p,3n) and (p,5n) reactions on the two naturally occurring stable isotopes of antimony (^{121}Sb and ^{123}Sb) [95,110–112]. Proton bombardment of natural antimony produces multiple radiotellurium isotopic impurities, which decay to radioantimony isotopic impurities, specifically the ^{121}Sb(p,4n)^{118}Te and ^{121}Sb(p,5n)^{117}Te reactions. These two radiotellurium impurities will feed ^{117}Sb ($t_{1/2}$ = 2.80 *1* h, EC = 100%, E_γ 158.562 *15* keV, I_γ = 85.9%) [72] and ^{118m}Sb ($t_{1/2}$ = 5.00 *2* h, EC = 100%, E_γ 253.678 *10* keV, I_γ = 99 *6* %, E_γ 1050.69 *3* keV, I_γ = 97 *5* %, E_γ 1229.6 keV, I_γ = 100%) [73] into the system. Though ^{117}Sb is a radioantimony imaging analogue to ^{119}Sb, these two radioantimony impurities have high yield emissions of high energy photons, delivering extra dose to patients and those handling/preparing radiopharmaceutical injections.

Because the overlap between (p,3n), (p,4n), and (p,5n) nuclear reactions creates unavoidable radioisotopic side products, optimal ^{119}Te radioisotopic purity requires irradiation of enriched ^{121}Sb with protons at or below 30 MeV [94]. Experimentally measured and predicted cross sections for various proton induced nuclear reactions upon enriched ^{121}Sb are plotted in **Figure 2** with ^{121}Sb(p,3n)^{119m,g}Te traces (black and gray) reaching their peak (~400 mb) at 30 MeV. Incident proton energies on ^{121}Sb below 30 MeV avoid the (p,4n) nuclear reaction and result primarily in (p,3n), (p,2n), (p,n), and (p,pn) nuclear reactions. ^{121}Sb(p,2n)^{120}Te gives stable ^{120}Te. Tellurium-121m,g (^{121m}Te, $t_{1/2}$ = 164.2 *8* d, IT = 88.6 *11* %, E_γ 212.189 *27* keV, I_γ = 81.5 %, ^{121g}Te, $t_{1/2}$ = 19.17 *4* d, E_γ 573.139 *11* keV, I_γ = 80.4 *22* %) [86] are significant long-lived, high-energy gamma-emitting impurities in the system generated by the (p,n) nuclear reaction. Though they decay to stable ^{121}Sb, ^{121m,g}Te create a radiation safety challenge, requiring shielding of generator operators from the 212 and 573 keV photon emissions. The continual formation of stable Sb decreases achievable molar activity.

The (p,pn) side channel reaction induced on ^{121}Sb produces ^{120m}Sb ($t_{1/2}$ = 5.76 *2* d, EC = 100 %, E_γ = 89.8 *3* keV, I_γ = 79.5 *16* %, E_γ = 197.3 *3* keV, I_γ = 87.0 *11* %, E_γ = 1023.3 *4* keV, I_γ = 99.4 *3* %, E_γ = 1171.7 *3* keV, I_γ = 100%) [74]. This radioisotopic impurity will decrease ^{119}Sb generator radioisotopic purity. Because Te is produced and separated from an antimony target, residual macroscopic stable Sb is difficult to fully separate and will be loaded onto the generator. The presence of stable Sb creates chelation problems and will decrease molar activity of subsequent radiopharmaceuticals. In creation of each new generator, the first elutions will contain significant ^{nat}Sb and ^{120m}Sb, resulting in lower radioisotopic purity and molar activity ^{119}Sb than later elutions. With a ^{121}Sb(p,3n)^{119}Te reaction threshold of 19.34 MeV, production of ^{119}Te requires cyclotrons capable of accelerating 20-30 MeV protons of which the International Atomic Energy Association (IAEA) cataloged 72 globally in 2020 [113]. Many of these cyclotrons accelerate protons at a much higher energy (>60 MeV) than desired, requiring beam tuning or energy degradation. This count does not include linear accelerators capable of accelerating 30 MeV protons.

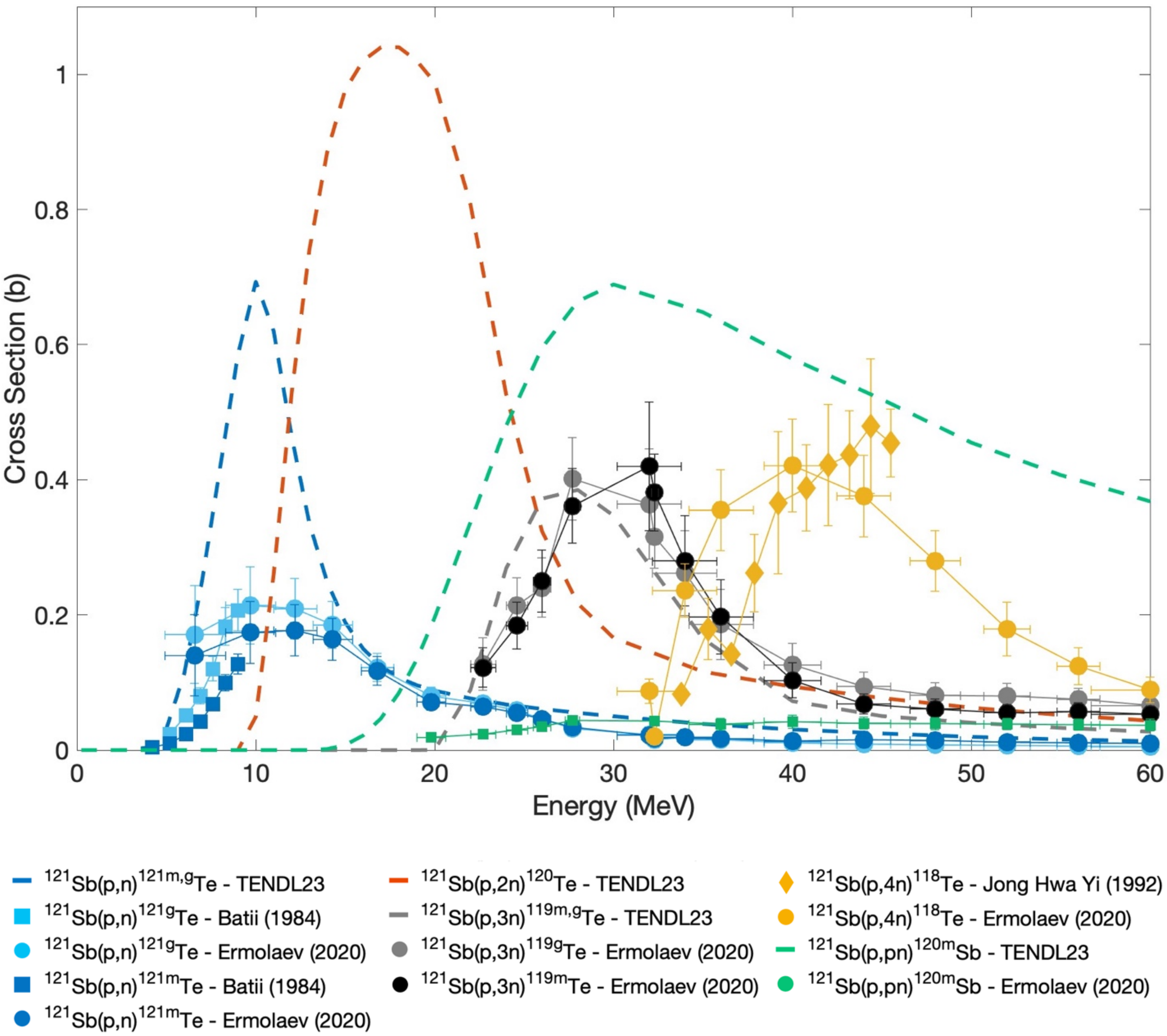

Figure 2: Experimentally measured and predicted values for proton induced nuclear reaction cross sections upon enriched ^{121}Sb targets [96,99,100,107].

Historically, most work in Te/Sb generator development has focused on ^{118}Te for the creation of the PET imaging agent, ^{118}Sb ($t_{1/2}$ = 3.6 *1* m, EC = 100 %, $E_{\beta+mean}$ = 1188.6 *14* keV, $I_{\beta+}$

= 73.2 *3 %*) [73]. The following experimental summaries in Te/Sb generator development include application of the tellurium and antimony parent/daughter radiotracer pairs ^{118}Te/^{118}Sb, ^{119}Te/^{119}Sb, and ^{125}Sb/^{125}Te.

Regarding isolation of radiotellurium from proton irradiated antimony targets, [110] developed a precipitation method that separated ^{118}Te from ^{nat}Sb target material, involving two solution matrix changes to co-precipitate Te and a final purification by distillation, resulting in 82% ^{118}Te radiochemical yield (RCY) and >99% radionuclide purity. At Los Alamos National Laboratory, a remotely handled radiochemical separation of ^{119}Te from medium energy proton irradiated ^{nat}Sb targets was developed [112]. The four-step separation process sequentially used CL resin (99% ^{119}Te RCY), Rare Earth resin (97% ^{119}Te RCY), AG 1-X8 anion resin (97% ^{119}Te RCY), and a Pre-Filter Resin (100% ^{119}Te RCY to remove excess sulfur and phosphor) to separate 2.7 Ci (5.9 x 10^{16} atoms, 100 nmol) of ^{119m,g}Te from grams (200 mmol) of ^{nat}Sb. Throughout chemical separation development, X-ray absorption near edge structure (XANES) and extended X-ray absorption fine structure (EXAFS) measurements characterized Te and Sb oxidation and speciation in various aqueous matrices and on solid-state chromatographic supports. This innovative analytical approach helped develop a system which reduced antimony target mass from 25 g to approximately 28 mg (2 ppm ^{nat}Sb in 14 mL final volume), a separation factor of 1000 [112].

An anion-exchange based separation of radiotellurium from dissolved ^{nat}Sb began with the concentrated hydrochloric acid (c.HCl) dissolved target solution diluted to 9 M HCl and 18 mg/mL Sb. 2 M HCl washed the column, and deionized water eluted radiotellurium (^{118}Te, ^{119}Te, ^{121m}Te). This new anion-exchange separation recovered 87-89% of tellurium radioisotopes with no detectable ^{118m}Sb [111]. After isolation and purification of radiotellurium from antimony targets, a generator could be synthesized. The purified tellurium elution was adjusted to pH 8 using NaOH and loaded onto activated charcoal columns sifted to mesh size either 120 – 180 or 180 – 300. Various mobile phases and mild oxidizers were monitored for generator optimization, as Sb(V) and Sb(III) have differing column affinities. Maximum recovery of ^{118}Sb was 85 – 88% in a 0.12 M boric acid / 0.020 M borax / 3.5 mM NaOCl solution, with ^{118}Te breakthrough of 0.01 – 0.07% by activity [111].

Around the same time, Miller and Sun reported optimized elution parameters for their aforementioned activated carbon based ^{118}Te/^{118}Sb generator [114]. They created the generator substrate by first pulverizing the carbon, sorting it with a 120 – 180 mesh sieve, slurring it with deionized water, packing the carbon into a 2.5 mL plastic pipette tip between two plugs of fine glass wool, and loading the generator substrate with previously purified ^{118}Te. Optimal ^{118}Te(IV) loading occurred in HCl at pH = 7 – 8 with no adsorption of ^{118}Sb(V) in pH 4-10. Five mL boluses of various mobile phases were tested for ^{118}Sb elution and ^{118}Te breakthrough over nine days. Borate (0.2 M) mobile phases had the highest ^{118}Sb yields (35 – 48%) and lowest ^{118}Te breakthrough (0.3 – 1.7%) [114]. In one Te/Sb generator study, a combination ion exchange column (1 cm neutral grade alumina and 4 cm $SnO_2[H^+]$) eluted a maximum [^{118}Sb]Sb-tartrate yield (12.5%) at pH 3.5 with 0.12% ^{118}Te breakthrough [115]. Recent reporting of a ^{125}Sb/^{125}Te generator for ^{125}Te source production describes a sulfuric acid (H_2SO_4) based distillation for purification of ^{125}Sb from ^{nat}Sn and the application of a zirconium-silico-tungstate gel matrix for ^{125}Sb retention (<0.01% ^{125}Sb breakthrough) and 88.7% ^{125}Te elution [116].

The greatest barrier facing ^{119}Sb production through a ^{119}Te/^{119}Sb generator is in the generator development. A generator needs to be developed with low retention of antimony, high retention of tellurium, and sufficient shielding. These features are necessary to provide safe operator handling, high ^{119}Sb elution in a chemical form suitable for chelation, and low ^{119m,g}Te breakthrough lest eluted ^{119}Sb gain a radioimpurity with dosimetric and chelation competition implications.

1.2.2. Purification of Antimony from Tin

Chemical separation of radioantimony from bulk tin targets has employed three main techniques: solvent extraction, precipitation, and ion-exchange chromatography. Many separation strategies require oxidation of tin and antimony to +4 and +5 oxidation states, respectively. Oxidation and subsequent speciation changes impact chelation strategies and target material recycling. Additionally, solvent extraction separation methods are difficult to automate, and final radionuclidic solutions include organic solvent contamination. [117] tested several extracting solvents, finding ethyl acetate best extracted macroscopic ^{nat}Sb as a citrate-oxalate-Sb complex from 1-2 M HCl. [118] studied sequential extraction separations of arsenic, antimony, bismuth and tin. Though successful in separating the four elements, their technique required multiple adjustments of H_2SO_4 and potassium iodide concentration in the aqueous solution. [119] investigated solvent extraction separation of Sb(III) and Bi(III) with Cyanex 302, and although the focus is the separation of antimony and bismuth, the study includes the ternary systems Sb-Sn-Cd and Sb-Sn-Tl. Though the 1.0×10^{-2} M Cyanex 302 in toluene solvent extracted Sb(III) from 0.25 M H_2SO_4 with Sn(IV) remaining in the aqueous phase [119], tin is a strong reducing agent, making a Sb(III)/Sn(IV) separation improbable.

Precipitation methods reach higher degrees of purification when combined with additional chemical techniques and processes. [120] separated tin and antimony phosphates. Three molar HCl dissolved the irradiated target, and added Br_2-H_2O oxidised the metals. Then, $(NH_4)_2HPO_4$ addition and pH 1 adjustment precipitated Sn(IV) phosphate, leaving antimony suspended in solution. In later steps, antimony precipitated as a sulfide. In both precipitation steps, stable metal impurities were added into the solution, which could impede future radiometal chelation.

Commonly, ion-exchange chromatography is applied to radiometal chemical separations. In 12 M HCl, Sb(V) adsorbs onto the strong cation exchanger Dowex 50 while In(III) and Sn(IV) elute [121]. In 0.2 M HCl, Sb(V) passes through a cation exchange column whereas Te(IV) and Sn(IV) adsorbed and were later eluted with 0.5–1 M HCl [122]. Three molar HCl loaded antimony, tin, and tellurium onto the strong cation exchanger Dowex 1. One hundred millimolar oxalic acid eluted Te, 100 mM oxalic acid pH 4.5 eluted Sb(V), and H_2SO_4 eluted Sn(IV). Despite using a long column (30 cm), tin and antimony cross contaminated 1% [123]. Two-to-three molar malonic acid pH adjusted to 4.8 using 9 M ammonium hydroxide (NH_4OH) loaded tin and antimony tracers onto the strong anion exchange resin Amberlite IRA-400. Three percent malonic acid pH 4.8 eluted Sb(V), and 9 M sulfuric acid eluted tin [124]. [125] developed a simple method for the separation of carrier-free ^{125}Sb from neutron-irradiated tin. c.HCl dissolved irradiated targets, and bromine addition to the dilute target solution oxidized the metals, yielding a solution of 1 M HCl / 1 M HBr. Under such conditions, Sn(IV) adsorbed to a strong anion-exchange resin, and Sb(V) passed through the column with a final 170 mL elution yielding 90 percent ^{125}Sb and >99.99% radiochemical purity. The large eluent volume would require evaporation and subsequent radioantimony concentration.

Also employing a strong anion exchange resin, [126] reproduced previously mentioned elution trends using Dowex 1, showing Sn(IV) eluted in 0.8 M HCl while Sb(V) eluted with 1 M HNO_3. The Heversy laboratory studied a weak anion exchange resin for the separation of tin and antimony [48]; however, their results exhibit a reversed trend as previously observed with Sb(V) eluting first from the weakly basic anion exchange resin AG 4-X4 at 0.8 M HCl [127].

1.3. Motivation

Clinical production of radionuclidically pure ^{119}Sb is scalable via ^{119}Sn(p,n)^{119}Sb or ^{118}Sn(d,n)^{119}Sb nuclear reactions, which require recycling of enriched $^{118/119}$Sn. Barriers in production and chemical coordination have limited ^{119}Sb dosimetry to *in silico* study. Limitations in the thickness of achievable tin electrodeposits have motivated implementation of slant target geometries, which are not as broadly employed as perpendicular geometries, to compensate for limited production capacity. Development of a target fabrication method, which electroplates a tin target energetically thick to a 16 MeV proton beam (>580 mg/cm^2) would eliminate this production barrier.

Various chemical separation techniques to remove bulk tin target material and isolate radioantimony have been reported [128], but bifunctional chelation of purified radioantimony has not been reported. Most research into the separation of antimony and tin has employed Sb(V) and Sn(IV), large elution volumes, or harsh, high acidity solvents. Little development has focused on Sb(III)/Sn(II) separation schemes. The thiophilic quality of pnictogens motivated exploration of a thiol functionalized resin for radioantimony purification reported within, and Sb(V)'s ability to extract from c.HCl solutions into ethers motivated development of a liquid-liquid solvent extraction method. No reporting of isotopically enriched ^{119}Sn target material recycling exists.

2. Materials and Methods

2.1. Chemicals

All reagents and starting materials were purchased from commercial vendors without further purification. All solutions were prepared with 18 MΩ*cm deionized water (MilliQ water). c.HCl, sodium hydroxide (NaOH), and ethanol (EtOH) were sourced from Fisher Chemicals (Hampton, NH, USA). VWR Life Sciences (Radnor, PA, USA) supplied DMSO.

2.2. Electroplating Tin Cyclotron Targets

A stannous sulfate ($SnSO_4$) electrolytic solution electroplated metallic tin targets (8 mm ⌀, 80-760 mg/cm^2, see **Table 6 and 7**) onto gold and silver target backings. Briefly, $SnSO_4$ (90 mg; Strem Chemicals, Newburyport, MA) was dissolved in 100 µL of concentrated H_2SO_4. After addition of phenol sulfonic acid (45 µL; Sigma-Aldrich), gelatin (2 mg; Dot scientific, Burton, MI), 2-naftol (1 mg; Chem CruzTM, Dallas, TX) and 100 µL MilliQ water, the solution was gently heated (50 °C) and vortexed. MilliQ water was added to bring the total volume to 1 mL. After transferring the solution to the electrodeposition chamber, a constant 3.0V voltage controlled bias (382200 DC Power Supply, Extech Instruments, Long Branch, NJ, USA) applied between a platinum wire anode and gold disk cathode resulted in ~50 mg of tin deposited onto the target backing surface over 48 hours. Bath constituents and electroplating conditions are reported in **Table 6**. These parameters plate ~50 mg metallic Sn per mL electrolyte, and for larger mass targets, larger electrolyte volumes were employed. Before electroplating the 96.3% isotopically enriched ^{119}Sn targets (**Table 7**, Isoflex, San Francisco, CA, USA), metal foil purchased in 2018 for 6 USD/mg was dissolved in c.HCl at room temperature and reclaimed using recycling techniques described below.

Table 6: Electroplating bath composition.

Component	**Value**	**Source**
Stannous sulfate	90 g/L	Strem Chemicals
Sulfuric acid	180 g/L	Fisher Chemical (trace metals grade)
Phenol sulfonic acid	60 g/L	Sigma-Aldrich
Gelatin	2 g/L	Dot Scientific
2-Naftol	1 g/L	Chem CruzTM
Current Density	6 mA/cm^2	

2.3. Target Irradiation and Activity Characterization

We irradiated Sn targets with up to 16 MeV protons and 8 MeV deuterons using a GE PETtrace cyclotron. A 500 μm thick aluminum degrader reduced an incident 16 MeV beam energy down to 12.5 MeV. To minimize unnecessary dose to radiation workers, proton irradiated targets were decayed overnight before use. Deuteron irradiated targets were decayed a minimum of 45 min before retrieval.

Table 7: Composition of ^{nat}Sn and ^{119}Sn targets irradiated within the following productions.

Stable Tin Isotopes	Natural Enrichment	Isotopically Enriched
Sn-112	0.97	< 0.001
Sn-114	0.66	< 0.001
Sn-115	0.34	0.006 ± 0.002
Sn-116	14.54	0.014 ± 0.001
Sn-117	7.68	0.019 ± 0.001
Sn-118	24.22	2.57 ± 0.02
Sn-119	8.59	96.30 ± 0.04
Sn-120	32.58	1.056 ± 0.006
Sn-122	4.67	0.019 ± 0.010
Sn-124	5.79	0.016 ± 0.010

End of bombardment (EOB)-corrected physical yields [129] for ^{117}Sb, ^{118m}Sb, ^{120m}Sb, ^{122}Sb, ^{124}Sb, and ^{125}Sb were quantified via gamma spectroscopy with an aluminum-windowed high purity germanium (HPGe) detector (AMETEK ORTEC, Knoxville, Tennessee) coupled to a Canberra (Concord, Ontario) Model 2025 research amplifier and multichannel analyzer calibrated with ^{241}Am, ^{133}Ba, ^{152}Eu, ^{137}Cs, and ^{60}Co sources (Amersham PLC, Little Chalfont, U.K.) for energy and efficiency. The system has a full width at half maximum (FWHM) resolution of 1.8 keV at 1333 keV. Antimony-117 ($t_{1/2}$ = 2.80 *1* h) and ^{117m}Sn ($t_{1/2}$ = 14.00 *5* d) share a 158.56 keV photon emission [72]. After ^{117}Sb decayed (>30 h post EOB), ^{117m}Sn activities were quantified and ^{117}Sb yields corrected for ^{117m}Sn signal contribution. Measured EOB corrected physical yields were compared against theoretically predicted yields from the IAEA medical isotope browser and TENDL sourced cross sections [106]. When radioantimony isotopes were not detected, yields are reported from limit of detection (LOD) measurements. Radioisotopic purity is reported as the percent activity of choice radioisotope within the sum of all radioactive isotopes.

Antimony-119 yields were measured using a Be-windowed cadmium telluride (CdTe, Amptek X-123) X-ray spectrometer calibrated for energy and efficiency using ^{241}Am, ^{133}Ba, and ^{152}Eu check sources. Quantifying ^{119}Sb activity in solution or solid, undissolved targets is challenging because of high susceptibility to attenuation and scatter of its sole, low-energy gamma (E_{γ} = 23.870 *8* keV, Iγ = 16.5 *2 %*). To obviate the need for attenuation correction, massless sources were made for spectrometry (**Figure 3**) and mounted perpendicular to the benchtop and in line with the CdTe detector face (**Figure 3 upper right**), preventing the walls of the plastic microcentrifuge tubes from impeding detected photons. After target dissolution and radioantimony purification, 10 μL of radioantimony was reserved in a microcentrifuge vial and dried overnight to form a massless source. These dried, uncovered aliquots of purified radioantimony were mounted in line with the CdTe detector face (**Figure 3**). In the low energy photon spectrum, ^{119}Sb's sole gamma (23.87 keV) overlaps X-ray emissions (~25 keV) from multiple radioantimony isotopes. We deconvolved the 23.87 keV peak area by fitting two overlapping gaussian distributions. To accurately quantify ^{119}Sb yields, the same massless sources were assayed on both the HPGe and CdTe detectors. The total target ^{119}Sb activity ($T_{119_{Sb}}$) was calculated using ^{120m}Sb as a tracer, measuring the fraction of ^{120m}Sb from the total target activity ($T_{120m_{Sb}}$) in the massless source ($S_{120m_{Sb}}$) to correct the ^{119}Sb massless source activity ($S_{119_{Sb}}$) (**Equation 1**).

Eq 1) $$T_{119_{Sb}} = (S_{119_{Sb}})\left(\frac{T_{120m_{Sb}}}{S_{120m_{Sb}}}\right)$$

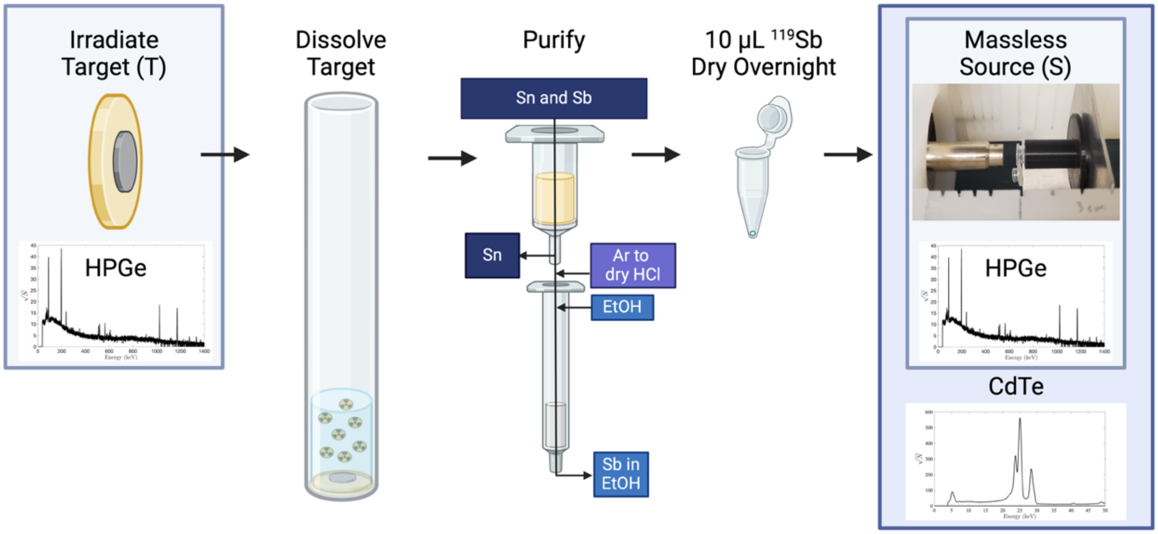

Figure 3: Illustration of ^{119}Sb massless source creation, spectra collection, and irradiated target yield correction workflow. Created with BioRender.com.

2.4. Radiochemical Isolation of Radioantimony from Target Material using Column Chromatography

We dissolved irradiated targets in 6 mL c.HCl at 90 °C for 1-2 h in a glass tube under N_2. The dissolved target solution was then removed from the heated glass chamber, and the inside of the chamber was washed with 2 mL c.HCl, creating a combined volume of 8 mL. Antimony was chemically separated from ^{nat}Sn or ^{119}Sn target material using two sequential chromatographic columns. A 100 mg mercaptopropyl functionalized silica gel resin (Sigma-Aldrich, 200-400 mesh) packed in an 8.8 mm inner diameter (ID) column (Sigma-Aldrich, 20 µm top and bottom frits) was preconditioned with 10 mL 1M HCl, 10 mL 0.1M HCl, and 10 mL MilliQ water. We packed a second column (5.5 mm ID, Sigma-Aldrich, 20 µm top and bottom frits) with 100 mg of a hydrophilic microporous acrylic ester polymeric resin (Prefilter resin, Eichrom, 100-150 mesh) and preconditioned it with 10 mL EtOH then 10 mL MilliQ water. We diluted the dissolved target solution 10x with MilliQ water and loaded it onto the mercaptopropyl resin. The loaded resin was washed with 5 mL 0.1 M HCl/99% EtOH prepared by combining 0.1 mL 10.5 M HCl with 10.4 mL EtOH. Antimony was eluted from the resin using 1.5 mL 5 M HCl in 48% EtOH, prepared by combining 5 mL 10.5M HCl with 5.5 mL EtOH, fractionated into two 750 µL volumes. The first 750 µL fraction was loaded onto the second column comprised of Prefilter resin. Argon was passed through the loaded Prefilter resin to evaporate acidic EtOH from the column. After 40 minutes of column drying, 5 mL of EtOH eluted the radioantimony from the column and was used for radiolabeling experiments.

2.5. Chemical Analysis of Column Chromatography Separation

Trace metal contamination was measured using an Agilent (Santa Clara, CA, USA) 5800 inductively coupled plasma optical emission spectrometer (ICP-OES). For samples in organic matrices, a 0.8 mm ID torch replaced the standard 1.2 mm ID torch. Calibration curves were generated by diluting commercially available standards of Sn, Zn, Cu, Ni, Fe, Co purchased from Sigma-Aldrich (St. Louis, MO, USA) and Sb (SPEX CertiPrep, Metuchen, NJ, USA) to the following concentrations: 50 ppm, 10 ppm, 5 ppm, 1 ppm, 0.5 ppm, and 0.1 ppm with sample matching solvent matrices. For transition metals, LODs are typically in the part per billion (ppb) range and part per million (ppm) range for metalloid elements.

To investigate high molarity HCl decomposition of the mercaptopropyl resin, eluent fraction thiol concentrations were quantified using Ellman’s reagent [130,131]—a UV-Vis active disulfide bond-containing compound that loses UV activity when reacted with thiols. Ellman’s reagent (Sigma-Aldrich) reacts 1:1 with free thiols, therefore its 412 nm absorbance measurement is linearly related to solution thiol concentration. Using an Ocean Optics UV-Vis spectrometer (USB-LS-450, Ocean Insight, Orlando, FL, USA) and OceanView software, a calibration curve was constructed by reacting solutions of known cysteine concentration (0.1 µM, 1 µM, 10 µM, 50 μM, 100 μM, 250 μM, and 500 μM) with 0.01M Ellman's reagent in 0.1M sodium phosphate buffer pH 7.5. Thiol resin elution fractions were neutralized with 1 M NaOH (highly acidic environments reduce Ellman's reagent), combined with equal volume Ellman's reagent solution, monitored for 412 nm absorbance, and compared against the calibration curve for thiol concentration determination.

2.6. Recycling Target Material

Sn target material was recycled by combining first column thiol resin load and wash fractions and neutralizing with NaOH, precipitating tin hydroxide ($Sn(OH)_2$). The solution was centrifuged to concentrate the $Sn(OH)_2$ precipitate into a pellet. The supernatant was twice discarded after $Sn(OH)_2$ was washed with MilliQ water. Afterwards, we added concentrated H_2SO_4 to the precipitated pellet, dissolving the $Sn(OH)_2$ and forming $SnSO_4$. We then added additional electroplating constituents according to ratios in **Table 8** and diluted it to a final volume with MilliQ water. The electrolyte was biased to 3V for 48 h with a platinum anode and target backing.

Table 8: Ratios of electroplating constituents used to recycle target material.

Component	Value
Dissolved Metallic Tin	250 mg
Conc. Sulfuric acid	500 μL
Phenol sulfonic acid	448 μL
Gelatin	10 mg
2-naftol	5 mg
Total Volume	5 mL

2.7. Radiochemical Isolation of Radioantimony from Target Material using Liquid-Liquid Extraction

Development of a liquid-liquid extraction (LLE) chemical separation scheme occurred in collaboration with researchers from TRIUMF, and radioantimony was created through proton irradiation of ^{nat}Sn foils. Natural tin foil targets (3.0 cm diameter, 0.127 mm thick, acquired from Sigma-Aldrich) were irradiated with protons (entrance energy 16 MeV for GE PETtrace and 12.8 MeV for TRIUMF's TR13) for 1 h with a current of 5 μA. At UW-Madison, the foil was water cooled. Irradiated targets were left in the cyclotron vault for 2 – 16 h following irradiation. We trimmed foils to remove non-irradiated portions and reduce tin mass.

Trimmed tin target foils (400 – 480 mg) were dissolved in 6 – 12 mL c.HCl in either a covered (not sealed) 16 mL borosilicate KIMAX tube (25 °C, overnight) or sealed glass tube under N_2 (90 °C, 2 h). The target solution was transferred into a 50 mL Falcon centrifuge tube. A small volume of c.HCl (800 μL) rinsed the dissolution tubes before being combined with the dissolved target, and heated solutions were cooled for 15 min using ice water. Added H_2O_2 (30 % w/w, 150 μL) oxidized Sb(III) and Sn(II) to Sb(V) and Sn(IV) over ~15 min. Equal volume dibutyl ether (DBE) was added to the oxidized target solution before vortexing for 5 min. After the solution settled, phases were separated by pipetting the organic phase from the Falcon centrifuge tube into a new 50 mL tube. At TRIUMF, DBE and dissolved target phases were not fully separated. A sacrificial 1 mL DBE volume remained to prevent contamination of the DBE phase with bulk tin. At UW-Madison, no DBE phase was sacrificed. Two washing steps (equal volume c.HCl) were combined, vortexed, and separated from the extracted DBE phase. Finally, we back extracted Sb from the organic phase into equal volume sodium citrate solution (0.1 M, pH 5.5) by vortexing for 5 min and separating as described above. We employed gamma spectroscopy to analyze the target solution, extracted target solution, HCl wash #1, HCl wash #2, extracted DBE solution, and final back extracted solution, tracking radioantimony retention and radionuclidic impurities.

Inductively coupled plasma mass spectrometry (ICP-MS) analysis was conducted using an

Agilent 8900 Triple Quadrupole ICP-MS. All measurements were acquired in helium mode. Collaborators at TRIUMF performed ICP-MS analysis on samples collected throughout LLE processing of 6 non-irradiated targets. Starting with 12 mL of the target solution, 1 mL of each fraction was reserved for analysis. The samples were dried overnight and converted to a 2% nitric acid matrix for analysis. Because H_2O_2 oxidizes Sn(II) to Sn(IV) and Sn(IV) does not electroplate from acidic electrolytic solutions, Sn target material processed by LLE was not recycled.

3. Results and Discussion

3.1. Electroplating Tin Targets for Cyclotron Targetry

Dense, thermally conductive ^{nat}Sn targets for proton/deuteron irradiation were created using an electrodeposition technique with strong adherence observed when electroplating onto either silver or gold target backings. Two such targets are shown in **Figure 4**. The technique achieves good visual uniformity and Sn thicknesses > 400 mg in 0.5 cm^2 (8 mm diameter, ~800 mg/cm^2), resulting in thick targets, which completely absorb the 16 MeV proton or 8 MeV deuteron beam energy. **Figure 4 right** shows accumulated, electrodeposited mass over time in this electroplating system. More than 80% of Sn(II) ($SnSO_4$) is electroplated within the first 24 hours. Although Sn electrodeposits onto either silver or gold, gold target backings were employed due to improved radiolabeling of isolated radioantimony.

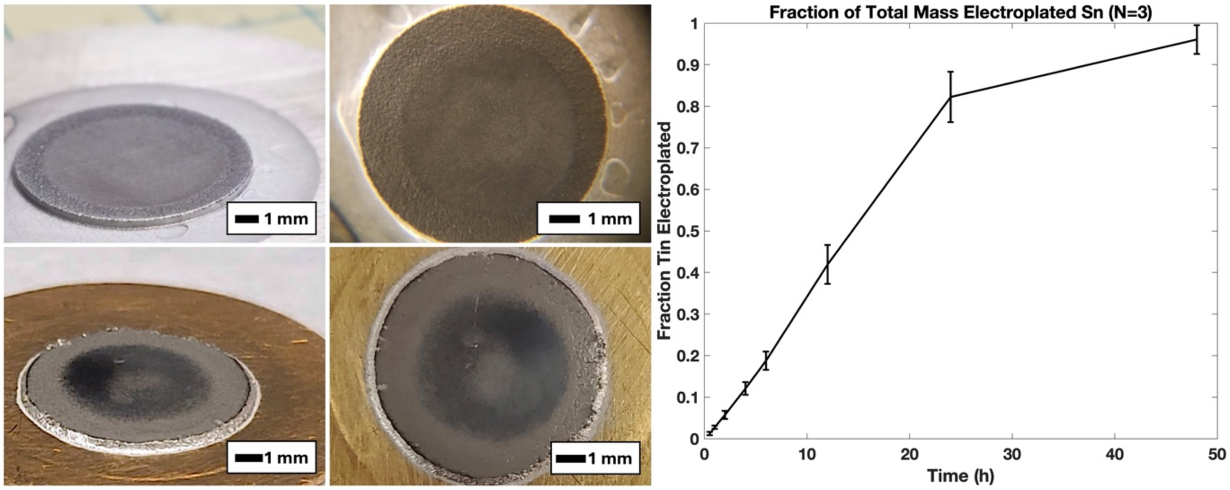

Figure 4: Two unirradiated, 150 mg (300 mg/cm^2) ^{nat}Sn cyclotron targets plated from non-recycled $SnSO_4$ stock onto silver (top left) and gold (bottom left) target backings with surface images shown to the right of their corresponding target image. (right) Sn electrodeposition vs time.

3.2. Target Irradiation and Activity Characterization

Charged particle beam tolerance primarily depends on the rates of beam energy deposition and removal from the target. Particle type, particle energy, target composition (electrical and thermal conductance of materials, melting temperature of material) and heat removal strategy bear on these parameters. We employ direct water cooling to the back of gold target disks. Electroplated Sn targets on gold backings with areal density ~300 mg/cm^2 withstood 16 MeV, 40 µA proton irradiation with physical deformations depicted in **Figure 5**. No physical deformations were observed over the dozens of 16 MeV, 35 µA proton irradiations for targets with areal density up to 500 mg/cm^2 (> 2 h). Targets with > 600 mg/cm^2 ^{nat}Sn electroplated onto gold have experienced small deformations at 35 µA of 16 MeV. One hundred mg (200 mg/cm^2) ^{nat}Sn targets withstood 40 µA of 8 MeV deuterons with no physical deformations.

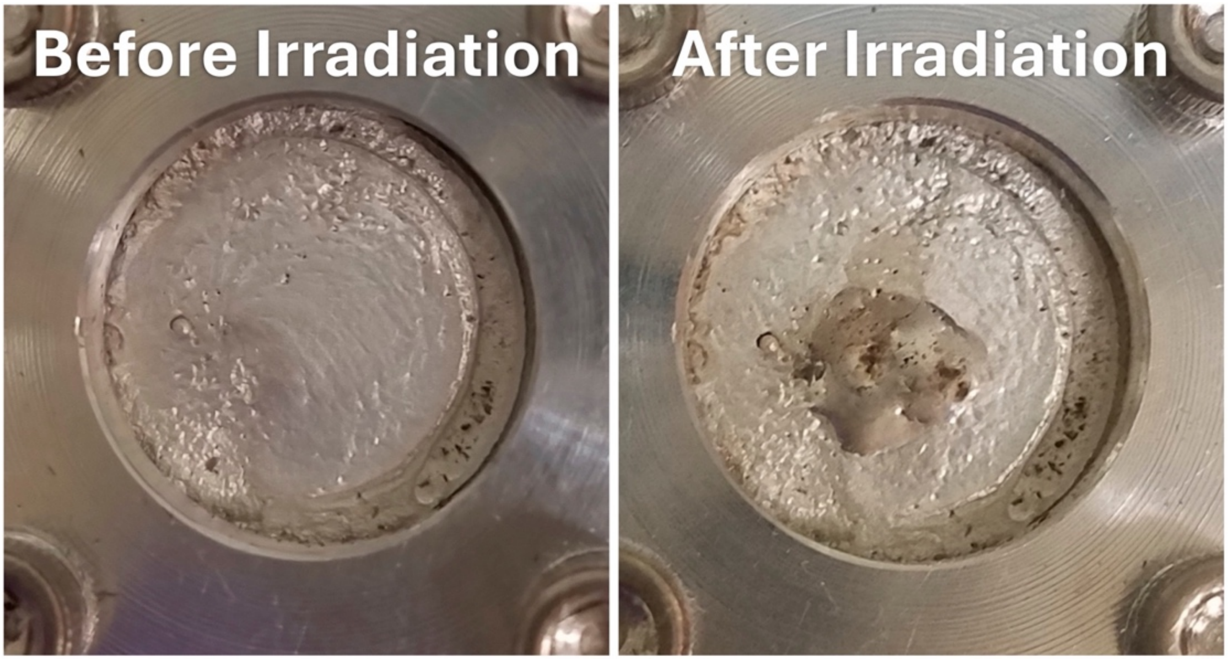

Figure 5: A representative 290 mg/cm^2 Sn target before (left) and after (right) proton irradiation with 40 μA 16 MeV protons for 6 min.

Proton irradiation of tin's ten naturally occurring isotopes with 12-16 MeV protons makes a cocktail of antimony, tin, and indium radioisotopes. The measured yields of these residuals are presented in **Figure 6** with EOB physical yields of relevant radioantimony isotopes and varied production parameters. Tabulated presentation of measured EOB physical yields is reported within **Table 9** and **Table 10**. In most cases, measured physical yields for ^{117}Sb, ^{118m}Sb, ^{119}Sb, and ^{120m}Sb were comparable to IAEA TENDL predicted values with measured 16 MeV proton yields ranging from 0.5-1.6x IAEA TENDL predicted values and 8 MeV deuteron yields ranging 0.3-2.3x predicted values.

Table 9: EOB-corrected measured physical yields (MBq/μAh) for irradiations. Uncertainty is reported as standard deviation of N = 3 measurement replicates.

	16 MeV p^+ Thick (>600 mg/cm^2) ^{nat}Sn	16 MeV p^+ 512-522 mg/cm^2 ^{nat}Sn	8 MeV d^+ Thick (164-205 mg/cm^2) ^{nat}Sn	16 MeV p^+ 134-162 mg/cm^2 96.3% ^{119}Sn
^{117}Sb	(4.9E+02) ± (2E+01)	(4.5E+02) ± (4E+01)	(2.4E+01) ± (3E+00)	(2.1E+01) ± (2E+00)
^{118m}Sb	(1.90E+01) ± (3E-01)	(1.6E+01) ± (2E+00)	(2E-01) ± (1E-01)	(2.5E+01) ± (2E+00)
^{119}Sb	(3.0E+01) ± (3E+00)	(4E+01) ± (1E+01)	(1.6E+00) ± (7E-01)	(1.2E+01) ± (1E+00)
^{120m}Sb	(4.8E-01) ± (2E-02)	(4.2E-01) ± (4E-02)	(2E-02) ± (1E-02)	(6E-03) ± (8E-04)
^{122}Sb	(7E-01) ± (1E-01)	(4.6E-01) ± (1E-02)	(1.2E-01) ± (7E-02)	(8.9E-06)*
^{124}Sb	(3E-02) ± (1E-02)	(2.3E-02) ± (8E-03)	(1.7E-02) ± (5E-03)	(6.4E-06)*
^{125}Sb	(3.6E-06)*	(8.6E-06)*	(3.7E-06)*	(1.3E-05)*

* LODs are reported when radioisotopes are undetected within production.

Observed differences between measured and predicted values could be due to the beam spot being larger than the target face [132] or TENDL over/underestimating cross section values. Thisgaard measured a ^{119}Sn(p,n)^{119}Sb cross section peak of 1.08 barns ± 0.07 barns at a proton energy of 11.0 MeV ± 0.15 MeV [133] while the TALYS model presented in the TENDL database predicts a cross section of 0.691 barns at 11 MeV [107]. Antimony-125 was never observed, and when using isotopically enriched ^{119}Sn targets, ^{124}Sb was also not observed. Our thick 16 MeV proton target yields for ^{117}Sb and ^{120m}Sb match those previously reported, and our ^{118m}Sb and ^{122}Sb yields equal less than half of those previously measured [108].

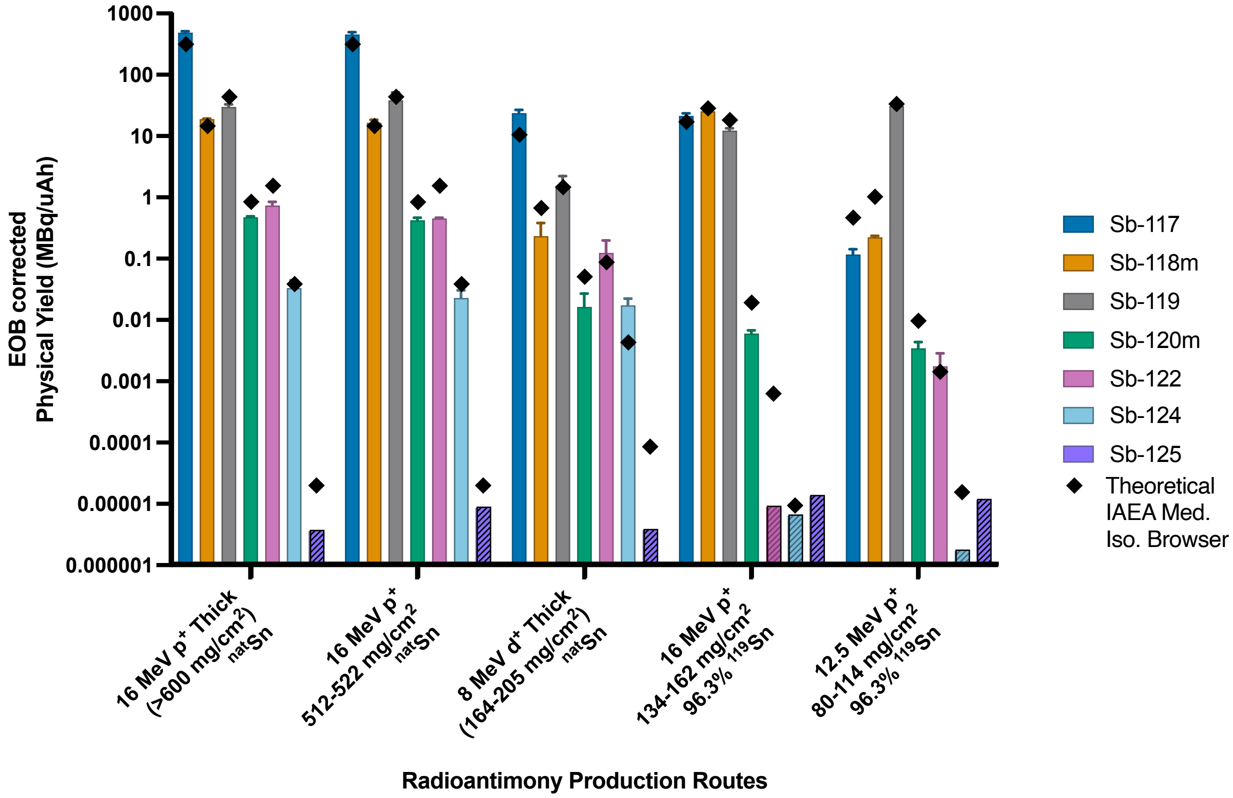

Figure 6: Comparison of EOB corrected measured physical and theoretical yields with LOD represented as cross-hatched yield bars for each experiment. Theoretical yields were calculated using the IAEA Medical Isotope Browser [106]. All data are N = 3 replicates.

Because of the impact of cross section on radionuclide production, particle type, particle energy, target isotopic composition, and target thickness are all variables that can be changed and leveraged to modify the resulting radioantimony production profile to desired application needs. Bombarding ^{nat}Sn with 16 MeV protons produces the greatest quantity of radioisotopic impurities when considering the radionuclidic purity of the two antimony radioisotopes with greatest medical interest (**Figure 7**) – ^{119}Sb and ^{117}Sb. The highest purity of ^{117}Sb (92.36% ± 2.00% at EOB) with the lowest contribution from higher dose, longer lived radioisotopic impurities (0.06% ± 0.04%

^{120m}Sb, 0.48% ± 0.26% ^{122}Sb, and 0.07% ± 0.01% ^{124}Sb at EOB) is produced via deuteron bombardment of ^{nat}Sn. Isotopically enriched ^{116}Sn or ^{117}Sn was not available for this work. Deuteron bombardment of ^{nat}Sn produces less longer-lived contaminants when compared to proton irradiation (~10-fold less ^{122}Sb and ~100-fold less ^{120m}Sb), facilitating pre-clinical imaging *in vivo* applications.

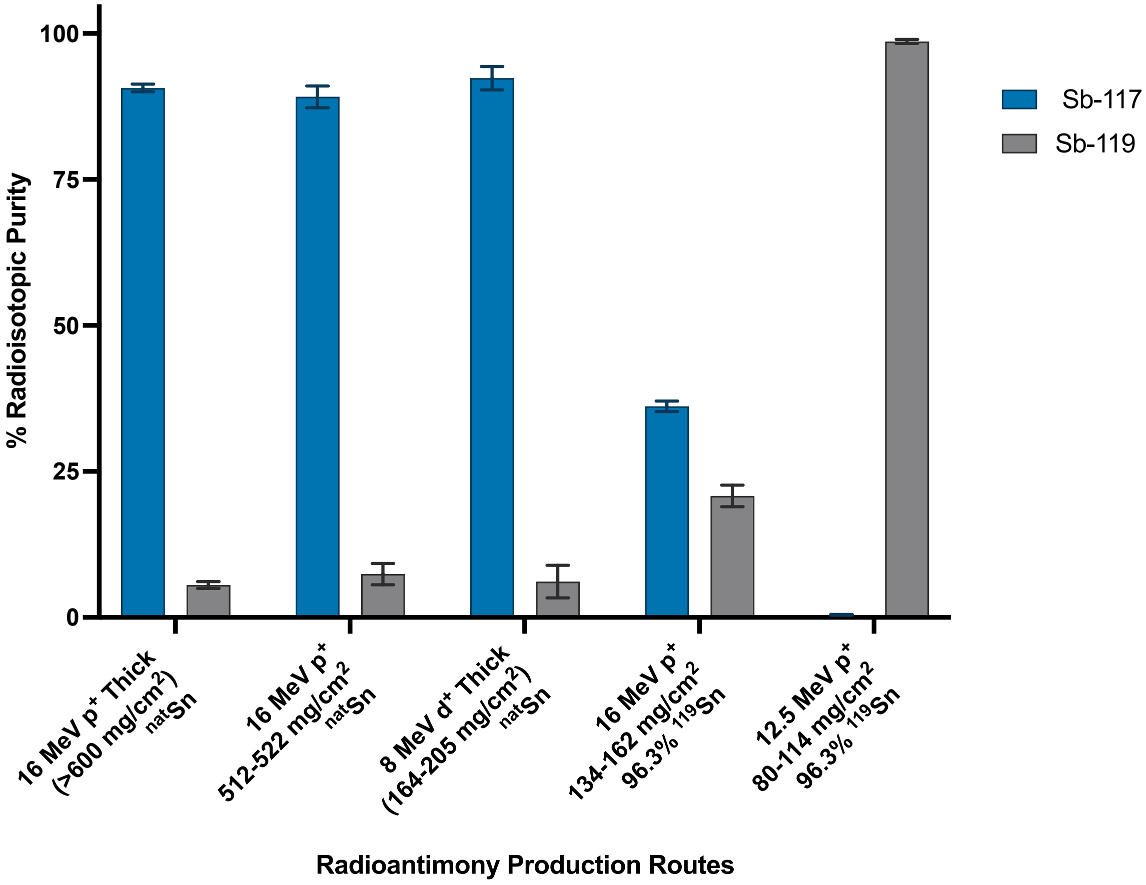

Figure 7: EOB corrected radionuclidic purity of ^{117}Sb and ^{119}Sb for various characterized production routes and 0.5 – 2 h irradiations. All data are N = 3 replicates.

The short half-life of ^{117}Sb (2.80 *1* h) requires timely handling and restricts workflows to <1 d. Also, the low energy photon emissions of ^{119}Sb (<30 keV) require specialized low energy detection techniques. Radioisotopes such as ^{120m}Sb and ^{122}Sb have half-lives on the order of days and emit high energy photons that (though easily shielded for radiation worker protection) can be detected with standard gamma detection equipment. For multi-day, small-scale radiochemical or targetry development with tracers, proton bombardment of ^{nat}Sn produces the greatest proportion of these antimony radioisotopes.

Figure 8 includes representative HPGe spectra from undissolved targets irradiated with protons and deuterons at varied energies. In some of the HPGe spectra, two peaks (133.98 keV, 77.35 keV) are observed from ^{197m,g}Hg produced within the gold target backings. We did not observe ^{197m,g}Hg in the radiochemically purified product, and the apparent 511 keV annihilation photons indicate positron emitters, including ^{117}Sb's 1.81% β⁺ branching ratio.

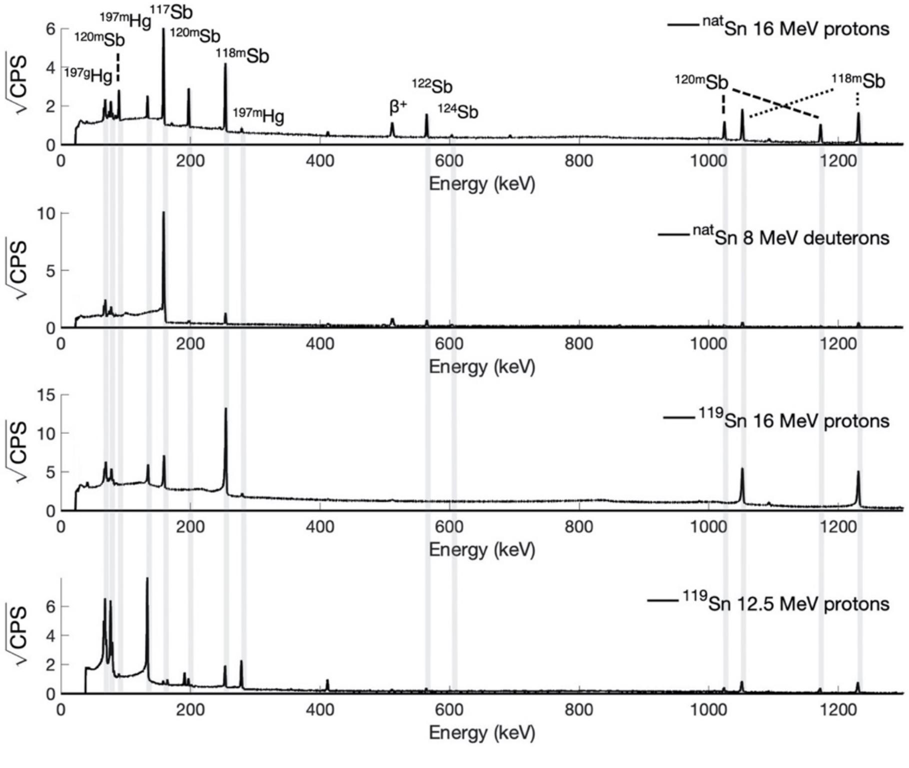

Figure 8: HPGe gamma spectra of representative irradiated targets depicting significant differences in radioantimony profiles produced via differing production routes. 8 MeV deuteron irradiated target spectrum was collected 1 h post EOB. Proton irradiated target spectra were collected 16 h post EOB.

Antimony-119 yields were measured directly in a massless source configuration. A representative low energy ^{119}Sb spectrum from the CdTe detector is presented within **Figure 9**. The characteristic 23.870 *8* keV gamma emission of ^{119}Sb can be clearly seen as a shoulder upon the convolved ~25 keV X-ray emissions from many radioantimony contributors. The two overlapping peaks were easily deconvolved into gaussians using Fityk version 1.3.1 [134] to separate out the distinct ^{119}Sb photon contribution.

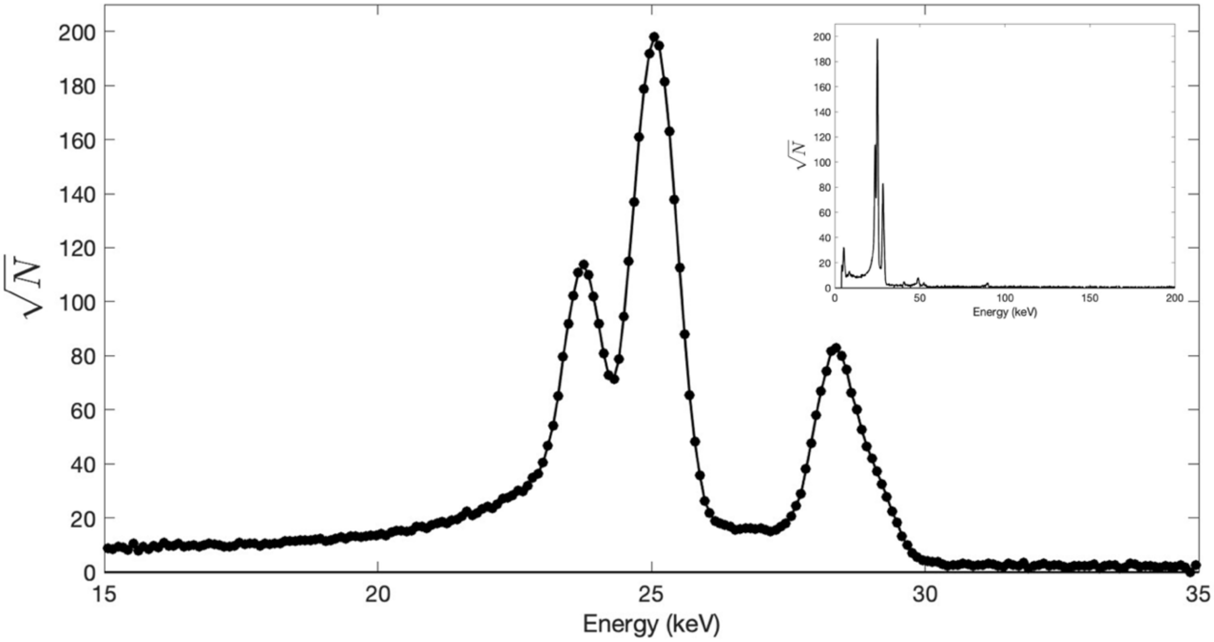

Figure 9: Low energy X-ray spectrum of purified ^{119}Sb (γ = 23.870 *8* keV, I_γ = 16.5 *2* %) via CdTe detector. Multiple radioantimony isotopes emit X-rays with energies of approximately 25 keV and 28 keV.

Using 96.3% isotopically enriched ^{119}Sn and 35 μA of 12.5 MeV proton energy for 1 h, three targets with areal density 80-114 mg/cm^2 produced measured physical yields reported in **Table 10** at a radioisotopic purity of 98.9%, decay-corrected to EOB. Target thicknesses were chosen to minimize use of expensive, enriched material. The largest radioantimony impurities, ^{117}Sb and ^{118m}Sb, have half-lives significantly shorter than that of ^{119}Sb, and, after the 6 h isolation and radiolabeling, the ^{119}Sb radioisotopic purity increased to >99.5% by activity. This is illustrated in **Figure 10**. A radioisotopic purity of >99% is maintained for 336 h post EOB. An average measured physical production yield of 27 MeV/μAh ± 9 MeV/μAh is greater than 10x those previously reported in literature for an enriched ^{119}Sn target irradiation (1.85 ± 0.12 MBq/μAh) [48].

Table 10: Measured EOB corrected physical yields for ^{119}Sb and radioisotopic impurities using 96.3% isotopically enriched ^{119}Sn targets and 12.5 MeV protons.

Target Mass (mg/cm^2)	**^{119}Sb Yield (MBq/μAh)**	**^{117}Sb Yield (kBq/μAh)**	**^{118}Sb Yield (kBq/μAh)**	**^{120m}Sb Yield (kBq/μAh)**	**^{122}Sb Yield (kBq/μAh)**	**^{124}Sb Yield (kBq/μAh)**
80.1	17.5	95.1	210.8	2.5	0.5	< 0.1*
93.8	27.5	110.1	226.1	4.2	2.4	< 0.1*
114.1	34.4	144.8	235.1	3.7	2.4	< 0.1*

* below detection limit of 3 kBq ^{124}Sb

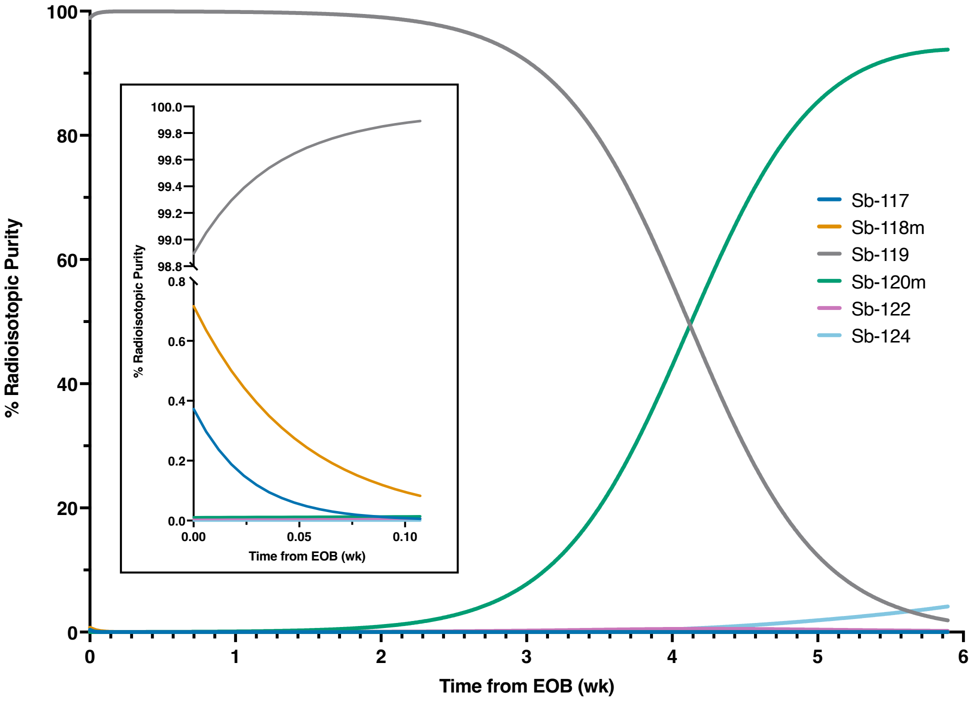

Figure 10: Radionuclidic purity vs. time for 12.5 MeV proton irradiation of 96.3% ^{119}Sn targets.

3.3. Radiochemical Isolation of Radioantimony from Target Material using Column Chromatography

Using HPGe quantification of ^{122}Sb and ^{117m}Sn, elution profiles for both the mercaptopropyl functionalized silica gel and Prefilter resin columns are depicted in **Figure 11**. In the separation chemistry, the first column yields 87.1% ± 3.4% (N = 3) of loaded radioantimony in 0.75 mL eluted acidic ethanol solution. The second column yields 83.7% ± 4.9% (N = 3) of loaded radioantimony in 1.39 mL ± 0.05 mL (N = 3) EtOH, for a combined RCY of 73.1% ± 6.9% (N = 3) ^{122}Sb. In the prefilter resin column step, ^{117m}Sn activities were below LODs and are plotted accordingly.

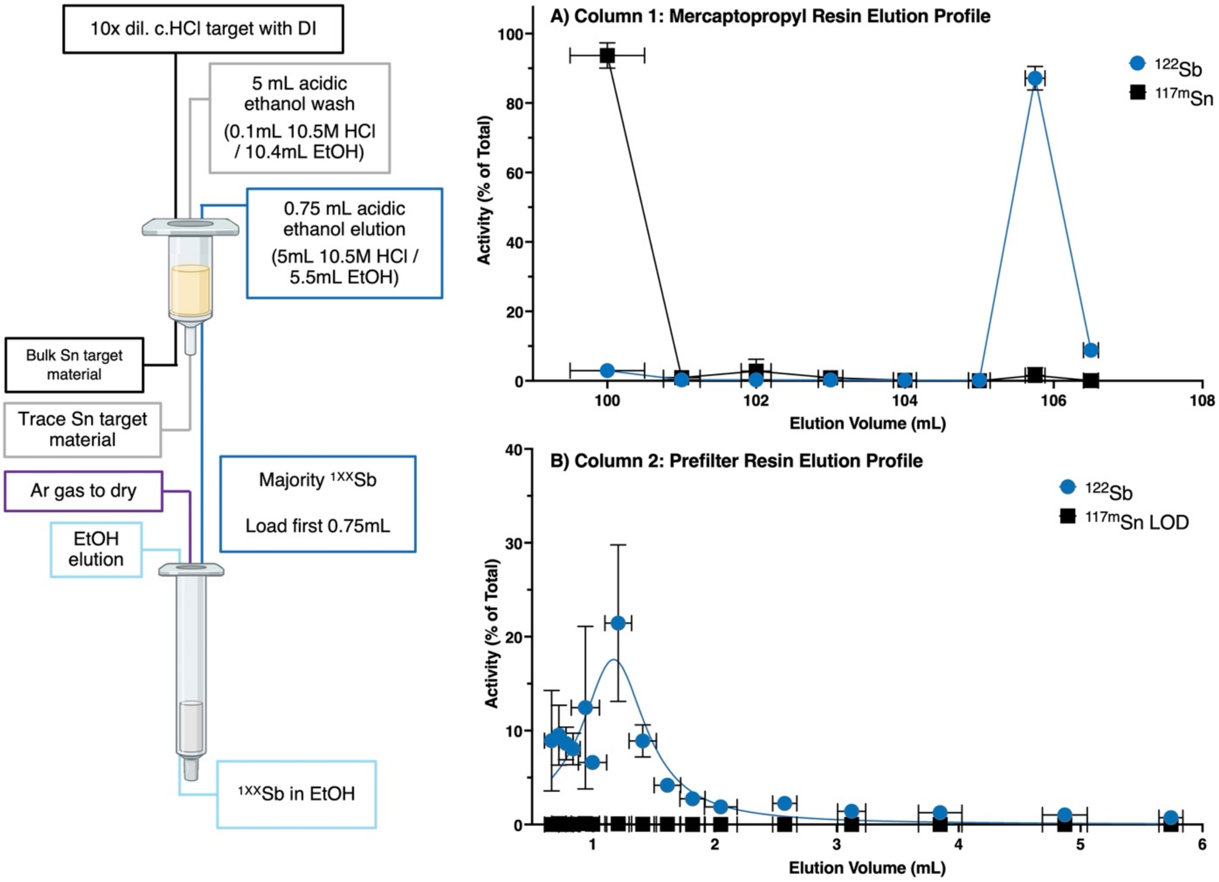

Figure 11: (left) scheme showing column chromatography separation to purify ^{1XX}Sb from Sn

target material. Activity elution profile for A) mercaptopropyl functionalized resin column and B) prefilter resin tracking percent ^{122}Sb and ^{117m}Sn activity. Both elution profiles represent N = 3 separations with uncertainty presented as the standard deviation of measurements. Created with BioRender.com

3.4. Chemical Analysis of Column Chromatography Separation

First column eluted fractions contained 55 ± 7 µM thiol functional groups, suggesting resin degradation from contact with 5 M HCl in 48% EtOH. Final eluted fractions from the prefilter resin show sub-µg trace metal content per half mL volume. ICP-OES measurements (**Figure 12**) of dissolved target solution before and after target loading of column 1 showed Sn mass loss of 6.3 ± 4.2 mg (N = 3). Comparing Sn mass loaded onto the column versus eluted from the column, a separation factor of $(6.4 \pm 3.7) \times 10^3$ (N = 3) for the first column and $(1.7 \pm 1.8) \times 10^2$ (N = 3) for the second column providing a combined separation factor of $(6.8 \pm 5.5) \times 10^5$ (N = 3). Being metalloids, Sn and Sb have ICP-OES LODs on the order of ppm (µg/mL) compared to the ppb LODs for transition metals Fe, Cu, Ni, and Co. Measurements of Sb within columns 1 and 2 are below a measured LOD of 0.1 ppm.

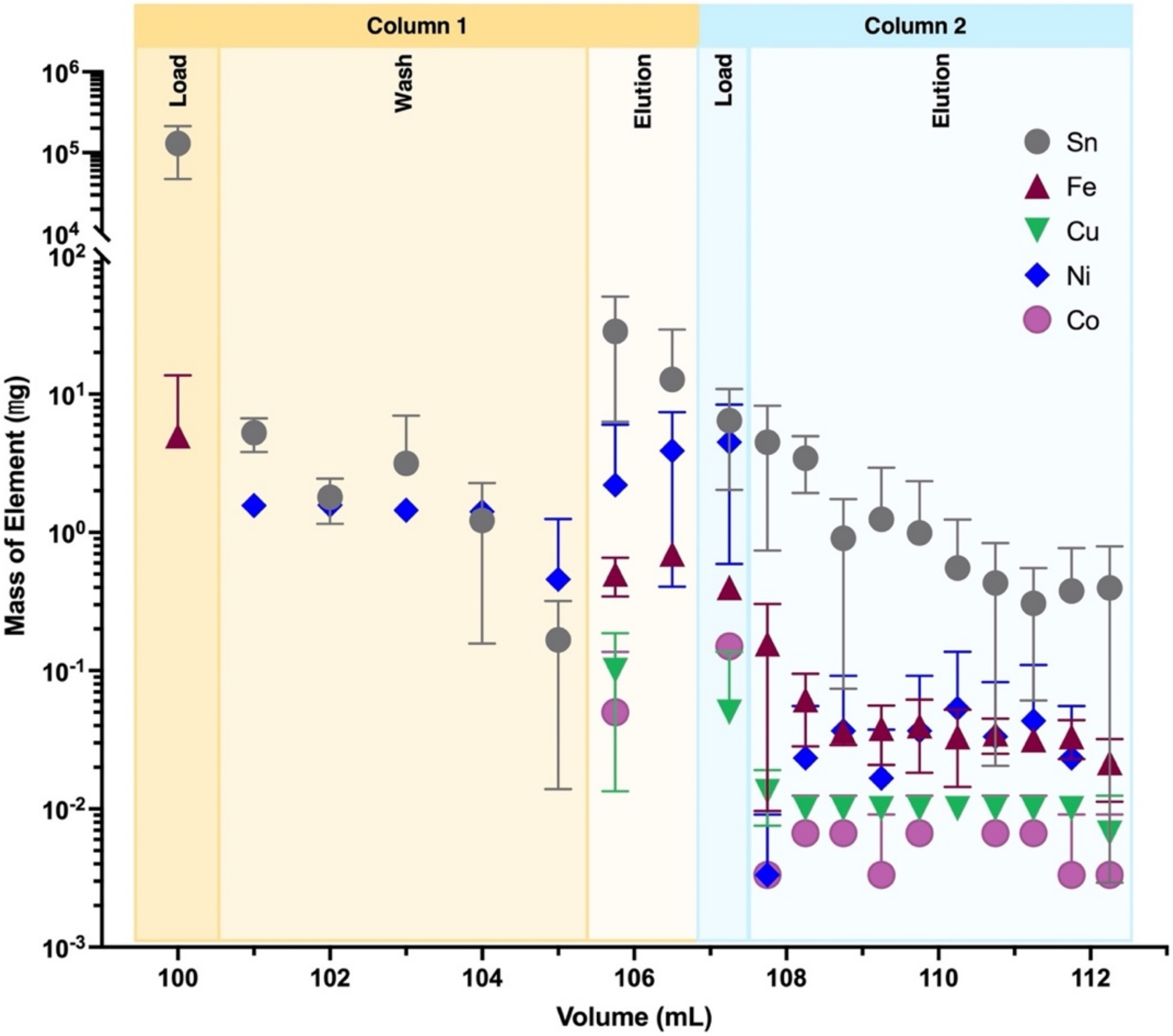

Figure 12: ICP-OES measured trace metal content in column elution fractions (N = 3).

3.5. Recycling Target Material

Iterative recycling of non-irradiated targets was conducted, monitoring the fraction of Sn reclaimed from previously dissolved targets. Comparisons of the time that the dissolved Sn remained in solution before recycling was found to have a significant impact on recycling efficiency, as shown in **Figure 13**. Targets with Sn dissolved 8 – 16 h were recycled with a cumulative efficiency of 91.3% ± 8.8% (N = 12) while targets dissolved >24 h had a cumulative recycling efficiency of 66% ± 11% (N = 12). Plotting via iteration of the same target (**Figure 13)** shows that recycling efficiency decreases significantly when targets are allowed to sit in the dilute dissolution solution for >24h before reclamation with final electrolytic solutions turning a dark brown color. We hypothesize loss of tin to oxidation of Sn(II) forming Sn(IV), which electrodeposits from alkaline as opposed to acidic solutions [135,136].

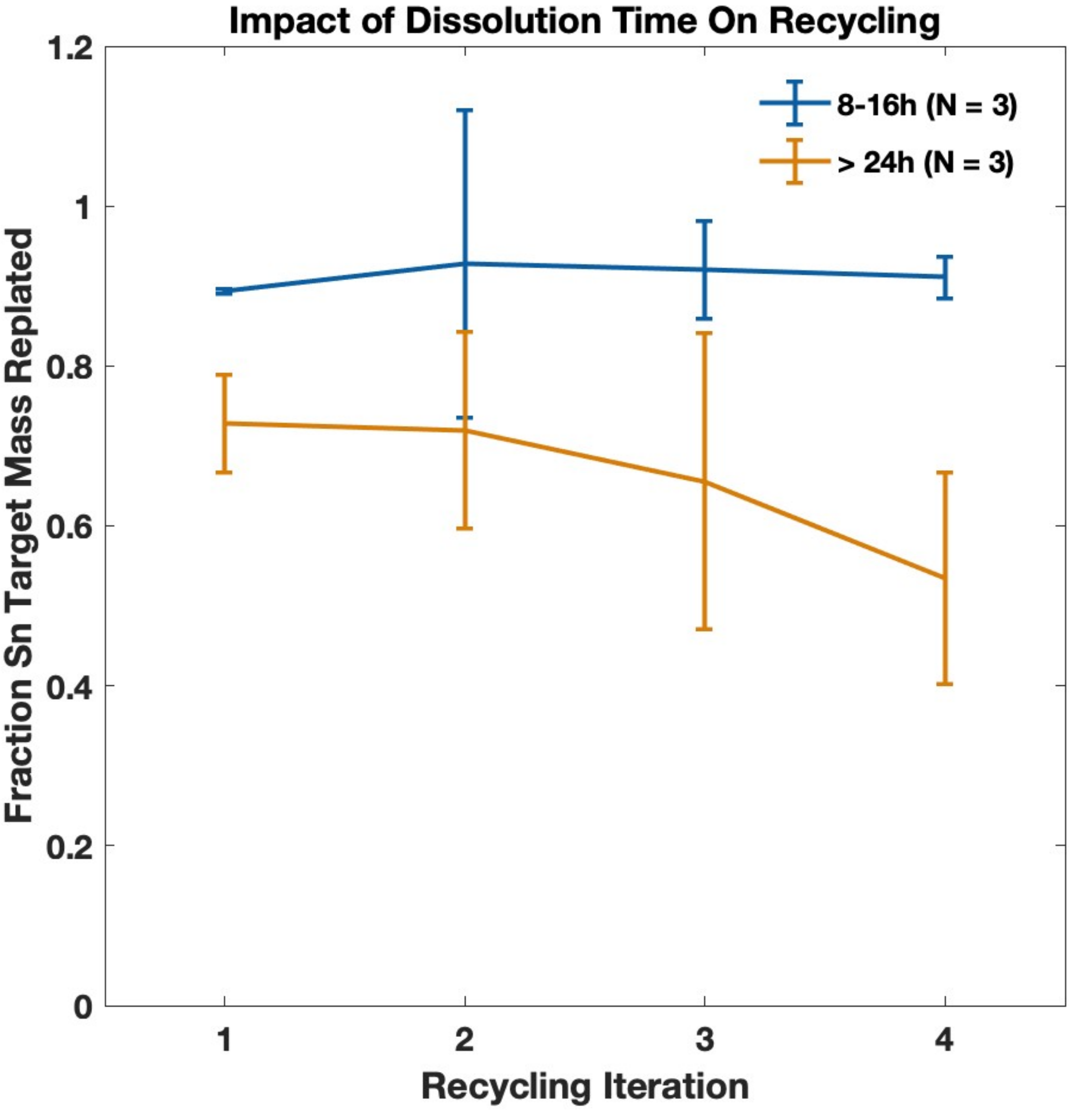

Figure 13: Non-irradiated target recycling, monitoring the amount of time that the dissolved target was in solution before recycling.

Iterative recycling of irradiated targets (N = 3) subjected to first column loading and recycling within 16 h of dissolution provided a cumulative recycling efficiency of 86.9% ± 7.8% (N = 12) (**Figure 14**) with representative images of recycled targets showing the capacity to retain metallic Sn quality of electroplates with no observed impact on production yield or beam tolerance. Additionally, irradiated, isotopically enriched ^{119}Sn targets were recycled at an efficiency of 80.2% ± 5.5% (N = 6) with 11.6 mg ± 0.8 mg (N = 6) lost, potentially to resin loading or oxidation during electroplating process.

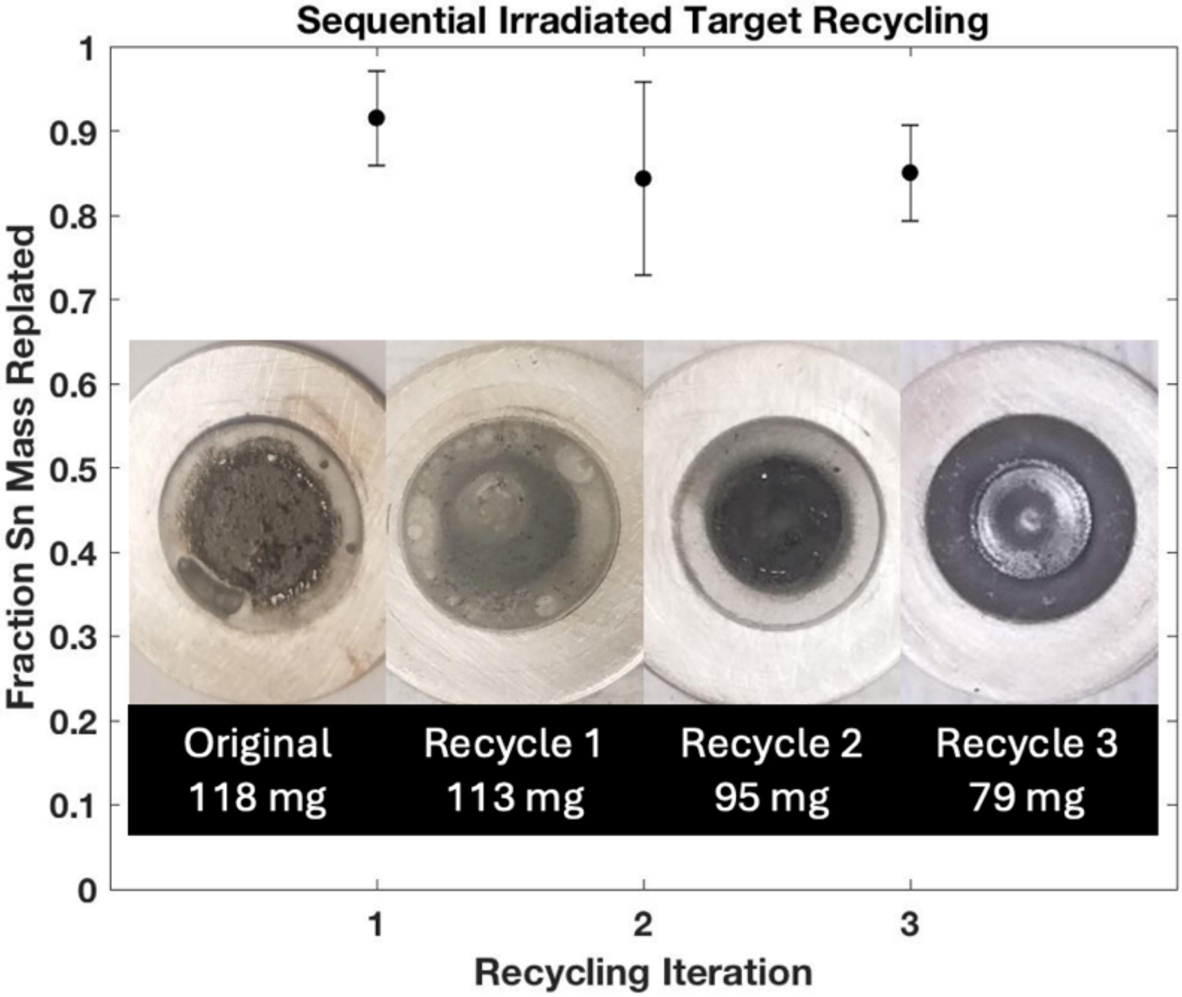

Figure 14: Iterative recycling of irradiated ^{nat}Sn targets (N = 3) processed through chromatographic chemical separation.

3.6. Radiochemical Isolation of Radioantimony from Target Material using Liquid-Liquid Extraction

Figure 15 illustrates the technique employed to separate radioantimony from bulk tin target material. It is crucial that H_2O_2 is added to the target solution shortly before performing the separation (as opposed to during target dissolution) otherwise the yield will be drastically reduced. We hypothesize this is necessary to ensure all antimony is oxidized to the pentavalent oxidation state. Once this has occurred, [^{120m}Sb]Sb(V) can be selectively extracted from the aqueous solution with DBE. Based on literature, Sn and Sb are present in strong HCl as $[SnCl_6]^{2-}$ and $[SbCl_6]^-$. Selective extraction of $[SbCl_6]^-$ into DBE is likely the result of a more diffuse charge distribution, resulting in a more hydrophobic species that prefers organic solvation [137]. Following separation of phases, two washing steps with c.HCl (not shown in diagram) help remove trace amounts of Sn(IV) that may have partitioned into the organic phase. Lastly, the Sb(V) is back extracted into a 0.1 M sodium citrate solution pH 5.5. The citrate mitigates Sb(V) hydrolysis [138]. All low molarity aqueous buffer and acid systems (0.1 M HCl, ammonium acetate (NH_4oAc) pH 2-6, phosphate buffered saline (PBS) pH 7.5) tested have facilitated radioantimony back extraction, and low pH (< pH 2) also prevents hydrolysis [139]. We report LLE RCY in **Table 11** and **Figure 16** depicts HPGe gamma spectra of the target solution, extracted target solution, and back extracted solution. The target solution most notably shows ^{120m}Sb (E_γ = 89.8 *3* keV, 197.3 *3* keV) [74], ^{111}In (E_γ = 171.28 *3* keV, 245.35 *4* keV) [140], and ^{117m}Sn (E_γ = 158.56 *2* keV) [72]. Indium-111 can be made from decay of ^{111}Sn produced via the ^{112}Sn(p,pn)^{111}Sn nuclear reaction. The ether extracted target solution retains a majority of ^{120m}Sb with minor ^{117m}Sn and ^{111}In contaminants. Finally, the back extracted solution contains no observable ^{117m}Sn or ^{111}In. Gamma emissions from ^{117m}Sn and ^{111}In in the dissolved target solution fraction decrease upon extraction into DBE and are not detected within aqueous back extraction solution.

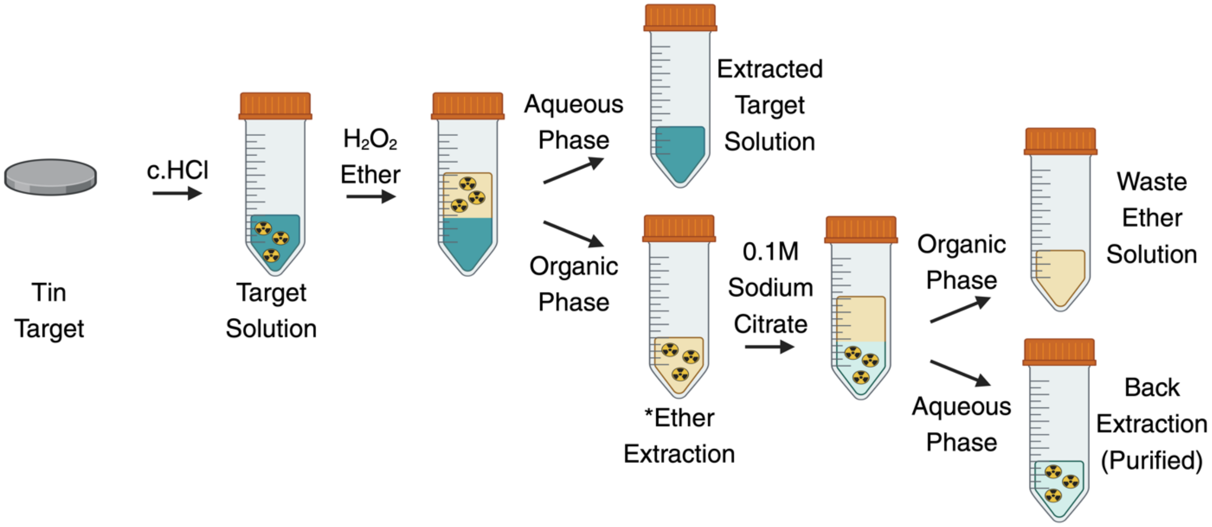

Figure 15: Visual representation of radioantimony purification. *Wash ether with equal volume c.HCl (x2) prior to back extraction. Created with BioRender.com.

Table 11: Activities of ^{120m}Sb and ^{117m}Sn collected at TRIUMF expressed as a fraction of total target solution activity.[a]

Solution	%^{120m}Sb Activity (100/initial activity)	% ^{117m}Sn Activity (100/initial activity)
Extracted Target Solution	2.4% ± 0.4%	98% ± 4%
HCl Wash #1	0.38% ± 0.07	N.D
HCl Wash #2	0.28 ± 0.05	N.D
Extracted Ether	0.07%[b]	N.D
Final Citrate Solution (net total)[c]	69% ± 2%	N.D
Final Citrate Solution (corrected)[d]	95% ± 2%	N.D

[a] Values calculated using activity concentration (Bq/mL) and volume, without correcting for sacrificed volume unless otherwise specified. Activity then divided by initial activity of purified target solution. Reported error is standard deviation (n = 3). N.D. = not detected;

[b] Due to N.D. in two trials, n = 1.

[c] Percent isolated activity over starting activity;

[d] Percent activity corrected for sacrificed volume over starting activity.

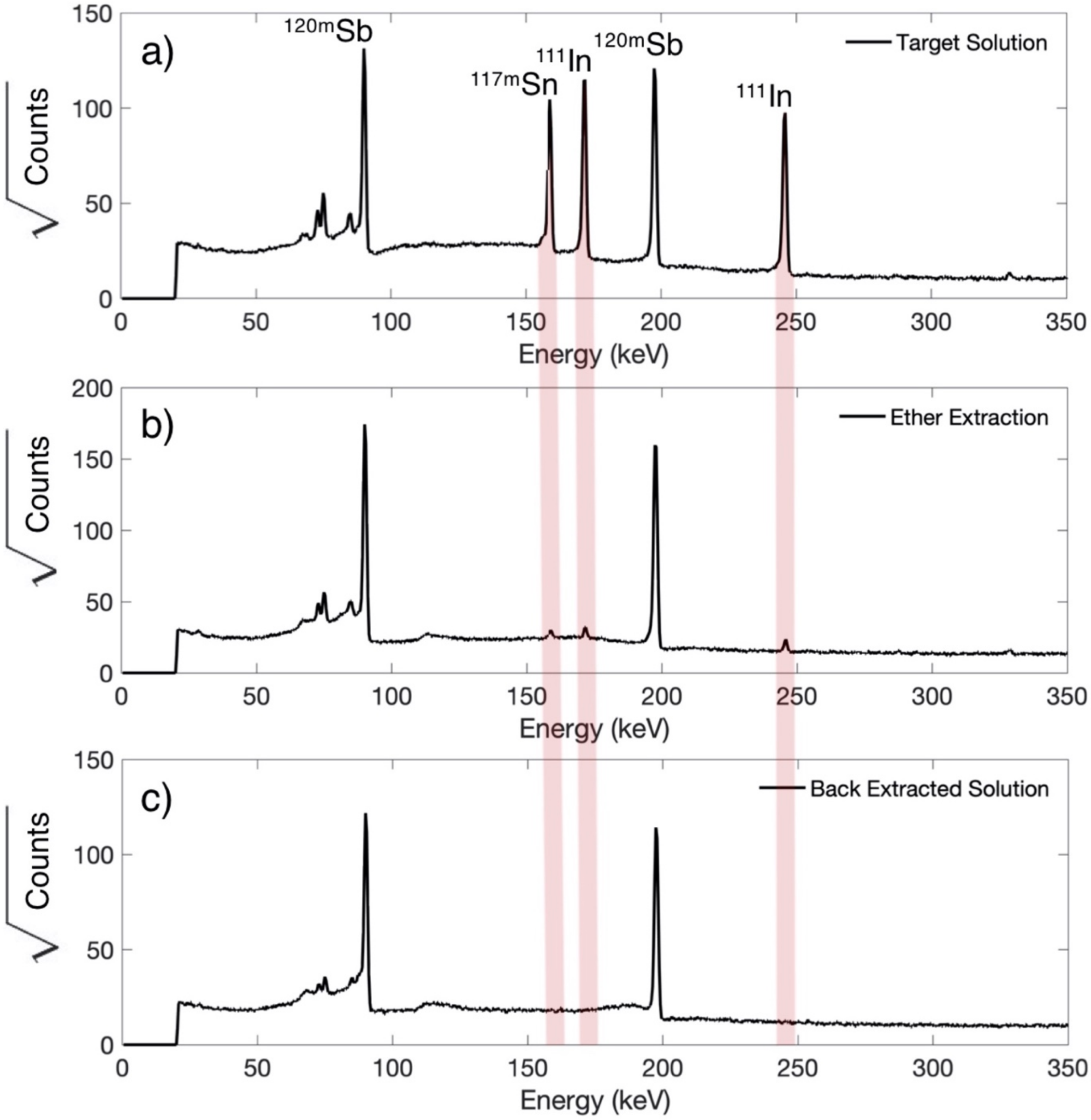

Figure 16: HPGe gamma spectra of a) target solution b) ether extraction solution c) back extracted solution. Red lines highlight radionuclidic impurities removed from solution and absent in final purified radioantimony.

Collaborators measured < 18 ppm (<170 μg in total) stable tin in the final solution, showing that >99.95 % of the bulk tin target is removed in the separation process. The amount of stable antimony present in the final solution was <40 μg. Without sacrificing DBE extraction volume, UW-Madison chemical separations provided a RCY of 94.6% ± 4.0% (N = 3) and ^{117m}Sn activity below a LOD 480 Bq. Using ^{117m}Sn LOD, <0.1 % original target Sn mass remained in the final solution.

4. Conclusions

We have reported physical yields for radioantimony isotopes produced with proton and deuteron beams on a small commercial cyclotron. Using low energy photon spectrometry of massless sources, ^{119}Sb activity and physical yields were quantified. Electroplated, sustainably recycled ^{119}Sn targets were irradiated to produce ^{119}Sb in a form and purity suitable for preclinical therapy studies. Gigabecquerel quantities of ^{119}Sb were produced with >99.5% radioisotopic purity using readily achievable cyclotron irradiation parameters (35 μA, 1 h). Our thiol resin separation strategy produced a radiochemical yield of 73.1% ± 6.9% (N = 3) without observable ^{117m}Sn contaminant, providing a Sn separation factor of (6.8 ± 5.5) x 10^5 (N = 3). Our LLE method isolated radioantimony from tin using with >90 % RCY and a separation factor >1700.

Low energy proton and deuteron induced nuclear reactions on natural and isotopically enriched ^{119}Sn produce a wide range of radioisotopic purity for ^{117}Sb and ^{119}Sb focused productions. When decay correcting to EOB, proton bombardment (16 MeV) of thick ^{nat}Sn targets produced the greatest ^{117}Sb activities, yet highest purity ^{117}Sb was achieved through deuteron bombardment (8 MeV) of thick ^{nat}Sn. Energetically thin (80-114 mg/cm^2) 96.3% isotopically enriched ^{119}Sn targets achieved the highest purity ^{119}Sb at proton energies of 12.5 MeV, with radioisotopic purity increasing for two weeks post EOB as shorter-lived radioisotopes (^{117}Sb and ^{118m}Sb) decay and greatest reported EOB yields.

Chapter 3: Radioantimony(III) Chelation Strategies

1. Introduction

1.1. Contributors

Section 1.2 is modified from [Randhawa, P.; Olson, A. P.; et. al. *Curr Radiopharm* **2021**, *14* (4), 394–419.] Most of the chapter is reprinted from [Aeli P. Olson, et al. Inorganic Chemistry **2021** 60 (20), 15223-15232]. Copyright [2021] American Chemical Society. The following work was done in collaboration Dr. Steven Kelley and Dr. Silvia Jurisson's Radiochemistry group at the University of Missouri. Prof. Dr. Silvia Jurisson, Prof. Dr. Heather Hennkens, Dr. Yutian Feng (Duke), Dr. Li Ma, and Chathurya Munindradasa from the University of Missouri in Columbia provided the trithiol chelator and the synthesis is described in [141].

1.2. Literature Review

1.2.1. Overview

Antimony is a metalloid capable of forming organometallic bonds [142–144]. Due to a final single step addition of a radionuclide in radiopharmaceutical synthesis, radiometal complexation via bifunctional chelator (BFC) is the preferred route to incorporate a radiometal into the pharmaceutical construct. Ideally, a BFC should be selective to the radiometal of choice, complexing trace radiometals (pmol) against non-radioactive impurities (mmol). The radiometal-complex must be stable and inert, surviving *in vivo* competition against endogenous complexation agents such as glutathione (GSH) and various amino acids. Furthermore, the BFC should complex the radiometal rapidly with high kinetic stability and incorporate an organic linker capable of functionalization to disease targeting moieties [145,146].

Lewis acidity is useful in exploring possible complexation environments as metal ions function as Lewis acids [147]. In hard-soft acid-base (HSAB) theory, highly polarizable atoms are described as being ‘soft’ and non-polarizable elements are referred to as ‘hard.’ Generally, elements become harder with increased electronegativity and softer with increased atomic size [148]. Metal ions with small size and high charge are generally considered hard Lewis acids and bond well with hard electron donors. Conversely, metals with low charge and large size generally bond well and form stable complexes with soft electron donor ligands [147].

1.2.2. Chemistry of Antimony(III)

A group 15 element with ground-state electron configuration $[\mathrm{Kr}]4d^{10}5s^{2}5p^{3}$ [143], antimony is classified as a pnictogen and shares many similarities (and differences) to other group 15 congeners. Within the literature, a general understanding of pnictogen chemistry and bonding is growing, with much interest driven by their emerging applications as catalysts [149–152]. Similar to arsenic and bismuth, antimony has two main oxidation states, Sb(III) and Sb(V) [143], but some antimony ores, such as breithauptite NiSb, have a negative oxidation state [142]. Antimony is uniquely susceptible to hydrolysis [153,154]. In ionic form, Sb(III) is only stable in aqueous solution at very high acidity [155], and conversion between Sb(III) and Sb(V) in highly acidic environments is slow [137]. Oxidation of Sb(III) to Sb(V) by hydrogen peroxide occurs in the presence of chlorine with chlorine free environments experiencing no H_2O_2 induced oxidation [156].

The most common coordination numbers (CN) are 3, 4, 5, and 6 [142,157] and subsequent frequently encountered geometries are trigonal pyramidal and trigonal planar (CN = 3), tetrahedral and disphoenoidal (CN = 4), trigonal bipyramidal, square planar, and square pyramidal (CN = 5), and octahedral (CN = 6) [142]. The unique pnictogen bonds formed with group 15 elements are non-covalent defined by their electrophilic interactions with an acceptor atom with bond strength typically decreasing as pnictogen electronegativity increases or polarizability decreases

[152,158,159]. Descending elements in group 15 (From N to Bi) results in decreased electronegativity and increased atomic size, resulting in higher energy of valence orbitals and poorer overlap with acceptor atoms [160], which explains aforementioned trends in pnictogen bond strength. With ionic atomic radii of 76 pm for Sb(III) [142,157], 60 pm for Sb(V) [142,143], and electric polarizability reported to be 42.61-44.57 (depending on computational method) [161–163], Sb(III) is a large, soft metal likely to bond well with other soft donor groups like sulfur, explaining antimony's observed thiophilicity [164–168].

1.2.3. Antimony Chelation

Treatment for the parasitic infection Schistosoma has historically employed potassium antimonyl tartrate (**Figure 17**) [169]. In 1969, Thakur reported the first and only complexation of radioantimony using tartrate, forming ^{117}Sb potassium antimonyl tartrate (PAT). The authors prepare PAT samples free from contamination and suitable for injection [170]. However, no mention of specific activity or radio-complex stability are included. Within this bidentate ligand complex, two Sb(III) atoms are buried in eight oxygen atoms, each metal ion forming four coordination bonds. Although insightful into Sb coordination environments, this chelation strategy is not suitable for organic linking to targeting vectors, which is required to provide radiopharmaceutical selectivity. 2,3-dimercaptopropane-1-sulfonic acid (DMPS) and meso-2,3-dimercaptosuccinic acid (DMSA) are chelators used clinically in the removal of antimony and its lighter congener arsenic from individuals being treated for heavy metal poisoning [171].

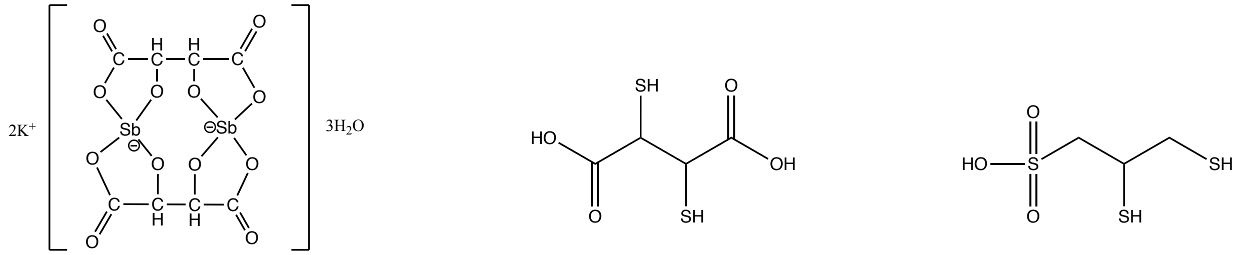

potassium antimony tartrate DMSA DMPS

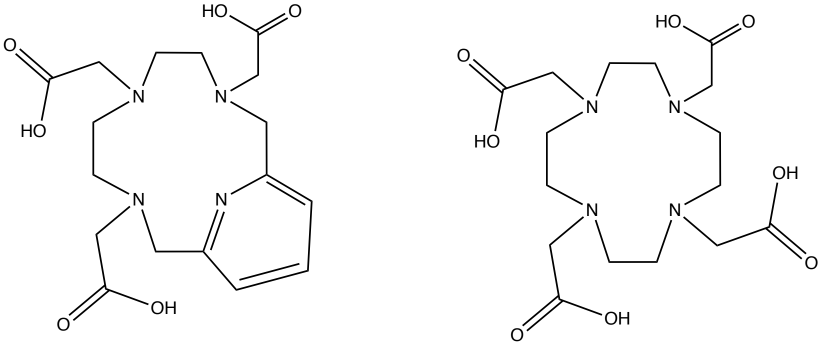

PCTA DOTA

Figure 17: Chelators used in or explored for antimony complexation.

On the macroscopic scale, the macrocyclic chelator 3,6,9,15-tetraazabicyclo[9.3.1]pentadeca-1(15),11,13-triene-3,6,9-triacetic acid (PCTA) stably bound Sb(III) after heating at 70 °C for 5-7 days. Measurements of complex stability found decomposition at physiological pH, which will inhibit translation. However, hydrolysis of Sb(III) is prevented until pH 9 [172]. By using EtOH as a solvent, antimony hydrolysis was circumvented, and a macroscopic Sb-DOTA complex was formed. Recrystallization by diluting the reaction mixture in water proved that Sb-DOTA was hydrolysis resistant; however, Sb-DOTA had low complex stability at biologically relevant pH, and competition reactions showed fast transmetalation with biologically relevant metals, proving Sb-DOTA would not be useful in radiopharmaceutical application [173].

1.3. Motivation

Exploration of ^{119}Sb's cell killing potential is limited to *in silico* studies due to a lack of stable complexing agents capable of functionalization to a targeting moiety. *In vitro* exploration of ^{119}Sb dosimetry requires a targeting vector to pull ^{119}Sb into cells, and stable complexation and chelation represent the first step to achieving this goal. No literature reports of stable radioantimony complexation by a BFC exist [128].

This work explores stable, selective chelation of radioantimony by a trithiol BFC originally developed for the complexation of arsenic [174–177]. Stable complexation would promote development of targeted radioantimony complexes, which would allow biological analysis and exploration of ^{119}Sb dosimetry. The trithiol chelator design includes three thiol functional groups to complex radioantimony and two carboxylic acid arms for linker incorporation, with collaborators having conjugated the trithiol chelator to a bombesin targeting peptide (RM2) and the poly(ADP-ribose) polymerase (PARP) inhibitor (Olaparib).

2. Materials and Methods

2.1. Chemicals and General Methods

All solutions were prepared with MilliQ water and optima grade HCl, EtOH, and acetonitrile (MeCN) from Fisher Chemical (Hampton, NH). Dimethyl 5-hydroxyisophthalate, pentaerythritol tetrabromide, tris(2-carboxyethyl)phosphine hydrochloride (TCEP), silica gel 60 Å, potassium thiocyanate, antimony trichloride ($SbCl_3$), methanol (MeOH), and potassium carbonate were purchased from Fisher Scientific (Waltham, MA) or Sigma-Aldrich (St. Louis, MO). Silica gel w/UV 254 thin layer chromatography (TLC) plates were purchased from Sorbtech Technologies (Norcross, GA). All solvents and reagent grade acids and bases were purchased from Fisher Scientific or Sigma-Aldrich and used without further purification.

Collaborators at the University of Missouri performed stable, macroscopic compound characterization. ^{1}H and ^{13}C NMR spectra were obtained in $CDCl_3$ or d_6-DMSO on a Bruker ARX-500 or 600 MHz spectrometer and calibrated with the respective residual solvent. Infrared spectra were obtained on a Thermo Nicolet Nexus 670 Fourier transform infrared spectrophotometer. Elemental analyses were performed by Atlantic Microlabs, Inc. (Norcross, GA). HRMS analyses were performed at the University of Missouri Charles W Gehrke Proteomics Center; briefly, collaborators loaded samples by an EASY-nLC system with MeOH and analyzed by nanoelectrospray ionization in positive-ion/negative-ion mode on a ThermoScientific LTQ Orbitrap XL mass spectrometer. MeOH solvent flowed at 600 nL/min. HRMS data were acquired for 5 min per sample (30,000 resolving power, 120−1000 m/z, 1 microscan, maximum inject time of 500 ms, automatic gain control = 5×10^5). Additionally, reversed phase high performance liquid chromatography (RP-HPLC) assessment of complexation implemented four RP-HPLC methods.

RP-HPLC Method A: Instrument: Agilent 1260 II system (Santa Clara, CA) with Ortec (AMETEK ORTEC, Oak Ridge, TN) detector. Column: Phenomenex (Torrance, CA) Jupiter C_{18} column (300 Å, 5 μm, 150 mm × 4.6 mm). Flow rate: 1 mL/min. Solvents: A = 0.1 M ammonium citrate (pH 4.5), B = 0.1% TFA in MilliQ water, C = 0.1% TFA in MeCN. Method: t = 0–5 min: A; 5–10 min: 95% B and 5% C; 10–30 min: linear ramp from 5 to 95% C; 30–35 min: 95% C and 5% B; 35–36 min: linear ramp from 95 to 5% C; 36–40 min: A.

RP-HPLC Method B: Instrument: Agilent 1260 II system (Santa Clara, CA) with Ortec (AMETEK ORTEC, Oak Ridge, TN) detector. Column: DIONEX (Sunnyvale, CA) Acclaim C_{18} column (120 Å, 5 μm, 250 mm x 4.6 mm). Flow rate: 1 mL/min. Solvents: A = 0.1% TFA in MilliQ water, B = MeCN. Method: t = 0−3.5 min: 25% B; 3.5−23.5 min:

linear ramp 25–50% B; 23.5–24 min: 50–90% B; 24–29 min: 90% B; 29–30 min: 90–25% B; 30–35 min: 25% B.

RP-HPLC Method C: Instrument: Agilent 1260 II system (Santa Clara, CA) with Ortec (AMETEK ORTEC, Oak Ridge, TN) detector. Column: DIONEX (Sunnyvale, CA) Acclaim C_{18} column (120 Å, 5 µm, 250 mm x 4.6 mm). Flow rate: 1 mL/min. Solvents: A = 0.1% TFA in MilliQ water, B = MeCN. Method: t = 0–20 min: 20–60% B; 20–21 min: 60–90% B;21–26 min: 90% B; 26–27 min: 90–20% B; 27-30 min: 20% B.

RP-HPLC Method D: Instrument: Agilent 1260 II system (Santa Clara, CA) with Ortec (AMETEK ORTEC, Oak Ridge, TN) detector. Column: 150 mm C_{18} Jupiter column (Phenomenex, Torrance, CA). Flow rate: 1 mL/min. Solvents: A = 0.1 M ammonium citrate (pH 4.5), B = 0.1% FA/H_2O, C = MeOH. Method: 0–5 min: 100% A; 5–10 min: 100% B; 10–30 min: linear ramp to 0% B / 100% C; 30–32 min: 100% B; 32–37 min, 100% A.

2.2. Preparation of Non-radioactive Sb-trithiol-diacid Complex

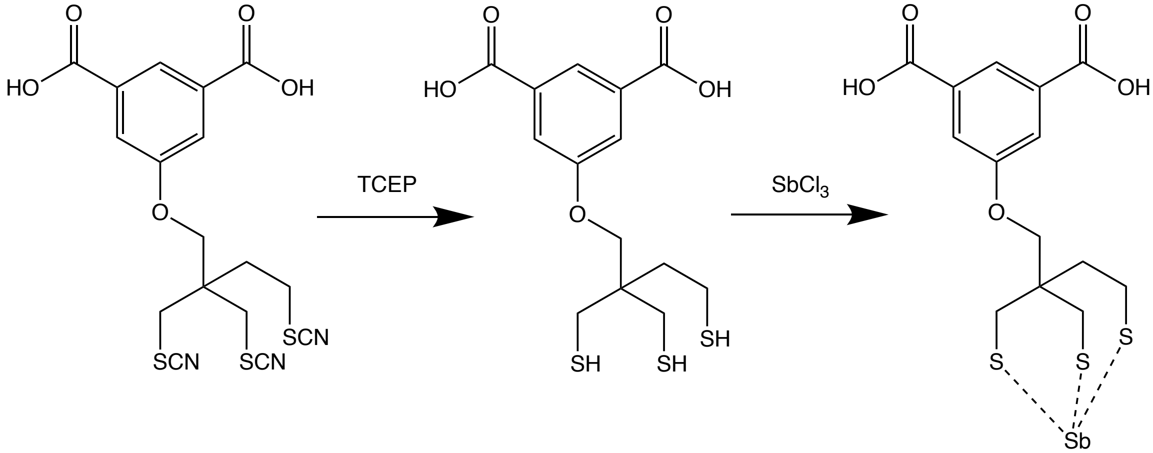

1 2 3

Figure 18: Reaction scheme for creation of **3**, Sb-trithiol-diacid

Collaborators at the University of Missouri (Dr. Li Ma, Dr. Silvia Jurisson) synthesized 5-(3-Thiocyanate-2,2-bis(thiocyanatomethyl)-propoxy)isophthalic Acid, compound **1,** as reported [141]. They grew X-ray quality crystals by dissolving **1** in a 70/30 (v/v) MeCN/H_2O at 70 °C and cooling to room temperature. Additionally, they synthesized the non-radioactive standard 5-((2,6,7-Trithia-1-stibabicyclo[2.2.2]octan-4-yl)-methoxy)isothalic Acid, [^{nat}Sb]Sb-trithiol-diacid, **3**. Compound **3** was synthesized (**Figure 18**) by two methods. Synthesis A: Compound **1** (15 mg, 0.0354 mmol) and TCEP (101.4 mg, 0.3538 mmol) were dissolved in 5 mL of 70% EtOH in water and stirred on a hot plate at 55 °C for 2 h. After the reductive deprotection reaction completed, collaborators added 1 mL $SbCl_3$ (11.81 mg, 0.0425 mmol) in EtOH, and the reaction mixture was kept at 55 °C for another 45 min. During this time, a white precipitate formed. The reaction mixture was cooled, and the white precipitate was collected by filtration, the sample was washed with water and diethyl ether, and the precipitant was dried *in vacuo*. Yield: 14.08 mg; 85%. X-ray quality crystals were grown by dissolving **3** (5 mg) in DMSO (2 mL) containing H_2O (200 μL) at 70 °C and allowing the mixture to sit at room temperature for 2 weeks. ^{1}H NMR (DMSO; 600 MHz) δ ppm: 3.193 (s, 6H, CH_2S), 3.828 (s, 2H, OCH_2), 7.649 (d, 2H, CH), 8.093 (t, 1H, CH). ^{13}C NMR (DMSO; 150 MHz) δ ppm: 28.66 (CH_2S), 56.02 ($C(CH_2)_3$), 76.46 (OCH_2), 119.28 (CH), 122.56 (CH), 132.60 (CCO), 158.58 ($COCH_2$), 166.32 (COOH). HRMS (m/z): 464.88606 (464.88795 calculated for $[M - H]^-$ of [$C_{13}H_{13}O_5S_3Sb$]). Elemental Analysis Calculated (found) for $C_{13}H_{13}O_5S_3Sb$: C, 33.42 (30.49); H, 2.80 (2.74); S, 20.59 (17.32). FT-IR (cm^{-1}): 1711 (C=O), 1197 (C–O). Note, ^{1}H NMR shows excess residual water at 3.30 ppm. Elemental Analysis Calculated (found) for $C_{13}H_{13}O_5S_3Sb{\cdot}2.5H_2O$: C, 30.48(30.49); H, 3.54 (2.74); S, 18.78 (17.32). (See **Appendix A Figures A1-A4**).

Synthesis B: Compound **1** (15 mg, 0.0354 mmol) and TCEP (101.4 mg, 0.3538 mmol) were dissolved in 2 mL of 70% EtOH in water in a 10 mL microwave vessel. Collaborators performed microwave reactions using a CEM Discover SP microwave reactor (CEM Corp., Matthews, NC). The vial was capped and placed into the microwave unit and set at a fixed power of 15 kW and a temperature of 70 °C for 5 min to generate **2**. Following the reduction reaction, collaborators dissolved $SbCl_3$ (11.81 mg, 0.0425 mmol) in 1 mL of EtOH before transferring into the reaction vessel and microwaving the vessel at a fixed power of 15 kW and a control temperature of 70 °C for 5 min. After cooling, the reaction mixture was centrifuged, the white precipitate was filtered, and the sample washed three times with water and ether. Yield: 14.88 mg; 90%.

2.3. X-ray Crystallography

Collaborators at the University of Missouri (Dr. Steven Kelley) collected and analyzed single-crystal X-ray diffraction data using a Bruker X8 Prospector diffractometer (Bruker-AXS, Inc., Madison, WI, USA) with Cu K_α radiation (l = 1.54178 Å) from a microfocus source. The crystals were cooled to 100 K during collection using a Cryostream 700 cryostat (Oxford Cryosystems, Oxford, UK). Hemispheres of data were collected out to resolutions of at least 0.81 Å using strategies of scans about the phi and omega axes. Unit cell determinations, data reduction, absorption corrections, and scaling were performed using the Bruker Apex3 software suite [178]. The crystal structure of trithiol-diacid precursor was solved by direct methods [179,180]. Both structures were refined by full-matrix least-squares refinement using SHELXL [181] implemented via Olex2 [182]. Non-hydrogen atoms were located from the difference maps and refined anisotropically. Hydrogen atoms were placed in calculated positions, and their coordinates and thermal parameters were constrained to ride on the carrier atoms. The crystal structure of **1** was found to contain regions of disordered solvent that could not be accurately modeled. These were treated by applying a solvent mask as implemented in PLATON SQUEEZE [183]. Six hundred thirty-seven electrons were removed from a total void volume of 2014 Å^3 per unit cell, equivalent to 1.5 acetonitrile molecules per formula unit. Crystal data, structure refinements, and bond distances and angles are reported in **Appendix A Table A1-A4**.

2.4. Trithiol-diacid Radiolabeling from Unseparated Target Solutions

The thiocyanate protected trithiol chelator (**1**, 10 mM in MeCN) was deprotected in 1:1 MeCN:H_2O using TCEP (100 mM in MilliQ water) to yield deprotected trithiol-diacid, compound **2**. After irradiation, 3 mL c.HCl dissolved the tin/radioantimony target (~50 mg) at 90 °C for 1 h, and without purification, the ^{1XX}Sb reacted *in situ* (30 min, 25 °C) with 0.01−1 mM **2**. A C8 Sep-Pak cartridge (400 mg resin, 55−105 μm particle size, 125 Å pore size; Waters Corporation, Milford, MA) was preconditioned with 5 mL of EtOH (Fisher Chemical) and 5 mL of MilliQ water. We diluted the labeled target solution (1:20) with MilliQ water and passed it through the preconditioned C8 cartridge. Passing 5 mL of MilliQ water through the cartridge removed unchelated tin target material, and 3 mL MeCN eluted [^{1XX}Sb]Sb-trithiol-diacid, which was dried under N_2. Next, 20 sequential 30 min HPGe activity assays quantified ^{118m}Sb, ^{120m}Sb, ^{122}Sb, and ^{124}Sb, and, by fitting the time activity curve for 159 keV emissions, determined ^{117}Sb and ^{117m}Sn activities in the final purified fraction.

2.5. Radiolabeling from Purified Solutions and Apparent Molar Activity Quantification

Deprotection of the thiocyanate protected trithiol chelator **1** occurred in 97% EtOH (2 mM, 0.6 mg, 580 μL EtOH) with TCEP (20 mM, 3.5 mg, 20 μL H_2O) heated at 55 °C for 2 h to yield deprotected trithiol-diacid, compound **2.** Column chromatography purified (**Chapter 2**) ^{1XX}Sb reacted (1 h, 55 °C) with **2** at final reaction concentrations of 0, 0.01, 0.1, and 1 mM**,** forming [^{1XX}Sb]Sb-trithiol-diacid.

TLC assessed complexation, spotting aliquots of radiolabeling solutions onto Al-backed Si TLC plates pre-spotted with MeOH, and developing the plates with MeOH mobile phase separated [^{1XX}Sb]Sb-trithiol-diacid ($R_f = 0.815 \pm 0.015$ (N = 3)) from free ^{1XX}Sb ($R_f = 0.019 \pm 0.009$ (N = 3)) where uncertainties are expressed as the standard deviation of measurement replicates. We employed autoradiography (Packard Cyclone Storage Phosphor) to quantify complexation. Using the MatLab cftool function, sigmoidal curve fitting of % ^{1XX}Sb activity complexation allowed calculation of 50% labeling and subsequent apparent molar activity (AMA) determination.

2.6. Serum Stability, Cysteine Challenges, and LogD$_{7.4}$ Measurement

The stability of the [^{1XX}Sb]Sb-trithiol-diacid complex was determined by challenging it with various chelating agents endogenous to biological systems. A C8 cartridge allowed purification of quantitative radiolabeling solutions (assessed via radio-TLC) as described above. After drying C8 eluent, the purified [^{1XX}Sb]Sb-trithiol-diacid was resuspended in either PBS (Thermo Scientific), 25 mM cysteine (Thermo Scientific) in PBS, or fetal bovine serum (FBS; ATCC, Manassas, VA) and allowed to sit at room temperature. At various time points (0, 24, 48, 72 h), aliquots were analyzed by RP-HPLC using **RP-HPLC Method B**. For the FBS challenge solutions, an equal volume of MeCN was added to the aliquot to precipitate large serum proteins, which were removed by centrifugation (12,000 rpm, 5 min; Beckman Coulter Microfuge 22R Centrifuge, Brea, CA) prior to RP-HPLC analysis.

For logD$_{7.4}$ determination, 10 μL of purified [^{1XX}Sb]Sb–trithiol-diacid in PBS was added to 990 μL PBS and 1 mL n-octanol (in triplicate) before vortexing samples for 15 min, allowing [^{1XX}Sb]Sb–trithiol-diacid to partition between the organic and aqueous phases. After vortexing, extraction solutions were allowed to settle, and we collected 0.5 mL aliquots from each phase to analyze samples for ^{120m}Sb activity via HPGe gamma spectroscopy. LogD$_{7.4}$ was calculated according to **Equation 2**.

Eq 2) $logD_{7.4} = log_{10}(\frac{Activity\ in\ Octanol}{Activity\ in\ PBS})$

2.7. Radiolabeling Conjugated Trithiol Compounds

2.7.1. Trithiol-RM2

Collaborators at the University of Missouri (Prof. Dr. Silvia Jurisson, Prof. Dr. Heather Hennkens, Dr. Li Ma, and Chathurya Munindradasa) synthesized conjugated trithiol compounds with a RM2 peptide for targeting bombesin receptors and characterized radioarsenic complexes [174,184]. Thiocyanate protective groups (**Figure 18**) required similar deprotection strategies employed for trithiol-diacid labeling (**Figure 18**). The trithiol-RM2 compound studied for antimony radiolabeling and stability had a glutathione and serine amino acid linker (**Figure 19**).

We deprotected the thiocyanate protected trithiol-RM2 molecule **4** (MW = 1735 g/mol) in 97% EtOH (0.5 mM, 0.2 mg, 188 µL EtOH) with 12 µL TCEP solution (0.6 mM, 10 mg, 57.1 µL MilliQ water) by heating it at 55 °C for 2 h, yielding deprotected trithiol-RM2 (compound **5**)**.** Column chromatography purified (**Chapter 2**), equal volume ^{120m}Sb (0.65 MBq, 17 µCi) and ^{122}Sb (57 MBq, 15 µCi) in EtOH reacted (1 h, 55 °C) with **4** (final concentration 0.25 mM), forming [^{1XX}Sb]Sb-trithiol-RM2 (compound **6**). After formation, semi-preparative **RP-HPLC Method C** allowed select purification of [^{1XX}Sb]Sb-trithiol-RM2. The collected [^{1XX}Sb]Sb-trithiol-RM2 peak (R_t = 16.5 min) was diluted 10x with MilliQ water, and loaded onto preconditioned C8 cartridge (5 mL EtOH, 5 mL MilliQ water). The cartridge was washed with 1 mL MilliQ water, and [^{1XX}Sb]Sb-trithiol-RM2 compound eluted with 2 mL EtOH.

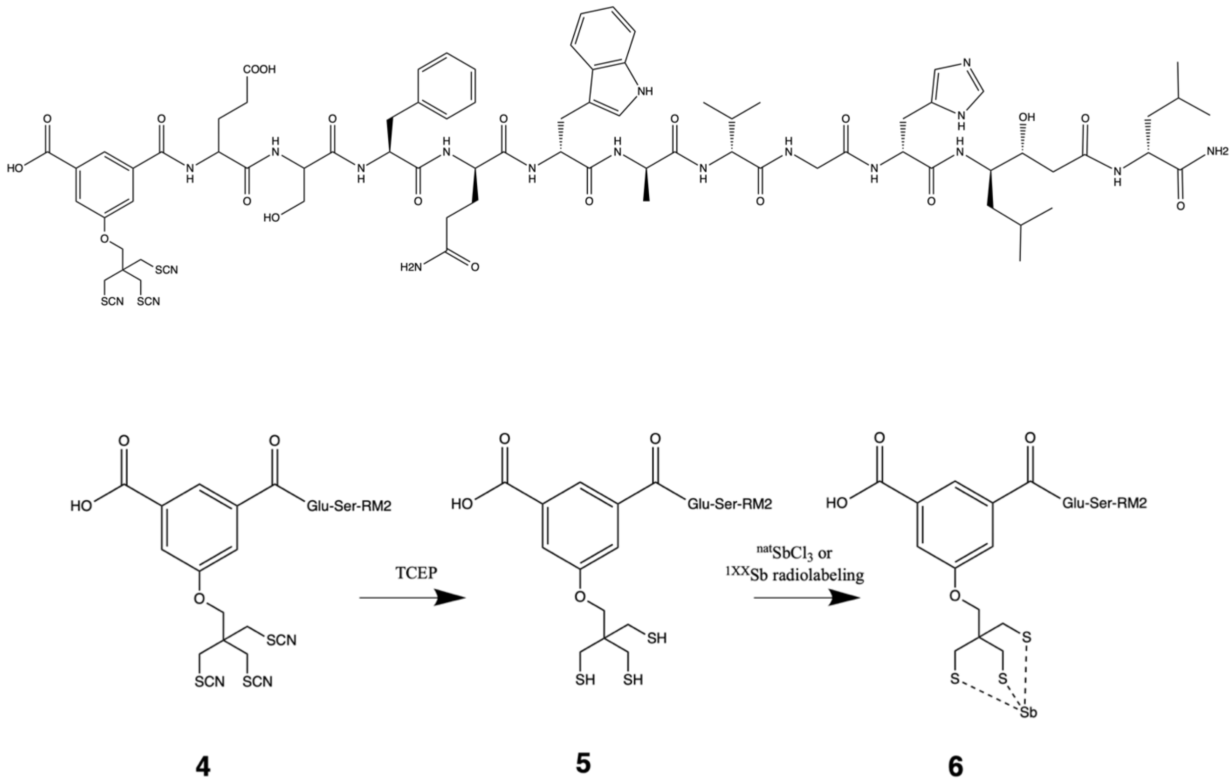

Figure 19: (top) structure of thiocyanate protected trithiol-RM2 peptide. (bottom) reaction scheme for synthesis of **6**, Sb-trithiol-RM2.

We created a non-radioactive Sb-trithiol-RM2 complex by first combining **4** (0.2 mg, 116 µL EtOH) with 10 µL 100 mM TCEP at final concentrations of 0.9 mM and 85 mM, respectively. This solution was heated at 55 °C for 2 h. Addition of equal volume $SbCl_3$ stock (7.4 mg $SbCl_3$, 740 µL EtOH) induced a cloudy precipitant, which was re-dissolved by adding 200 µL EtOH. The reaction was heated for 2 h at 55 °C before RP-HPLC characterization. Collaborators at the University of Missouri verified the creation of a $[^{nat}Sb]$Sb-trithiol-RM2 complex via liquid chromatography mass spectrometry (LCMS) to use for RP-HPLC retention time determination. After reception of the purified complex at UW-Madison, the sample was resuspended in MeCN, filtered using 20 µm filter needle, and immediately analyzed via **RP-HPLC Method C**.

2.7.2. Trithiol-Olaparib

Collaborators at Duke University Medical Center (Prof. Dr. Yutian Feng) synthesized a conjugated trithiol compound to the poly(ADP-ribose) polymerase (PARP) inhibitor Olaparib (**Figure 20**). Trithiol-Olaparib, compound **8** (MW = 695 g/mol) was synthesized using trityl protecting groups [175], which were deprotected using TFA prior to the compound being sent to UW-Madison. Thiol groups readily oxidize [185], resulting in compound **7**. The identity of **7** was verified by LCMS prior to being sent to UW-Madison.

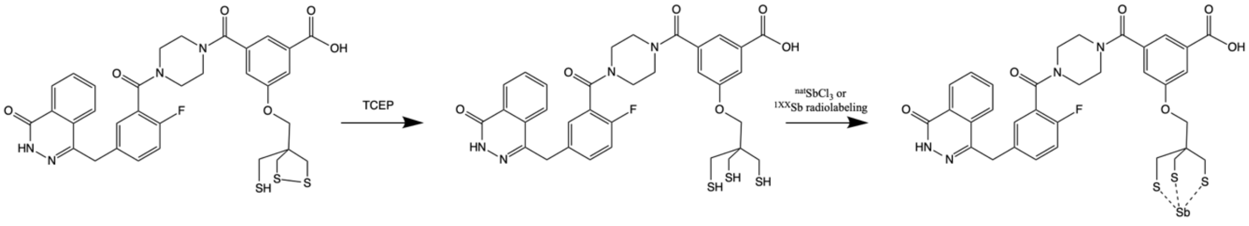

7 **8** **9**

Figure 20: reaction scheme for synthesis of **9**, Sb-trithiol-Olaparib.

Reduction of oxidized thiols, forming **8**, occurred through heating 50 μL trithiol-Olaparib (0.1 mg, MeOH), 100 μL EtOH, and 2.5 μL 10 mM TCEP in MilliQ water (final concentration 1 mM **7**, 0.16 mM TCEP) at 55 °C for 2 h. Addition of 175 μL column chromatography purified (**Chapter 2**) ^{120m}Sb (1.3 MBq, 34 μCi) and ^{122}Sb (1.1 MBq, 30 μCi) reacted (1 h, 55 °C) to form [^{1XX}Sb]Sb-trithiol-Olaparib (final concentration 0.5 mM), compound **9**. After formation, we diluted the radiolabeling solution 10x with MilliQ water, loaded it onto a preconditioned C8 cartridge (5 mL EtOH, 5 mL MilliQ water), washed the cartridge with 1 mL MilliQ water, and eluted the [^{1XX}Sb]Sb-trithiol-Olaparib compound with 2 mL EtOH.

Creation of a non-radioactive Sb-trithiol-Olaparib complex began by first combining **7** (0.1

mg, 161 μL EtOH) with 3 μL 100 mM TCEP in MilliQ water at final concentrations of 0.9 mM and 1.8 mM, respectively. We heated the solution at 55 °C for 20 min. Addition of equal volume $SbCl_3$ stock (7.4 mg $SbCl_3$, 740 μL EtOH) labeled **8** by heating the solution for 2 h at 55 °C. **RP-HPLC Method C** characterized crude reaction product.

2.7.3. PBS Stability and $LogD_{7.4}$ Measurement

For both radioantimony complexed, trithiol conjugated molecules, $LogD_{7.4}$ values were measured as described above in **section 2.6**. We added 400 μL PBS to C8 elution fractions of [^{1XX}Sb]Sb-trithiol-RM2 or [^{1XX}Sb]Sb-Olaparib, and a stream of N_2 (25 °C) evaporated off EtOH. Complete conversion from EtOH into PBS was monitored via mass (~1 h). Radio-RP-HPLC monitoring of complex stability began (t = 0) at first addition of PBS to EtOH elution fraction. At select time intervals, **RP-HPLC Method D** chromatograms of injected aliquots of radioantimony compounds showed uncomplexed ^{1XX}Sb eluting with the solvent front, and comparison of peak integrations allowed determination of complex stability through calculation of % intact activity.

3. Results and Discussion

3.1. Preparation of Non-radioactive Sb-trithiol-diacid Complex

Antimony-trithiol-diacid was successfully synthesized according to reactions in **Figure 18**. Collaborators evaluated [^{nat}Sb]Sb-trithiol-diacid synthesis for both conventional and microwave heating methods. Both reaction methods provided high yields (>85% product); however, using microwave, the reactions formed faster (10 min vs 45 min). ^{1}H NMR and ^{13}C NMR spectroscopy, Fourier-transform infrared spectroscopy, HRMS, and elemental analysis characterized and confirmed creation the [^{nat}Sb]Sb-trithiol-diacid complex. X-ray quality crystals were obtained from a DMSO/H_2O mix (**Figure 22**; **Appendix A Figures A7 & A8**). The ^{1}H NMR spectrum shows expected disappearance of the –SH protons and a downfield shift of the $-CH_2S$ protons of trithiol-diacid on coordination to Sb. The FT-IR shows the expected stretches from the –COOH groups at 1711 cm^{-1} (C–O) and 1197 cm^{-1} (C–O).

3.2. X-ray Crystallography

Collaborators at the University of Missouri found compound **1** crystallized from MeCN and water in the rhombohedral $R\bar{3}$ space group. It packed forming hydrogen bonded rings containing six molecules, all interacting through the carboxylic acid groups. The six-molecule rings stacked above and below each other and interfaced through the thiocyanate groups, which interacted with each other through electric dipole interactions and with the phenyl π system. Bond lengths and angles are very similar to other previously characterized trithiocyanate protected trithiol ligands [177]. Selected bond distances and angles are listed in **Table 12**.

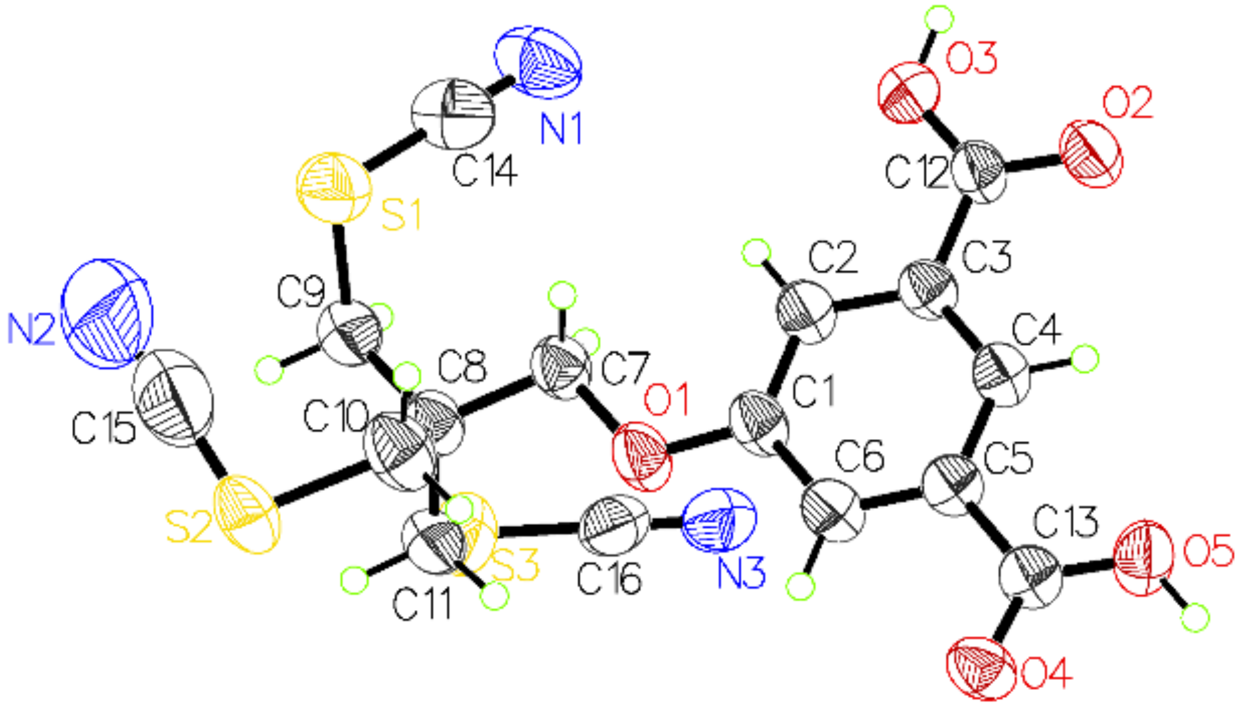

Figure 21: X-Seed representation of **1** (CCDC #2071806) showing 50% ellipsoids.

University of Missouri collaborators discovered that compound **3** crystallized from DMSO and water over 2 weeks. The crystal structure of compound **3** (**Figure 22**) confirms the expected molecular structure and is consistent with its solution structure as determined through NMR and HRMS characterization. The molecule crystallized with 2 molar equivalent of DMSO in the monoclinic space group $P2_1/c$. Both acid groups are protonated, and the three thiols are coordinated trigonally to the Sb(III), making a discrete, neutral molecule. The geometry about the Sb atom is trigonal pyramidal, but the S–Sb–S bond angles are all closer to 90° (an octahedron missing 3 vertices) than they are to 109.5° (a tetrahedron missing one vertex). The S–Sb–S bond angles in the structure agree with those previously reported [186–188]. Previously characterized arsenic-trithiol complexes have bond angles about arsenic close to 97° [177]. The average Sb–S bond length is 2.440(8) Å, which agrees with the previously reported average Sb–S (2.447(7) Å) bond distance [186–188]. Selected bond distances and angles are listed in **Table 12**.

Several different interactions influence the crystal packing of this compound. An important interaction appears to be between the Sb atom and the S atoms of adjacent molecules, which organize the molecules into chains along the *a* axis (**Appendix A Figure A8**). Each Sb atom interacts with 2 S atoms from one neighboring molecule (Sb·····S2 = 3.6987(6) Å, Sb·····S3 = 3.5370(6) Å) and a third S atom from a second neighboring molecule (Sb·····S1 = 3.2529(5) Å), although they are not octahedrally arranged about the Sb. This interaction between the Lewis acidic Sb and the Lewis basic nonbonding S lone pair has been previously observed [186–188]. Collaborators observed two short S·····S distances between neighboring molecules (S1·····S2 = 3.3212(7) Å, S2·····S3 = 3.3829(7) Å) which polymerize the structure into an infinite chain parallel to the *a* axis (**Appendix A Figure A8**). Additionally, the carboxylic acid groups each donate a hydrogen bond to the oxygen of a DMSO molecule (**Table 12**) and accept a hydrogen bond from the methyl group of a different DMSO molecule. These hydrogen bonds cross-link the chains into a network.

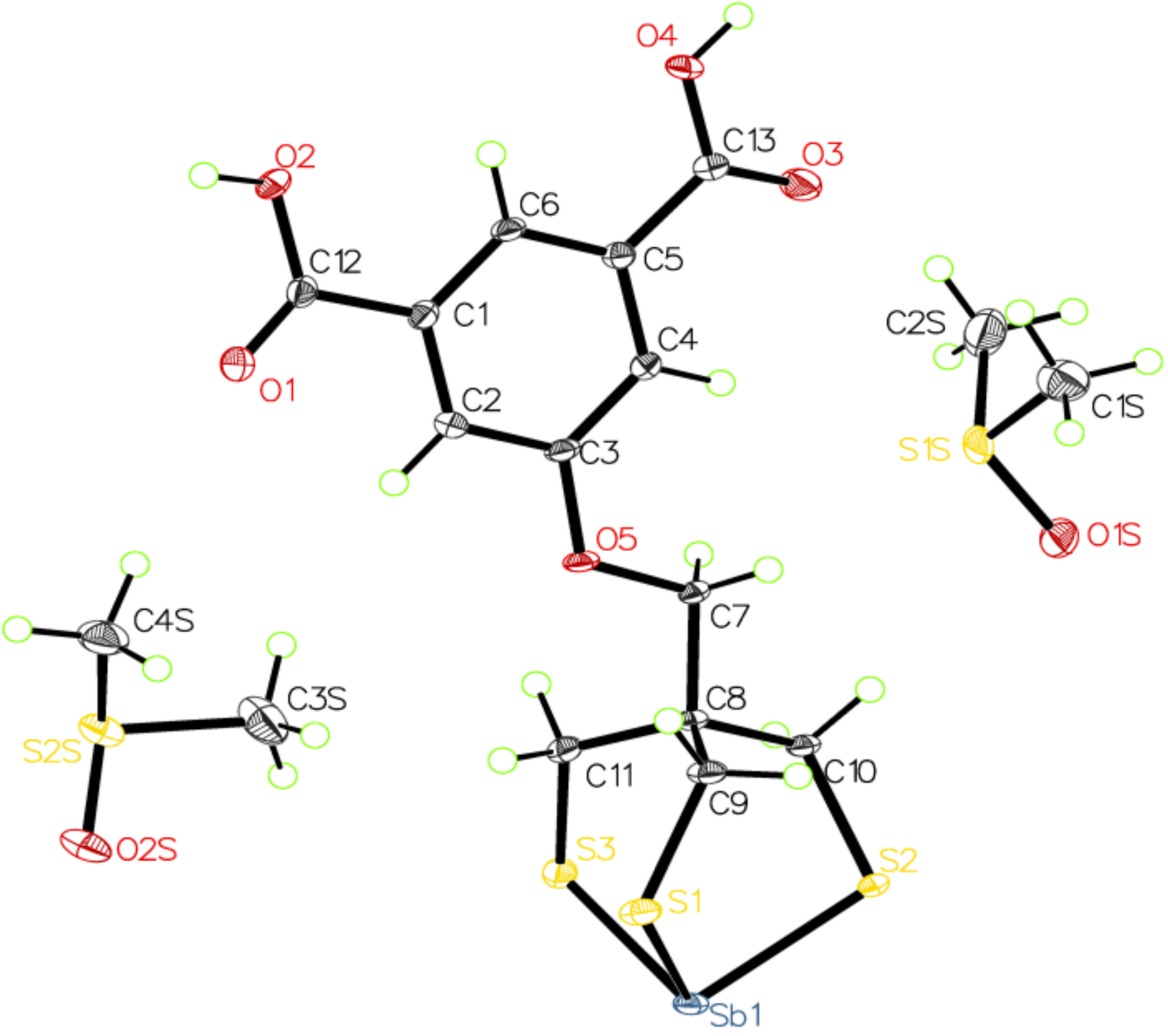

Figure 22: X-Seed representation of **3** (CCDC #2071807)

Table 12: Selected Bond Distances (Å) and Angles (deg) for **1** and **3**.

Trithiol-diacid (1) (CCDC #2071806)		**Sb-trithiol-diacid (3) (CCDC# 2071807)**	
Bond distances (Å)			
S1-C9	1.836(5)	Sb-S1	2.4416(5)
S1-C14	1.681(6)	Sb-S2	2.4314(5)
S2-C10	1.858(5)	Sb-S3	2.4465(5)
S2-C15	1.658(5)	S1-C9	1.832(2)
S3-C11	1.806(5)	S2-C10	1.832(2)
S3-C16	1.672(5)	S3-C11	1.832(2)
N1-C14	1.172(7)		
N2-C15	1.198(12)	O2$_{(acid)}$ ····O1S$_{(DMSO)}$	2.602(2)
N3-C16	1.171(6)	O4$_{(acid)}$ ····O1S$_{(DMSO)}$	2.562(2)
Bond angles (deg)			
N1-C14-S1	177.6(6)	S1-Sb-S2	92.25(2)
N2-C15-S2	173.9(8)	S1-Sb-S3	91.965(16)
N3-C16-S3	176.1(5)	S2-Sb-S3	90.62(2)

3.3. Trithiol-diacid Radiolabeling from Unseparated Target Solutions

Trithiol-diacid rapidly complexes n.c.a. pmol quantities of antimony in 30 min at room temperature in the presence of mmol quantities of tin target material (10^8-fold excess) at ligand concentrations down to 0.01 mM. At low radiolabeling concentrations of 10 μM, 30 nmol of ligand was used to complex 5.8 pmol of various antimony isotopes. RP-HPLC traces of radioantimony unbound and bound by trithiol-diacid are shown (**Figure 23a and 23b**). The non-radioactive [^{nat}Sb]Sb-trithiol-diacid standard coelutes with radioactive [^{1XX}Sb]Sb-trithiol-diacid with a retention time of 23.7 min (**Figure 23**). The trithiol chelator **4** has a strong selectivity for antimony over tin as seen by the full chelation of radioantimony (< nM) in the presence of macroscopic quantities of tin and harsh (~6 M HCl) solvent conditions. The ability to directly radiolabel radioantimony quantitatively from unseparated target material greatly simplifies radiopharmaceutical production. Greater than 99% of [^{1XX}Sb]Sb-trithiol-diacid activity was trapped onto the C8 cartridge and eluted with a RCY of 65% ± 20% (N = 3).

Unchelated compound **2** has a retention time of 24.5 min (**Figure 23a**), which is approximately 0.5 min longer than [^{1XX}Sb]Sb-trithiol-diacid, and the two peaks would be distinguishable and separable. The molar activity of the final solution can be increased by removing non-radiolabeled chelator from [^{1XX}Sb]Sb-trithiol-diacid. The reaction of trithiol chelator **2** with antimony is the first reported complexation of radioantimony with a BFC capable of both stably retaining the radiometal and providing a linker group that can be conjugated to disease targeting moieties.

Fractions isolated from the RP-HPLC [^{1XX}Sb]Sb-trithiol-diacid peak, R_t = 24.0 min, were assayed by HPGe, and the spectra are shown in **Figure 24 left**. To determine the degree to which trithiol-diacid complexes solely antimony and not tin target material, ^{117m}Sn activity within a RP-HPLC purified fraction was measured. Antimony-117 decays to ground state ^{117}Sn [72]. The fitted, logged decay of the sample enabled a half-life measurement that distinguishes ^{117}Sb (2.80 *1* h) from ^{117m}Sn (13.76 *4* d) [72]. Fitting the 158.562 *15* keV photopeak over a 30-h span constructed the decay curve (**Figure 24 right**) and measured a half-life of 2.86 ± 0.02 h, 2.3% larger than the true ^{117}Sb half-life, 2.80 *1* h [72]. A measured half-life larger than the true half-life indicates the presence of a longer-lived radionuclide, in this case, ^{117m}Sn.

Double exponential decay equations describe and quantify relative activities of mixed radionuclide samples in time; using this fit, the ^{117m}Sn activity coeluting with [^{1XX}Sb]Sb-trithiol-diacid at HPLC separation was calculated to be 11.29 ± 0.12 Bq, and comparing initial reaction to final purified ^{117m}Sn activity provides a tin decontamination factor of 1.41 × 10^3. This decontamination factor, describing the high level at which tin target material was removed from the radiopharmaceutical, is impressive for a nontraditional radiochemical production and resulted in a final formulation of tin mass that is orders of magnitude below the estimated daily intake of 4.003 mg inorganic tin for an adult in the United States [189]. For a target with lineal mass density of 120 mg/cm^2, the final sample holds an estimated 45 μg of tin. The Agency for Toxic Substances and Disease Registry reports no evidence that inorganic tin is a neurotoxin, mutagen, carcinogen, or immunotoxin or affects reproduction or development in humans [189]. No radionuclidic impurities were observed besides the various radioantimony isotopes useful for radioantimony activity quantification and ^{117m}Sn (**Figure 24 left**).

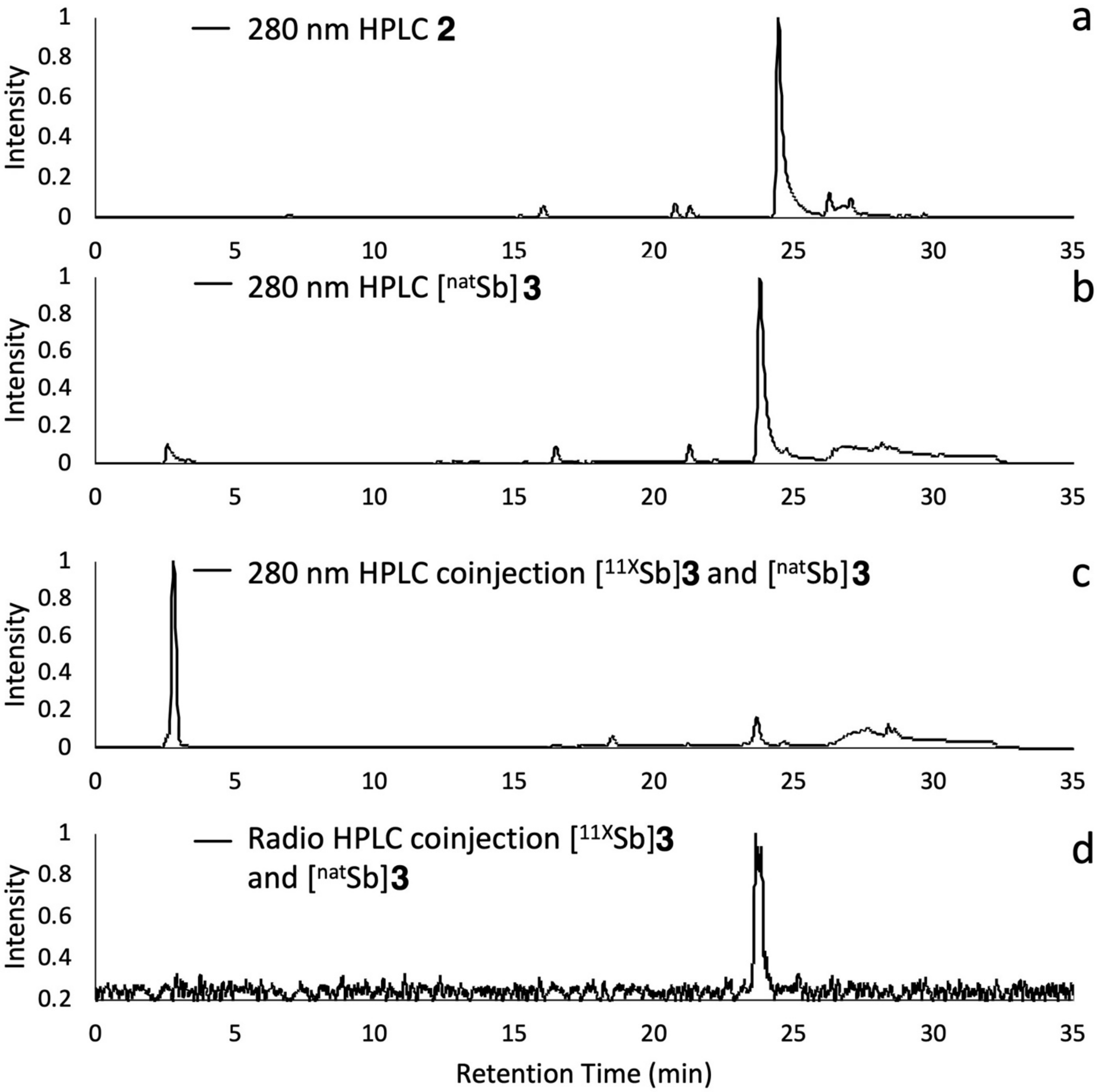

Figure 23: RP-HPLC of [$^{nat/1XX}$Sb]Sb-trithiol-diacid. a) 280 nm UV-Vis chromatogram of trithiol-diacid R_t = 24.5 min, b) 280 nm UV-Vis spectrum of [^{nat}Sb]Sb-trithiol-diacid **3** standard R_t = 23.8 min, c) 280 nm UV-Vis spectrum of co-injection containing both [^{11X}Sb]Sb-trithiol-diacid and [^{nat}Sb]Sb-trithiol-diacid standard R_t = 23.7 min, c) Radio-trace of matching co-injected [$^{nat/11X}$Sb]**5** R_t = 23.7 min. **RP-HPLC Method B**: Instrument: Agilent 1260 II system (Santa Clara, CA) with Ortec (AMETEK

ORTEC, Oak Ridge, TN) detector. Column: DIONEX (Sunnyvale, CA) Acclaim C_{18} column (120 Å, 5 μm, 250 mm x 4.6 mm). Flow rate: 1 mL/min. Solvents: A = 0.1% TFA in MilliQ water, B = MeCN. Method: t = 0−3.5 min: 25% B; 3.5−23.5 min: linear ramp 25−50% B; 23.5−24 min: 50−90% B; 24−29 min: 90% B; 29−30 min: 90−25% B; 30−35 min: 25% B.

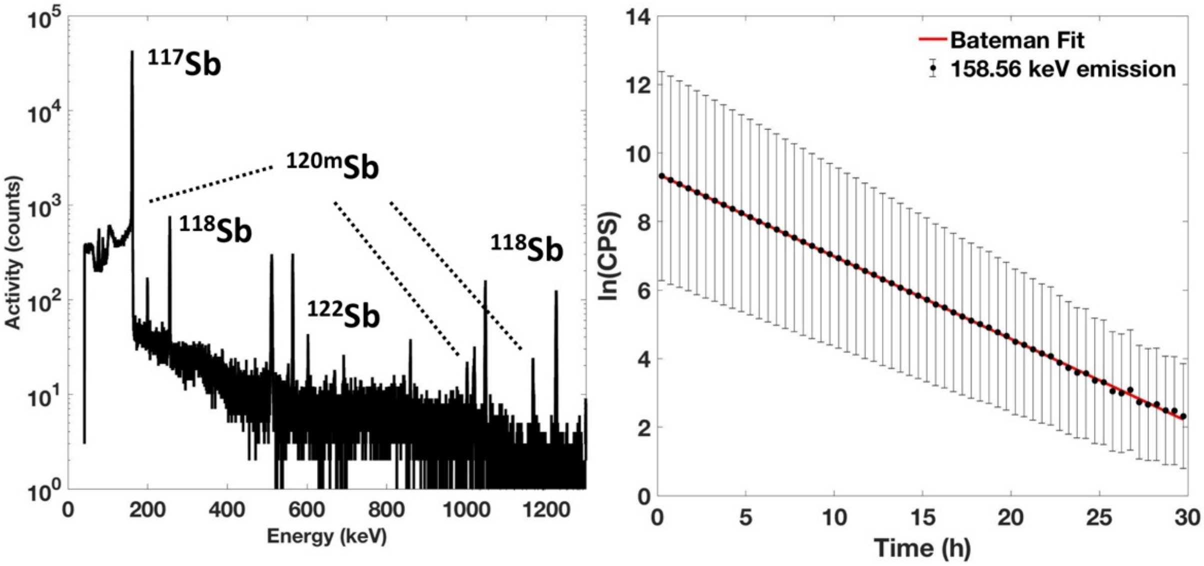

Figure 24: HPGe gamma spectrum and produced activity curves (left), HPGe gamma spectrum labelled with characteristic emissions, displaying radionuclidic purity (right), Bateman equation fitting of time activity curve.

3.4. Radiolabeling from Purified Solutions and Apparent Molar Activity Quantification

Reacting **1 (Figure 25a**) with 10x TCEP at 55°C for 2 h resulted in full deprotection of thiocyanate protected functional groups, resulting in **2** (**Figure 25b**). Addition of ^{1XX}Sb in EtOH for an additional 45 min at 55°C resulted in the formation of [^{1XX}Sb]Sb-trithiol-diacid (**Figure 25c and 25d**). Using a titration method, we measured the AMA of radioantimony produced using ^{nat}Sn targets (510 – 757 mg/cm^2) irradiated with 28.3 – 75 μAh 16 MeV protons at 550 ± 80 MBq

^{118m}Sb/μmol trithiol-diacid (15 ± 2 mCi ^{118m}Sb/μmol), 20.4 ± 2.8 MBq ^{120m}Sb/μmol (0.55 ± 0.08 mCi ^{120m}Sb/μmol), 32 ± 11 MBq ^{122}Sb/μmol (0.87 ± 0.32 mCi ^{122}Sb/μmol), and 1 ± 0.4 MBq ^{124}Sb/μmol (0.03 ± 0.01 mCi ^{124}Sb/μmol).

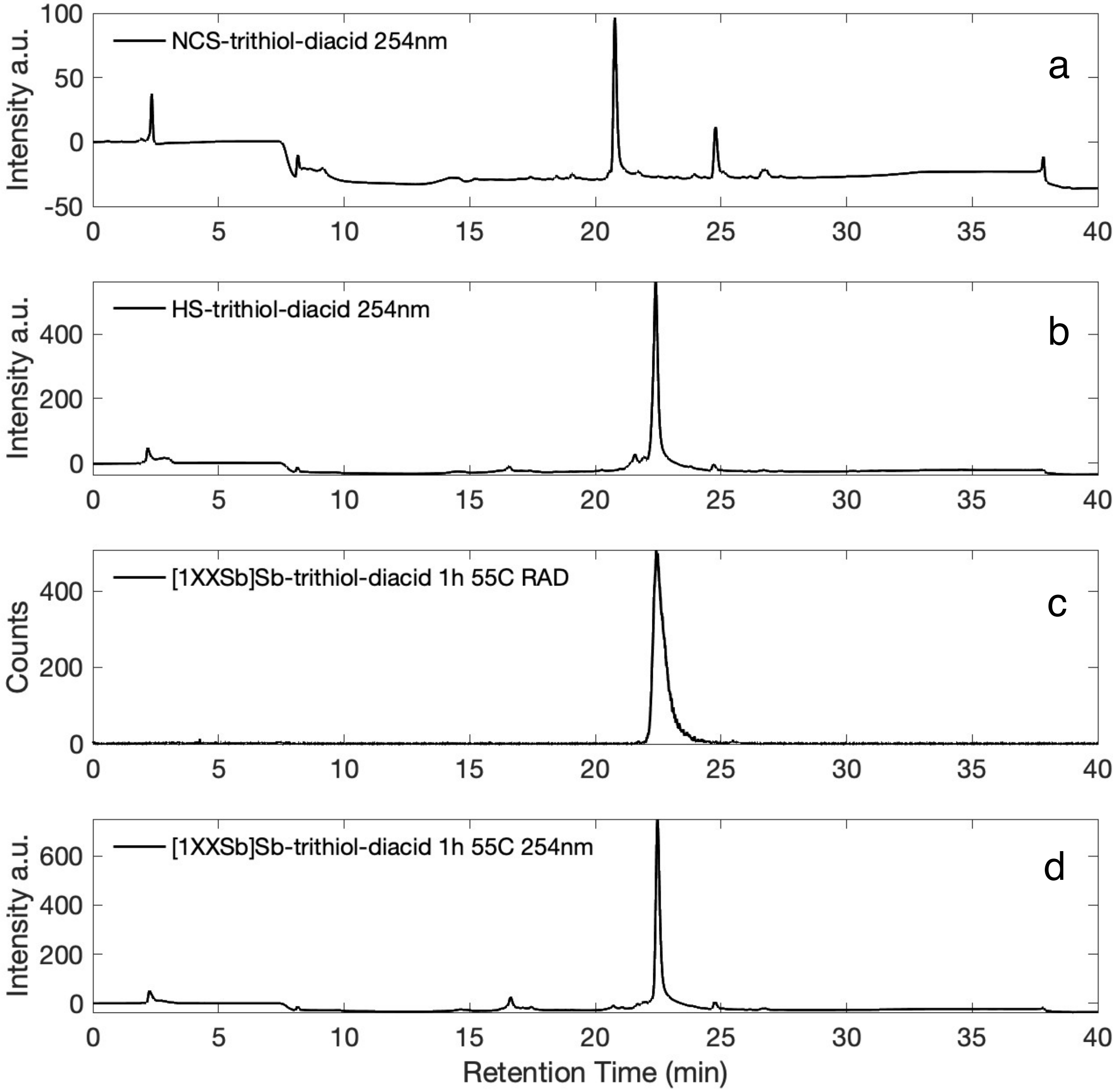

Figure 25: RP-HPLC of trithiol-diacid deprotection and radiolabeling. a) thiocyanate protected trithiol-diacid, b) TCEP deprotected trithiol-diacid, c) radio-HPLC chromatogram of trithiol-diacid complexed ^{1XX}Sb, d) corresponding 254 nm UV-Vis chromatogram of radiolabeling solution. **RP-HPLC Method A:** Instrument: Agilent 1260 II system

(Santa Clara, CA) with Ortec (AMETEK ORTEC, Oak Ridge, TN) detector. Column: Phenomenex (Torrance, CA) Jupiter C_{18} column (300 Å, 5 μm, 150 mm × 4.6 mm). Flow rate: 1 mL/min. Solvents: A = 0.1 M ammonium citrate (pH 4.5), B = 0.1% TFA in MilliQ water, C = 0.1% TFA in MeCN. Method: t = 0–5 min: A; 5–10 min: 95% B and 5% C; 10–30 min: linear ramp from 5 to 95% C; 30–35 min: 95% C and 5% B; 35–36 min: linear ramp from 95 to 5% C; 36–40 min: A.

3.5. Serum Stability, Cysteine Challenges, and $\mathrm{LogD}_{7.4}$ Measurement

$[^{1XX}\mathrm{Sb}]$Sb-trithiol-diacid was stable over 72 h when challenged with biologically relevant complexing agents. Radio-RP-HPLC traces of $[^{1XX}\mathrm{Sb}]$Sb-trithiol-diacid challenged with 25 mM cysteine and FBS at 24 h are reported in **Figure 26**. After 72 h, HPLC analyses showed $[^{1XX}\mathrm{Sb}]$Sb-trithiol-diacid to be 91% ± 9% (N = 3) intact in 25 mM cysteine (**Figure 27c**) and 97.5% ± 1.6% (N = 3) intact in FBS (**Figure 27d**), and we expect $[^{1XX}\mathrm{Sb}]$Sb-trithiol-diacid to be stable *in vivo*. A $\mathrm{logD}_{7.4}$ of -1.6 ± 0.1 (N = 3) indicates $[^{1XX}\mathrm{Sb}]$Sb-trithiol-diacid preferentially associates with PBS phase and is hydrophilic, which is expected due to the two carboxylic acid arms available for conjugation. Radioarsenic-trithiol-diacid $\mathrm{logD}_{7.4}$ values have not been reported; however, the RM2 peptide bioconjugated forms are reported as -0.21 ± 0.02 for $[^{77}\mathrm{As}]$As-trithiol-serine-serine-RM2 and -1.26 ± 0.05 for $[^{77}\mathrm{As}]$As-trithiol-glutamine-serine-RM2 [184].

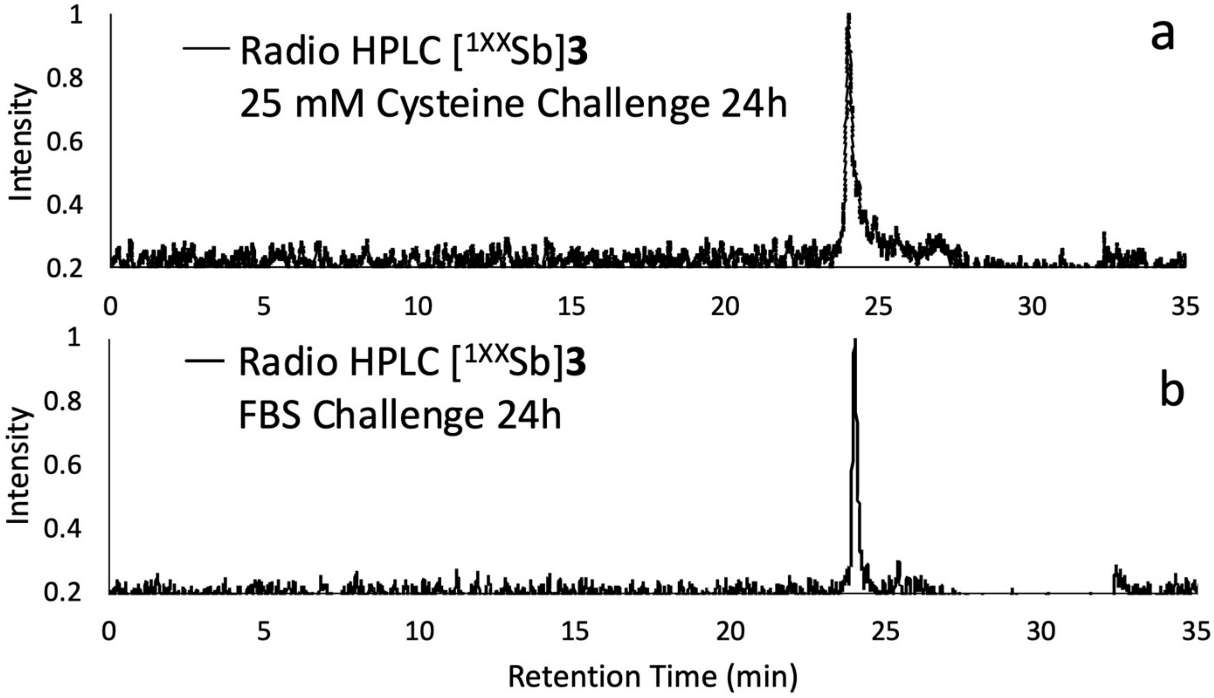

Figure 26: HPLC radiation detector traces showing [^{1XX}Sb]Sb-trithiol-diacid stability. a) 24 h 25 mM cysteine challenge R_t = 24.0 min, b) 24 h FBS challenge R_t = 23.9 min. **RP-HPLC Method B**: Instrument: Agilent 1260 II system (Santa Clara, CA) with Ortec (AMETEK ORTEC, Oak Ridge, TN) detector. Column: DIONEX (Sunnyvale, CA) Acclaim C_{18} column (120 Å, 5 µm, 250 mm x 4.6 mm). Flow rate: 1 mL/min. Solvents: A = 0.1% TFA in MilliQ water, B = MeCN. Method: t = 0–3.5 min: 25% B; 3.5–23.5 min: linear ramp 25–50% B; 23.5–24 min: 50–90% B; 24–29 min: 90% B; 29–30 min: 90–25% B; 30–35 min: 25% B.

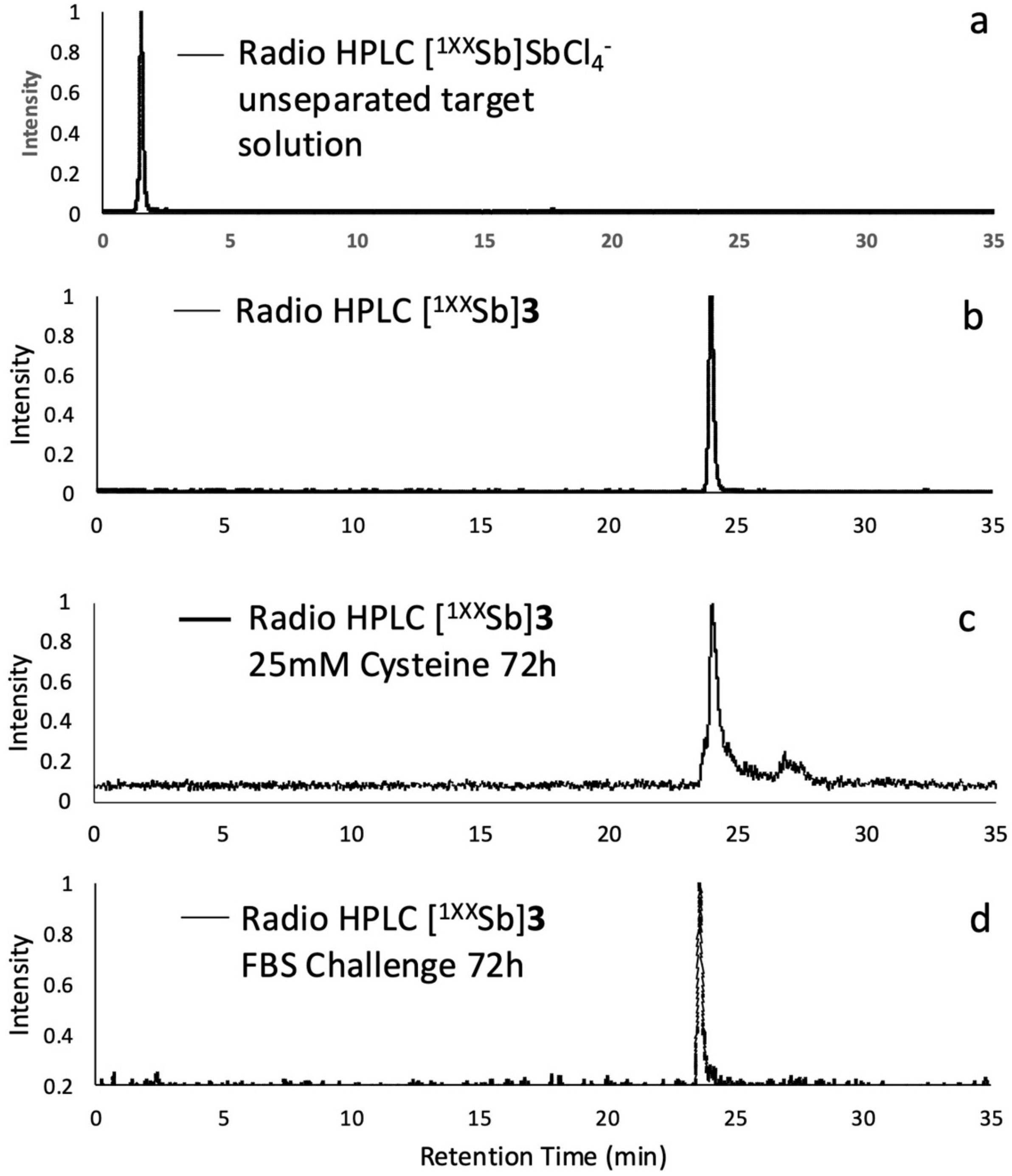

Figure 27: RP-HPLC traces showing chelation of radioantimony using trithiol chelator **2**. a) unchelated radioantimony $R_f = 1.5$ min, b) direct radiolabeling of radioantimony from unseparated solution using **2** $R_f = 24.0$, c) 72 h 25 mM cysteine challenge $R_f = 24.0$ d) 72 h FBS challenge $R_f = 23.6$. **RP-HPLC Method B**: Instrument: Agilent 1260 II

system (Santa Clara, CA) with Ortec (AMETEK ORTEC, Oak Ridge, TN) detector. Column: DIONEX (Sunnyvale, CA) Acclaim C_{18} column (120 Å, 5 µm, 250 mm x 4.6 mm). Flow rate: 1 mL/min. Solvents: A = 0.1% TFA in MilliQ water, B = MeCN. Method: t = 0–3.5 min: 25% B; 3.5–23.5 min: linear ramp 25–50% B; 23.5–24 min: 50–90% B; 24–29 min: 90% B; 29–30 min: 90–25% B; 30–35 min: 25% B.

3.6. Radiolabeling Conjugated Trithiol Compounds

3.6.1. Trithiol-RM2

The thiocyanate protected compound **4** (**Figure 28a**, R_t = 14.3 min) reacts with TCEP to cleave thiocyanate groups and produce the deprotected trithiol-RM2 compound **5** (**Figure 28b**, R_t = 16.9 min). After heating **5** with [$^{nat/1XX}$Sb]$SbCl_3$ for 1 h at 55 °C, four peaks are formed (**Figure 28c and 28d,** R_t = 16.5, 18.0, 19.2, and 23.2 min), with a radioactive antimony labeling primary species at R_t = 19.2 min. LCMS conducted by collaborators confirmed formation of [^{nat}Sb]Sb-trithiol-RM2, and RP-HPLC sample injection confirmed identity of [^{1XX}Sb]Sb-trithiol-RM2 as R_t = 16.5 min (**Figure 28e**). Semi-preparative RP-HPLC allowed isolation of R_t = 16.5 min prior to solvent conversion to PBS and further stability tests.

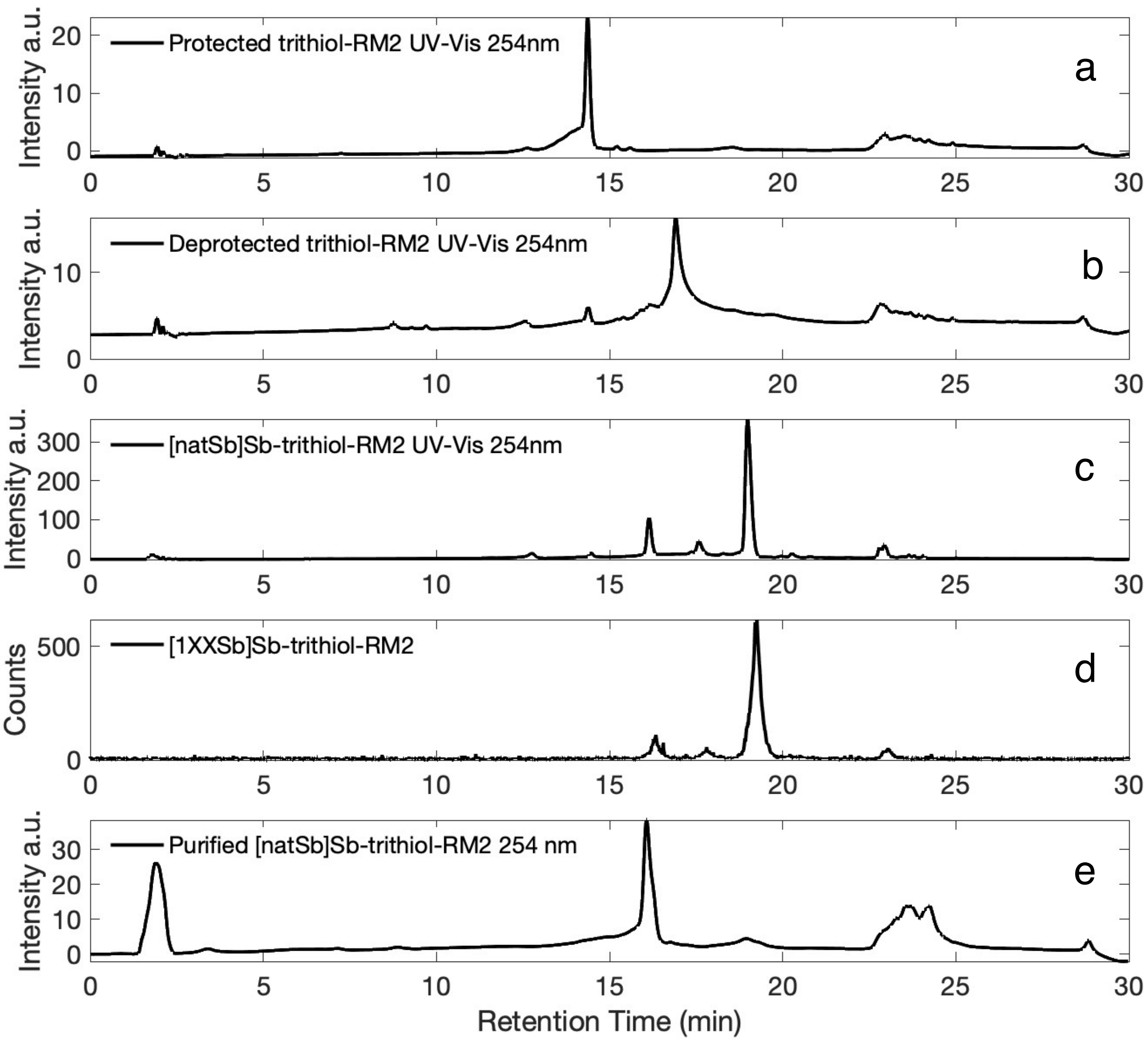

Figure 28: RP-HPLC traces showing a) 254 nm UV-Vis chromatogram of protected compound **4**, b) 254 nm UV-Vis chromatogram of deprotection of **4** to form **5**, c) 254 nm UV-Vis chromatogram of crude labeling of **5** with $^{\text{nat}}$Sb forming [$^{\text{nat}}$Sb]Sb**6**, d) radiolabeling reaction of **5** forming [$^{\text{1XX}}$Sb]Sb**6**, e) non-radioactive standard [$^{\text{nat}}$Sb]Sb**6**. **RP-HPLC Method C:** Instrument: Agilent 1260 II system (Santa Clara, CA) with Ortec (AMETEK ORTEC, Oak Ridge, TN) detector. Column: DIONEX (Sunnyvale, CA) Acclaim C$_{18}$ column (120 Å, 5 µm, 250 mm x 4.6 mm). Flow rate: 1 mL/min. Solvents: A = 0.1% TFA in MilliQ water, B = MeCN. Method: t = 0–20

min: 20–60% B; 20–21 min: 60–90% B;21–26 min: 90% B; 26–27 min: 90–20% B; 27-30 min: 20% B.

3.6.2. Trithiol-Olaparib

Both non-radioactive and radioactive antimony labeling of trithiol-Olaparib formed a singular, uniform species with R_t = 14.6 min (**Figure 29b and 29c**), which differs from the reduced trithiol-Olaparib compound **8** (**Figure 29a**, R_t = 15.4 min). The complex remains stable through C8 purification in EtOH (**Figure 29d**).

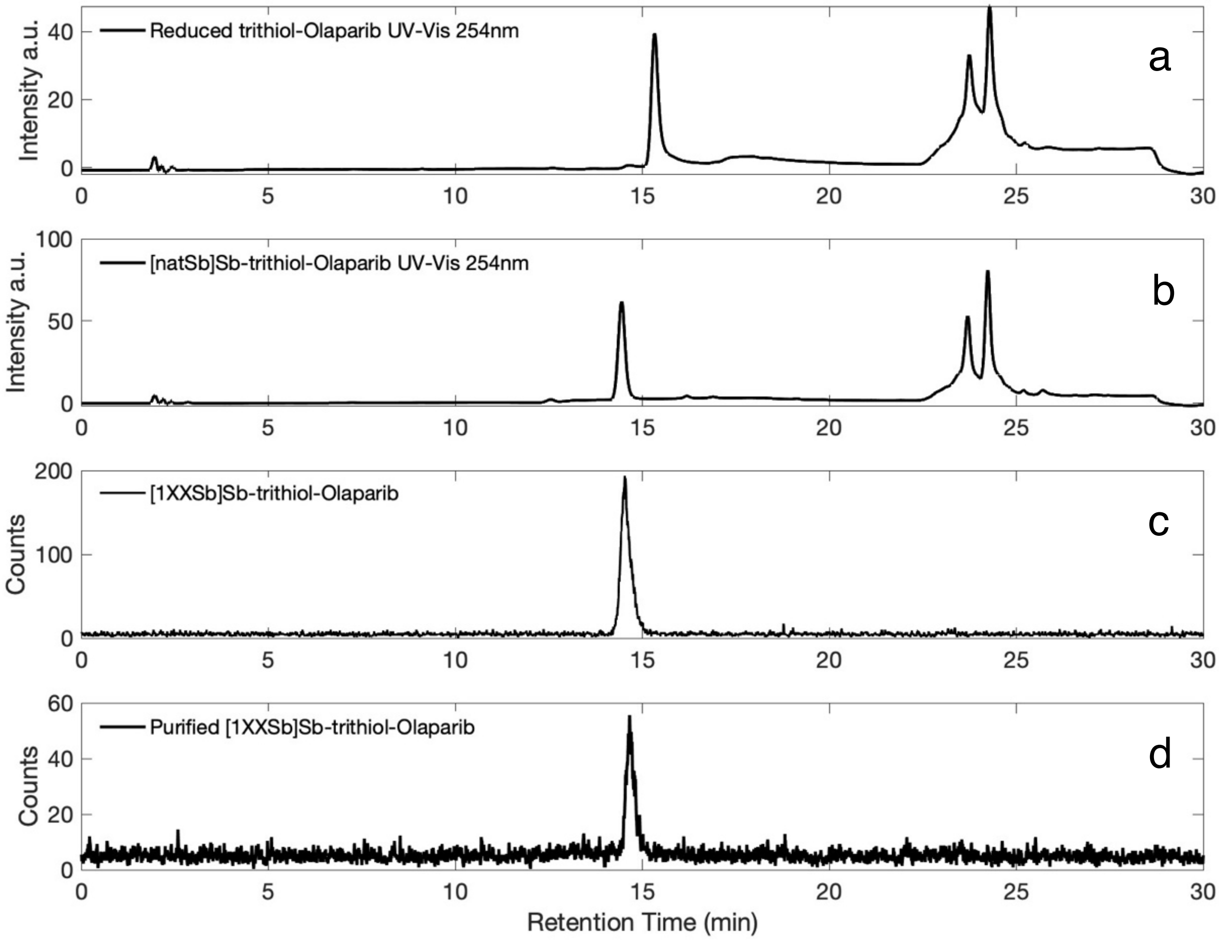

Figure 29: RP-HPLC traces showing a) 254 nm UV-Vis chromatogram of reduced compound **8**, b) 254 nm UV-Vis chromatogram of crude labeling of **8** with $^{nat}SbCl_3$ forming

[^{nat}Sb]Sb**9**, c) ^{1XX}Sb radiolabeling reaction of **8** forming [^{1XX}Sb]Sb**9**, d) C8 cartridge purified [^{1XX}Sb]Sb**9**. **RP-HPLC Method C:** Instrument: Agilent 1260 II system (Santa Clara, CA) with Ortec (AMETEK ORTEC, Oak Ridge, TN) detector. Column: DIONEX (Sunnyvale, CA) Acclaim C_{18} column (120 Å, 5 µm, 250 mm x 4.6 mm). Flow rate: 1 mL/min. Solvents: A = 0.1% TFA in MilliQ water, B = MeCN. Method: t = 0–20 min: 20–60% B; 20–21 min: 60–90% B;21–26 min: 90% B; 26–27 min: 90–20% B; 27-30 min: 20% B.

3.6.3. PBS Stability and $LogD_{7.4}$ Measurement

We purified both [^{1XX}Sb]Sb-trithiol-RM2 and [^{1XX}Sb]Sb-trithiol-Olaparib complexes using C8 cartridges, eluting in EtOH with stability intact before converting the solvent matrix to PBS. Upon addition of PBS, complex solutions were monitored for stability via RP-HPLC. **Figure 30** shows example chromatograms of [^{1XX}Sb]Sb-trithiol-Olaparib at t = 0, 2, 15, and 48 h. Comparison of activity eluting at the solvent front and intact complex at R_t allowed calculation of intact complex, with [^{1XX}Sb]Sb-trithiol-Olaparib and [^{1XX}Sb]Sb-trithiol-RM2 stability time courses presented in **Figure 31**. After 16 h in PBS, 3.0% of the [^{1XX}Sb]Sb-trithiol-RM2 complex remains intact, and after 24 h, 5.5 % of [^{1XX}Sb]Sb-trithiol-Olaparib is intact (**Figure 31**).

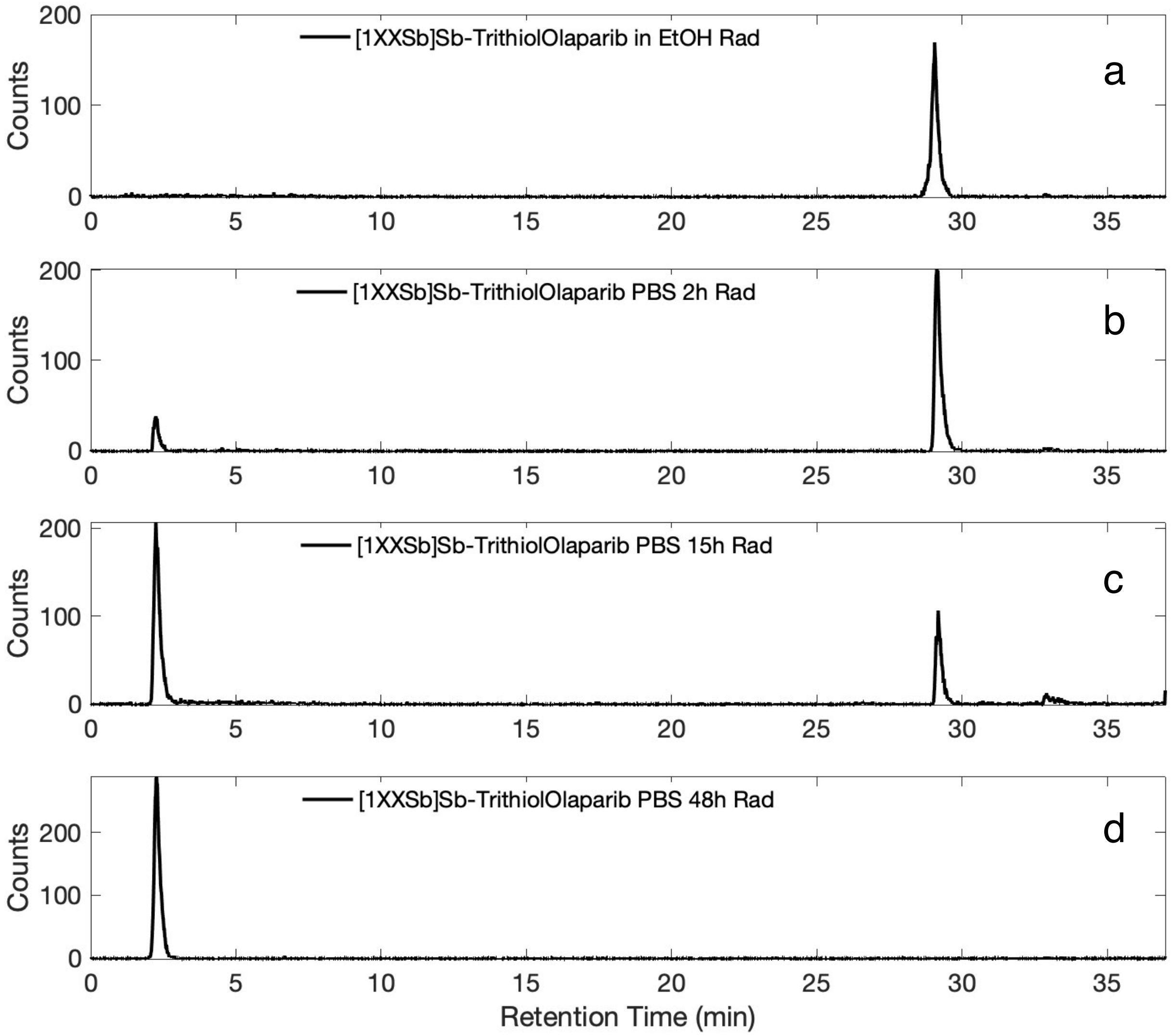

Figure 30: radio-RP-HPLC traces analyzing [^{1XX}Sb]Sb**9** complex stability in EtOH and PBS. a) purified in EtOH b) 2 h in PBS, c) 15 h in PBS, d) 48 h in PBS. **RP-HPLC Method D:** Instrument: Agilent 1260 II system (Santa Clara, CA) with Ortec (AMETEK ORTEC, Oak Ridge, TN) detector. Column: 150 mm C_{18} Jupiter column (Phenomenex, Torrance, CA). Flow rate: 1 mL/min. Solvents: A = 0.1 M ammonium citrate (pH 4.5), B = 0.1% FA/H_2O, C = MeOH. Method: 0–5 min: 100% A; 5–10 min: 100% B; 10–30 min: linear ramp to 0% B / 100% C; 30–32 min: 100% B; 32–37 min, 100% A.

Although [^{1XX}Sb]Sb-trithiol-Olaparib quickly decomposes in PBS, the compound remains stable 24 h in EtOH (**Figure 32**). We hypothesize that complex decomposition is driven by hydrolysis or interactions between Sb and the phosphates within PBS. [^{1XX}Sb]Sb-trithiol-RM2 and [^{1XX}Sb]Sb-trithiol-Olaparib have measured LogD$_{7.4}$ values of -0.51 ± 0.09 (N = 3) and -1.80 ± 0.05 (N = 3), respectively. The [^{1XX}Sb]Sb-trithiol-Olaparib complex has a more negative logD$_{7.4}$ value than [^{1XX}Sb]Sb-trithiol-diacid, meaning greater portion associates with the aqueous phase. With more positive logD$_{7.4}$, the [^{1XX}Sb]Sb-trithiol-RM2 molecule is more lipophilic than both the [^{1XX}Sb]Sb-trithiol-diacid and [^{1XX}Sb]Sb-trithiol-Olaparib compounds. This is corroborated by RP-HPLC retention times where [^{1XX}Sb]Sb-trithiol-Olaparib (R_t = 14.6 min) elutes almost 2 min earlier than [^{1XX}Sb]Sb-trithiol-RM2 (R_t = 16.5 min). Aforementioned, [^{77}As]As-trithiol-glutamine-serine-RM2 (the radioarsenic labeled analogue) has a reported LogD$_{7.4}$ of -1.26 ± 0.05 [184]. Labeling the trithiol-RM2 compound with antimony as opposed to arsenic increased compound lipophilicity.

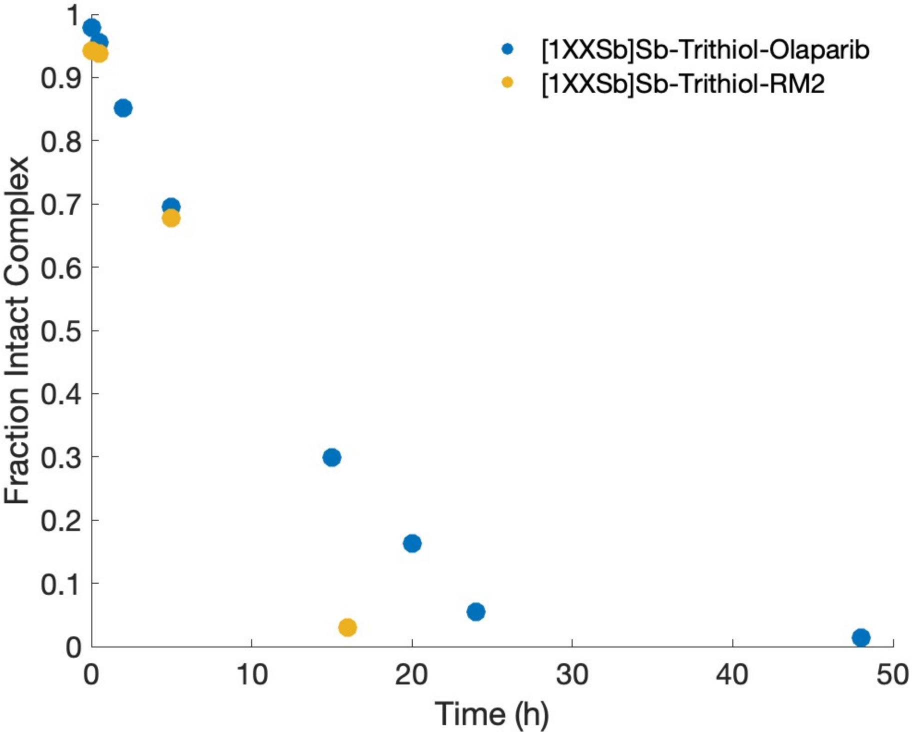

Figure 31: Fraction of intact complex for [^{1XX}Sb]Sb**6** and [^{1XX}Sb]Sb**9** calculated via comparing integrated peaks of radio-RP-HPLC chromatograms, assessing stability in PBS.

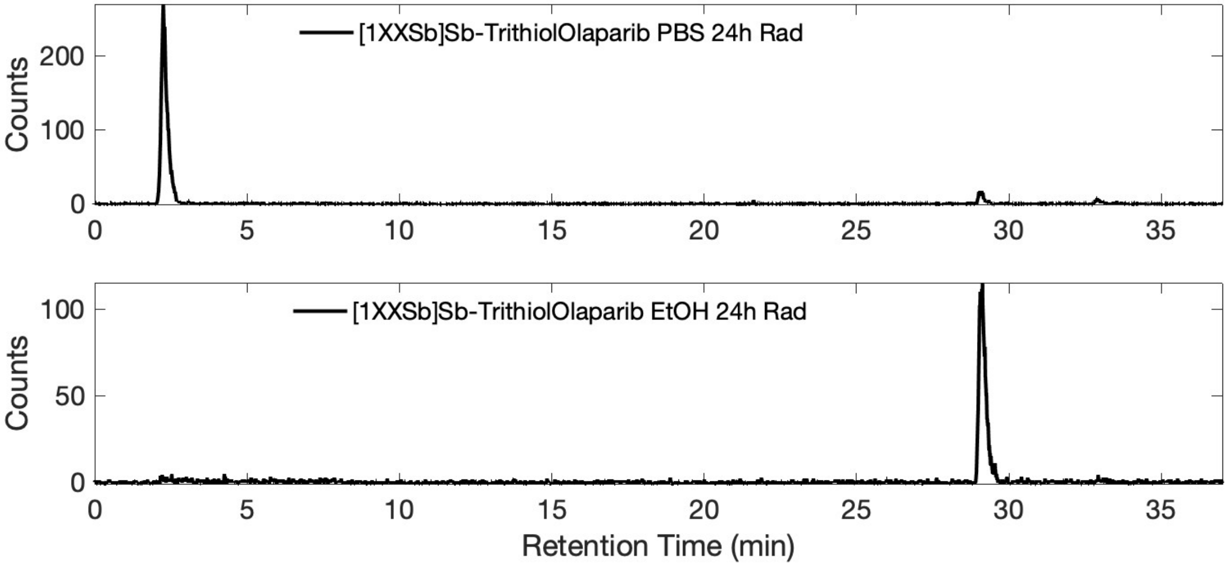

Figure 32: radio-RP-HPLC traces analyzing [^{1XX}Sb]Sb**9** complex stability in EtOH and PBS. a) [^{1XX}Sb]Sb**9** in PBS 24 h, b) [^{1XX}Sb]Sb**9** in EtOH 24 h. **RP-HPLC Method D:**

Instrument: Agilent 1260 II system (Santa Clara, CA) with Ortec (AMETEK ORTEC, Oak Ridge, TN) detector. Column: 150 mm C_{18} Jupiter column (Phenomenex, Torrance, CA). Flow rate: 1 mL/min. Solvents: A = 0.1 M ammonium citrate (pH 4.5), B = 0.1% FA/H_2O, C = MeOH. Method: 0–5 min: 100% A; 5–10 min: 100% B; 10–30 min: linear ramp to 0% B / 100% C; 30–32 min: 100% B; 32–37 min, 100% A.

4. Conclusions

We have described development of radioantimony chelation, using a novel, functionalizable trithiol ligand capable of direct labeling from unseparated target solution, circumventing usual radionuclide isolation from dissolved accelerator targets. This is the first report of radioantimony complexation with a BFC—an essential step towards exploration of ^{117}Sb and ^{119}Sb in theranostic, targeted radionuclide therapeutic contexts. We report complexation of radioantimony with the trithiol-diacid chelator in conditions (EtOH, 55 °C) compatible with many targeting vector strategies, particularly small molecules and short peptide chains. The [^{1XX}Sb]Sb-trithiol-diacid complex remains intact when challenged with either 25 mM cysteine or FBS for over 72 h.

Antimony radiolabeling of trithiol-RM2 formed radioactive species with R_t matching a [^{nat}Sb]Sb-trithiol-RM2 standard. Unique R_t and formation of primary radioactive species speaks to likely formation of radioantimony labeled trithiol-Olaparib complex. These complexes withstood purification, retaining complex integrity in EtOH. However, both complexes experienced instability in PBS. [^{1XX}Sb]Sb-trithiol-RM2 degraded within 16 h of exposure to PBS and [^{1XX}Sb]Sb-trithiol-Olaparib degraded within approximately 24 h of PBS addition. Non-radioactive complexes with matching R_t were formed in crude, EtOH-based conditions, but high instability hindered characterization of purified product, inhibiting confirmation of species via additional spectral techniques. This work represents a first labeling of targeted molecular construct with radioantimony.

Chapter 4: Radioantimony(V) Chelation Strategies

1. Introduction

1.1. Contributors

The content from this chapter can be found within the review article [Randhawa, P.; Olson, A. P.; et. al. *Curr Radiopharm* **2021**, *14* (4), 394–419.] published by Bentham Science and a manuscript under review at Angewandte Chemie – International Edition with collaborators from Oak Ridge National Laboratory (ORNL) (Dr. Nikki Thiele, Dr. Alexander Ivanov, Dr. Briana Schrage, Dr. Faizul Islam, Dr. Lesta Fletcher, Dr. Darren Driscoll, Dr. Vilmos Kertesz, Dr. Frankie White, Megan Simms) and UW-Madison Chemistry (Morgan Dierolf, Owen Glaser, and Prof. Dr. Eszter Boros). Francesca Verich assisted with all mouse imaging and *ex vivo* experiments. Justin Jeffery conducted tail vain injections, helped operate scanners, and guided ^{117}Sb phantom image characterization and scanner calibration.

1.2. Literature Review

1.2.1. Chemistry of Antimony(V)

Upon oxidation, Sb(V) increases in Lewis acidity [150,152] where it is expected to best interact with hard donor groups and strong Lewis bases. The increased Lewis acidity of Sb(V) is uniquely strong and warrants classification as a super acid [190]. The aqueous chelation chemistry of Sb(V) has scarcely been explored beyond a few studies evaluating interaction with low molecular weight ligands [26,36,37]. In comparison to Sb(III), Sb(V) has higher charge density and lacks a hemidirecting lone pair, properties which may promote complex stability. In oxic conditions at low pH, Sb-di-carboxylic acid complexes form with greatest proportion. At higher pH, Sb(V) readily forms complexes as hydroxyl-carboxylic, aliphatic-hydroxyl, and aromatic-hydroxyl forms [191]. Studies indicate stable complexes with Sb(V) require low molecular weight organic ligands with oxygen atoms on two adjacent functional groups to form bidentate structures, as seen by stable complexes formed with citric, salicylic, oxalic acids, catechol, mannitol, and xylitol [139].

1.2.2. Biological Applications of Antimony

Current and historic clinical treatment for the parasitic infections Schistosomiasis and Leishmaniasis employ pentavalent Sb-based complexes (sodium stibogluconate and meglumine antimoniate, **Figure 33**) [192]. After reduction of Sb(V) to Sb(III) inside of the parasite, Sb(III) interferes with the parasite's thiol redox metabolism, effluxing trypanothione and glutathione (GSH) from the cell and inhibiting trypanothione reductase enzymatic activity [193]. The interaction of antimony with biological molecules provides supporting evidence toward the strong interaction of Sb with thiol donor atoms. Due to this proposed mechanism of action, anti-tumor properties of Sb(III) and Sb(V) compounds (studied in DTPA and thiol coordinated systems) have drawn interest [194,195] toward development of new monodentate thiol complexes [166]. As mentioned in **Chapter 3**, DMPS (2,3-dimercaptopropane-1-sulfonic acid) and DMSA (meso-2,3-dimercaptosuccinic acid) are used for clinical treatment of antimony heavy metal poisoning [171].

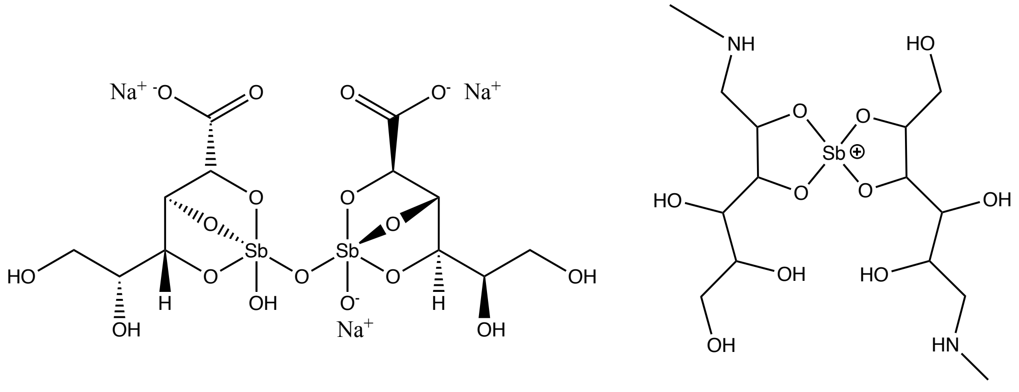

sodium stibogluconate

meglumine antimoniate

Figure 33: chemical structures of antimony-based pharmaceuticals used for treatment of parasitic infections.

1.2.3. Biodistribution of Radioantimony

Studies motivated by environmental contamination concerns have primarily measured organ distribution and biological impact of inorganic Sb speciation. The biological distributions of nuclear reactor produced carrier added (c.a.) $^{124}SbCl_3$ were measured for tumor bearing male mice [196] and rats [197]. Although non-tumor targeting, researchers reported highest $^{124}SbCl_3$ uptake within the liver, kidney, and bone at 3 and 4 h post injection (p.i.) for both mice and rats. Within piglets, an exponential non-radioactive $KSb(OH)_6$ dose dependent response curve measured kidney uptake >2x liver uptake, and linear response curves depicted hair and metacarpal bone uptake >3x that of the spleen with no blood accumulation [198]. After inhalation of c.a. $[^{122/124}Sb]SbH_3$ gas, guinea pigs had greatest organ accumulation of Sb within the liver, spleen, and kidney [199].

Antimony administered to male rats as Sb(III) (Sb_2O_3) accumulated primarily within Red Blood Cells (RBC) through association with hemoglobin. Additionally, the spleen and lung accumulated elevated amounts of Sb, possibly through RBC uptake. Urinary excretion of inorganic Sb in the 5+ oxidation state suggests oxidation, as opposed to methylation, as the primary metabolic processing mechanism [200]. Within human whole blood samples, Sb(V) is reduced by GSH to Sb(III), which is unstable under oxic conditions and readily oxidized back to Sb(V). This redox cycling increased superoxide dismutase activity for protection against free radicals [201]. Optical absorbance measurements of Sb(III) resulting from reduction of administered Sb(V) with GSH as a function of time, temperature, pH, and GSH concentration found ready reduction of Sb(V) to Sb(III) at a stoichiometry of 5:1 GSH:Sb(V) at pH 3.5 – 5, forming $Sb(GSH)_3$. Little reduction of Sb(V) was observed at biologically relevant conditions (pH 7.2, 37 °C). Samples were flushed with argon prior to reaction incubation and kept in oxygen free environments to prevent re-oxidation of Sb(III) to Sb(V); however, the deconvolution of these possible redox cycling processes were not experimentally confirmed [202].

Ion chromatograms of plasma samples from Rhesus monkeys receiving meglumine antimoniate treatment for Leishmaniasis infection showed slow release of Sb(V) from drug construct and subsequent conversion from Sb(V) to Sb(III). *Ex vivo* biodistribution measurements of organs, tissues, and other biological samples found greatest Sb uptake within the urine (20.9 μg/g tissue), thyroid (10.4 μg/g tissue), nails (5.7 μg/g tissue), liver (3.3 μg/g tissue), gallbladder (2.2 μg/g tissue), and spleen (1.6 μg/g tissue) [203]. Female BALB/c mice infected with Leishmaniasis were treated with c.a. [$^{122/124}$Sb]Sb-meglumine, and *ex vivo* biodistributions were collected up to 72 h p.i.. Antimony did not accumulate within the brain, heart, lungs, or uterus. Within the spleen, $^{122/124}$Sb uptake quickly (< 3min p.i.) peaked before slowly excreting, and a maximum liver uptake at 15 min p.i. (~50 %IA/g) was observed [204].

Another study using female BALB/c mice measured higher antimony levels within parasite infected footpads as compared to uninfected controls and a 50 h p.i. liver uptake of ~10 %IA/g. For meglumine antimonate, similar scale %IA/g clearance time courses were measured within the kidney and small intestine [205]. Twenty-one days p.i. with meglumine antimony, male rats had highest Sb uptake within the spleen (81.9 μg/g tissue), femur (18.3 μg/g tissue), thyroid (18.0 μg/g tissue), lungs (7.7 μg/g tissue), adrenal glands (5.9 μg/g tissue), and kidney (5.4 μg/g tissue) [206]. In human patients receiving clinical treatment for Leishmaniasis infection, meglumine antimoniate modulated immune gene expression—at various timepoints upregulating genes related to T_H1, neutrophil recruitment, and membrane receptor expression [207].

In summary, Sb is non-tumor targeting, and, due to environmental contamination concerns, Sb biological distribution has primarily been studied with inorganic species. In oxic conditions, Sb(III) readily oxidizes to Sb(V) and is subsequently reduced via GSH complexation, providing redox cycling which explains observed biological toxicities. Antimony is cleared from the body through the urinary system as Sb(V), meaning oxidation is the primary metabolic processing route. Finally, Sb accumulates in the liver, kidney, bone, thyroid, spleen, and lung, with accumulation in the latter two organs likely due to RBC association.

1.2.4. Imaging Applications of Radioantimony

Having few low energy X-ray and gamma emissions, ^{119}Sb is well suited for therapeutic applications. Researchers have proposed ^{117}Sb ($t_{1/2}$ = 2.80 *1* h, EC = 100%, E_γ = 158.562 *15* keV, I_γ = 85.9%, $E_{\beta+}$ = 261.9 *39* keV, $I_{\beta+}$ = 1.81 *11 %*) [72] as a radioisotopic SPECT imaging analogue and shown adequate imaging capabilities using a Jazczak phantom. Antimony-117 planar scintigraphy and SPECT images distinguish all cold rods in the scintigraphy image, the three largest cold spheres (∅38 mm, ∅31.8 mm, and ∅25.4 mm), and a modelled hot tumor over background signal [48]. With a 3.6 min half-life, generator produced, untargeted ^{118}Sb was used for PET imaging with significant limitations in resolution and time course imaging beyond 5 min p.i. [115]. PET imaging of ^{118m}Sb and ^{117}Sb have not been reported.

1.3. Motivation

Densely charged, hydrolysis-prone metal ions such as Zr^{4+}, Nb^{5+}, Ga^{3+}, and Ti^{4+} are stably complexed by the tris-catechol chelator TREN-CAM (**Figure 34**) [39–42]. Because Sb(V) forms stable complexes with three catechols [139], and TREN-CAM has complexed metals prone to hydrolysis, we hypothesized its ability to stably complex Sb(V). In addition to emitting photons suitable for SPECT imaging, ^{117}Sb emits a β^+ with branching ratio 1.81 *11 %*, which should allow PET imaging. To ascertain *in vivo* complex stability, we propose production of ^{117}Sb via deuteron bombardment of ^{nat}Sn targets and imaging via SPECT and PET modalities.

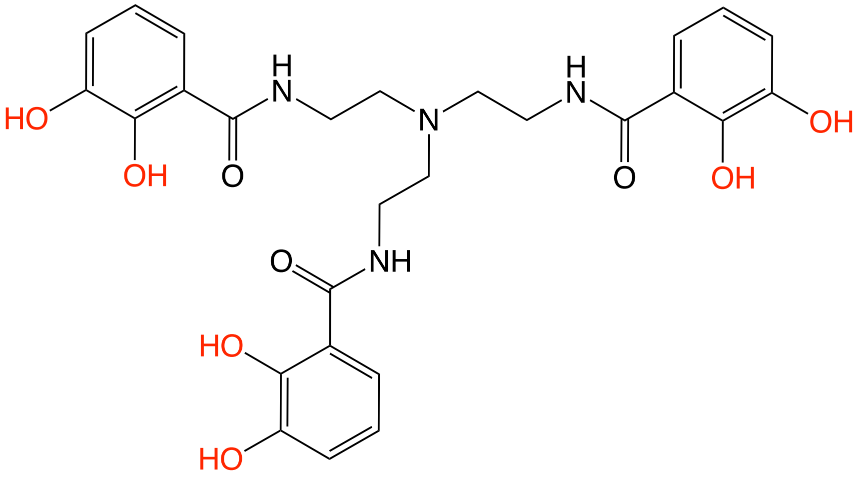

Figure 34: Structure of tris(2-aminoethyl)amine (TREN) catecholamide (CAM).

2. Materials and Methods

2.1. Chemicals and General Methods

All reagents were purchased from commercial vendors and used without further purification. All solutions were prepared with MilliQ water. Fisher Chemicals (Pittsburg, PA, USA) supplied c.HCl, 30% H_2O_2, and EtOH. DBE, MeOH, MeCN, *n*-octanol, $SbCl_3$, and NH_4OH were purchased from Sigma-Aldrich (Burlington, MA, USA). We purchased DMSO from VWR Life Sciences (Radnor, PA, USA), NH_4OAc from EMD Chemicals (Gibbstown, NJ, USA), citric acid from Avantor Sciences (Radnor, PA, USA), and PBS from Lonza (Walkersville, MA, USA).

Collaborators prepared stock solutions of TREN-CAM in 20% DMSO/80% H_2O for radiolabeling reactions in HCl or NH_4OAc. We prepared NH_4OAc buffers (0.5 M, pH 4, 6, 7, and 7.4) using NH_4OAc (Sigma-Aldrich) and glacial HOAc (Sigma-Aldrich). For radiolabeling reactions in DMSO/MeOH, stock solutions of TREN-CAM were prepared in 100% DMSO or EtOH. Normal human serum as a lyophilized powder was purchased from Jackson ImmunoResearch (Ely, UK) and reconstituted at 2x concentration in MilliQ water.

ORNL collaborators recorded NMR spectra on a Bruker Avance III-400 MHz NMR spectrometer equipped with a BBO probe. Chemical shifts are reported in ppm. NMR spectra were acquired in either deuterated MeOH (CD_3OD) or deuterated DMSO ($(CD_3)_2SO$) and referenced to the residual solvent signal (3.31 ppm) or the tetramethylsilane internal standard (0 ppm), respectively. The splitting of proton resonances in the reported ^1H NMR spectra is defined as: s = singlet, d = doublet, t = triplet, q = quartet, m = multiplet, and br = broad. HRMS were obtained on either a Bruker MaXis ultra-high resolution quadrupole TOF mass spectrometer or a Q Exactive HF Orbitrap mass spectrometer (Thermo Scientific) in positive electrospray ionization mode. Samples were introduced into the Q Exactive HF Orbitrap using an Open Port Sampling Interface on the instrument. Elemental analysis was performed by Atlantic Microlab, Inc. (Norcross, GA). Four different analytical HPLC methods allowed visualization of Sb-TREN-CAM complexation and speciation and are referenced as follows.

ORNL cold HPLC: 14.8 min (Peak 1), **21.3 min** (Peak 2) Instrument: Shimadzu. Column: Restek Ultra Aqueous C_{18} column (100 Å, 5 μm, 250 mm × 21.2 mm). Flow rate: 1 mL/min. Solvents: A = 0.1% Formic Acid (FA)/H_2O, B = 0.1% FA/MeCN. Method: 0–5 min: 10% B; 5–25 min: linear ramp 10–100% B; 25–30 min: 100% B.

ORNL radio-HPLC: 22.8 min (Peak 1), **35.7 min** (Peak 2) Instrument: Shimadzu coupled to a LabLogic Flow-Ram detector equipped with Laura software. Column: Restek Ultra Aqueous C_{18} column (100 Å, 5 μm, 250 mm × 21.2 mm). Flow rate: 1 mL/min. Solvents: A = 0.1 M ammonium citrate (pH 4.5), B = 0.1% FA/H_2O, C = 0.1% FA/MeCN. Method: 0–5 min: 100% A; 5–10 min: 100% B; 10–35 min: linear ramp to 0% B / 100% C; 35–40 min: 100% C; 40–46 min, 100% A.

UW-Madison radio-HPLC method A: 23.7 min (Peak 1), **30.0 min** (Peak 2) Instrument: Agilent

1260 II system (Santa Clara, CA) with Ortec (AMETEK ORTEC, Oak Ridge, TN) detector. Column: 150 mm C_{18} Jupiter column (Phenomenex, Torrance, CA). Flow rate: 1 mL/min. Solvents: A = 0.1 M ammonium citrate (pH 4.5), B = 0.1% FA/H_2O, C = MeOH. Method: 0–5 min: 100% A; 5–10 min: 100% B; 10–30 min: linear ramp to 0% B / 100% C; 30–32 min: 100% B; 32–37 min, 100% A.

UW-Madison radio-HPLC method B: 17.6 min (Peak 1), **22.8 min** (Peak 2) Instrument: Agilent 1260 II system (Santa Clara, CA) with Ortec (AMETEK ORTEC, Oak Ridge, TN) detector. Column: 150 mm C_{18} Jupiter column (Phenomenex, Torrance, CA). Flow rate: 1 mL/min. Solvents: A = 0.1 M ammonium citrate (pH 4.5), B = 0.1% TFA/H_2O, C = 0.1% TFA/MeCN. Method: 0–5 min: 100% A; 5–10 min: 95% B / 5% C; 10–30 min: linear ramp to 5% B / 95% C; 30–35 min: 5% B / 95% C; 35–36 min: linear ramp to 95% B / 5% C; 36–40 min, 100% A.

2.2. Oxidation State Verification

After shipment to ORNL, ^{1XX}Sb produced and purified at UW-Madison, as described in **Chapter 2** via column chromatography, existed in a mixture of oxidation states. Under a variety of experimental conditions, collaborators analyzed the oxidation state of ^{1XX}Sb by anion-exchange radio-HPLC (Shimadzu instrument; LabLogic Flow-Ram detector; Hamilton PRP-X100 column, 150 × 4.1 mm; 5 μm) using a method established in the literature for non-radioactive Sb [208]. Using an isocratic 0.1 M ammonium citrate (pH 4.5, 1 mL/min, 35 min) mobile phase, radio-HPLC with an anion-exchange column separated ^{1XX}Sb(V) and ^{1XX}Sb(III) from injected samples of mixed oxidation state. Gamma counting (Perkin Wizard2 gamma counter, open window) of collected fractions confirmed total ^{1XX}Sb activity recovery regardless of whether samples were mixed with mobile phase prior to injection. To study the impact of temperature on oxidation state, samples were heated at 25 °C or 80 °C for 1 h before anion exchange radio-HPLC analysis. Collaborators verified Sb(III) and Sb(V) anion-exchange retention times by reacting ^{1XX}Sb with oxidizing or reducing agents. After 24 h at 25 °C, the following oxidation/reduction reactions were diluted with ammonium citrate before anion exchange radio-HPLC analysis.

Sb(V) through H_2O_2 oxidation: 20 μL of ^{1XX}Sb (570 nCi), 90 μL of 0.5 M NH_4OAc (pH 4), 40 μL of H_2O_2 (50 wt%)

Sb(V) through iodobead oxidation: 20 μL of ^{1XX}Sb (570 nCi), 130 μL of 0.5 M NH_4OAc (pH 4), 1 iodobead functionalized with N-chloro-benzenesulfonamide (Pierce iodination bead, Thermo Scientific)

Sb(III) through mercaptoacetic acid reduction: 20 μL of ^{1XX}Sb (570 nCi), 130 μL of 0.5 M NH_4OAc (pH 4), mercaptoacetic acid (10 μL in H_2O, 7.5 μmol)

2.3. Preparation of Non-radioactive Sb-TREN-CAM Complex

Collaborators at ORNL synthesized TREN-CAM as previously described [209] and modified a ^{nat}Sb-TREN-CAM synthetic scheme developed at UW-Madison for further macroscopic characterization. Two methods were explored to synthesize ^{nat}Sb–TREN-CAM, starting from either Sb(III) or Sb(V). Both procedures yielded the same final product, as determined by spectral characterization. In **Method A** developed at UW-Madison**,** $SbCl_3$ (72.9 mg, 0.337 mmol) dissolved in CD_3OD (~100 μL) before addition of 50% H_2O_2 (31 μL, 0.54 mmol), oxidizing Sb(III) to Sb(V) and forming a white precipitate. Diluting the mixture to 3.5 mL with CD_3OD redissolved the precipitate, yielding a 95.5 mM stock solution of Sb(V). In **Method B** modified at ORNL, CD_3OD diluted anhydrous $SbCl_5$ (26 μL, 0.203 mmol) to a final volume of 5 mL, yielding a 40 mM stock solution of Sb(V). Separately, TREN-CAM (137.2 mg, 0.2 mmol) dissolved in 5 mL of *d*$_6$-DMSO resulted in a stock solution of TREN-CAM (40 mM).

To form the Sb TREN-CAM complex, an aliquot of concentrated deuterated ammonium hydroxide (ND_4OD) (55 µL, 0.8 mmol) deprotonated TREN-CAM (1.5 mL, 0.06 mmol) catechol groups before addition of Sb(V) from either **method A** or **method B**. Each reaction solution was heated at 80°C for 24 – 48 h before HPLC (**Figure 38**) and NMR (**Figures 44 & 45 and Appendix B Figures B5-B13**) characterization. No significant spectral differences between reaction mixtures were observed when using non-deuterated solvents. When analyzed by HPLC, two peaks (14.8 min, minor; 21.3 min, major) were apparent in the reaction mixture. Collaborators isolated unique species from the crude reaction mixture by semi-preparative RP-HPLC using a Shimadzu instrument equipped with a Restek Ultra Aqueous C_{18}, (100 Å, 5 µm, 250 mm × 4.6 mm) column. At a flow rate of 1 mL/min, the following 0.1% FA/H_2O and 0.1% FA/MeCN gradient was employed: 0–5 min: 10% 0.1% FA/MeCN; 5–35 min: 10–100% 0.1% FA/MeCN; 35–45 min: 100% 0.1% FA/MeCN. Appropriate fractions were combined and lyophilized overnight to obtain the pure complexes corresponding to Peaks 1 and 2. Peak 1: HRMS: *m*/*z* 669.0592; calculated for $[C_{27}H_{24}N_4O_9Sb]^-$: 669.0587. *m*/*z* 705.0802; calculated for $[C_{27}H_{24}N_4O_9Sb + 2H_2O]^-$: 705.0798. Peak 2: ^{1}H NMR (400 MHz, DMSO-*d*$_6$) δ 8.61 (t, *J* = 4.9 Hz, 3H), 7.28 (d, *J* = 8.3 Hz, 3H), 7.06 (d, *J* = 7.9 Hz, 3H), 6.80 (t, *J* = 8.1 Hz, 3H), 6.54 (s, 2H), 3.50 (br s, 6H), 2.50 (br s, 6H, overlapped with residual DMSO peak). ^{13}C{^{1}H} NMR (101 MHz, DMSO-*d*$_6$) δ 163.8, 145.9, 144.8, 120.5, 119.0, 118.8, 116.0, 34.6. HRMS: *m*/*z* 669.0592; calculated for $[C_{27}H_{24}N_4O_9Sb]^-$: 669.0587. Because retention times often vary between labs, instruments, columns, and methods, we reinjected a fraction corresponding to each peak onto all our HPLC instruments to ascertain the retention times for each system. This analysis allowed us to compare results across ORNL and UW-Madison labs (**Appendix B Figure B4**).

2.4. X-ray Absorption Spectroscopy (XAS) and Crystallography

Collaborators from ORNL prepared samples for X-ray absorption spectroscopy (XAS) (Dr. Briana Schrage) and X-ray crystallography (Dr. Md Faizul Islam). For XAS, Dr. Schrage prepared Sb(V) samples of Sb_2O_3 (solid), Sb_2O_5 (solid), and $KSb(OH)_6$ in MilliQ water. $KSb(OH)_6$ samples with catechols and TREN-CAM were prepared in water at various pHs. Using RP-HPLC, Dr. Islam isolated $[^{nat}Sb(TREN\text{-}CAM)]^-$ and grew a crystal suitable for X-ray diffraction. Dr. Alexander Ivanov and Dr. Darren Driscoll collected and analyzed XAS data. Dr. Frankie White collected and analyzed crystallography data. **Appendix B** includes detailed descriptions of collaborators' methods.

2.5. Radiolabeling from Liquid-Liquid Extraction Purified Solutions

In all situations, radioantimony was produced at UW-Madison. Radiolabeling experiments were conducted at both ORNL and UW-Madison.

2.5.1. Radiolabeling in NH_4OAc Buffers

Radio-TLC. Collaborators at ORNL performed radiolabeling experiments in triplicate at each TREN-CAM concentration by addition of chelator sub-stock (10 μL) and radioantimony (21 kBq, 0.57 μCi total activity from ^{120m}Sb, ^{122}Sb, and ^{124}Sb in 30 μL of 0.1 M HCl) to polypropylene screw-capped tubes containing 110 μL of either HCl (10 mM, pH ~2) or NH_4OAc buffer (pH 4 or pH 6). Final chelator concentrations ranged from 10^{-8} to 10^{-3} M. MilliQ water substituted chelator solutions in control samples. After heating to 80 °C for 60 min, 10 μL of 0.3 M oxalic acid was added to each sample. Heating at 80 °C was resumed for 10 min, after which aliquots (5 μL) were spotted onto a TLC strip (aluminum-backed silica gel 60 RP-18, F_{254}, Merck). TLC strips were developed using an oxalic acid mobile phase (0.25 M) allowing complexed radionuclide to remain at the baseline and the free radionuclide to migrate with the solvent front. TLC imaging using an AR-2000 scanner system equipped with P-10 gas and WinScan 3 imaging software (Eckert & Ziegler Radiopharma Inc) characterized activity distribution. Dividing the counts associated with complexed radionuclide by the total counts integrated along the length of the TLC plate provided RCYs. Indicator strips confirmed sample pH. Collaborators studied the effects of time (10, 30, 60, 120 min) and temperature (25, 37, 60, 80 °C) on TREN-CAM radiolabeling at a single concentration (1×10^{-3} M) and pH 4. One sample was prepared for each timepoint/temperature pair. At designated timepoints, 10 μL of 0.3 M oxalic acid was added, and each sample was heated at 80 °C for 10 min before spotting on a TLC strip for analysis.

Radio-HPLC. Dozens of TREN-CAM radiolabeling experiments were performed in a manner like that described above for radio-TLC experiments. Generally, these studies included 0.5 M NH_4OAc buffer at pH 2 – 7.5, 0.001-1mM final TREN-CAM concentrations, and heating solutions 37 – 80 °C for 1 h. Below, select reactions are highlighted to illustrate innate variability of final Sb-TREN-CAM speciation when radiolabeling from aqueous solutions with LLE produced radioantimony. To clarify which experiments were conducted with specific unique productions, productions are labeled A-C but do not represent chronological productions.

At ORNL, pH-dependent radiolabeling from **production A** (N = 1 per pH), TREN-CAM sub-stock (10 μL, 6.5×10^{-4} M final concentration) and radionuclide (21 kBq, 0.57 μCi total activity from ^{120m}Sb, ^{122}Sb, and ^{124}Sb, 20 μL, in 0.1 M HCl) were added to polypropylene screw-capped tubes containing 110 μL of either HCl (10 mM, pH ~2) or NH_4OAc buffer (pH 4, 6, 7, or 7.4). After heating samples at 80 °C for 1 h, collaborators analyzed samples by radio-HPLC (**ORNL radio-HPLC**). Radiolabeling reactions were performed in 0.5 M NH_4OAc (pH 4) using 6.5×10^{-4}–6.5×10^{-6} M TREN-CAM and analyzed by **ORNL radio-HPLC**. Using the same batch of radioantimony from **production A**, labeling was performed in parallel at UW-Madison using **UW-Madison radio-HPLC method A**. 100 µL ^{120m}Sb (178 kBq, 4.8 µCi) and ^{122}Sb (137 kBq, 3.7 µCi) back extracted into either 0.1 M HCl or NH_4OAc pH 4 radiolabeled 1.5 µL TREN-CAM in EtOH (final concentration 0.1mM) with 48.5 µL NH_4OAc buffer at pH 4 and 80 °C for 1 h.

Smaller scale concentration and pH dependent radiolabeling experiments from **production B** were performed at UW-Madison by combining 30 µL ^{120m}Sb (125 kBq, 3.4 µCi) and ^{122}Sb (122 kBq, 3.3 µCi) in 0.1M HCl with 10 µL TREN-CAM in 20% DMSO (final concentrations 0.1 and 1 mM) and 60 µL 0.5 M NH_4OAc buffer pH 4 or 6. With **production C**, ^{1XX}Sb was back extracted into NH_4OAc at pH 6. Then, we combined 240 µL ^{120m}Sb (707 kBq, 19 µCi) and ^{122}Sb (656 kBq, 18 µCi) with 60 µL TREN-CAM in 20% DMSO (final concentration 2 mM) and heated the radiolabeling solution for 1 h at 80 °C.

2.5.2. Radiolabeling in MeOH/DMSO

For these experiments, ^{1XX}Sb was taken to dryness under N_2 from the DBE phase in a glass vial (without back extraction) and reconstituted in MeOH, yielding a solution containing 4.3 MBq (120 µCi) ^{120m}Sb and 3.8 MBq (100 µCi) ^{122}Sb in a final volume of 500 µL. We compared species formation due to base addition. First, 10 µL ^{1XX}Sb in MeOH, 1.2 µL 10 mM TREN-CAM in EtOH, 38.8 µL MeOH, and 70 µL DMSO were heated at 80 °C for 60 min. A second solution with base was prepared by combining 10 µL ^{1XX}Sb in MeOH, 1.2 µL 10 mM TREN-CAM in EtOH, 38.8 µL MeOH, and 61.3 µL DMSO, and 8.7 µL of a 1:1000 dilution of concentrated NH_4OH in DMSO. We analyzed samples by radio-HPLC (**UW-Madison radio-HPLC method B**). Time and temperature dependance were explored by preparing three radiolabeling reactions of 90 µL ^{1XX}Sb in MeOH, 3.6 µL 10 mM TREN-CAM in EtOH, 59.4 µL MeOH, and 210 µL DMSO and heating them at 37 °C, 60 °C, and 80 °C. Radio-HPLC chromatograms (**UW-Madison radio-HPLC method B**) of sample aliquots at t = 1 h, 2 h, 3 h, 4 h (60 °C only), and 3 d (37 °C only) characterized RCY and species distribution.

2.6. Radiolabeling from Column Chromatography Purified Solutions

Radioantimony produced via column chromatography purification (**Chapter 2**) and allowed to oxidize overnight resulted in ^{1XX}Sb(V) in EtOH. 300 µL containing ^{122}Sb (2.2 MBq, 60 µCi) and ^{120m}Sb (3.7 MBq, 100 µCi) in EtOH was combined with 600 µL 0.5 M NH_4OAc at pH 6 and 100 µL TREN-CAM (final concentration 1 mM) in 20% DMSO/H_2O and heated for 60 min at 80 °C.

AMA was measured via titration. 10 µL TREN-CAM stock solution (20% DMSO in MilliQ water), 80 µL 0.5 M NH_4OAc buffer pH 6, and 10 µL chemically purified ^{117}Sb (0.7-2.5 MBq) produced via 8 MeV deuteron bombardment of ^{nat}Sn were combined at final reaction concentrations of 0.01 mM, 0.1 mM, 0.5 mM, and 1 mM TREN-CAM and heated at 80°C for 1h. We assessed complexation via TLC, spotting aliquots of radiolabeling solutions onto Al-backed Si TLC plates and developing the plates with MeOH mobile phase separated [^{117}Sb]Sb-TREN-CAM ($R_f = 0.755 \pm 0.005$ (N = 3)) from the free ^{117}Sb ($R_f = 0.019 \pm 0.009$ (N = 3)). Uncertainties are expressed as the standard deviation of measurement replicates. Autoradiography (Packard Cyclone Storage Phosphor) quantified complexation.

The necessity of NH_4OAc buffer in radiolabeling from ^{1XX}Sb produced in EtOH was studied by creating two samples, one with addition of 0.5 M NH_4OAc pH 4 and the other with EtOH. For both, 100 µL ^{122}Sb (3.7 MBq, 100 µCi) and ^{120m}Sb (6.3 MBq, 170 µCi) in EtOH, 1.5 µL of 10 mM TREN-CAM (final concentration 0.1 mM) in EtOH, and 48.5 µL of either EtOH or 0.5

M NH_4OAc pH 4 buffer were combined and heated for 1 h at 80 °C before labeling was assessed via **radio-HPLC UW-Madison method B**.

2.7. Serum Stability and $LogD_{7.4}$ Measurement

For serum stability preparation, ^{122}Sb (2.2 MBq, 60 μCi) and ^{120m}Sb (3.7 MBq, 100 μCi) were back extracted into 0.5 M NH_4OAc (pH 6, 0.9 mL), which resulted in a solution with a pH of 4. To this solution, we added TREN-CAM (100 μL of 10 mM stock) in 20% DMSO/H_2O, heated the reaction for 60 min at 80 °C, diluted it to ~10 mL with MilliQ water, and loaded [^{1XX}Sb]Sb-TREN-CAM onto a Waters C8 Sep-Pak cartridge pre-conditioned with 5 mL of EtOH and 5 mL of MilliQ water. The cartridge was dried using air, and EtOH eluted [^{1XX}Sb]Sb-TREN-CAM from the cartridge. The first nine drops were discarded, and the following 12 drops were collected and counted to confirm elution of >60% of the original activity. After collecting the eluate, PBS (200 μL) was added to the solution. The EtOH was removed from the solution using a stream of N_2 until no further change in mass was detected. We analyzed the [^{1XX}Sb]Sb-TREN-CAM solution via radio-HPLC (**UW-Madison radio-HPLC method B**) to confirm speciation and purity before adding an equal volume of 2x human serum. For control samples, ^{1XX}Sb was back extracted directly into PBS, and the pH was re-adjusted to 7.5 using 1 M NaOH before combination with an equal volume of 2x human serum. Samples were incubated at 37 °C. At t = 1, 2, and 3 d (N = 1 per timepoint), aliquots of human serum [^{1XX}Sb]Sb–TREN-CAM challenge solutions were diluted with an equal volume of MeCN and centrifuged, precipitating and pelleting serum proteins out of the solution. The pellets were not washed, and therefore we expect a small fraction of activity arising from residual supernatant to be present within each fraction. HPGe gamma spectra of each fraction quantified ^{120m}Sb activity distribution within pelleted proteins. We diluted the supernatant

1.5-fold with citric acid (pH 4.5, 100 mM) before radio-HPLC (**UW-Madison method A**) analysis, determining the percent of intact complex.

For logD$_{7.4}$ quantification, TREN-CAM (1 mM) was quantitatively radiolabeled (assessed via **radio-HPLC UW-Madison method A**) with 450 kBq ± 0.8% (12 μCi) ^{120m}Sb (uncertainty expressed as counting uncertainty) after 1 h at pH 4.0 (NH_4OAc buffer) and 80°C (N = 1). The solution was diluted 10x with MilliQ water and passed through a preconditioned (10 mL EtOH, 10 mL MilliQ water) C8 Sep-Pak cartridge (Waters, Milford, MA), trapping [^{1XX}Sb]Sb–TREN-CAM. We passed MilliQ water (1 mL) through the loaded C8 cartridge to remove residual salts and EtOH (1 mL) to elute purified [^{1XX}Sb]Sb–TREN-CAM from the cartridge. 200 μL PBS was added to the purified [^{1XX}Sb]Sb–TREN-CAM eluent, and a stream of N_2 removed EtOH. In triplicate, 50 μL of purified [^{1XX}Sb]Sb–TREN-CAM in PBS was added to 950 μL PBS and 1 mL *n*-octanol. The samples were vortexed for 15 min, allowing [^{1XX}Sb]Sb–TREN-CAM to partition between the organic and aqueous phases. After vortexing, the extraction solution was allowed to settle and 0.5 mL aliquots from each phase were collected and analyzed for ^{120m}Sb activity by HPGe gamma spectroscopy. LogD$_{7.4}$ was calculated according to **Equation 2** reported within **Chapter 3**.

2.8. Imaging Applications for *in vivo* Complex Stability Assessment

2.8.1. Antimony-117 Preparation

For mouse imaging, PET vs. SPECT image characterization, *in vivo* stability, and biodistribution measurements, we prepared ^{117}Sb by three different solvent extraction methods. To measure biodistribution of unchelated ^{117}Sb as a control for *in vivo* stability measurements, Sb was back extraction directly into PBS aqueous phase, likely resulting in [^{117}Sb]Sb$(OH)_6^-$ [139,210]. For phantom imaging experiments, ^{117}Sb back extracted into 0.1 M HCl, labeled as [^{117}Sb]SbCl_5. After separation of the two phases, we removed residual DBE by heating to 50°C and blowing argon over the sample. For preparation of [^{117}Sb]Sb–TREN-CAM, radioantimony in the extracted DBE phase was evaporated under N_2 (without back extraction) in a glass vial and reconstituted in 0.5 mL MeOH. When radiolabeling, 428.4 µL of 100 MBq (2.7 mCi) ^{117}Sb in MeOH was combined with 630 µL DMSO and 121.6 µL of TREN-CAM (as a 10 mM solution in EtOH) and heated to 80°C for 1 h, reacting at a molar activity of 2.2 mCi/µmol TREN-CAM. Quantitative radiolabeling was confirmed via HPLC. We passed a 10x dilution of radiolabeling solution through a preconditioned (5 mL EtOH, 5 mL MilliQ water) C8 Sep-Pak cartridge (400 mg, Waters, Milford, MA, USA), trapping [^{117}Sb]Sb–TREN-CAM. The cartridge was rinsed with 1 mL MilliQ water, and [^{117}Sb]Sb–TREN-CAM was eluted with EtOH, collecting dropwise. Purified [^{117}Sb]Sb–TREN-CAM was diluted with PBS (800 µL), and the EtOH was evaporated from the solution using a gentle N_2 flow. Prior to injection, HPLC confirmed product speciation. For imaging studies, 17.9 MBq ± 0.9% (0.57 mCi) [^{117}Sb]Sb–TREN-CAM was prepared for injection (uncertainty is expressed as statistical counting uncertainty). For comparison with unchelated ^{117}Sb, the studies used 62.5 MBq ± 1.5% (1.7 mCi) of [^{117}Sb]Sb(OH)$_6^-$ produced in PBS. Phantoms filled with ^{117}Sb at activity concentration 3.33 MBq/mL ± 0.05 MBq/mL (90.2 µCi/mL ± 1.2 µCi/mL) allowed characterization.

2.8.2. PET and SPECT Phantom Image Characterization

For ^{117}Sb PET and SPECT characterization and comparison, a linear channel Derenzo D271020 phantom (**Figure 35 left**, Phantech, Madison, WI) with rod sizes ∅ 1.0, 1.2, 1.4, 1.6, 1.8, 2.0 mm filled with ~5.5 MBq (~150 µCi) ^{117}Sb was imaged from the center of scanner beds using the following imaging conditions. Thirty-minute SPECT/CT and PET/CT images were collected using a MILabs U-SPECT/CTUHR or Siemens Inveon μPET/CT. SPECT image reconstructions windowed 159 keV for ^{117}Sb's primary emission, and PET imaging timing and energy windows of 3.432 ns and 350-650 keV measured 511 keV coincidence photons emitted from positron annihilation. Previously, we calibrated the scanners by imaging three vials of 4.2 – 10 MBq ^{117}Sb (115 – 270 μCi) and correcting image-derived volumetric activity concentrations to activity measured via HPGe gamma spectroscopy. CT images collected after each SPECT or PET image were used to attenuation-correct and co-register datasets. 3-D ordered subset expectation maximization / maximum a posteriori (OSEM3D/MAP) without scatter correction was used to reconstruct CT attenuation-corrected PET images. SPECT images (energy window 147.1–170.9 keV) were reconstructed with attenuation-correction and a pixel-based, accelerated similarity-regulated ordered subsets expectation maximization (SROSEM) algorithm with 128 subsets, 5 iterations, 0.4 mm voxel size, and 1.4 mm gaussian blurring.

Figure 35: phantoms used for ^{117}Sb PET and SPECT image characterization. (left top) picture of filled Derenzo phantom (left bottom) CAD drawing of Derenzo phantom channels (middle) CAD drawing of PVE phantom (right) picture of filled PVE phantom.

After image reconstruction, central axial slices were exported, and line profiles of rod signal intensity created using the open-source software ImageJ (NIH) to draw lines intersecting the center of the central most rod with the center of the outermost rod for each rod size cluster. The spatial resolutions of the systems were expressed as FWHM of the central most rod with contrasts (C_{rod}) of the systems calculated according to **Equation 3**, where R_{max} is the maximum and R_{min} the minimum rod signal intensity values determined from the line profiles.

Eq 3) $C_{\mathrm{rod}} = \left(\frac{R_{max}-R_{min}}{R_{max}+R_{min}}\right)$

To measure and correct for partial volume effects (PVE), PET and SPECT images using aforementioned parameters were collected using a linear channel spherical PVC27-GrIT PVE phantom (**Figure 35 right**, Phantech, Madison, USA). Spheres with sizes ∅ 2.5, 3, 4, 5, 7.5, 10, and 12 mm were filled with 3.33 MBq/mL ± 0.05 MBq/mL (90.2 µCi/mL ± 1.2 µCi/mL) ^{117}Sb. Using co-registered CT images, manual volume-of-interest (VOI) delineation of spherical phantom structures allowed activity concentration measurement using either Inveon Research Workstation (Siemens) for PET VOI analysis or Imalytics 3.0 (MILabs) for SPECT VOI analysis. Dividing the average activity concentration (A_{image}) within each VOI by the known activity concentration (A_{real}) allows calculation of a recovery coefficient (RC_{sphere}) for each sphere size (**Equation 4**):

Eq 4) $RC_{sphere} = \frac{A_{image}}{A_{real}}$

2.8.3. *In Vivo* PET and SPECT Image Characterization

Two groups of healthy 3-month-old male BALB/c mice (N = 3) (Jackson River Laboratories) were administered 150 µL ^{117}Sb solutions via tail vein injection. The control, unchelated Sb group received 12.51 MBq ± 0.04 MBq (338.0 µCi ± 1.0 µCi) ^{117}Sb, and the [^{117}Sb]Sb-TREN-CAM group received 4.5 MBq ± 0.1 MBq (121 µCi ± 3 µCi) injected ^{117}Sb activity. Thirty-minute SPECT/CT images were collected using a MILabs U-SPECT/CTUHR at 20, 90, and 240 min timepoints p.i. For SPECT imaging, we imaged all 3 mice simultaneously in the prone position under isoflurane anesthesia (3% induction, 1.5% maintenance) with the MILabs general purpose rat and mouse collimator (GP-RM, 1.0 mm pinhole size, 0.8 mm resolution, >700 CPS/MBq). SPECT image reconstructions windowed both ^{117}Sb (159 keV) and ^{119}Sb (~25 keV) emissions. Twenty-minute PET/CT images (time window 3.432 ns; energy window 350–650 keV) of two mice in the prone position were collected 150 min p.i. using a Siemens Inveon micro-

PET/CT under isoflurane anesthesia as noted above. In both cases, the scanner was calibrated by imaging vials of ^{117}Sb activity and calibrating image-derived volumetric activity concentrations to activity measured via HPGe gamma spectroscopy. CT images collected after each SPECT or PET image were used to attenuation-correct and anatomically co-register datasets. 3-D ordered subset expectation maximization / maximum a posteriori (OSEM3D/MAP) without scatter correction was used to reconstruct CT attenuation-corrected PET images. SPECT images (energy window 147.1–170.9 keV) were reconstructed with attenuation-correction and a pixel-based, accelerated similarity-regulated ordered subsets expectation maximization (SROSEM) algorithm with 128 subsets, 5 iterations, 0.4 mm voxel size, and 1.4 mm gaussian blurring. Using co-registered CT images, manual VOI delineation of tissues allowed activity biodistribution measurement, as expressed as percent injected activity per gram of tissue (%IA/g) using either Inveon Research Workstation (Siemens) for PET VOI analysis or Imalytics 3.0 (MILabs) for SPECT VOI analysis. Calculated %IA/g within PET and SPECT VOI were corrected for measured PVE.

2.8.4. *Ex vivo* Biodistribution and Metabolite Analysis

Five h p.i., animals were sacrificed using CO_2 asphyxiation with cardiac exsanguination as secondary euthanasia confirmation. For *ex vivo* biodistribution measurements, tissues and organs were harvested and weighed, and the ^{117}Sb activity within these tissues was counted using a PerkinElmer Gamma Counter (Waltham, MA, USA) calibrated with known ^{117}Sb activity standards quantified via HPGe gamma spectroscopy.

In a separate study exploring metabolite analysis, three healthy 3-month-old male BALB/c mice (Jackson River Laboratories) were injected with 0.47 MBq ± 0.17 MBq (12.7 μCi ± 4.5 μCi) [^{117}Sb]Sb–TREN-CAM in 150 mL PBS. Here, the uncertainty is expressed as the standard deviation of replicates. Thirty minutes p.i., animals were sacrificed, and intact gallbladders were harvested. Gallbladders were lanced, and their contents washed with MeOH (50 μL). Aliquots of the supernatant (5 μL) were spotted on Al-backed Si TLC plates next to triplicate [^{117}Sb]Sb–TREN-CAM controls. The TLC plates were developed using a MeOH mobile phase. Under these conditions, TREN-CAM-complexed radio-Sb migrates near the solvent front, whereas unchelated radio-Sb remains near the baseline. Radio-TLC visualization with a Packard Cyclone phosphor plate reader allowed activity distribution and measurement of R_f for both metabolized [^{117}Sb]Sb–TREN-CAM and controls.

2.9. Radiolabeling DUPA Conjugated TREN-CAM in MeOH:DMSO

Collaborators at UW-Madison (Morgan Dierolf, Owen Glaser, Prof. Dr. Eszter Boros) conjugated TREN-CAM to the prostate specific membrane antigen (PSMA) targeting agent 2-[3-(1,3-dicarboxypropyl)ureido]pentanedioic acid (DUPA), shown in **Figure 36**. Initial radiolabeling employed MeOH/DMSO methods. We produced ^{1XX}Sb via LLE, dried the DBE extractant, and reconstituted the 4.3 MBq (120 μCi) ^{120m}Sb and 3.8 MBq (100 μCi) ^{122}Sb in 500 μL MeOH. Previously, approximately 50 nmol TREN-CAM-DUPA was portioned into an Eppendorf vial and dried under N_2. We reconstituted the TREN-CAM-DUPA in 100 μL ^{1XX}Sb MeOH stock before adding 70 μL DMSO and heating the reaction at 80 °C for 1 h. Radio-HPLC of injected reaction provided radiolabeling quantification (**UW-Madison method B**).

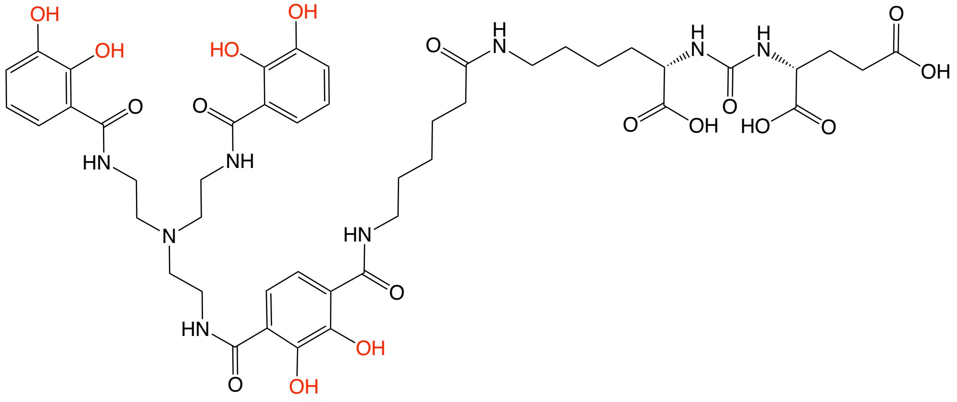

Figure 36: Structure of TREN-CAM-DUPA

3. Results and Discussion

3.1. Oxidation State Verification

Collaborators observed a single anion exchange chromatogram peak (R_t = 3 min) for the sample mixed with ammonium citrate mobile phase prior to injection, whereas the sample without pre-mixing displayed two chromatogram peaks (R_t = 1.5 min and 3 min, **Figure 37**). Within literature, the 3 min peak has been assigned to Sb(V)–citrate [208]. As such, we postulate that the peak at 1.5 min is an Sb(V)–acetate species from the NH_4OAc buffer.

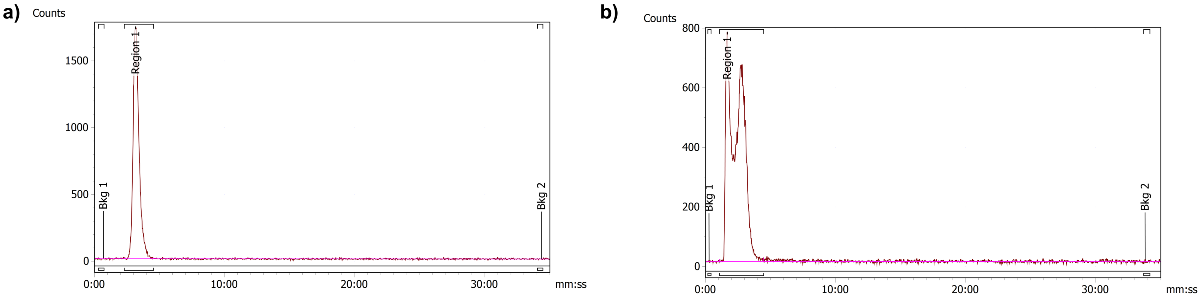

Name	Start (mm:ss)	End (mm:ss)	Retention (mm:ss)	Area (Counts)	%ROI (%)	%Total (%)
Bkg 1	0:18	0:44	0:41			
Region 1	2:17	4:32	3:09	51789	100.00	97.77
Bkg 2	34:03	34:28	34:21			
1 Peak				51789	100.00	97.77

CPM of non-injected sample: 2,053,464
CPM of combined fractions of injected sample: 2,211,252

Name	Start (mm:ss)	End (mm:ss)	Retention (mm:ss)	Area (Counts)	%ROI (%)	%Total (%)
Bkg 1	0:10	0:25	0:16			
Region 1	1:04	4:28	1:40	53439	100.00	97.73
Bkg 2	33:41	34:10	33:48			
1 Peak				53439	100.00	97.73

CPM of non-injected sample: 1,989,576
CPM of combined fractions of injected sample: 2,097,258

Figure 37: Anion exchange chromatogram of ^{1XX}Sb in NH_4OAc (pH 4) with and without pre-mixing the samples with citrate. (left) sample mixed with an equal volume of

ammonium citrate (pH 4.5, 0.1 M) prior to injection. (right) sample injected without ammonium citrate.

To determine how temperature impacts oxidation state, collaborators prepared two ^{1XX}Sb samples (0.0038 µCi/µL) and heated (25 and 80 °C) them for 1 h. No ammonium citrate was added to the samples prior to HPLC injection (**Figure 38**), and near identical chromatograms show ^{1XX}Sb remains in the same oxidation state at elevated temperature.

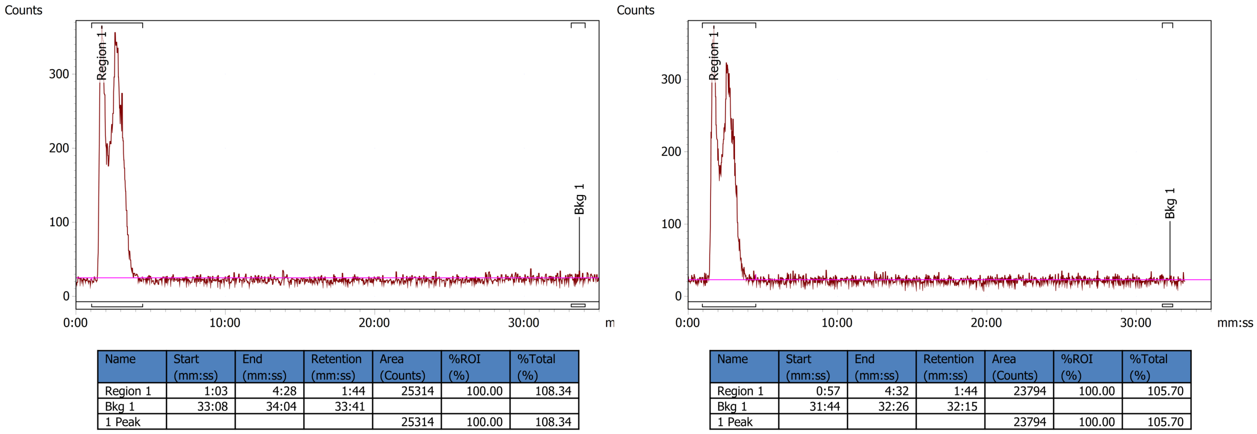

Name	Start (mm:ss)	End (mm:ss)	Retention (mm:ss)	Area (Counts)	%ROI (%)	%Total (%)
Region 1	1:03	4:28	1:44	25314	100.00	108.34
Bkg 1	33:08	34:04	33:41			
1 Peak				25314	100.00	108.34

Name	Start (mm:ss)	End (mm:ss)	Retention (mm:ss)	Area (Counts)	%ROI (%)	%Total (%)
Region 1	0:57	4:32	1:44	23794	100.00	105.70
Bkg 1	31:44	32:26	32:15			
1 Peak				23794	100.00	105.70

Figure 38: Anion exchange chromatograms of ^{1XX}Sb in NH_4OAc (pH 4) with and without heating. (left) 25 °C and (right) 80 °C for 1 h.

To validate the 3 min Sb(V) retention time, collaborators explored the effects of various oxidizing and reducing agents on the ^{1XX}Sb anion exchange column retention time. For this experiment, partially oxidized ^{1XX}Sb was used as a control, which displayed peaks at both 3 min and 8 min (**Figure 39a**). Oxidizing agents (H_2O_2 and iodobeads) fully converted ^{1XX}Sb analytes to species with R_t = 3 min (**Figure 39 b and c**), and the reducing agent mercaptoacetic acid completely converted ^{1XX}Sb to an 8 min peak (**Figure 39d**), confirming Sb(V) elution at R_t = 3 min and Sb(III) elution at R_t = 8 min. An anion exchange chromatography peak elution at 3 min for LLE produced ^{1XX}Sb confirmed 5+ oxidation state prior to TREN-CAM radiolabeling.

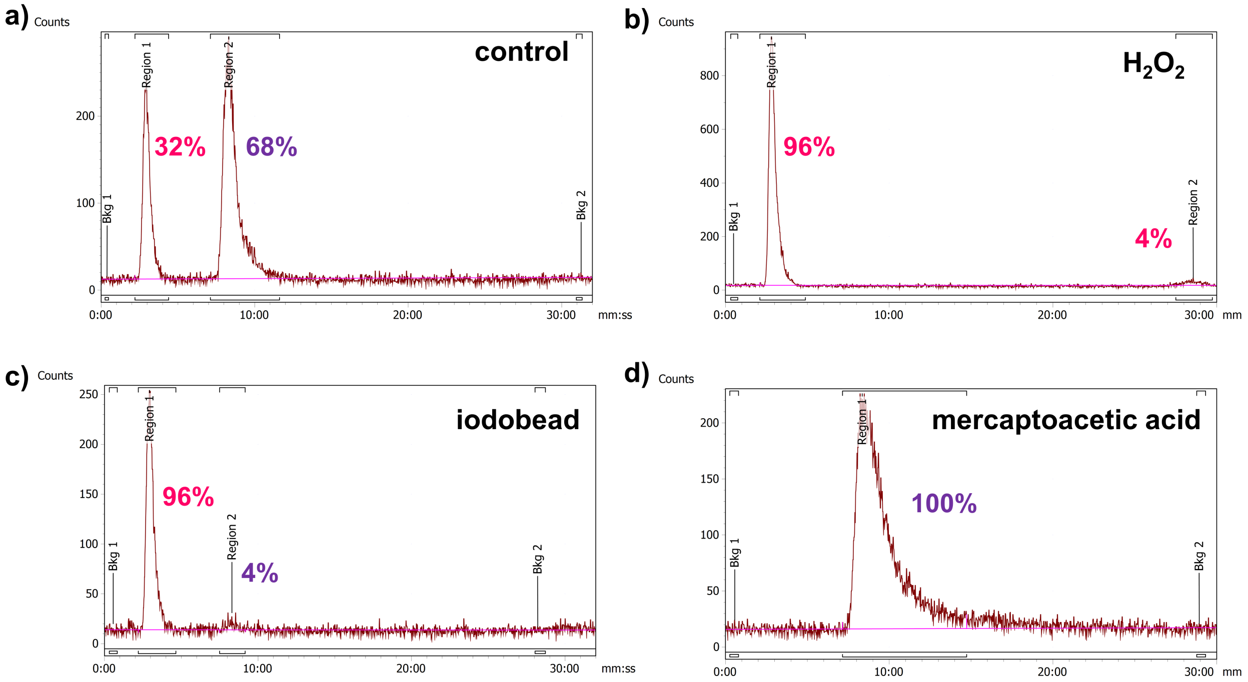

Figure 39: Comparison of anion exchange chromatograms of ^{1XX}Sb before (a) and after treatment overnight at 25 °C with (b) H_2O_2, (c) iodobeads, or (d) mercaptoacetic acid.

3.2. Preparation of Non-radioactive Sb-TREN-CAM Complex

Crude labeling reactions produced two primary species (**Figure 40**). After isolation and lyophilization of each peak (**Figure 41**), HRMS assigned them mass-to-charge ratios (*m*/*z*) of 669.0592 and 705.0802 (**Figure 42 and 43**). With molecular formula $[C_{27}H_{24}N_4O_9Sb]^-$, $[Sb(TREN\text{-}CAM)]^-$ has a calculated *m*/*z* of 669.0587. The second mass peak and isotope patterning matches calculated *m*/*z* values for $[C_{27}H_{24}N_4O_9Sb + 2H_2O]^-$ (705.0798), a probable hydroxy antimony TREN-CAM species $[Sb(H_2TREN\text{-}CAM)(OH)_2]^-$. Depicted in **Figure 42**, both mass peaks are observed after reconstitution of Peak 1 isolated samples, suggesting partial conversion of $[Sb(H_2TREN\text{-}CAM)(OH)_2]^-$ (Peak 1) to $[Sb(TREN\text{-}CAM)]^-$ (Peak 2). Synthesis of ^{nat}Sb-TREN-CAM using **method A** was verified at UW-Madison (**Figure 44**) through HRMS of purified Peak 2.

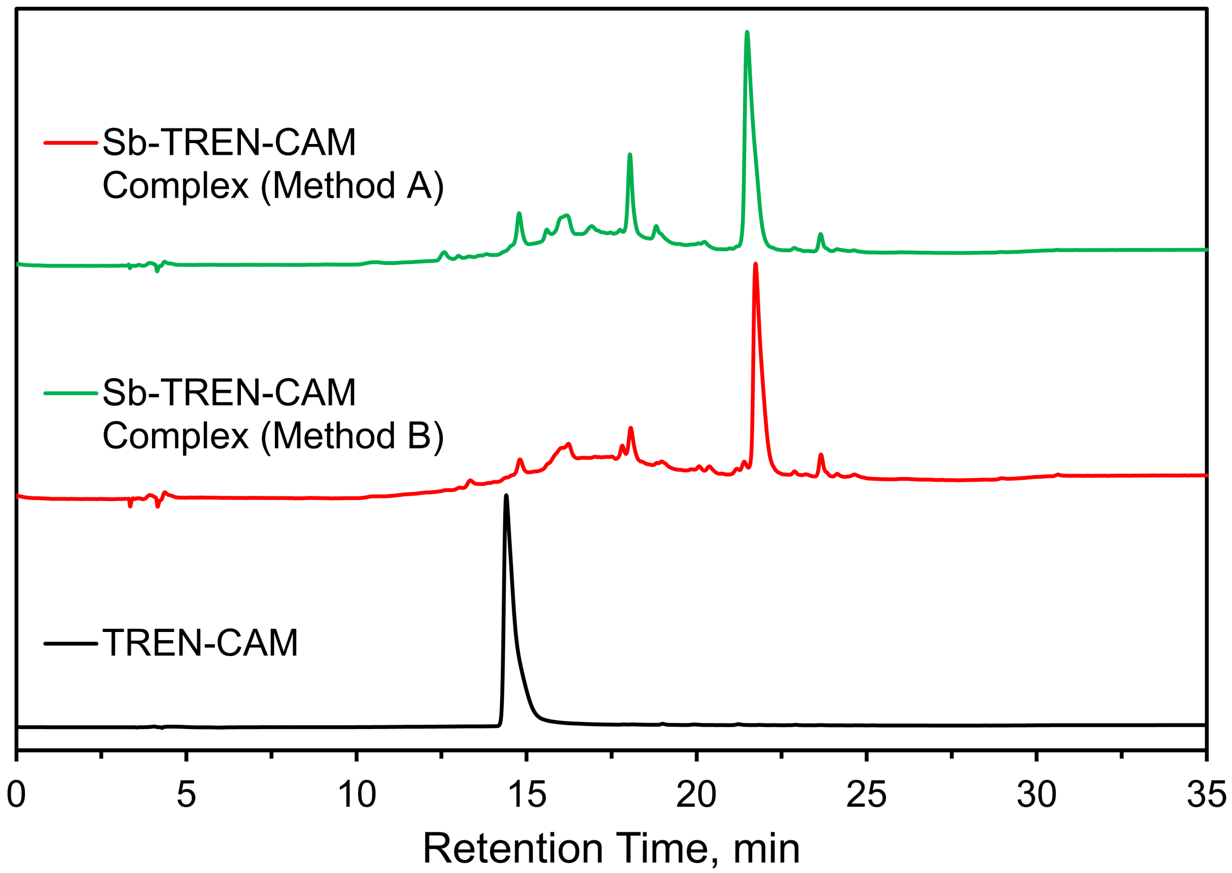

Figure 40: Comparison of HPLC chromatograms of crude ^{nat}Sb–TREN-CAM reaction mixtures prepared using either **method A** (top, $SbCl_3 + H_2O_2$) or **method B** (middle, $SbCl_5$) in DMSO/MeOH. Each reaction solution was heated at 80 °C for 48 h before analysis. The chromatogram of TREN-CAM (bottom) is provided for reference. **ORNL cold HPLC**. Instrument: Shimadzu. Column: Restek Ultra Aqueous C_{18} column (100 Å, 5 µm, 250 mm × 21.2 mm). Flow rate: 1 mL/min. Solvents: A = 0.1% FA/H_2O, B = 0.1% FA/MeCN. Method: 0–5 min: 10% B; 5–25 min: 10–100% B; 25–30 min: 100% B.

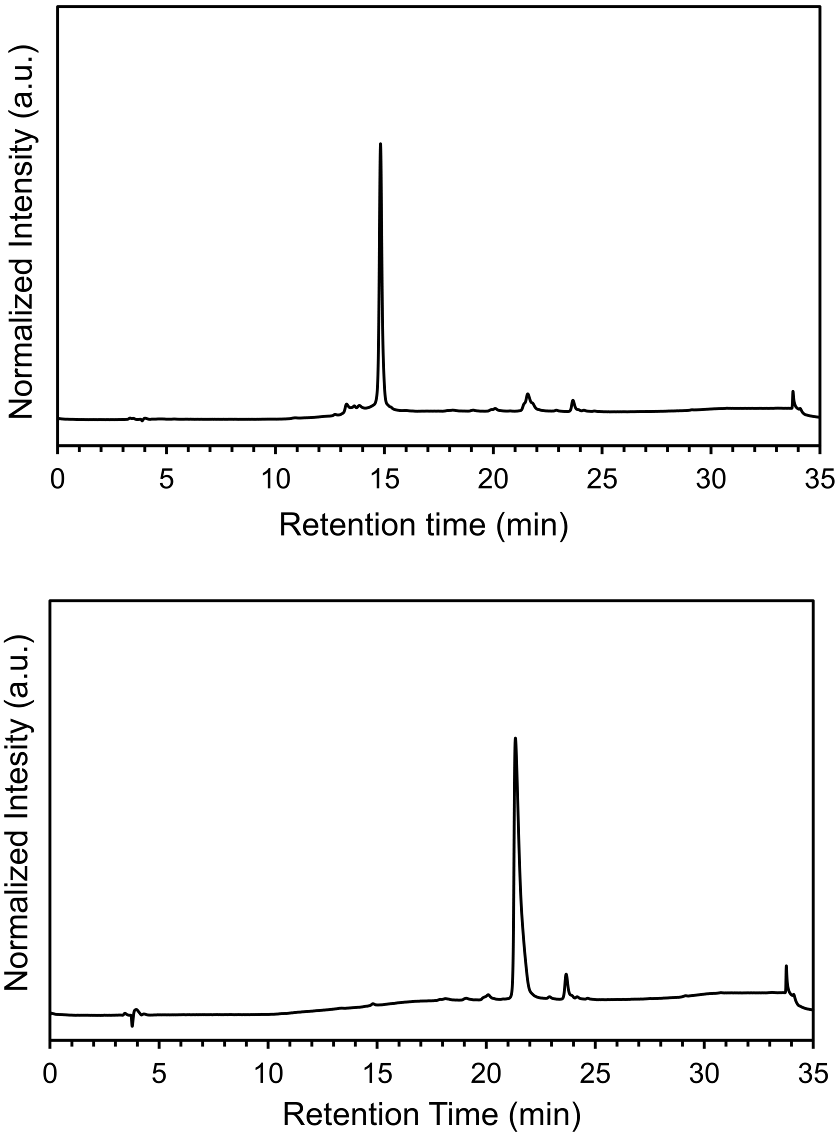

Figure 41: HPLC chromatogram of (top) Peak 1 (R_t = 14.8 min) and (bottom) Peak 2 (R_t = 21.3 min) after purification of the ^{nat}Sb–TREN-CAM reaction mixture. **ORNL cold RP-HPLC.** Instrument: Shimadzu. Column: Restek Ultra Aqueous C_{18} column (100 Å, 5 µm, 250 mm × 21.2 mm). Flow rate: 1 mL/min. Solvents: A = 0.1% FA/H_2O, B = 0.1% FA/MeCN. Method: 0–5 min: 10% B; 5–25 min: 10–100% B; 25–30 min: 100% B.

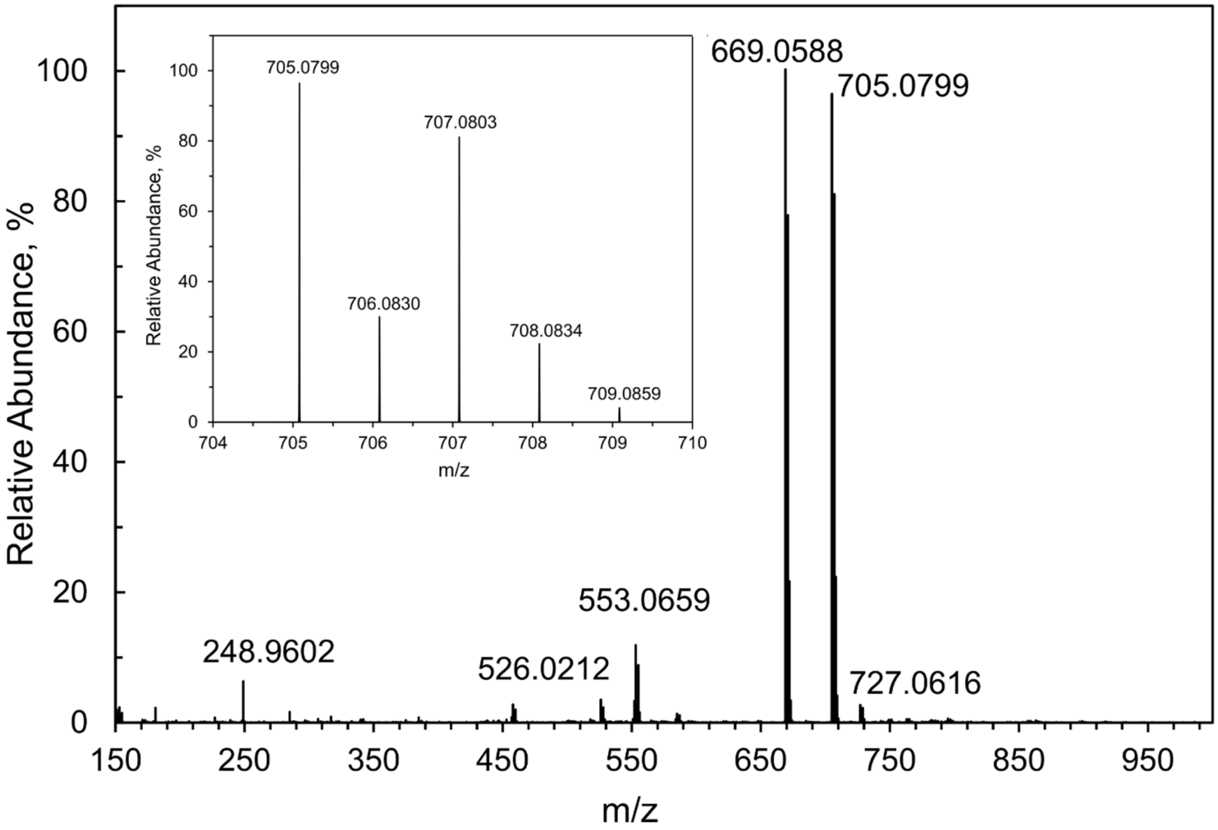

Figure 42: HRMS of Peak 1 purified from non-radioactive ^{nat}Sb–TREN-CAM produced at ORNL with prominent mass peaks at *m/z* 669.0592 (669.0587 calculated for $[C_{27}H_{24}N_4O_9Sb]^-$) and 705.0802 (705.0798 calculated for $[C_{27}H_{24}N_4O_9Sb + 2H_2O]^-$) with ^{nat}Sb isotope patterning. These ions correspond to $[Sb(TREN\text{-}CAM)]^-$ and $[Sb(H_2TREN\text{-}CAM)(OH)_2]^-$, respectively.

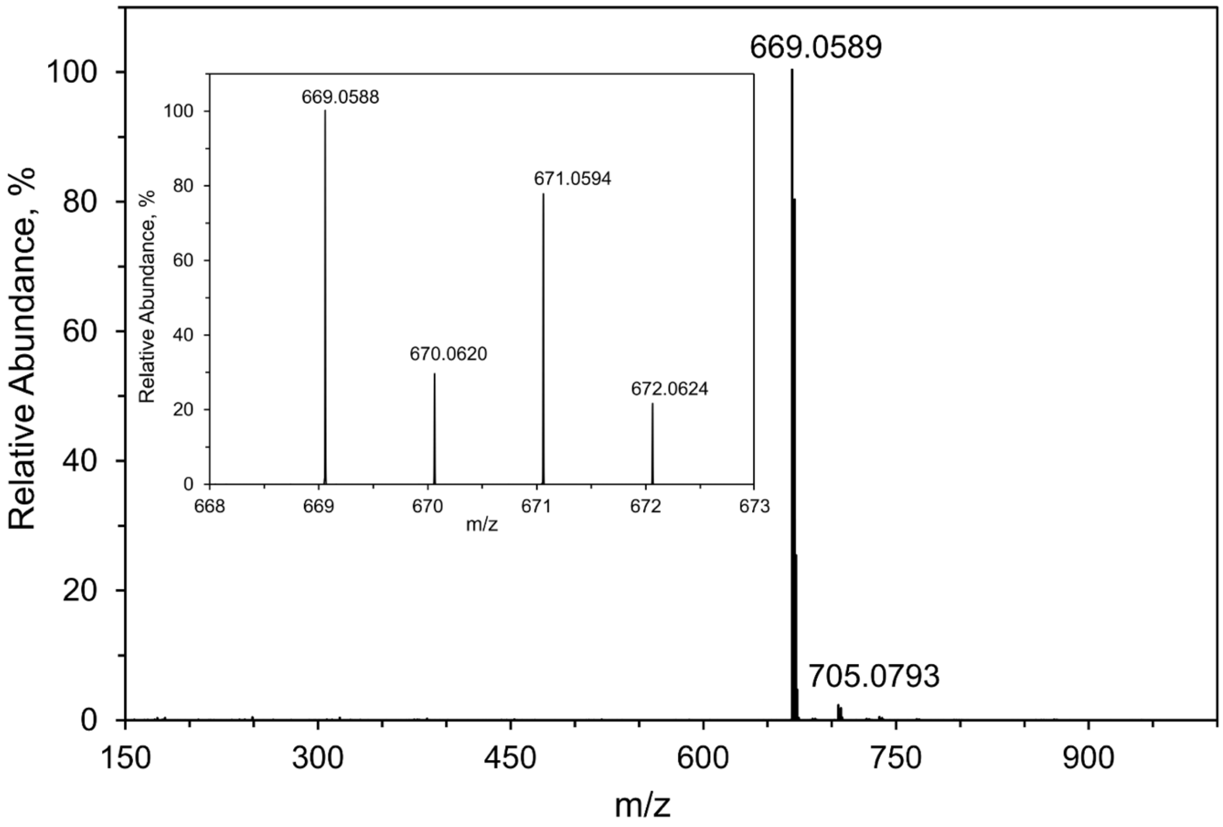

Figure 43: HRMS of Peak 2 purified from non-radioactive ^{nat}Sb–TREN-CAM produced at ORNL with a prominent mass peak at *m/z* 669.0592 (669.0587 calculated for $[C_{27}H_{24}N_4O_9Sb]^-$) with ^{nat}Sb isotope patterning, corresponding to the ion [Sb(TREN-CAM)]$^-$.

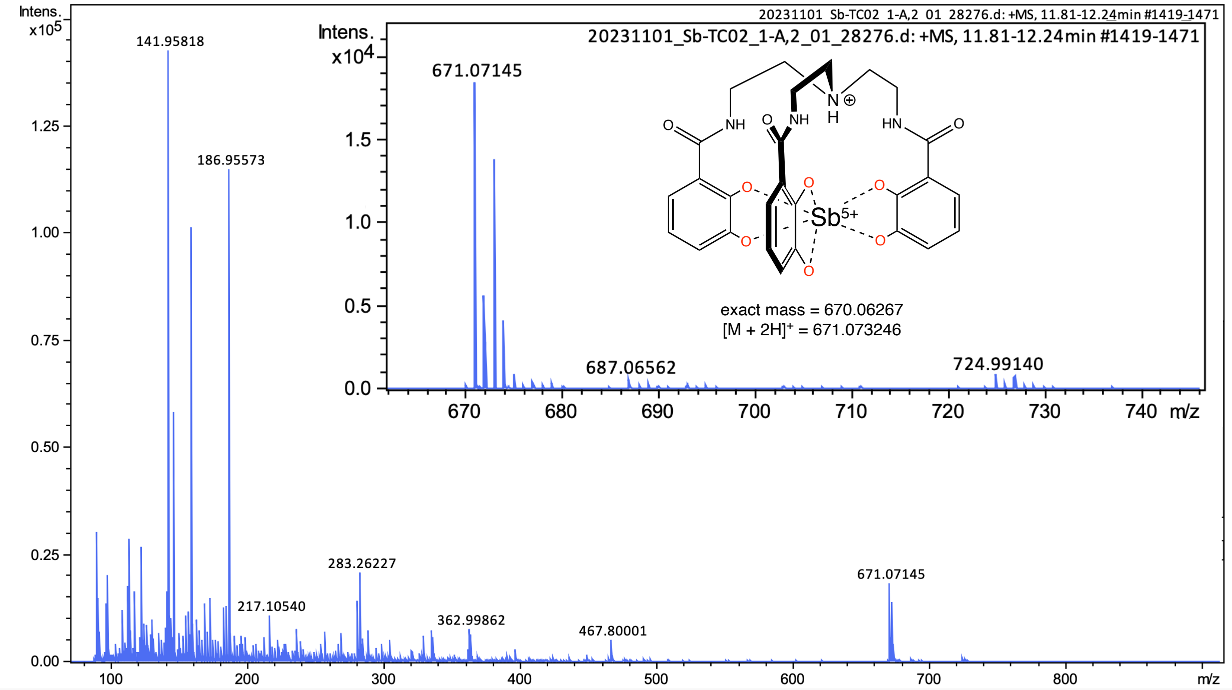

Figure 44: HRMS of Peak 2 purified from non-radioactive ^{nat}Sb–TREN-CAM produced at UW-Madison, with prominent mass peak at *m/z* 671.07145 (671.073246 calculated for [$C_{27}H_{26}N_4O_9Sb$]$^+$), confirming existence of [H_2Sb(TREN-CAM)]$^+$ with isotope patterning matching that expected for ^{nat}Sb. Spectra obtained using electron spray ionization in positive mode with a Bruker MaXis ultra-high resolution quadrupole TOF mass spectrometer.

Using ^{1}H and ^{13}C NMR, collaborators confirmed synthesis of and further characterized the structural chemistry of [^{nat}Sb(TREN-CAM)]$^-$. Due to poor D_2O solubility, [^{nat}Sb(TREN-CAM)]$^-$ was dissolved in d_6-DMSO, and NMR was collected for both the crude reaction and purified product (**Figures 45 and 46**, **Appendix B Figures B5-B13**). Because of molecular symmetry, deprotonated [TREN-CAM]$^{6-}$ has 6 unique protons, illustrated in **Figure 45**. Aromatic protons generally have measured chemical shift values 6 – 8 ppm, and the influence of electron withdrawing oxygens within the catechol and amide functional groups shift signals (two doublets

(**Figure 45** proton 2 and 3) and one triplet (**Figure 45** proton 4)) to the 6 – 7.25 ppm range. Upon coordination of catechol groups to antimony, further electron withdrawing is observed in the upshift of doublet (**Figure 45** proton 2) and triplet (**Figure 45** proton 4) peaks. The proton spectrum of $[^{nat}Sb(TREN\text{-}CAM)]^{-}$ is similar to spectra obtained for TREN-CAM Ga(III) and Ti(IV) complexes with significant downfield shifting of Sb-TREN-CAM aromatic resonances (Ga: 6.10–6.79 ppm [209]; Ti: 6.16–6.93 ppm [211]; Sb: 6.78–7.29 ppm (**Figure 45, Appendix Figure B10 and B11**)).

^{13}C NMR confirms molecular symmetry as 9 peaks (**Figure 46**) are identified for 9 unique carbons on the 27 carbon molecule. TREN-CAM deprotonation caused changes in the ^{13}C spectra; however, complexation with Sb caused only a slight peak shift. Similar spectra are observed before and after purification (**Figure 46**).

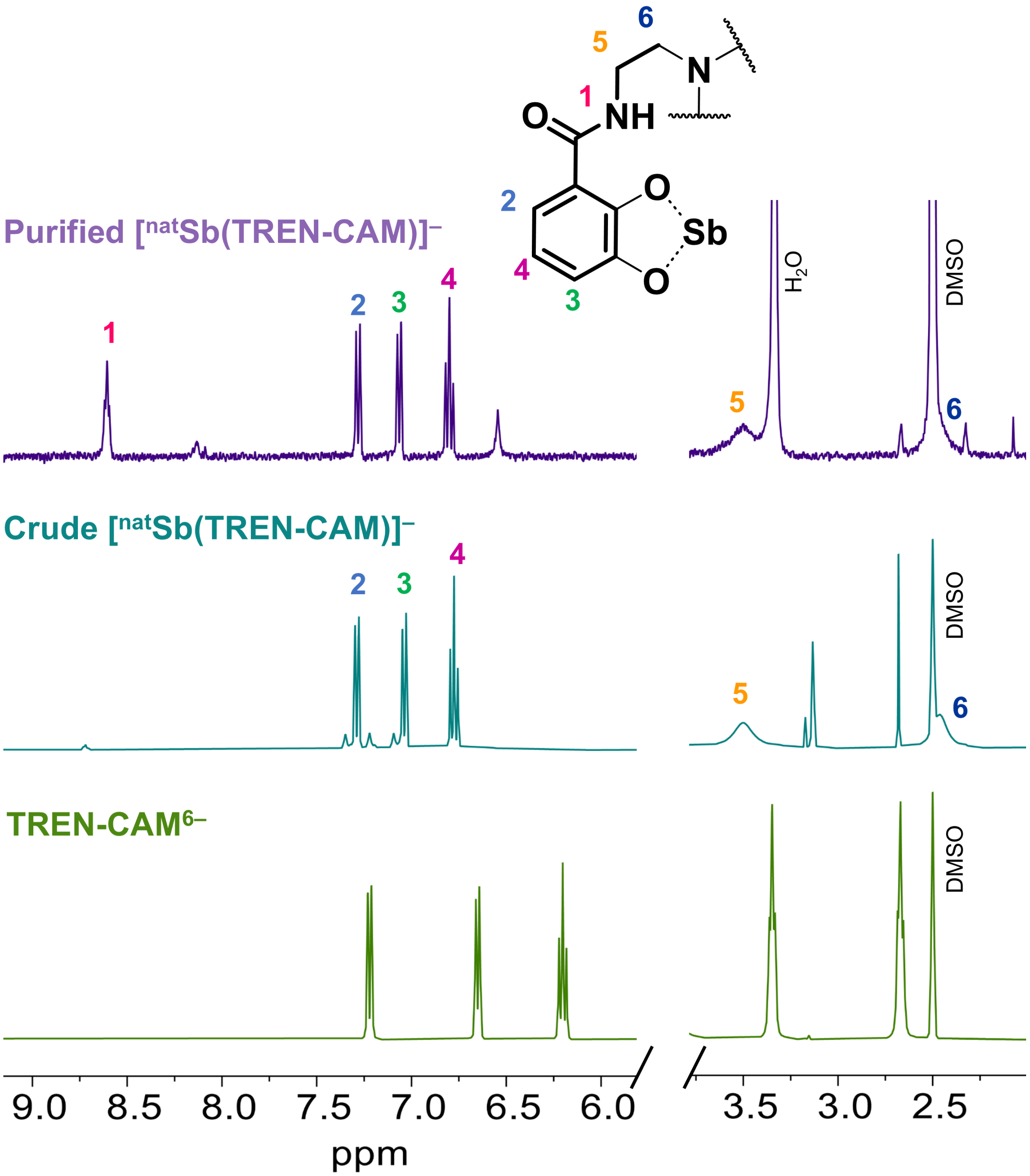

Figure 45: ^{1}H NMR spectra of TREN-CAM (bottom) and its Sb(V) complex (middle, crude and top, purified) in d_6-DMSO. TREN-CAM was deprotonated using NH_4OH prior to the addition of Sb(V).

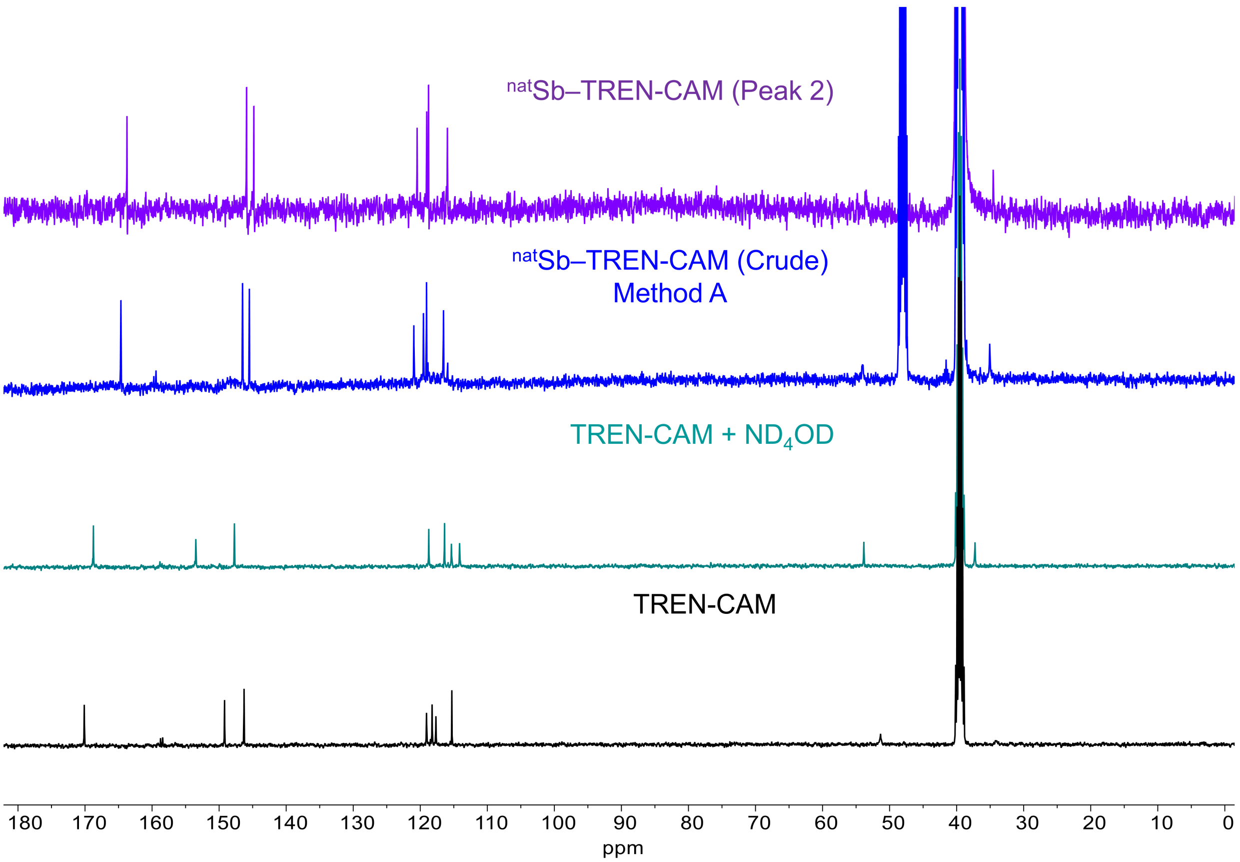

Figure 46: Stacked $^{13}C\{^{1}H\}$ NMR spectra (400 MHz, DMSO-d_6) of TREN-CAM before and after complexation with Sb(V).

3.1. X-ray Absorption Spectroscopy (XAS) and Crystallography

ORNL collaborators performed primary data analysis for XAS (Dr. Alexander Ivanov and Dr. Darren Driscoll) and X-ray crystallography (Dr. Frankie White). Their detailed analysis is included in **Appendix B**.

Collected X-ray absorption near-edge structure (XANES) spectra show an absorption edge for the $[^{nat}Sb(TREN\text{-}CAM)]^-$ complex similar to Sb_2O_5, indicating Sb is in the 5+ oxidation state after coordination (**Appendix B Figure B2a**). The shape of the $[^{nat}Sb(TREN\text{-}CAM)]^-$ XANES spectra is similar to that of aqueous $KSb(OH)_6$, showing a similar octahedral environment (**Appendix B Figure B2a**). Fourier transforms of measured EXAFS data provided coordination numbers and bond distances between Sb, O, and C (**Appendix B Table B2**). Data for [^{nat}Sb(TREN-CAM)]$^-$ nicely matches that of [Sb(catechol)$_3$]$^-$ and is similar to previously reported Sb catechol complexes [139,191]. From XANES analysis, Sb is coordinated by TREN-CAM's catechols.

ORNL collaborators obtained an X-ray diffraction crystal structure of [^{nat}Sb(TREN-CAM)]$^-$ (**Figure 47**), showing Sb(V) complexation by TREN-CAM's three catechol arms and corroborating XAS results. Similarly to the reported [^{nat}Ti(TREN-CAM)]$^{2-}$ complex structure [211], amide hydrogens are buried inside the cavity and form hydrogen bonds with the ortho catechol oxygens.

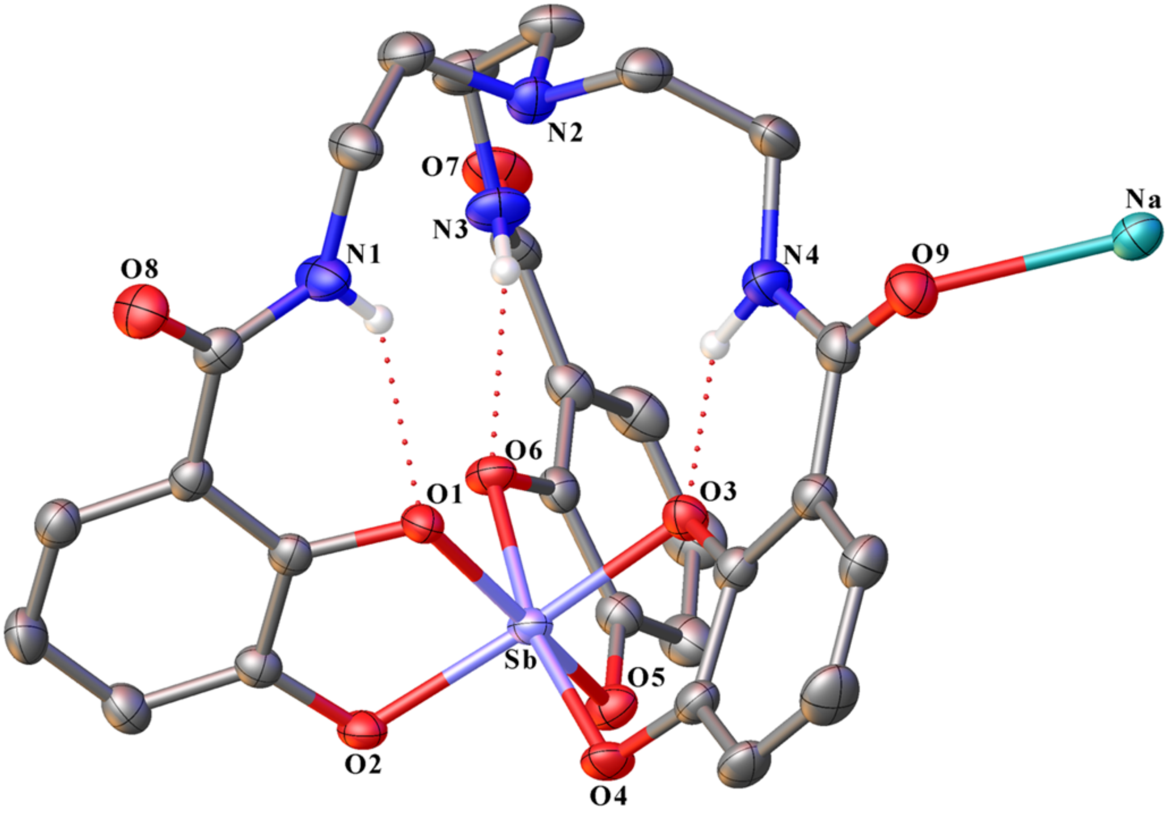

Figure 47: X-ray crystal structure of Na[Sb(TREN-CAM)]·2DMF. Ellipsoids for carbons and heteroatoms are drawn at the 50% probability level. Solvent molecules and hydrogen

atoms attached to carbon centers have been omitted for clarity. Hydrogen bonding interactions are indicated by red dotted lines.

3.2. Radiolabeling from Liquid-Liquid Extraction Purified Solutions

3.2.1. Radiolabeling in NH_4OAc Buffers

Seeking to establish optimal conditions for radiolabeling TREN-CAM with ^{1XX}Sb in NH_4OAc buffered solutions, collaborators prepared samples at a single chelator concentration (1 mM), pH 4, and activity of 21 kBq (0.57 μCi) ^{1XX}Sb. After incubation for 10, 30, 60, or 120 min at temperatures of 25, 37, 60, and 80 °C, samples were analyzed by radio-TLC. By aliquoting them onto reversed-phase C_{18} aluminum-backed plates and developing with a 0.25 M oxalic acid mobile phase. Under these conditions, [^{1XX}Sb]Sb–TREN-CAM remains at the baseline ($R_f = 0$) and "free" ^{1XX}Sb migrates with the solvent front ($R_f = 1$). Analysis of control samples, however, revealed that in the absence of chelator, ~10% of the activity remained bound to the origin, which would confound the accurate determination of RCY, a phenomenon observed previously in ^{44}Sc radiolabeling studies [212]. Collaborators found that adding a small amount of oxalic acid directly to the reactions and heating them at 80 °C for 10 min ensured migration of all unchelated ^{1XX}Sb in solution, presumably via oxalate complex formation. RCYs increased as a function of time (**Figure 48a**), albeit only slightly for complexation reactions conducted at 25 °C. Similarly, elevated temperatures resulted in higher RCYs, with complete radiolabeling after 60 min at 80 °C or 120 min at 60 °C. While heating at 80 °C for 60 min, radiolabeling was interrogated as a function of pH and chelator concentration (**Figure 48b**). Interestingly, RCY decreased as pH increased, likely due to increased hydroxide competition at higher pH, which favors the formation of unchelated Sb(V) as $Sb(OH)_6^-$. Nevertheless, TREN-CAM quantitatively complexed ^{1XX}Sb at a concentration of 10^{-3} M across all pH values studied. Furthermore, nearly complete complexation was observed using 10^{-4} M chelator concentration at both pH 2 and 4. Overall, these studies confirm the ability of TREN-CAM to effectively bind ^{1XX}Sb(V) in aqueous solution.

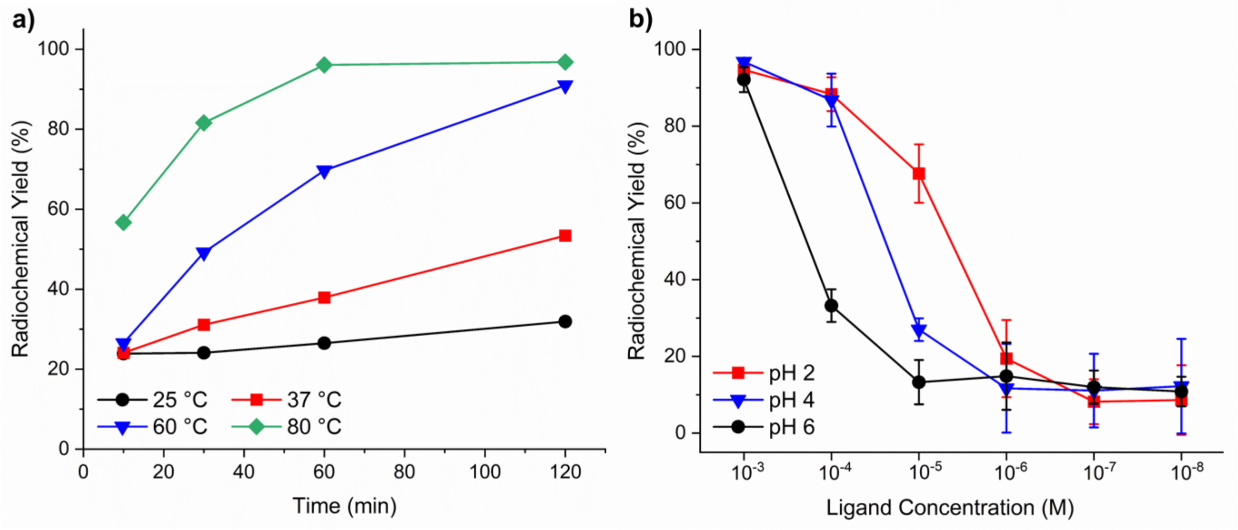

Figure 48: Radiolabeling of TREN-CAM with ^{1XX}Sb. (a) Radiochemical yields as a function of time and temperature (N = 1). (b) Radiochemical yields as a function of ligand concentration and solution pH (N = 3).

Using radioantimony produced from LLE into aqueous solutions, Sb-TREN-CAM complexes are formed in various proportions with significant inconsistencies between each production. At ORNL, changes in concentration and pH resulted in changes to free, uncomplexed ^{1XX}Sb eluting with the solvent front (**Figure 49**) with primarily Peak 1 hydroxy-Sb-TREN-CAM species and little to no differences in conversion from Peak 1 to Peak 2, the fully complexed [^{1XX}Sb]Sb-TREN-CAM (**Figure 50**). For this production, formation of primarily Peak 1 was confirmed between institutions (**Figure 51**). At UW-Madison, primarily Peak 1 was formed (15.7% Peak 2) after labeling TREN-CAM with radioantimony at a ^{1XX}Sb molar activity of 0.57 mCi/µmol TREN-CAM (**Figure 51**), which roughly corresponds to ORNL's concentration dependent radiolabeling at 0.0065 mM (**Figure 49 bottom**, 0.63 mCi/µmol TREN-CAM), resulting in significantly poorer RCY. ORNL's radiolabeling at 0.065 mM (**Figure 49 middle**, 63 µCi/µmol) had a species distribution more similar to UW-Madison **production A** test labeling.

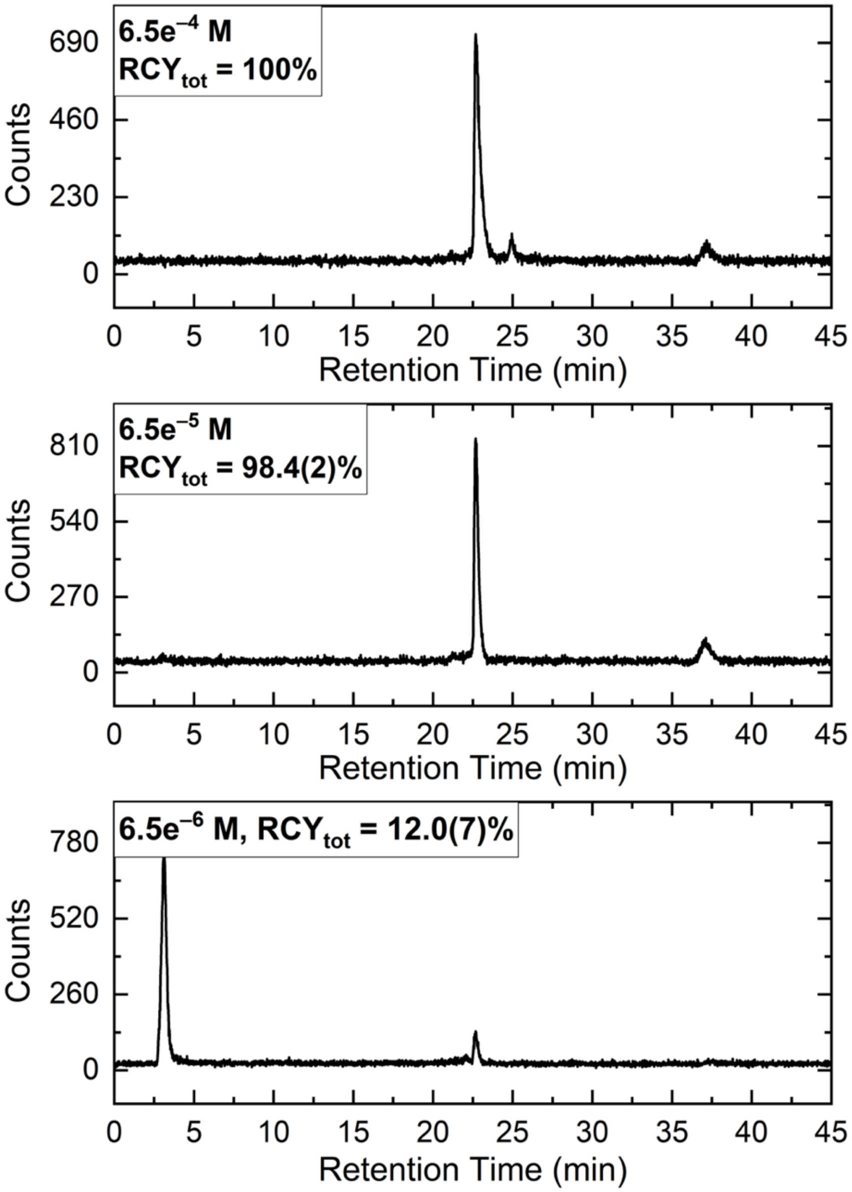

Figure 49: Radio-HPLC traces showing radiolabeling of TREN-CAM with ^{1XX}Sb in NH_4OAc as a function of chelator concentration. Reaction conditions: 0.5 M NH_4OAc (pH 4), 60 min, 80 °C, 0.57 µCi of [^{1XX}Sb]Sb^{5+}, $6.5 \times 10^{-4} - 6.5 \times 10^{-6}$ M TREN-CAM, $V_{tot} = 150$ µL (n = 3 per concentration). The values in parentheses are one standard deviation of

the last significant figure. Under these conditions, $[Sb(H_2TREN\text{-}CAM)(OH)_2]^-$ is the predominant species formed (R_t = 22.8 min). **ORNL radio-HPLC**. Instrument: Shimadzu. Column: Restek Ultra Aqueous C_{18} column (100 Å, 5 µm, 250 mm × 21.2 mm). Flow rate: 1 mL/min. Solvents: A = 0.1% FA/H_2O, B = 0.1% FA/MeCN. Method: 0–5 min: 10% B; 5–25 min: linear ramp 10–100% B; 25–30 min: 100% B.

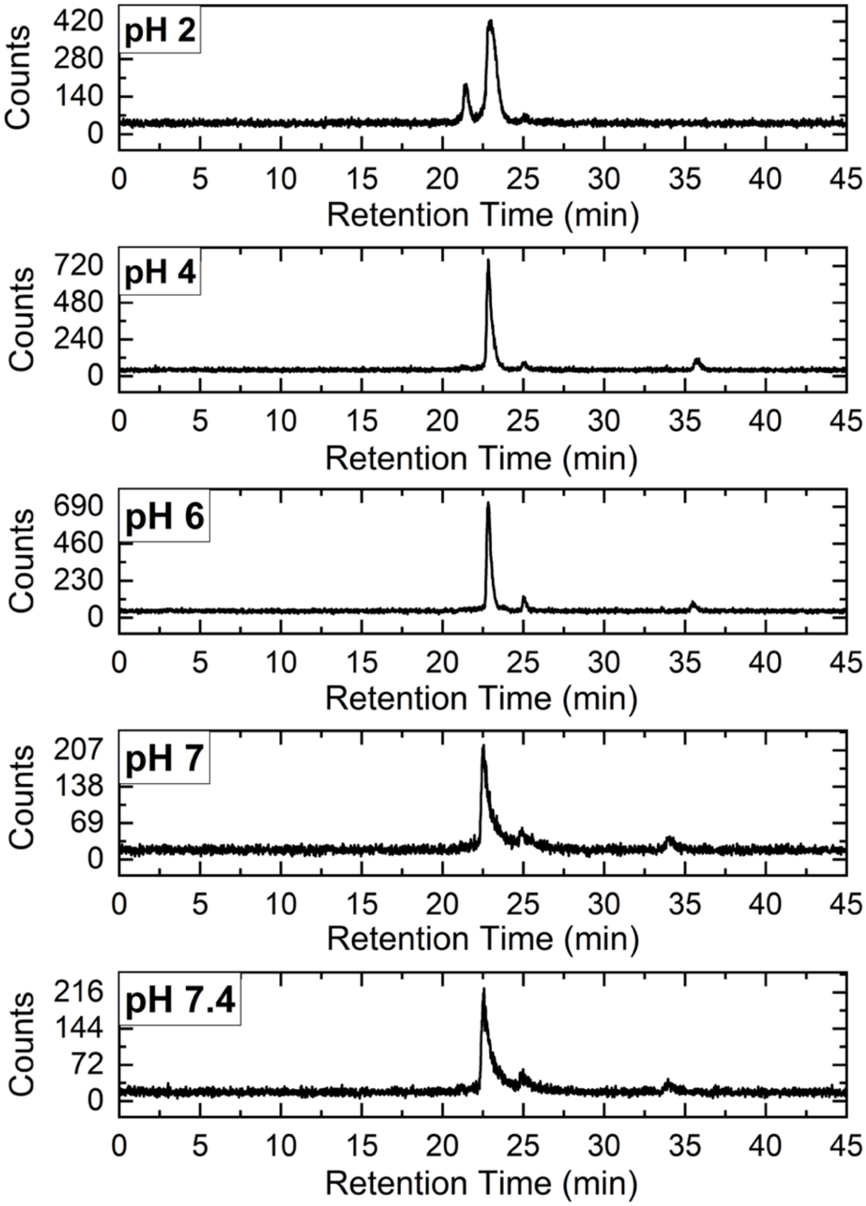

Figure 50: Radio-HPLC traces showing radiolabeling of TREN-CAM with ^{1XX}Sb in NH_4OAc as a function of pH. Reaction conditions: 10 mM HCl (pH 2) or 0.5 M NH_4OAc (pH 4, 6,

7, 7.4), 60 min, 80 °C, 0.57 μCi of [^{1XX}Sb]Sb^{5+}, 6.5 × 10^{-4} M TREN-CAM, V$_{tot}$ = 150 μL (N = 1 per pH). Under these conditions, [Sb(H$_2$TREN-CAM)(OH)$_2$]$^-$ is the predominant species formed (R$_t$ = 22.8 min). **ORNL radio-HPLC**. Instrument: Shimadzu. Column: Restek Ultra Aqueous C$_{18}$ column (100 Å, 5 μm, 250 mm × 21.2 mm). Flow rate: 1 mL/min. Solvents: A = 0.1% FA/H$_2$O, B = 0.1% FA/MeCN. Method: 0–5 min: 10% B; 5–25 min: linear ramp 10–100% B; 25–30 min: 100% B.

Occasionally, radioantimony was produced by back extraction with 0.5 M NH$_4$OAc pH 6 buffer (as opposed to 0.1M HCl), resulting in a final pH of 4 due to residual HCl in the DBE phase. **Figure 51** shows nearly identical radio-HPLC chromatograms of radiolabeling performed from either 0.1 M HCl or 0.5 M NH$_4$OAc back extractions, dissuading impact of aqueous back extraction solution low molarity salt upon resultant Sb-TREN-CAM speciation.

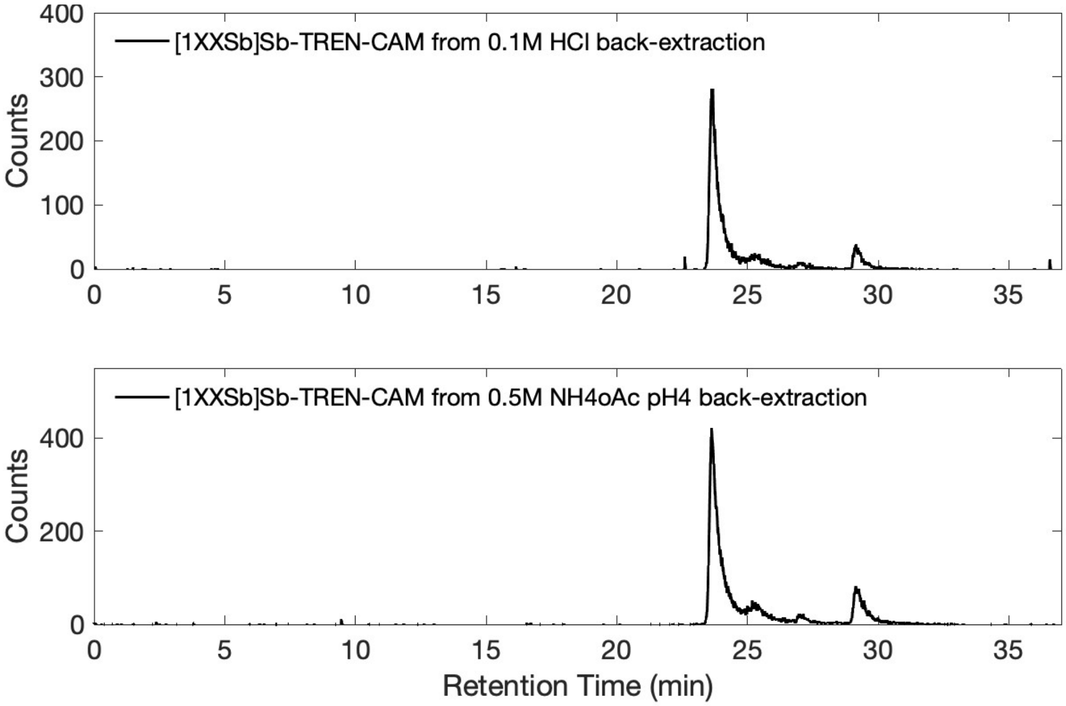

Figure 51: Radio-HPLC traces showing radiolabeling of TREN-CAM with ^{1XX}Sb back-extracted into either 0.1 M HCl or NH$_4$OAc). [Sb(H$_2$TREN-CAM)(OH)$_2$]$^-$ is the predominant

species formed (R_t = 23.7 min). **UW-Madison radio-HPLC method A**. Instrument: Agilent 1260 II system (Santa Clara, CA) with Ortec (AMETEK ORTEC, Oak Ridge, TN) detector. Column: 150 mm C18 Jupiter column (Phenomenex, Torrance, CA). Flow rate: 1 mL/min. Solvents: A = 0.1 M ammonium citrate (pH 4.5), B = 0.1% FA/H2O, C = MeOH. Method: 0–5 min: 100% A; 5–10 min: 100% B; 10–30 min: linear ramp to 0% B / 100% C; 30–32 min: 100% B; 32–37 min, 100% A.

Within **production B**, small scale comparison of pH and concentration resulted in differing speciation distribution as compared to **production A** radiolabeling. **Figure 52** shows comparisons of radioantimony labeled TREN-CAM at molar activities of 67 µCi/µmol (1 mM TREN-CAM) and 0.67 mCi/µmol (0.1 mM TREN-CAM), a similar molar activity range as previous labelings. At 1 mM TREN-CAM (67 µCi/µmol) 49.3% of ^{1XX}Sb activity was within the species [^{1XX}Sb]Sb-TREN-CAM at pH 6, dropping to 41.0% [^{1XX}Sb]Sb-TREN-CAM at pH 4. ORNL observed increases in [^{1XX}Sb]Sb-TREN-CAM between pH 2 HCl and pH 4 NH_4OAc but no significant change in speciation between pH 4 and pH 6 (**Figure 50**). Though higher pH should promote antimony hydrolysis, increased formation of [^{1XX}Sb]Sb-TREN-CAM at pH 6 versus pH 4 could be due to greater deprotonation of TREN-CAM catechols whose acid dissociation constants (pka) are 9.25 and 13 [213].

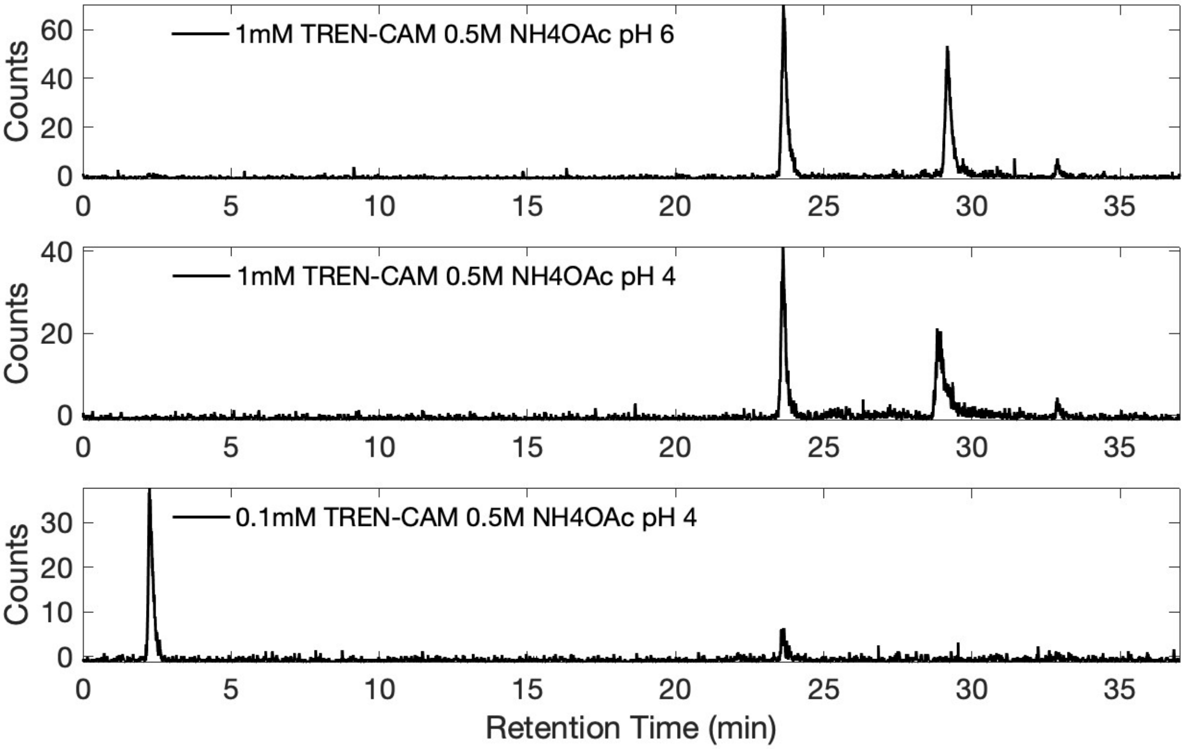

Figure 52: Radio-HPLC traces showing radiolabeling of TREN-CAM with differing pH NH_4OAc buffer or concentration. $[Sb(H_2TREN\text{-}CAM)(OH)_2]^-$ is the predominant species formed (R_t = 23.7 min), with greater proportion $Sb(TREN\text{-}CAM)]^-$ at 1 mM TREN-CAM in pH 6 buffer. **UW-Madison radio-HPLC method A**. Instrument: Agilent 1260 II system (Santa Clara, CA) with Ortec (AMETEK ORTEC, Oak Ridge, TN) detector. Column: 150 mm C_{18} Jupiter column (Phenomenex, Torrance, CA). Flow rate: 1 mL/min. Solvents: A = 0.1 M ammonium citrate (pH 4.5), B = 0.1% FA/H_2O, C = MeOH. Method: 0–5 min: 100% A; 5–10 min: 100% B; 10–30 min: linear ramp to 0% B / 100% C; 30–32 min: 100% B; 32–37 min, 100% A.

Antimony from **production C** radiolabeled TREN-CAM with complete speciation $[^{1XX}Sb]$Sb-TREN-CAM at a molar activity of 62 µCi/µmol and a pH of 6 (**Figure 53**). **Figure 51** previously showed no difference in species distribution when back extracting into 0.1 M HCl versus 0.5 M NH_4OAc pH 6. From this, we can be assured back extraction is not the cause of the 100% fully complexed speciation. Additionally, **production A** radioantimony at a molar activity 10x less and the same pH 6, resulted in almost entirely Peak 1 hydroxy species (**Figure 51**), and **production B** with the same pH 6 and similar molar activity (67 µCi/µmol, **Figure 52**) resulted in complete radioantimony complexation but majority hydroxy species (Peak 1, 49.3%) and minority [^{1XX}Sb]Sb-TREN-CAM (Peak 2, 49.5%).

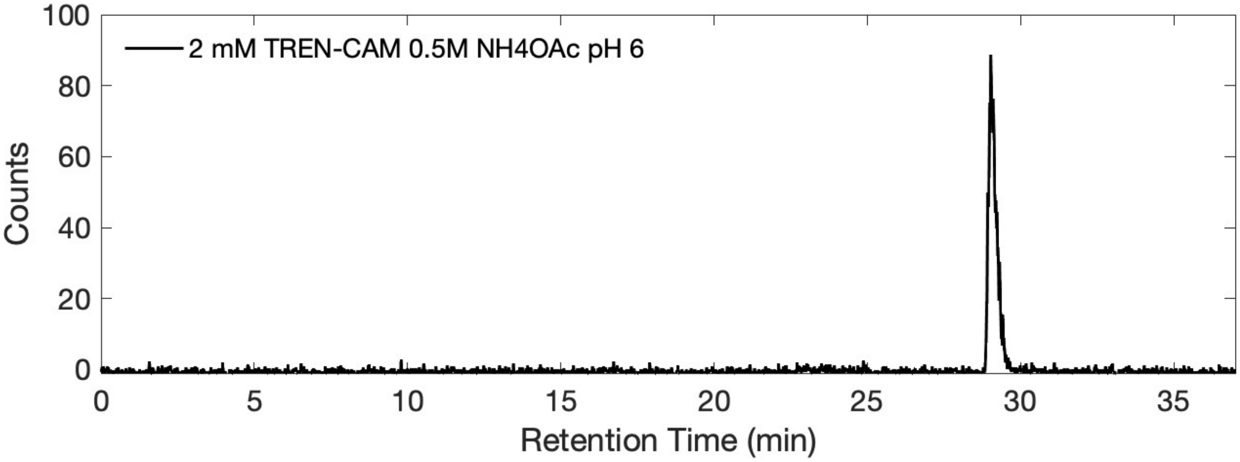

Figure 53: Radio-HPLC trace showing quantitative radiolabeling of TREN-CAM from production C. Sb(TREN-CAM)]$^-$ is the predominant species formed. **UW-Madison radio-HPLC method A.** Instrument: Agilent 1260 II system (Santa Clara, CA) with Ortec (AMETEK ORTEC, Oak Ridge, TN) detector. Column: 150 mm C_{18} Jupiter column (Phenomenex, Torrance, CA). Flow rate: 1 mL/min. Solvents: A = 0.1 M ammonium citrate (pH 4.5), B = 0.1% FA/H_2O, C = MeOH. Method: 0–5 min: 100% A; 5–10 min: 100% B; 10–30 min: linear ramp to 0% B / 100% C; 30–32 min: 100% B; 32–37 min, 100% A.

Manual execution of LLE produced radioantimony includes many variables difficult to control, which greatly impacts oxidation state, acid concentration, and subsequent speciation uncertainty. Tin is a strong reducing agent, and excess H_2O_2 is required during LLE separation to oxidize all Sn(II) into Sn(IV) before oxidation of Sb(III) can occur. Secondly, it is observed that high HCl concentration (>9 M) is required for Sb(V) to extract into the DBE phase. Differing mass tin targets, differing volumes of HCl, and differing heated dissolution times could cause variation in HCl concentration post dissolution and require slight modification of added H_2O_2 and HCl before successful extraction. It is believed that this inherent variation and uncertainty in the LLE method may cause differences in radioantimony TREN-CAM speciation. As hydrolysis of antimony is driven by factors including exposure to oxidants, pH, and H_2O, non-aqueous radiolabeling conditions were explored with the hypothesis of greater formation of fully complexed, non-hydroxy species [^{1XX}Sb]Sb-TREN-CAM.

3.2.1. Radiolabeling in MeOH/DMSO

Inspired by unoptimized conditions for macroscopic ^{nat}Sb-TREN-CAM, radiolabeling from an organic solvent comprised of 1.4:1 MeOH:DMSO created majority complexed [^{1XX}Sb]Sb-TREN-CAM (93.0%) when heated for 1 h at 80 °C (**Figure 54 middle**). To save time during production, the DBE extractant phase was taken to dryness and reconstituted in MeOH before addition of DMSO and TREN-CAM. In macroscopic labeling, addition of NH_4OH at 13x the molar equivalent TREN-CAM deprotonated TREN-CAM's catechols and was necessary for complexation; however, during radiolabeling, the addition of base inhibited formation of Peak 2 and promoted formation of the hydroxy-Sb-TREN-CAM complex (**Figure 54 top**). Considering the susceptibility of antimony to hydrolysis in aqueous solutions [210], this observation makes sense. Radiolabeling ^{1XX}Sb from a MeOH/DMSO solution resulted in formation of a primary Peak 2 complex with greater reproducibility and less variability between LLE productions.

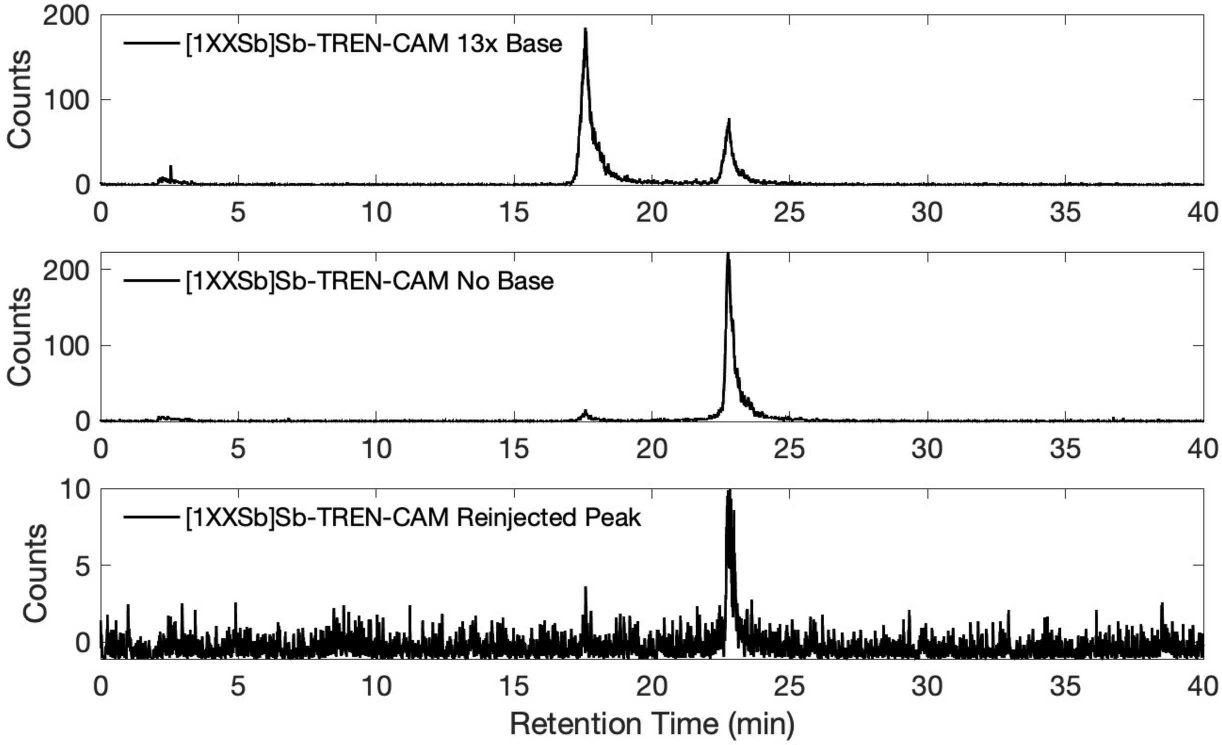

Figure 54: Radio-HPLC trace showing radiolabeling of TREN-CAM from MeOH/DMSO solutions. With addition of 13x NH_4OH, $[Sb(H_2TREN\text{-}CAM)(OH)_2]^-$; however, without base, $Sb(TREN\text{-}CAM)]^-$ is the predominant species formed. Following injection of no base sample, the 22.8 min peak was collected and re-injected. **UW-Madison radio-HPLC method B**. Instrument: Agilent 1260 II system (Santa Clara, CA) with Ortec (AMETEK ORTEC, Oak Ridge, TN) detector. Column: 150 mm C_{18} Jupiter column (Phenomenex, Torrance, CA). Flow rate: 1 mL/min. Solvents: A = 0.1 M ammonium citrate (pH 4.5), B = 0.1% TFA/H_2O, C = 0.1% TFA/MeCN. Method: 0–5 min: 100% A; 5–10 min: 95% B / 5% C; 10–30 min: linear ramp to 5% B / 95% C; 30–35 min: 5% B / 95% C; 35–36 min: linear ramp to 95% B / 5% C; 36–40 min, 100% A.

Acetic acid does not complex antimony in either Sb(III) or Sb(V) forms [139,191,214], and Sb(V) exists primarily as $Sb(OH)_6^-$ in aqueous, oxic conditions and pH > 1.5 [139,210,215]. $SbCl_6^-$ readily hydrolyzes in pH >2 as an average value hydrolysis rate constant of (2.74 ± 0.12) x 10^{-5} s^{-1} has been reported [215]. In the previously reported aqueous radiolabeling at pH >2, TREN-CAM complexed ^{1XX}Sb in NH_4OAc buffer with smaller proportion hydroxy species observed at pH 6 over pH 4. While measuring Sb hydrolysis rate constants, Willis and Neumann observed non-linearity with ammonium buffer concentration versus linearity with sodium and potassium buffer concentrations, attributing results to the formation of an ammonia antimony adduct [215]. An ammonia antimony adduct could help stabilize ^{1XX}Sb at higher pH, explaining improved TREN-CAM complexation due to catechol deprotonation in spite of greater hydrolysis susceptibility, lack of complexation from acetate, and correspondingly worsened speciation in MeOH/DMSO solvents. Semi-preparative HPLC collection and subsequent RP-HPLC reinjection of Peak 2 from the sample '[^{1XX}Sb]Sb-TREN-CAM No Base' (**Figure 56 bottom**) shows retention of primarily Peak 2. We observed higher noise from lower injected activity concentration. With conservative peak integrations, 84.4% [^{1XX}Sb]Sb-TREN-CAM remained intact.

Time and temperature dependent labeling showed fast (<1h) complexation of radioantimony with creation of primarily Peak 1, partially complexed [[^{1XX}Sb]Sb(H_2TREN-CAM)$(OH)_2$]$^-$, at 37 °C (71.1%) and primarily Peak 2, fully complexed [^{1XX}Sb]Sb-TREN-CAM at 60 °C (54.5 %) and 80 °C (90.8 %). Over time, Peak 1 transitions to Peak 2 (**Figure 55 and 56**). When heating at 60 °C, significant conversion between species is seen between 1 h (37.4% Peak 1, 54.5% Peak 2) and 2 h (15.3% Peak 1, 82.4% Peak 2). At 2 h radiolabeling, a significant increase in Peak 2 is shown (**Figure 56**) with increased Peak 2 yields observed at increased temperatures. The transition from Peak 1 into Peak 2 with increased time and temperature supports the identity of Peak 1 as a partially complexed Sb-TREN-CAM species. Improved creation of Peak 2 over

Peak 1 in organic versus aqueous solvents and HRMS measurements promotes Peak 1 identity as a hydroxy antimony TREN-CAM species. In time, RCY of >95% Peak 2 are observed for all temperatures tested (**Table 13, Figure 57**).

Table 13: Radiochemical yields of time and temperature dependent labeling experiments.

Temperature	Time	Peak 2 RCY
37	3 d	97.0%
60	4 h	96.0%
80	3 h	98.4%

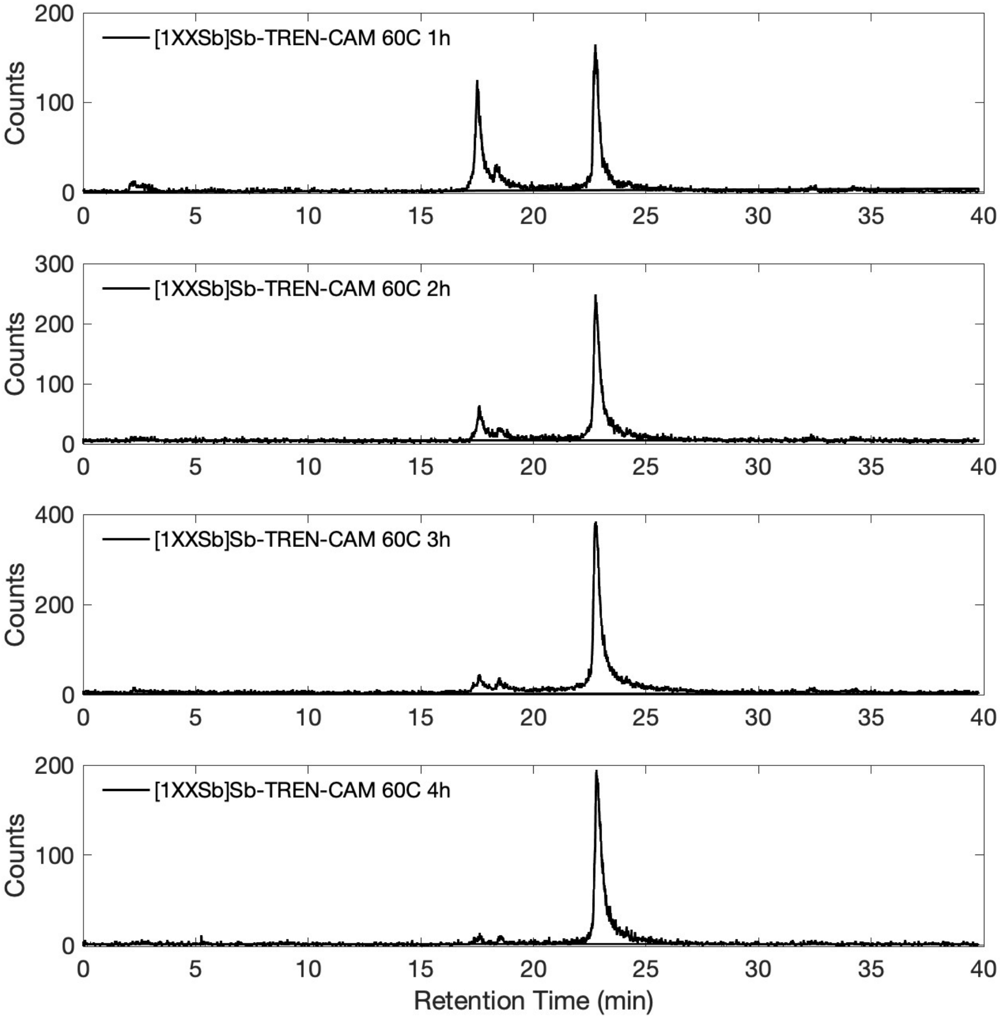

Figure 55: Radio-HPLC trace showing radiolabeling of TREN-CAM from MeOH/DMSO heated at 60 °C for up to 4 h. Peak 1 (R_t = 17.6 min) is seen converting to Peak 2 (R_t

= 22.8 min), ultimately forming Sb(TREN-CAM)]⁻ as the predominant species. **UW-Madison radio-HPLC method B.** Instrument: Agilent 1260 II system (Santa Clara, CA) with Ortec (AMETEK ORTEC, Oak Ridge, TN) detector. Column: 150 mm C_{18} Jupiter column (Phenomenex, Torrance, CA). Flow rate: 1 mL/min. Solvents: A = 0.1 M ammonium citrate (pH 4.5), B = 0.1% TFA/H_2O, C = 0.1% TFA/MeCN. Method: 0–5 min: 100% A; 5–10 min: 95% B / 5% C; 10–30 min: linear ramp to 5% B / 95% C; 30–35 min: 5% B / 95% C; 35–36 min: linear ramp to 95% B / 5% C; 36–40 min, 100% A.

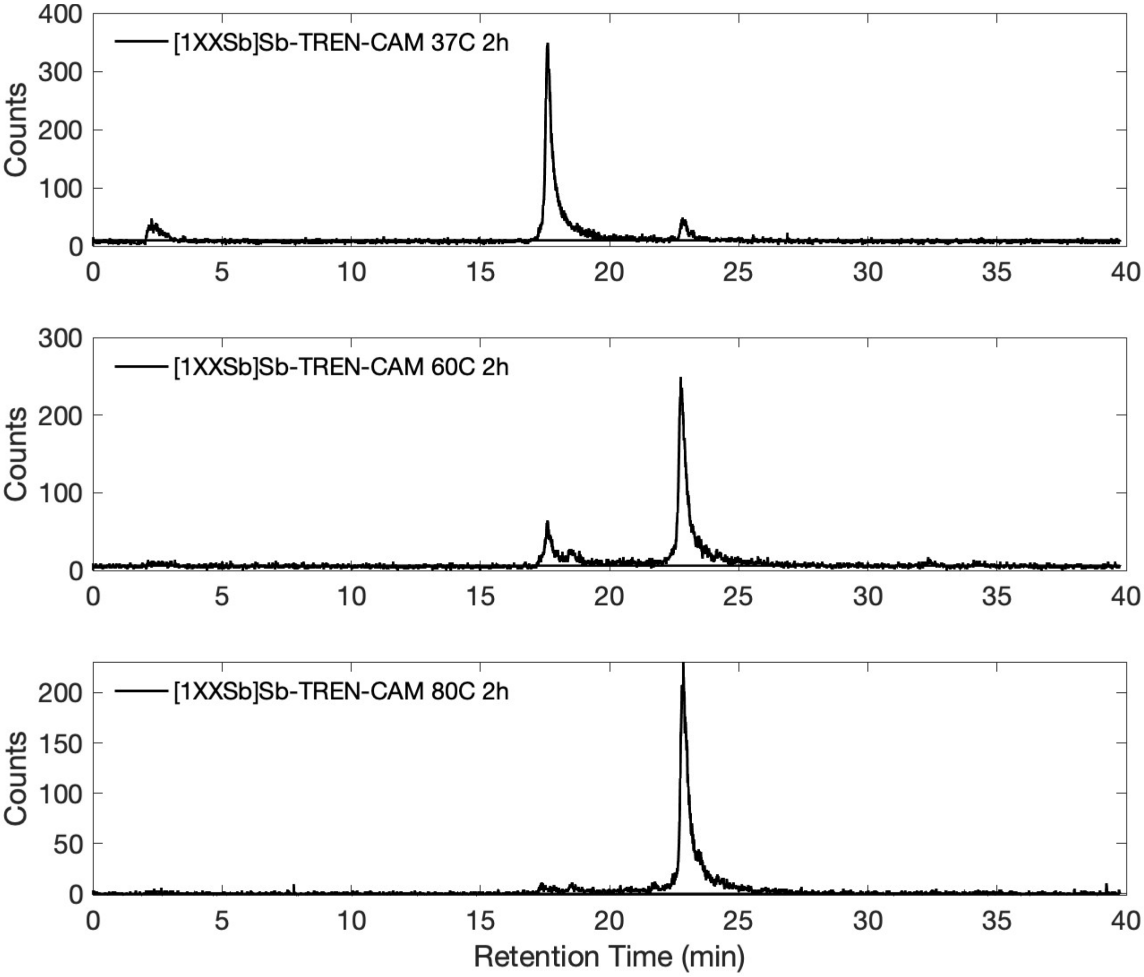

Figure 56: Radio-HPLC trace showing radiolabeling of TREN-CAM from MeOH/DMSO heated for 2 h at 37, 60, or 80 °C. Peak 1 (R_t = 17.6 min) is the dominant species at

lower temperature with Peak 2 (R_t = 22.8 min) Sb(TREN-CAM)]$^-$ forming as the predominant species at increased temperature. **UW-Madison radio-HPLC method B**. Instrument: Agilent 1260 II system (Santa Clara, CA) with Ortec (AMETEK ORTEC, Oak Ridge, TN) detector. Column: 150 mm C_{18} Jupiter column (Phenomenex, Torrance, CA). Flow rate: 1 mL/min. Solvents: A = 0.1 M ammonium citrate (pH 4.5), B = 0.1% TFA/H_2O, C = 0.1% TFA/MeCN. Method: 0–5 min: 100% A; 5–10 min: 95% B / 5% C; 10–30 min: linear ramp to 5% B / 95% C; 30–35 min: 5% B / 95% C; 35–36 min: linear ramp to 95% B / 5% C; 36–40 min, 100% A.

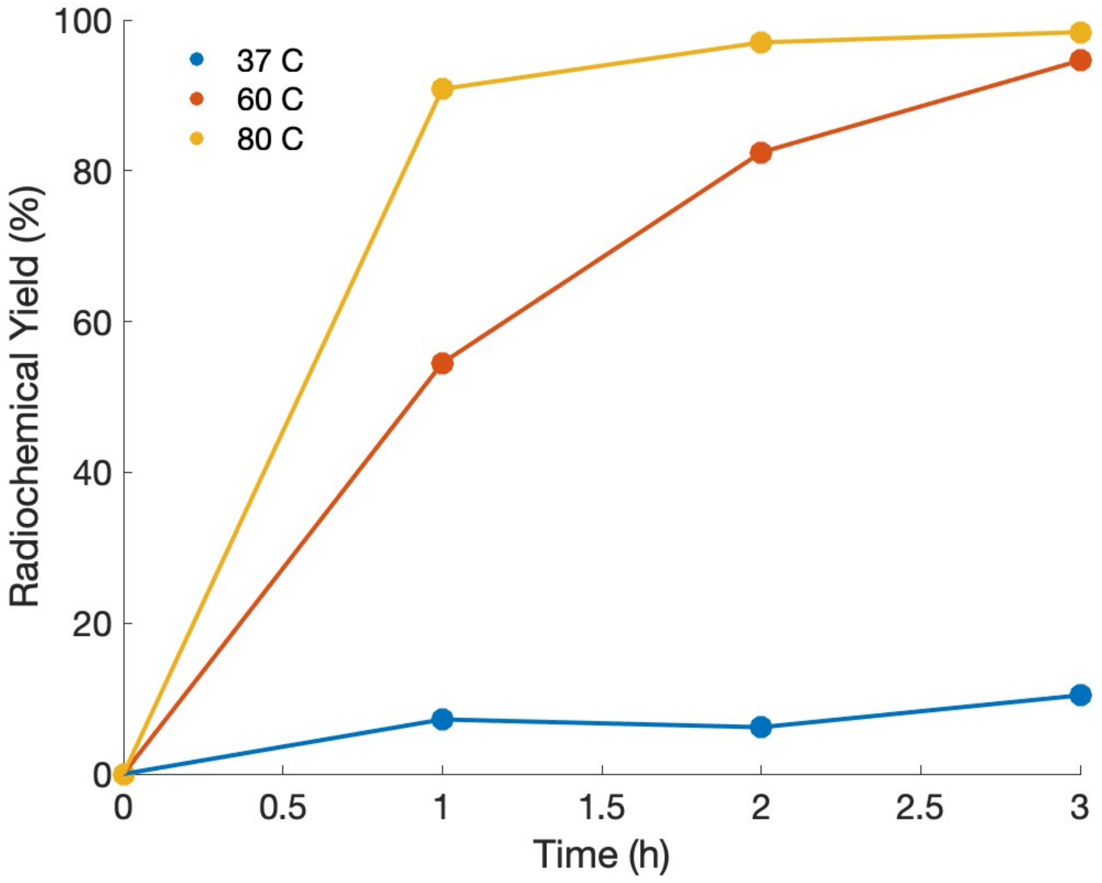

Figure 57: Time and temperature dependance (N = 1) of Sb(TREN-CAM)]$^-$ RCYs while radiolabeling from MeOH/DMSO using **UW-Madison radio-HPLC method B**.

3.3. Radiolabeling from Column Chromatography Purified Solutions

As target recycling strategies require Sn(II) (**Chapter 2**) and LLE results in Sn(IV), we adapted radiolabeling strategies to column chromatography purified radioantimony solutions. Successful formation of fully complexed [^{1XX}Sb]Sb-TREN-CAM occurred with RCY 98% when labeling with ^{1XX}Sb (60 µCi ^{120m}Sb, 100 µCi ^{122}Sb, 160 µCi total ^{1XX}Sb) produced from column chromatography methods (**Figure 58**) at molar activity 0.16 µCi/µmol. We measured AMA for three productions via deuteron bombardment of ^{nat}Sn targets to be 42.4 ± 25 MBq ^{117}Sb/µmol TREN-CAM (1.1 ± 0.7 mCi/µmol) decay corrected to EOB. Because TLC was implemented to ascertain complexation, we did not differentiate between partially complexed hydroxy species and fully complexed [^{1XX}Sb]Sb-TREN-CAM. When attempting to label TREN-CAM with ^{1XX}Sb (100 µCi ^{120m}Sb, 170 µCi ^{122}Sb, 270 µCi total ^{1XX}Sb) at molar activity 18 mCi/µmol (**Figure 59**) NH_4OAc buffer pH 4 improved radiochemical yields, resulting in 76.1% [^{1XX}Sb]Sb-TREN-CAM compared to 11.8% when using exclusively EtOH as a solvent.

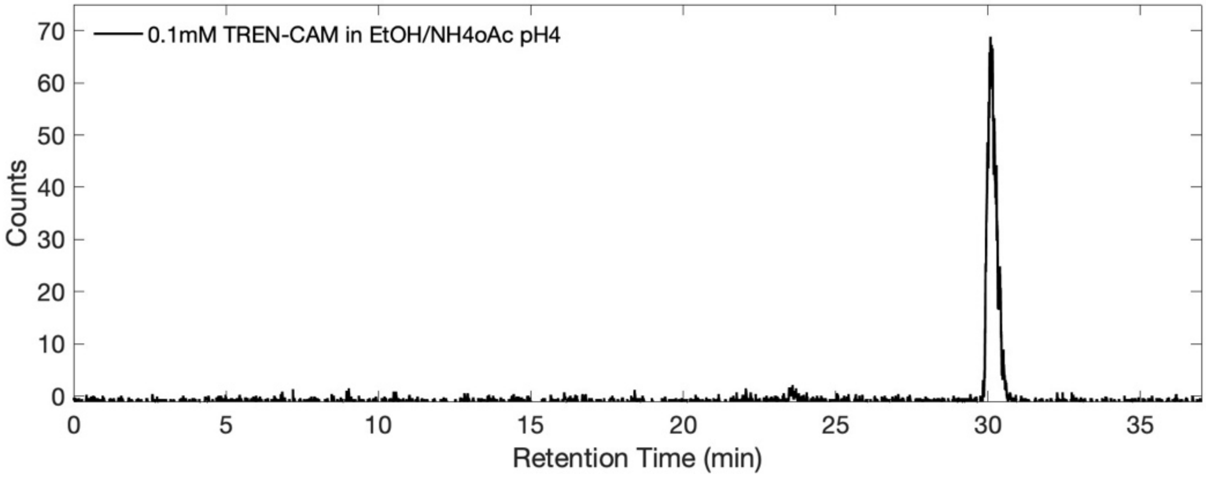

Figure 58: Radio-HPLC showing radiolabeling of TREN-CAM from EtOH/NH_4OAc pH 4 heated at 80 °C for 1 h using ^{1XX}Sb produced from column chromatography production methods. Sb(TREN-CAM)]$^-$ is the predominant species. trace **UW-**

Madison radio-HPLC method A. Instrument: Agilent 1260 II system (Santa Clara, CA) with Ortec (AMETEK ORTEC, Oak Ridge, TN) detector. Column: 150 mm C_{18} Jupiter column (Phenomenex, Torrance, CA). Flow rate: 1 mL/min. Solvents: A = 0.1 M ammonium citrate (pH 4.5), B = 0.1% FA/H_2O, C = MeOH. Method: 0–5 min: 100% A; 5–10 min: 100% B; 10–30 min: linear ramp to 0% B / 100% C; 30–32 min: 100% B; 32–37 min, 100% A.

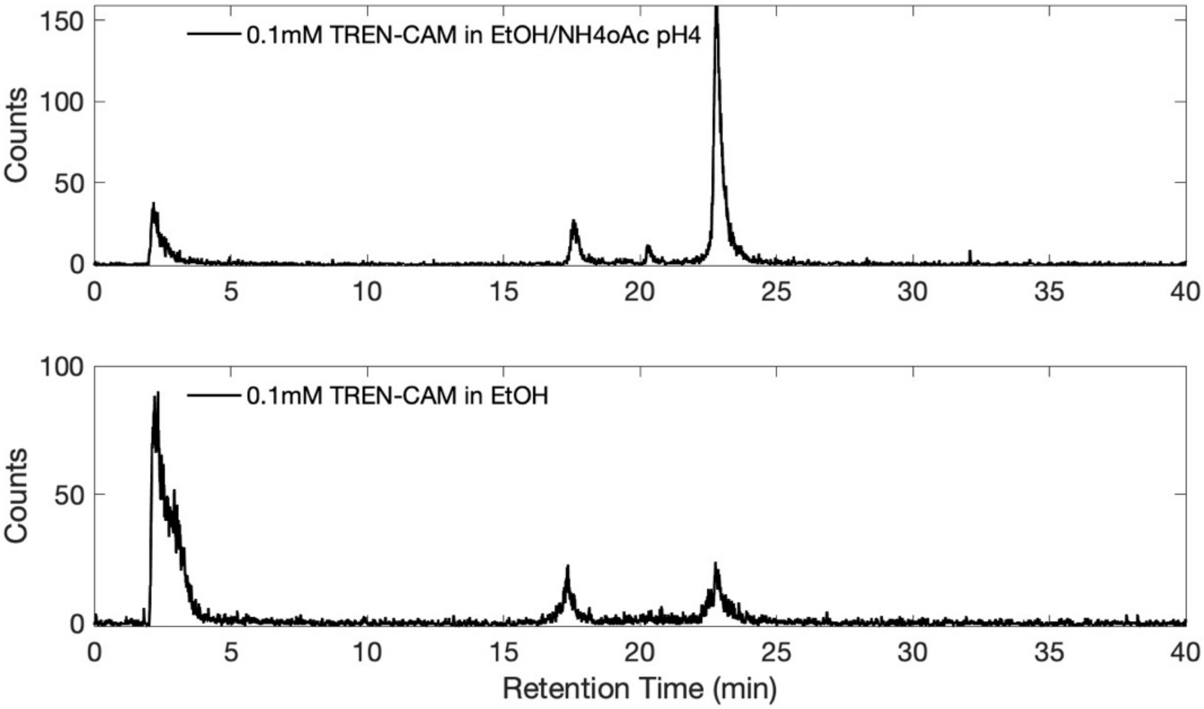

Figure 59: Radio-HPLC trace showing radiolabeling of TREN-CAM from EtOH and EtOH/NH_4OAc pH 4 heated at 80 °C for 1 h using ^{1XX}Sb produced from column chromatography production methods. Sb(TREN-CAM)]$^-$ is the predominant species when using NH_4OAc buffer. **UW-Madison radio-HPLC method B**. Instrument: Agilent 1260 II system (Santa Clara, CA) with Ortec (AMETEK ORTEC, Oak Ridge, TN) detector. Column: 150 mm C_{18} Jupiter column (Phenomenex, Torrance, CA). Flow rate: 1 mL/min. Solvents: A = 0.1 M ammonium citrate (pH 4.5), B = 0.1%

TFA/H_2O, C = 0.1% TFA/MeCN. Method: 0–5 min: 100% A; 5–10 min: 95% B / 5% C; 10–30 min: linear ramp to 5% B / 95% C; 30–35 min: 5% B / 95% C; 35–36 min: linear ramp to 95% B / 5% C; 36–40 min, 100% A.

3.4. Serum Stability and LogD$_{7.4}$ Measurement

Having established that TREN-CAM can bind ^{1XX}Sb(V), we next evaluated the complex's stability. This property is extremely important when considering the use of a radioactive metal or metalloid complex for nuclear medicine applications because any release of the radioactive ion *in vivo* can give rise to off-target toxicity. Stability of [^{1XX}Sb]Sb–TREN-CAM through C8 purification and solvent conversion into PBS was confirmed via HPLC (**Appendix B: Figure B16**). As an indicator of physiological stability, we incubated the [^{1XX}Sb]Sb–TREN-CAM complex in human serum at pH 7.4 and measured its stability over the course of several days via radio-HPLC (**UW-Madison method A**, **Figure 60**). The retention time of radiolabeled [^{1XX}Sb]Sb-TREN-CAM (R_t = 29.8 min) matched that of a ^{nat}Sb-TREN-CAM standard (**Figure 60**), confirming radiolabeling prior to adding serum. After 24, 48, and 72 h, human serum samples were aliquoted and diluted with an equal volume of MeCN to precipitate out the serum proteins prior to HPLC analysis. Under these conditions, >96% of [^{1XX}Sb]Sb-TREN-CAM remained intact over 72 h in serum. Precipitated proteins were not washed, resulting in expected residual activity from protein pellet dead volume and adherence to vial walls. Even so, low (< 20%) ^{120m}Sb activity remains within protein pellet vial post MeCN crash (**Figure 61**).

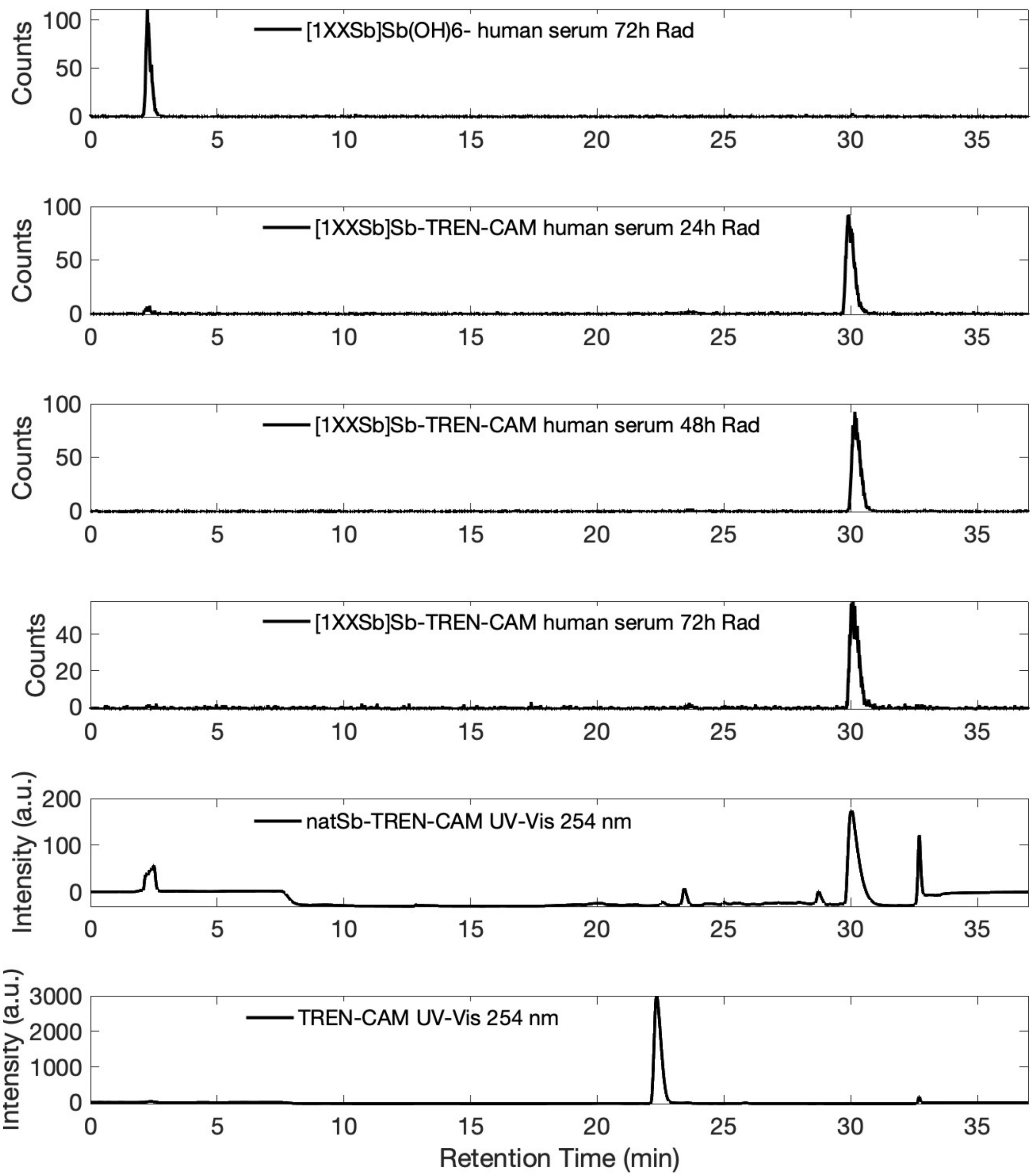

Figure 60: Radio-HPLC assessment of [^{1XX}Sb]Sb–TREN-CAM stability in human serum showing that the complex remains intact for up to 72 h. Chromatograms from top to bottom: UV chromatogram (254 nm) of TREN-CAM; UV chromatogram (254 nm) of ^{nat}Sb-TREN-CAM complex; radio chromatogram of TREN-CAM radiolabeled with ^{1XX}Sb; radio

chromatogram of [^{1XX}Sb]Sb–TREN-CAM after 24 h in 75% human serum; radio chromatogram of [^{1XX}Sb]Sb–TREN-CAM after 72 h in 75% human serum; radio chromatogram of ^{1XX}Sb control. **UW-Madison radio-HPLC method A**. Instrument: Agilent 1260 II system (Santa Clara, CA) with Ortec (AMETEK ORTEC, Oak Ridge, TN) detector. Column: 150 mm C_{18} Jupiter column (Phenomenex, Torrance, CA). Flow rate: 1 mL/min. Solvents: A = 0.1 M ammonium citrate (pH 4.5), B = 0.1% FA/H_2O, C = MeOH. Method: 0–5 min: 100% A; 5–10 min: 100% B; 10–30 min: linear ramp to 0% B / 100% C; 30–32 min: 100% B; 32–37 min, 100% A.

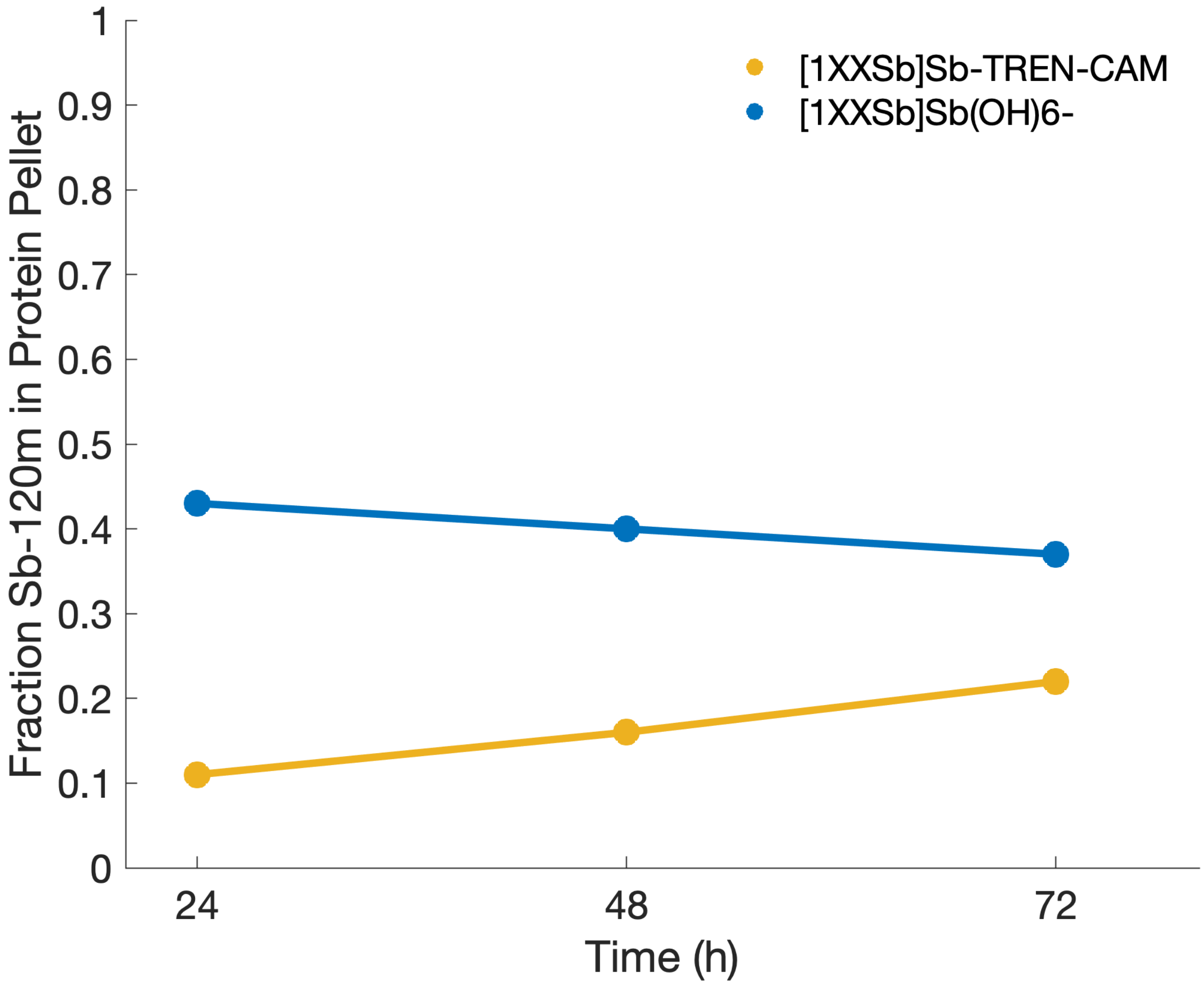

Figure 61: Serum stability using protein crash method, fraction of ^{120m}Sb activity that remained within the protein crash fraction after supernatant transfer (N = 1).

Finally, log $D_{7.4}$ measurements for [^{1XX}Sb]Sb-TREN-CAM were conducted to assess the complex's lipophilicity, a property which influences the biodistribution of radiolabeled constructs. This study partitioned [^{1XX}Sb]Sb-TREN-CAM between *n*-octanol and PBS before HPGe gamma spectroscopy analysis of the activity fraction within each phase. We measured a log $D_{7.4}$ value of 0.299 ± 0.049 (N = 3), revealing that the Sb(V) complex of TREN-CAM preferentially associated with the *n*-octanol phase and is highly lipophilic. By contrast, the log $D_{7.4}$ value for [^{45}Ti]Ti-TREN-CAM was recently reported to be –1.88 [211], which indicates that it is more hydrophilic than [^{1XX}Sb]Sb-TREN-CAM. This difference is quite dramatic considering the small difference in overall charge between the complexes (–1 versus –2), underscoring the effect that the metal/metalloid ion can have on complex lipophilicity.

3.5. Imaging Applications for *in vivo* Complex Stability Assessment

3.5.1. Antimony-117 preparation

After separation, ^{117}Sb was back extracted into PBS. With a hydrolysis constant of 2.72 for $Sb(OH)_5$ [155], the speciation of uncomplexed Sb(V) at pH 7.4 is likely to be $Sb(OH)_6^-$. Radio-HPLC of injected [^{117}Sb]Sb-TREN-CAM shows 95.5% purity as [^{1XX}Sb]Sb-TREN-CAM (**Figure 62**) with < 5% $Sb(OH)_6^-$ contamination. Collaborators working with [^{45}Ti]Ti-TREN-CAM have observed stability issues when using FA gradients and exclusively apply TFA, but FA induced instability in [^{117}Sb]Sb-TREN-CAM radio-RP-HPLC chromatogram was not confirmed.

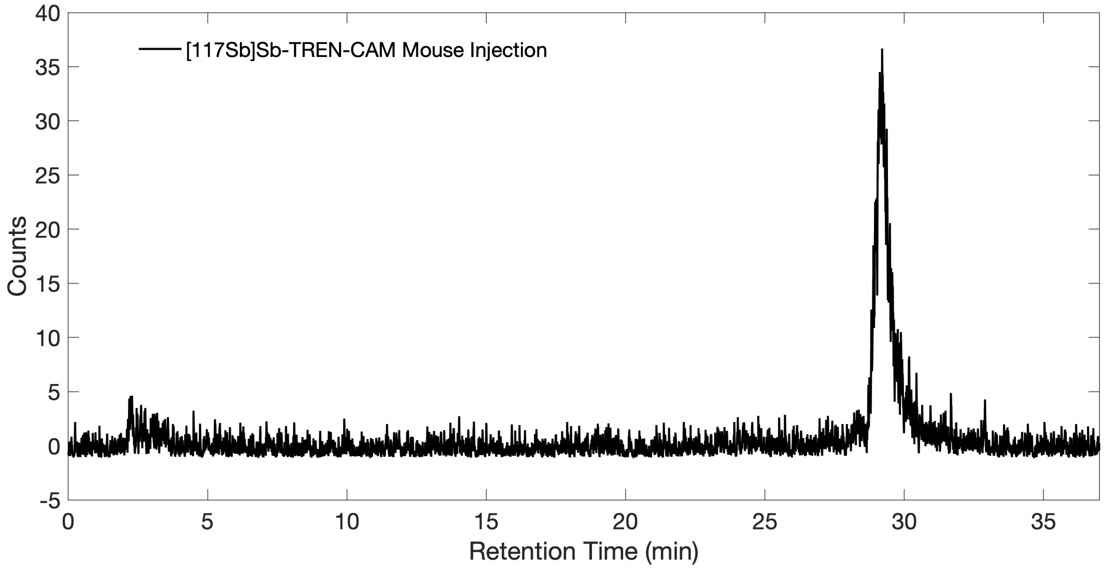

Figure 62: Radio-HPLC of injected sample for mouse *in vivo* experiments showing complexed [^{117}Sb]Sb-TREN-CAM. **UW-Madison radio-HPLC method A**. Instrument: Agilent 1260 II system (Santa Clara, CA) with Ortec (AMETEK ORTEC, Oak Ridge, TN) detector. Column: 150 mm C_{18} Jupiter column (Phenomenex, Torrance, CA). Flow rate: 1 mL/min. Solvents: A = 0.1 M ammonium citrate (pH 4.5), B = 0.1% FA/H_2O, C = MeOH. Method: 0–5 min: 100% A; 5–10 min: 100% B; 10–30 min: linear ramp to 0% B / 100% C; 30–32 min: 100% B; 32–37 min, 100% A.

With activity greater than 100-1000x other radionuclides, ^{117}Sb is the dominant radioisotope (**Figure 63**). Radioantimony isotopes produced within the injected solutions that have contributing positron branching ratios include ^{117}Sb (β^+ = 1.81 *11 %*) [72] and ^{118m}Sb (β^+ = 0.160 *7* %) [73]. Over the 20 min PET scan collected 150 min p.i., injected ^{118m}Sb activities of 314 kBq ± 1 kBq (8.49 μCi ± 0.02 μCi) [^{118m}Sb]Sb(OH)$_6^-$ and 112 kBq ± 3 kBq (3.03 μCi ± 0.08 μCi) [^{118m}Sb]Sb-TREN-CAM contribute approximately 0.22% of β^+ emitted for both radioantimony species. Antimony-118m provided minimal contamination to PET images, allowing accurate ^{117}Sb quantification.

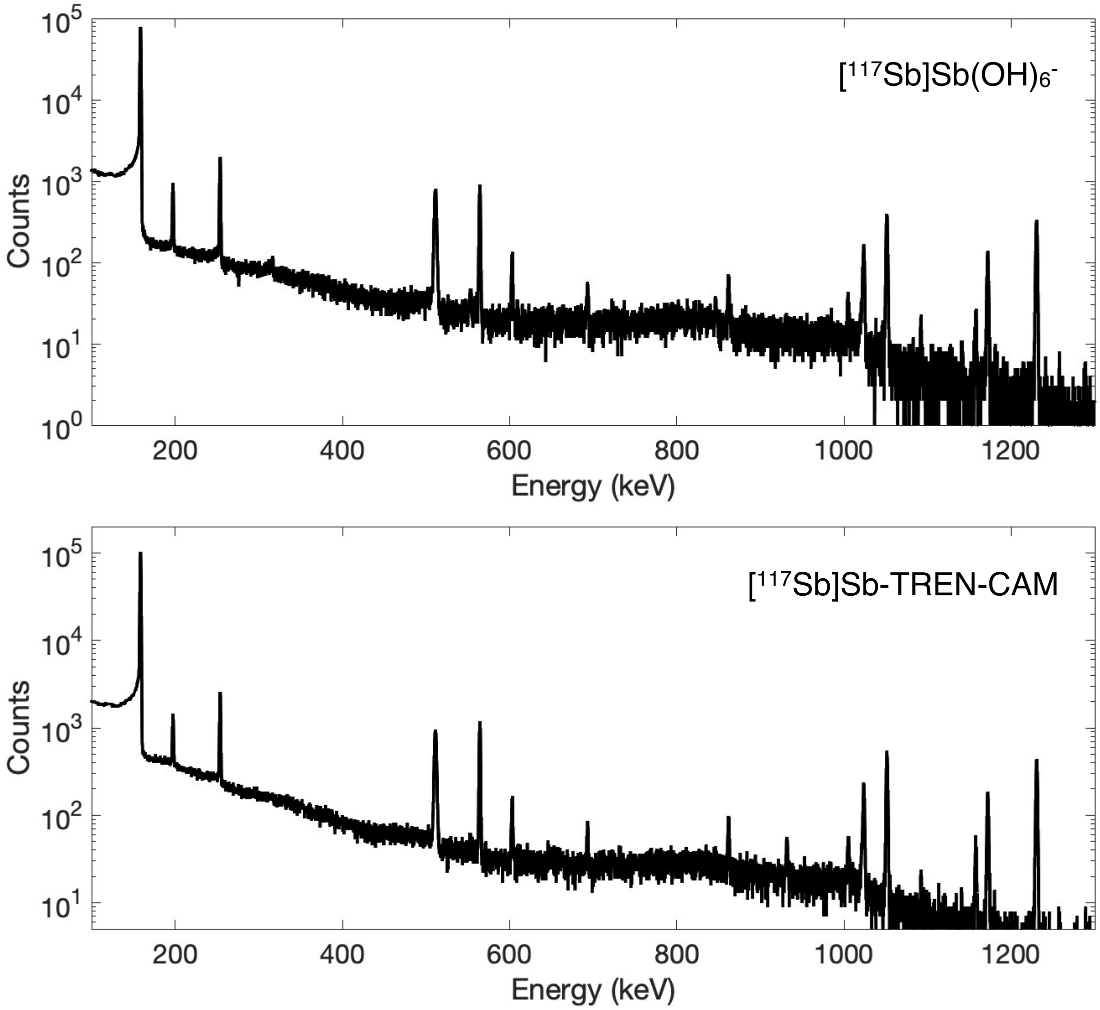

Figure 63: HPGe gamma spectra of injected solutions depicting radionuclidic purity of ^{nat}Sn(d,n)^{117}Sb.

3.5.2. PET and SPECT Phantom Image Characterization

When comparing Derenzo phantom contrast and resolution metrics (**Figure 64**), PET and SPECT had similar contrast with PET achieving slightly poorer resolution as defined by FWHM. Visually, all ∅ 1.2 mm rods are delineated from the SPECT imaging system with only partial PET rod delineation.

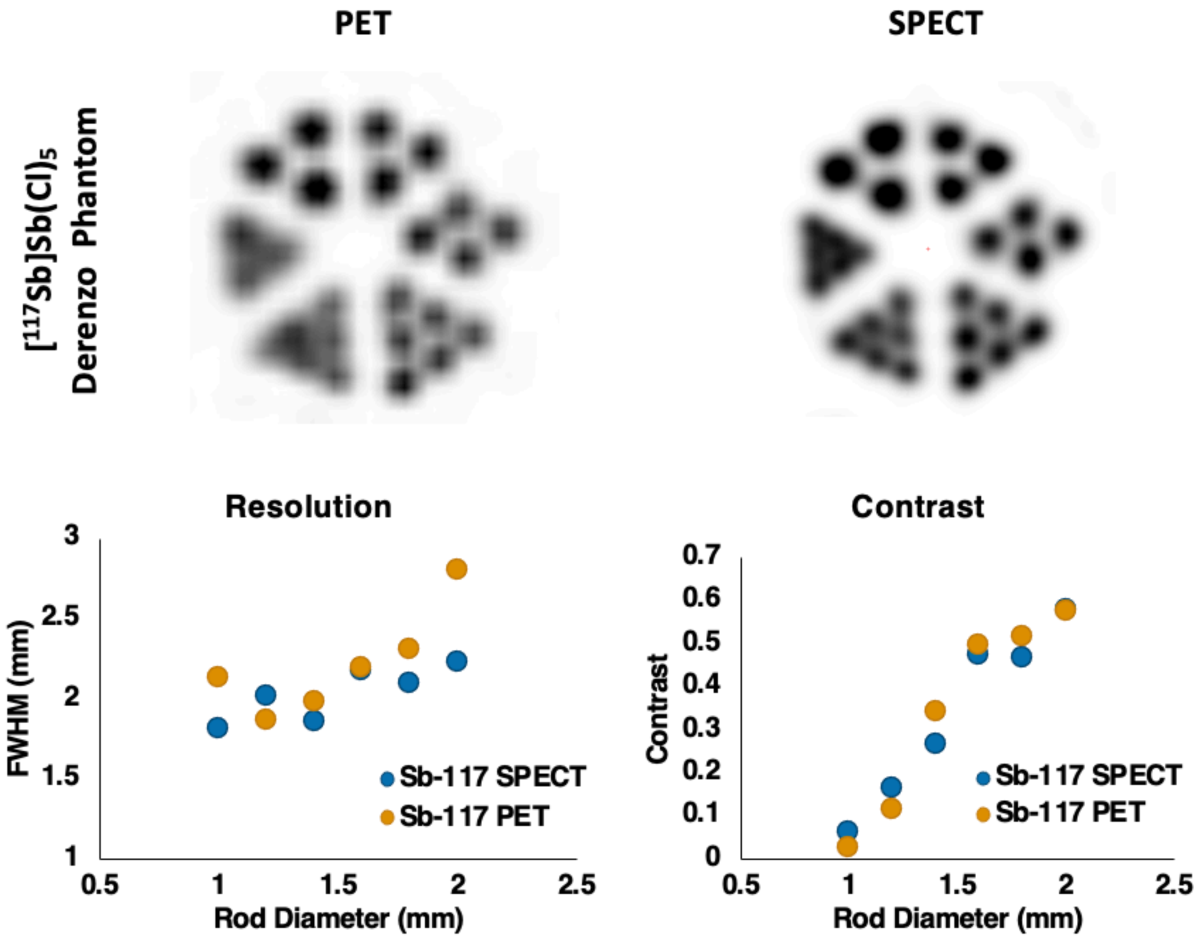

Figure 64: Comparison of ^{117}Sb PET vs. SPECT imaging using contrast and resolution measurement from Derenzo phantom images with rod sizes ∅ 1.0, 1.2, 1.4, 1.6, 1.8, 2.0 mm.

All imaging systems have finite spatial resolution in which voxels do not perfectly align with tissue region boundaries. Limitations of an imaging system's finite spatial resolution and the distance a positron travels before annihilation in PET imaging contribute to an underestimation of tracer activity concentration within small structures in reconstructed PET and SPECT images—referred to as the partial volume effect (PVE). In emission tomography techniques, PVE measures the intrinsic 3-dimmensional 'blurring' of the system, similar to line spread function [216–218].

When small structures and lesions are <3x FWHM, scanner spatial resolution is the primary contributor to PVE [217]. With spatial resolution ~1.5 mm [216], small animal PET scanners are significantly impacted by PVE. Reconstructed PET and SPECT images of ^{117}Sb filled PVE phantom (**Figure 65**) allowed quantification of image derived activity concentrations and subsequent calculation of PVE recovery coefficients.

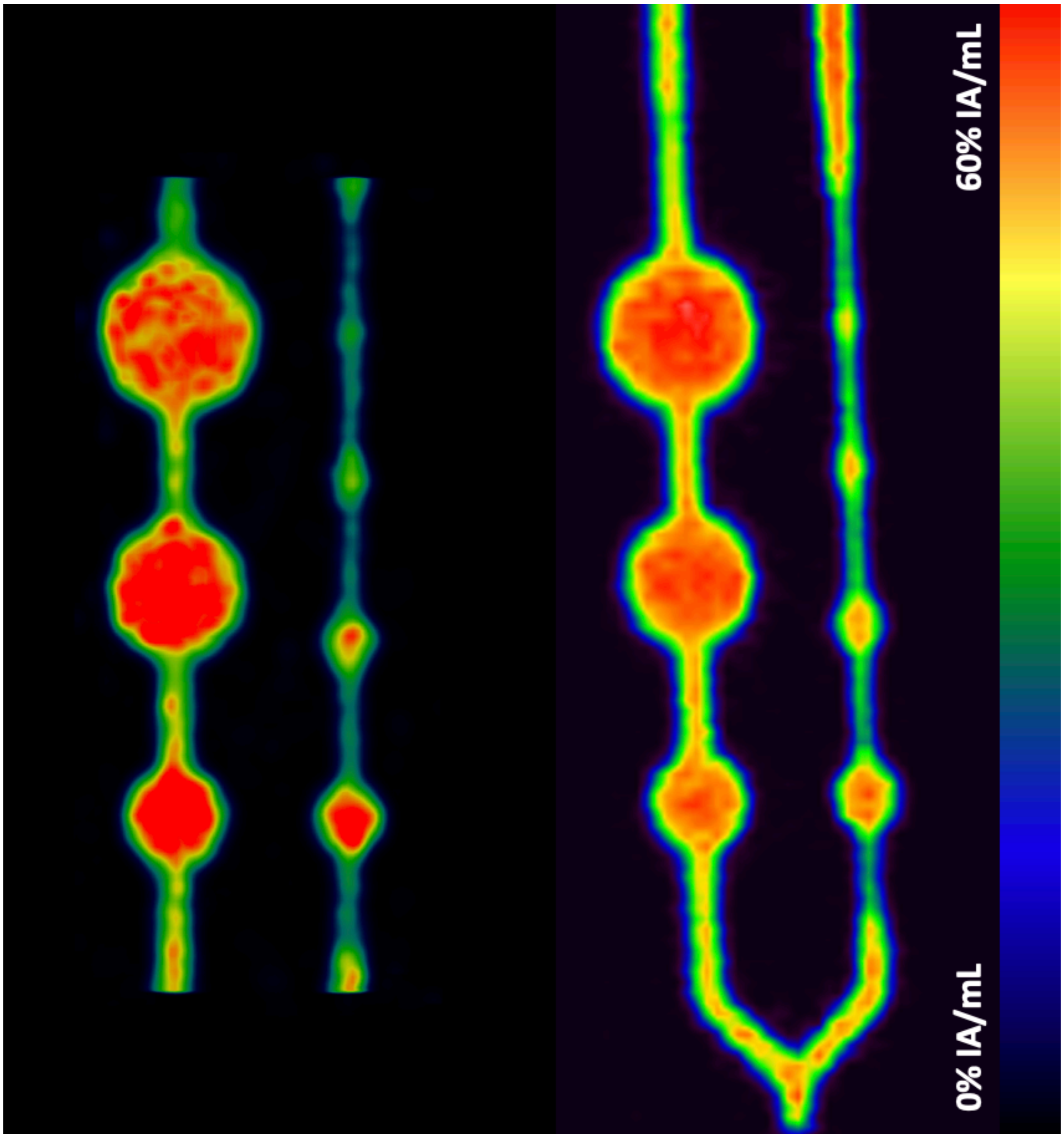

Figure 65: (left) ^{117}Sb SPECT image, (right) ^{117}Sb PET image.

PVE greatly impacted ability to accurately determine ^{117}Sb activity concentration within both PET and SPECT imaging with both modalities having a similar dependance of volume on recovery coefficient (**Figure 66**). PVE recovery coefficient determination allowed correction of image derived biodistributions to match *ex vivo* measurements. With volumes <200 mm^3, a sharp increase in RC is observed for both imaging systems with a significantly lower slope at volume >200 mm^3.

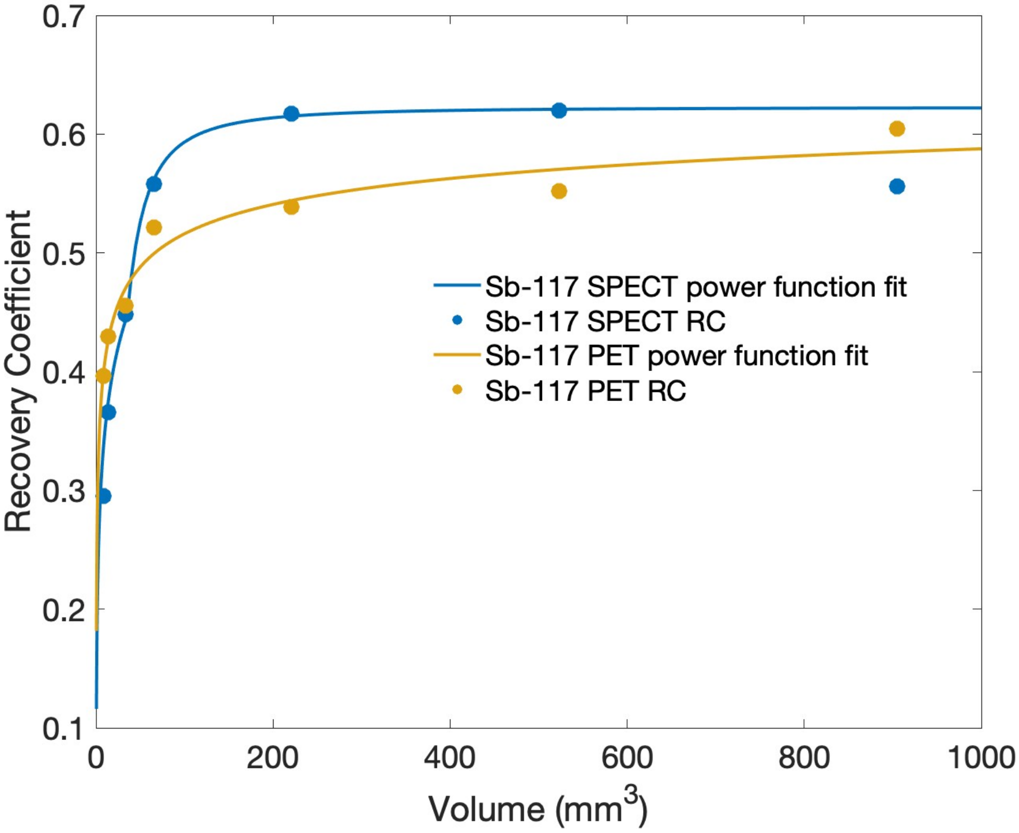

Figure 66: Comparison of ^{117}Sb PET vs. SPECT PVE recovery coefficient measurements from phantom images with power function fits.

3.5.3. *In Vivo* PET and SPECT Image Characterization

Though SPECT and PET show similar resolution and contrast in Derenzo phantom studies (**Figure 64**), ^{117}Sb *in vivo* imaging benefits from PET's greater sensitivity. As observed in both imaging modalities, [^{117}Sb]Sb(OH)$_6^-$ was primarily cleared renally through the kidneys and bladder, with some additional uptake in the liver and, at the early 20-min timepoint, in the gallbladder. However, with its greater sensitivity, PET images also clearly display uptake of [^{117}Sb]Sb(OH)$_6^-$ into the bone (**Figure 67**). By contrast, both PET (**Figure 67**) and SPECT (**Figure 68**) images of mice administered [^{117}Sb]Sb–TREN-CAM show the highest uptake of activity in the gallbladder and intestines, indicating that the complex is predominately excreted via the hepatobiliary pathway. Similar liver uptake and less bladder uptake is observed in comparison to [^{117}Sb]Sb(OH)$_6^-$. Additionally, negligible activity was taken up by the bone.

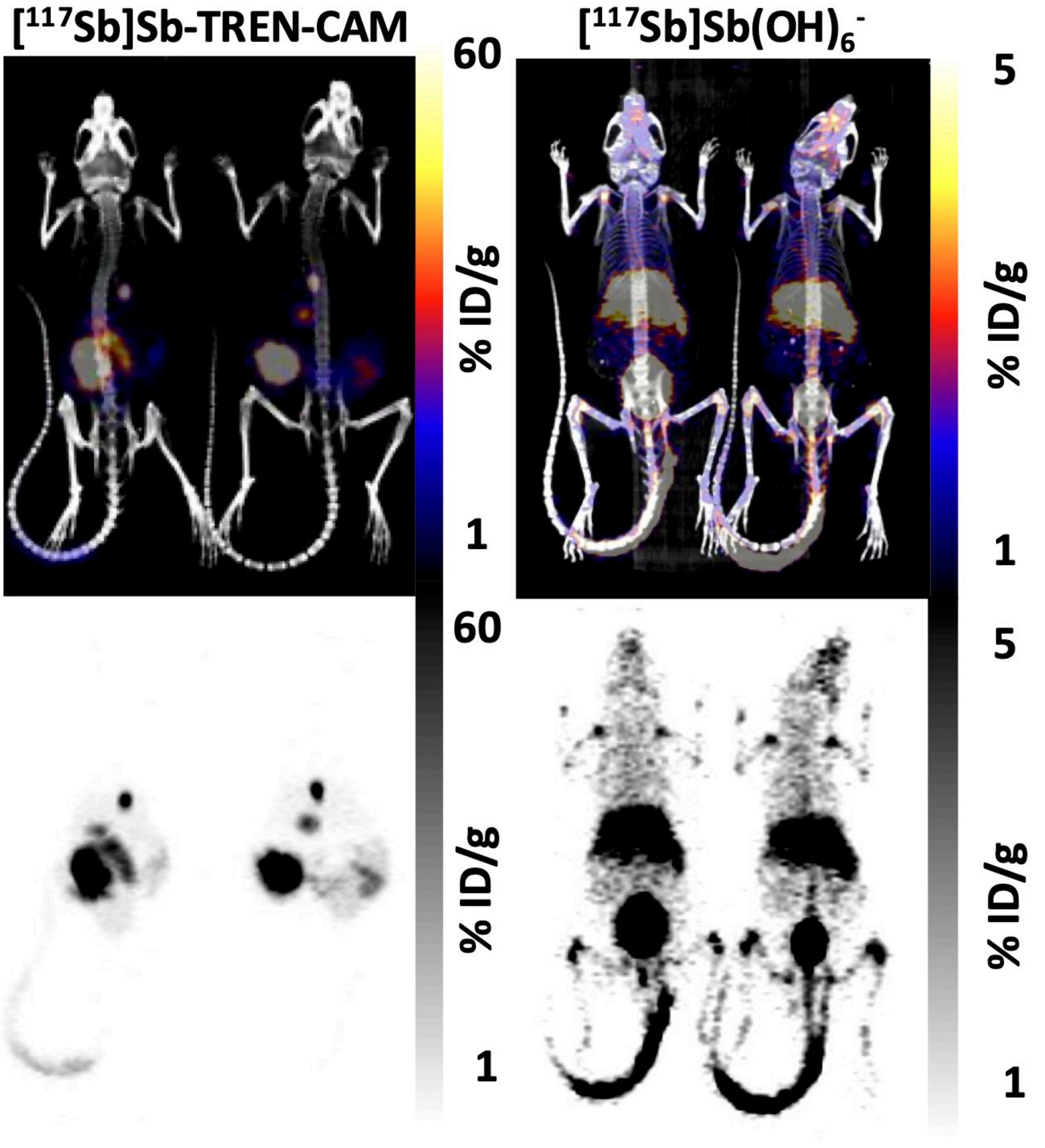

Figure 67: Maximum intensity projection μPET/CT fused images (top two images) and grayscale μPET images (bottom two images) of mice collected at 150-min p.i. of [^{117}Sb]Sb–TREN-CAM (left two images) or [^{117}Sb]Sb(OH)$_6^-$ (right two images).

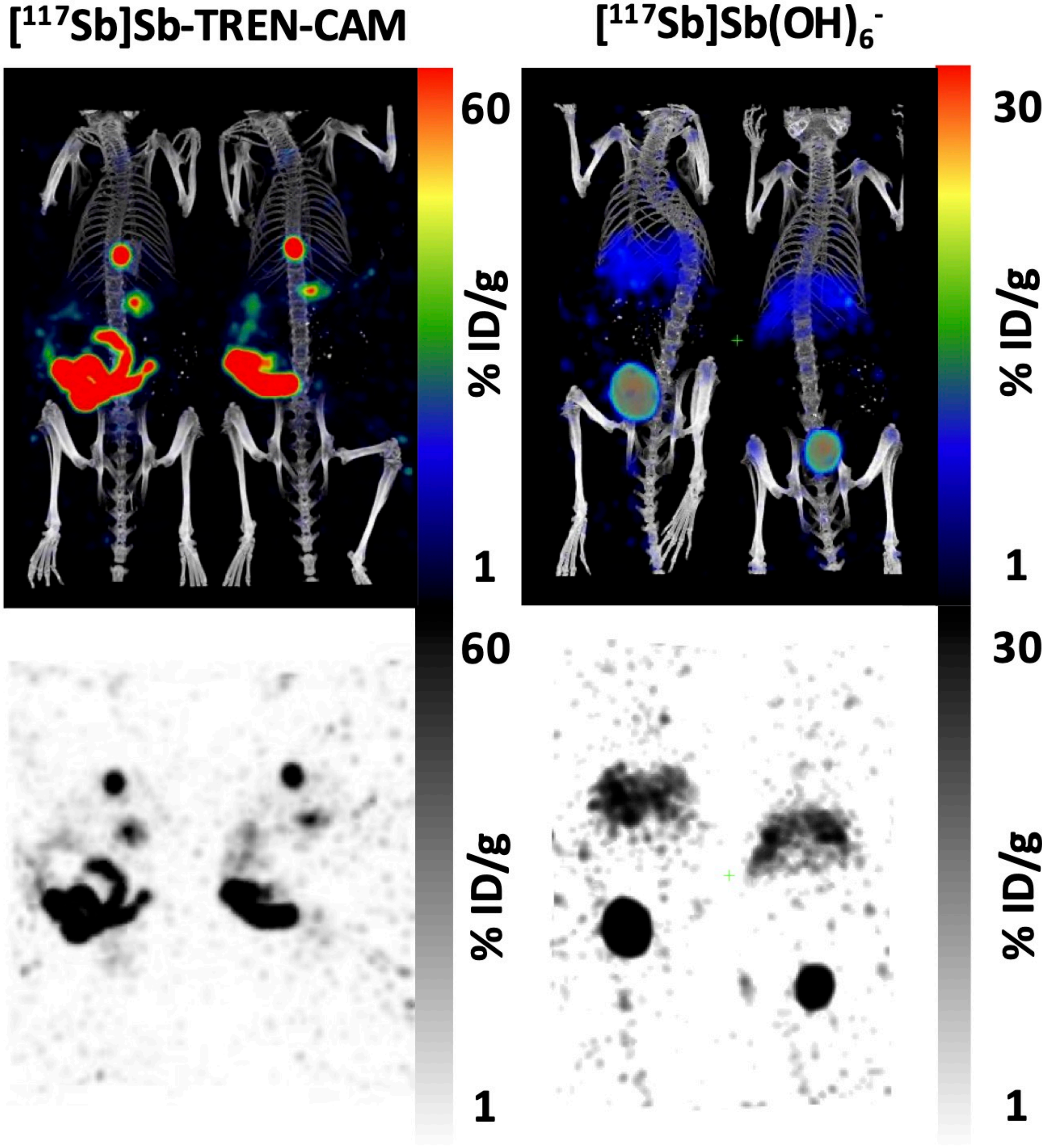

Figure 68: Maximum intensity projection μSPECT/CT fused images (top row) and grayscale μSPECT images (bottom row) of mice collected at 90-min p.i. of [^{117}Sb]Sb–TREN-CAM (left images) or [^{117}Sb]Sb(OH)$_6^-$ (right images).

3.5.4. *Ex vivo* Biodistribution and Metabolite Analysis

We conducted *Ex vivo* biodistribution analysis following euthanasia of mice 5 h p.i. with measurements confirming *in vivo* imaging observations (**Figure 69**) – lower bone and spleen uptake and higher intestinal and gallbladder uptake for mice administered [^{117}Sb]Sb–TREN-CAM versus [^{117}Sb]Sb(OH)$_6^-$. These results match previously reported trends in inorganic antimony organ accumulation [199,200,203,204]. Image derived biodistributions (**Figure 68**) show [^{117}Sb]Sb(OH)$_6^-$ clearing quickly from the gallbladder and high uptake of [^{117}Sb]Sb-TREN-CAM within the intestines and gallbladder, confirming suspected hepatobiliary clearance from the gallbladder into intestines.

In a separate study, the gallbladders were excised from mice 30 min p.i. of [^{117}Sb]Sb–TREN-CAM. Gallbladder contents were collected and analyzed by radio-TLC. Metabolized gallbladder contents migrated with an $R_f = 0.752 \pm 0.045$ ($N = 3$, uncertainty expressed as standard deviation of measurements), which is similar to the $R_f = 0.811 \pm 0.005$ ($N = 3$) for unmetabolized [^{117}Sb]Sb-TREN-CAM (**Figure 70**). These results, in conjunction with the markedly different clearance routes of free versus complexed ^{117}Sb revealed by the imaging studies, suggest that the [^{117}Sb]Sb-TREN-CAM complex remains intact over the time course of the study. Thus, these findings mark the first observation of a stable radio-Sb complex *in vivo*. Furthermore, the success of SPECT and PET imaging with ^{117}Sb highlight this radioisotope as a promising diagnostic partner to ^{119}Sb.

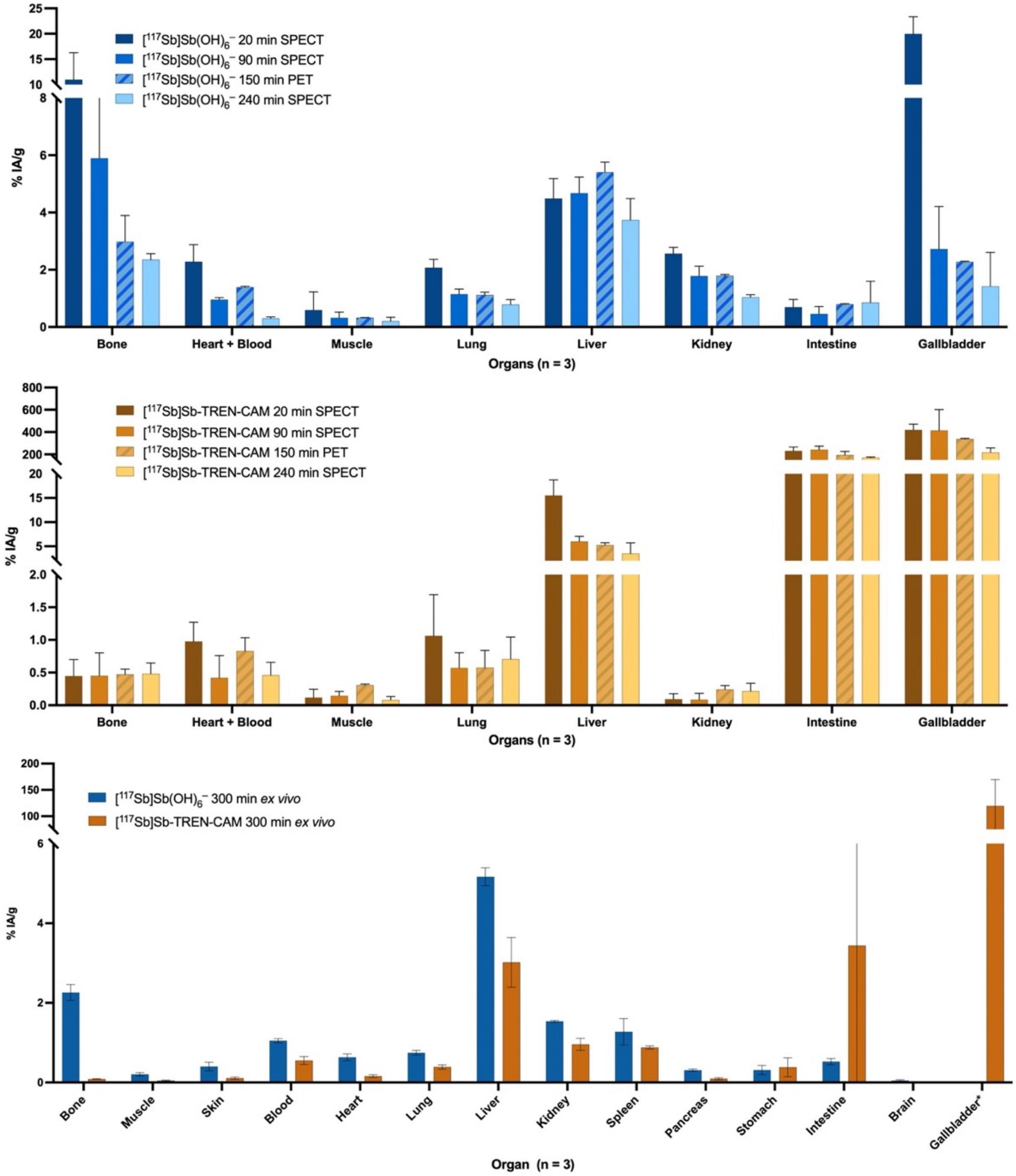

Figure 69: Comparison of organ biodistributions of [^{117}Sb]Sb–TREN-CAM (yellow) and [^{117}Sb]Sb(OH)$_6^-$ (blue) over time following intravenous injection in mice. µSPECT and µPET image-derived temporal *in vivo* biodistribution of [^{117}Sb]Sb(OH)$_6^-$ (top) and [^{117}Sb]Sb–TREN-CAM (middle). *Ex vivo* biodistribution of both radiotracers (bottom).

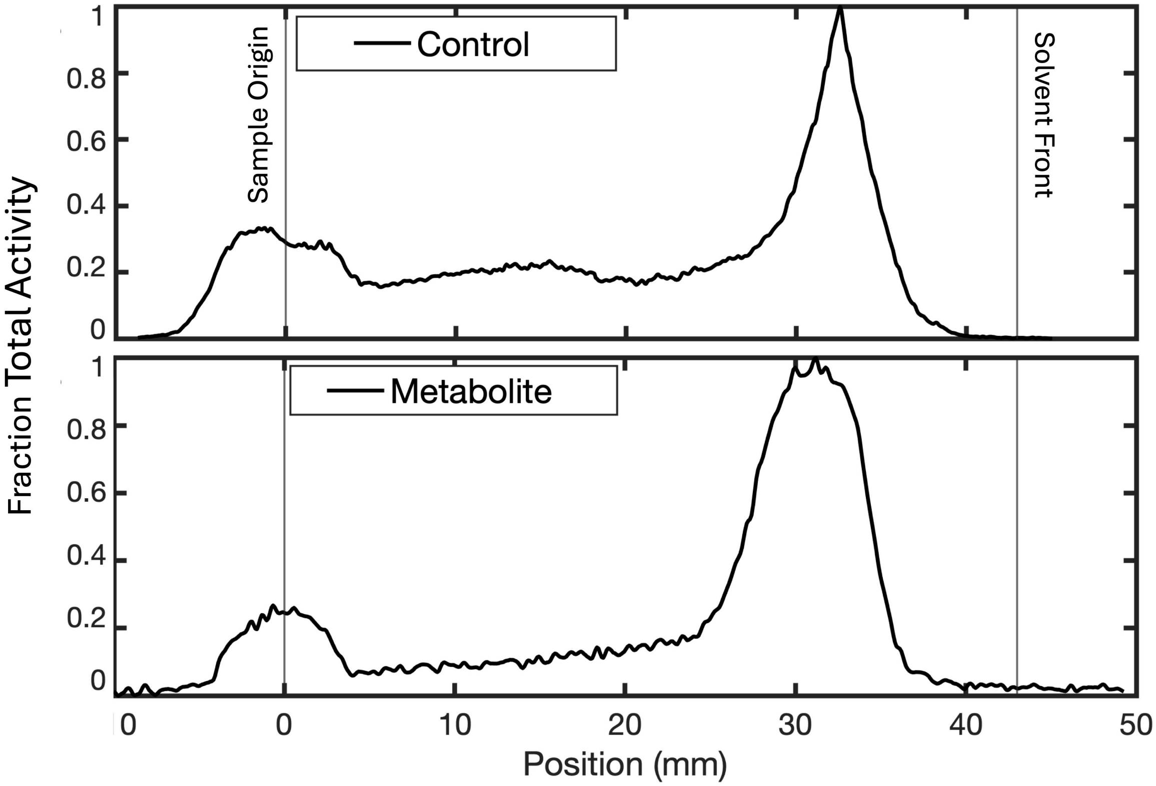

Figure 70: Representative radio-TLC of [^{1XX}Sb]Sb-TREN-CAM mouse metabolite analysis using Al-backed Si stationary phase and MeOH mobile phase, where [^{1XX}Sb]Sb–TREN-CAM moves near the solvent front. Control sample was injected fraction of [^{1XX}Sb]Sb–TREN-CAM in PBS pH 7.5. Metabolite fraction was a MeOH wash of *ex vivo* excised gallbladder contents.

3.6. Radiolabeling DUPA Conjugated TREN-CAM in MeOH/DMSO.

A single radioactive complex with R_t = 20.5 min (**Figure 71**) was created, and ^{1XX}Sb fully labeled. This represents a unique retention time and is promising support for the creation of a targeted radioantimony complex. We suspect the increased baseline signal R_t = 17.5—22.5 min being due to radiolysis. Further non-radioactive characterization is required to confirm identity as

[^{1XX}Sb]Sb-TREN-CAM-DUPA before stability and targeting property retention testing.

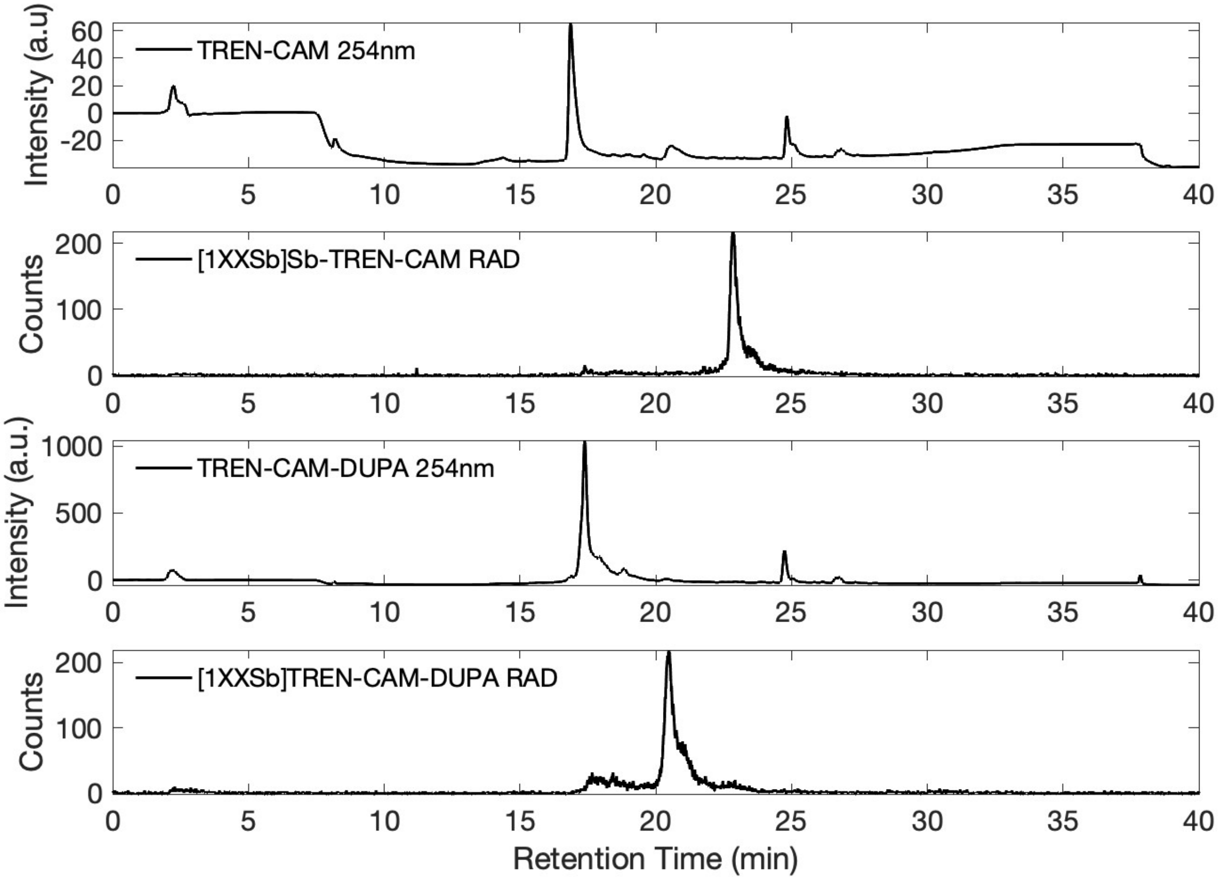

Figure 71: HPLC of TREN-CAM and TREN-CAM-DUPA ^{1XX}Sb radiolabeling using **UW-Madison radio-HPLC method B**. Instrument: Agilent 1260 II system (Santa Clara, CA) with Ortec (AMETEK ORTEC, Oak Ridge, TN) detector. Column: 150 mm C_{18} Jupiter column (Phenomenex, Torrance, CA). Flow rate: 1 mL/min. Solvents: A = 0.1 M ammonium citrate (pH 4.5), B = 0.1% TFA/H_2O, C = 0.1% TFA/MeCN. Method: 0–5 min: 100% A; 5–10 min: 95% B / 5% C; 10–30 min: linear ramp to 5% B / 95% C; 30–35 min: 5% B / 95% C; 35–36 min: linear ramp to 95% B / 5% C; 36–40 min, 100% A.

4. Conclusions

Herein, we report the complexation of n.c.a., high specific activity radioantimony (^{1XX}Sb) in the +5 oxidation state by the tris-catecholate ligand TREN-CAM. Our studies show that TREN-CAM can quantitatively complex ^{1XX}Sb(V) in aqueous and organic solutions within 60 min at pH 2–6 and 80 °C. Uniform speciation of Sb(TREN-CAM)]$^-$ is formed when using LLE produced ^{1XX}Sb and MeOH/DMSO solvents. Spectroscopic studies support the formation of a hexacoordinate complex in which all 6 phenolate donor atoms of TREN-CAM interact with an Sb(V) center. The [^{1XX}Sb]Sb–TREN-CAM complex displays high stability over the course of several days when challenged with human serum. These results establish TREN-CAM as the first chelator capable of stabilizing radioantimony(V) *in vivo*.

We achieved the first *in vivo* imaging of BFC complexed antimony and used it to study [^{117}Sb]Sb-TREN-CAM complex stability. Despite its small 1.81 *11 %* β^+ branching ratio, ^{117}Sb produces quantifiable PET images in mice up to at least 2.5 h p.i. with injected activities as low as 4.5 MBq ± 0.1 MBq (121 µCi ± 3 µCi) ^{117}Sb. Dramatically different biodistribution profiles between mice administered [^{117}Sb]Sb(OH)$_6^-$ and [^{117}Sb]Sb–TREN-CAM support the conclusion of high *in vivo* [^{117}Sb]Sb–TREN-CAM complex stability. PET and SPECT images of ^{117}Sb provide similar contrast measurement with SPECT images achieving slightly higher resolution.

Chapter 5: Conclusions and Future Directions

Therapeutic applications of ^{119}Sb, a most promising CE/AE-emitting radionuclide, have been limited to *in silico* study due to barriers in production, chemical isolation, target material recycling, and stable complexation with chelators capable of conjugation to a targeting moiety. We have worked to overcome these barriers, allowing future characterization and applications of a targeted ^{119}Sb radiopharmaceutical for ^{119}Sb CE/AE dosimetry and cell killing potential.

Chapter 2 is written as a practical guide to increase accessibility, availability, and exploration of $^{119/117}$Sb theranostics through reporting methods for tin target synthesis, $^{119/117}$Sb production via charged particle irradiation, chemical separation to purify radioantimony from tin, and isotopically enriched Sn target material recycling. By adapting electrodeposition methods from [136], metallic, thermally and electrically conductive tin targets were created with thicknesses >400 mg (800 mg/cm^2). A 16 MeV proton (energy achieved using a GE PETtrace) will penetrate approximately 600 mg/cm^2 (CSDA range [219]) or 825 μm into tin of theoretical metallic density (7.31 g/cm^3 [220]). Using reported methods, we can make thick targets capable of absorbing the entirety of a 16 MeV proton's energy. This represents a factor of 53x [53] and 28x [108] increase in electroplated tin target thickness as compared to previously reported methods. Because of the low melting temperature of tin (232 °C [220]), our targets had a maximum beam tolerance of 35 μA. Future work could re-design targets and target fabrication techniques to increase beam tolerance. One such strategy is electroplating a tin alloy. Tin readily co-electroplates with many transition metals (e.g. Cu, Ni, Zn) [221–223], and when designing accelerator targets with low melting temperatures, alloys improve beam tolerance [132,224]. A thoughtfully chosen co-deposited metal could increase melting temperature without competing with radioantimony for chelator complexation, which would decrease AMA. Also, chemical separation and enriched material recycling strategies may need to be modified to accommodate an additional metal contaminant. Spark plasma sintering (SPS), a technology recently available in the UW-Madison cyclotron group, creates ceramics and densifies intermetallic elemental combinations [225,226]. This technique uses heat, high pressure, and high electrical current to fabricate powders into a solid mass [226]. A tin oxide ceramic could be explored, particularly for Sn(IV) recycling. Being the only reported recycling of Sn(IV) targets in the literature, [90] recycled 75% of Sn(IV) target material at thicknesses of 12-15 mg/cm^2. SPS target fabrication from tin(IV) oxide could recycle enriched Sn(IV) from separation chemistries such as LLE at greater target thicknesses than previously achievable. Because of the presence of oxygen atoms, tin atom density in the target will be lower than electroplated targets, impacting yields. With a melting point of 1127 °C [227], tin(IV) oxide could withstand higher beam currents, which could compensate for lower atomic density.

Radionuclide production is greatly influenced by variables including particle type, particle energy, target thickness, target isotopic composition, and target physical and chemical properties. Changing these parameters will modify the resulting distribution of radionuclides produced. When using ^{nat}Sn target material, we produced remarkably different yields of radioantimony isotopes when bombarding targets with 16 MeV protons or 8 MeV deuterons. Bombarding thick targets with 16 MeV protons produced a greater proportion of longer lived, higher energy gamma-emitting radioisotopic impurities, which are convenient antimony radiotracers for benchtop research and development.

Recently, a mouse therapy study using the AE-emitting radionuclide ^{58m}Co observed complete remission in 1 of 6 mice when administering two 144 MBq (3.4 mCi) doses of [^{58m}Co]Co-DOTA-PSMA-617 [228]. AE-emitter specific dosimetry and therapeutic treatment activities are not conclusively known, but using this recent study as a surrogate, preclinical studies will require gigabecquerel level ^{119}Sb productions. Preclinical quality productions should maximize radionuclide purity (> 90%) while minimizing long-lived contaminants to aid in radiation waste handling. Clinical quality productions generally employ >99.9% radionuclidic purity, depending on contaminant emissions and half-life [229].

Production of preclinical quality (98.6% ± 0.3% radionuclidic purity at EOB) and quantity (27 MBq/μAh ± 9 MBq/μAh) ^{119}Sb was achieved with thin, 80-114 mg/cm^2, 96.3% isotopically enriched ^{119}Sn targets irradiated at 35 μA with 12.5 MeV protons, the greatest reported measured physical yield of radionuclidically pure ^{119}Sb. We measured ^{119}Sb activities and yields through developing a low energy (23.87 keV) photon detection method.

Production of preclinical quality and quantity ^{117}Sb implemented deuteron bombardment of ^{nat}Sn targets, producing physical yields of 24 MBq/μAh ± 3 MBq/μAh at 92% ± 2% radionuclidic purity at EOB. Preclinical mouse imaging studies require tens of megabecquerel radionuclide quantities. With 16 MeV protons, the ^{117}Sn(p,n)^{117}Sb nuclear reaction is worth exploring to increase radionuclidic purity beyond 92%. Although pre-clinical quality ^{117}Sb can be produced via ^{nat}Sn(d,n)^{117}Sb, clinical quantity and quality ^{117}Sb would require isotopically enriched targets, applying ^{116}Sn(d,n)^{117}Sb or ^{117}Sn(p,n)^{117}Sb nuclear reactions. Although the half-life of ^{117}Sb is shorter than ^{119}Sb (2.80 *1* h vs 38.19 *22* h) [71,72], ^{117}Sb may be a theranostic surrogate for ^{119}Sb with fast clearing antimony radiopharmaceuticals. Additionally, measured cross sections for the nuclear reaction ^{118}Sn(d,n)^{119}Sb do not exist. Future work should explore production via this route as isotopically enriched ^{118}Sn is cheaper than isotopically enriched ^{119}Sn.

With 20 – 30 MeV protons or 15 – 25 MeV alphas, researchers could produce ^{119m,g}Te and study ^{119m,g}Te/^{119}Sb generator development. Between these energy ranges, ^{121}Sb(p,3n)^{119m,g}Te and

^{116}Sn(α,n)^{119m,g}Te nuclear reactions have similar cross section intensities, with (α,n) potentially 2x greater [98,102–104] than (p,3n). Currently, 30 MeV proton accelerators exist with greater availability than 25 MeV alpha machines, many of which are multiparticle machines [113]. As an element with two fewer protons than tellurium, tin has a greater chemical difference from tellurium than antimony, which will allow development of a chemical separation strategy with a higher separation factor. Also, the (α,n) production route does not have as many overlapping reaction cross sections as compared to 20 – 30 MeV protons. Although, due to ^{119m,g}Te's high energy emissions, a ^{119m,g}Te/^{119}Sb generator has unavoidable shielding problems, generators increase radionuclide accessibility. After increasing ^{119m,g}Te production, a Te/Sb generator could be developed as designs reported in literature need increased ^{1XX}Sb elution yields, increased eluted ^{119}Sb radionuclidic purity, and decreased ^{1XX}Te breakthrough.

This work reports two chemical separation strategies—a column chromatography technique separating Sb(III)/Sn(II) and a liquid-liquid extraction technique separating Sb(V)/Sn(IV). The column chromatography technique achieves RCY 73.1% ± 6.9% (N = 3), decontaminates Sn by a factor of (6.8 ± 5.5) x 10^5 (N = 3), radiolabels chelators explored in both chapter 3 and chapter 4, and allows recovery and recycling of enriched target material. We developed methods for creation and recycling of enriched ^{119}Sn targets, having 86.9% ± 7.8% (N = 12) natural tin target material recycled and 11.6 mg ± 0.8 mg (N = 6) losses of 96.3% enriched ^{119}Sn. An extension of this work includes developing Sn(IV) recycling methods, potentially using reducing agents prior to Sn precipitation and conversion of Sn(II) into the sulfuric acid based electrolytic solution.

Chemical separation, recycling methodology, and chelator development would all benefit from greater exploration and understanding of antimony speciation chemistry, specifically in aqueous, oxic conditions. Variables such as time, heat, exposure to atmosphere, oxidation state, pH, and water confounded many Sb productions. Antimony chemistry, its delicate. More resin constructs should be explored for Sb/Sn separation. In the Sb(III)/Sn(II) column chromatography separation method reported in Chapter 2, ^{1XX}Sb is released from the thiol column through destroying the resin, letting thiol resin fragments contaminate eluted radioantimony. Development of a different thiol resin which could release Sb without resin destruction would prevent final product thiol fragment contamination, which could interfere with radioantimony complexation. Also, the manual liquid-liquid separation technique varies in quality of produced radioantimony. Ether inspired functionalized resin constructs are currently under development in other research groups, and additional work into Sb(V)/Sn(IV) column chromatography separation chemistry development could increase RCY, increase Sn separation factor, decrease Sb(V) elution volumes, and produce ^{1XX}Sb in solution matrices compatible with radiolabeling. Both separation chemistries could benefit from automation by increasing reliability and decreasing user dose.

Chapter 3 explored application of the trithiol chelator for first reported stable radioantimony chelation. We measured high [^{1XX}Sb]Sb-trithiol-diacid complex stability over 72 h in both 25 mM cysteine (91% ± 9% (N = 3)) and FBS (97.5% ± 1.6% (N = 3)). After conjugation of the trithiol chelator to a targeting moiety, radioantimony complex stability decreased. In PBS, [^{1XX}Sb]Sb-trithiol-RM2 had 3.0% of the complex intact at 16 h, and 5.5% of [^{1XX}Sb]Sb-trithiol-Olaparib was intact after 24 h in PBS. The larger RM2-functionalized moiety degraded faster than smaller Olaparib-functionalized moiety. The larger conjugated group could withdraw electron density from thiol functional groups, leading to decreased covalent bond strength and complex vulnerability. Thiol based chelation of Sb(III) encourages design of different thiol chelators. The conjugated trithiol radioantimony complexes were stable in EtOH for 24 h, yet they fell apart after

24 h in PBS, possibly from hydrolysis-driven instability. In the antimony trithiol chelator structure, antimony was attracted to thiol functional groups but released from a protective pocket. A thiol-based chelator with macrocyclic structure or protective arms to wrap around the metal core could help prevent hydrolysis. Binding the exposed lone pair might prevent it from interacting with external chemical moieties and increase complex stability.

The trithiol chelator was originally designed and developed for stable complexation of radioarsenic. With the chemical similarities of arsenic and antimony and limited antimony radioisotopic imaging analogues, we hypothesize application of radioarsenic for ^{119}Sb theranostics. Arsenic-72 ($t_{1/2}$ = 26.0 *1* h, β^{+} = 1117.0 *19* keV, $I_{\beta+}$ = 64.2 *14 %*) [230] emits positrons and has half-life more similar to that of ^{119}Sb than ^{117}Sb. For longer circulating radiopharmaceuticals, ^{72}As could be an imaging surrogate. Chapter 3 measured different $\log D_{7.4}$ values for [^{1XX}Sb]Sb-trithiol-RM2 (-1.80 ± 0.05 (N = 3)) than reported for [^{77}As]As-trhithiol-RM2 (-1.26 ± 0.05 [184]), but comparative biodistribution experiments are required to discern biological implications of $\log D_{7.4}$ differences.

In chapter 4, TREN-CAM stably chelated radioantimony from the 5+ oxidation state, as seen through serum stability and *in vivo* imaging studies. This labeling represents the first Sb(V) complexation with a BFC and subsequent conjugation. Speciation studies determined that first, a hydrolyzed compound formed ([^{1XX}Sb]Sb(H_2TREN-CAM)($OH)_2$), which, with added time and temperature, converted to ([^{1XX}Sb]Sb-TREN-CAM) in organic solvent. As conjugation of the trithiol-diacid to the targeting moiety decreased radioantimony complex stability, the stability of a radioantimony-labeled TREN-CAM conjugated drug complex needs to be assessed.

After verification of stability and retention of target binding of ^{119}Sb-TREN-CAM targeted moieties, researchers can conduct work exploring the biological applications of ^{119}Sb. For decades at this point, ^{119}Sb has been promised as an influential cell killing CE/AE-emitting radionuclide, and development of a stable radioantimony labeled targeted molecular construct will open exploration of dosimetry questions. Is this most promising CE/AE-emitting radionuclide capable of effective cell killing when targeted to locations outside the nucleus? Do all AE-emitting radionuclides need to be delivered to the DNA to cause a biological cell killing effect? A targeted ^{119}Sb radiopharmaceutical will become a tool for not only dosimetric analysis of cell killing potential but also for exploration of low energy electron-emitting radiopharmaceutical therapy specific biological response.

Experiments with ^{119}Sb radiopharmaceuticals can compare dosimetry and cell killing efficacy when 1) targeting differing regions of the cell (e.g., nucleus, cytoplasm, cell wall), 2) targeting the same cellular regions with radionuclides that emit differing particles (e.g., CE/AE, β^-, α), or 3) targeting the same regions with AE-emitting radionuclides with different emitted electron energy spectra. In all examples, researchers should record cellular response to radiation including monitoring DNA lesion formation, DNA gene expression and upregulation, and cell signaling molecule production (e.g., ATP for cell viability and cytochrome C signaling apoptosis). Experiments detailing AE-emitter cellular response will educate future therapeutic radiopharmaceutical design choices, helping create more effective therapeutic radiopharmaceuticals. Combination therapies administering differing activities and pairings of β^-, α, and CE/AE-emitters is another application of a targeted ^{119}Sb moiety.

We produced ^{117}Sb with suitable activity and radionuclidic purity for *in vivo* mouse imaging to assess *in vivo* complex stability. To our knowledge, this represents the first *in vivo* SPECT imaging of radioantimony (^{117}Sb) and the first useful *in vivo* PET imaging of a radioantimony compound. Although previously only reported as a SPECT imaging agent, we show that PET imaging of ^{117}Sb provides similar image metrics as SPECT, and *in vivo* ^{117}Sb imaging benefits from PET's greater sensitivity. Future work will target a cancer disease model with an ^{117}Sb radiopharmaceutical—a first ever achievement.

TREN-CAM chelates other radiometals (^{68}Ga [209], ^{45}Ti [211]), and any with half-lives greater than that of ^{117}Sb should be explored as a theranostic imaging analogues to ^{119}Sb. If found to chelate arsenic, combination and comparative dosimetry studies between ^{119}Sb and the β^- emitting arsenic radioisotope ^{77}As ($t_{1/2}$ = 38.79 *5* h, β^- = 228.8 *7* keV, $I_{\beta+}$ = 97.0 *3* %) [231] would be interesting future work. The future of ^{119}Sb radiotherapy and radiobiology application is vast with innumerable interesting ideas and applications to explore.

Appendix A: Chapter 3 Data

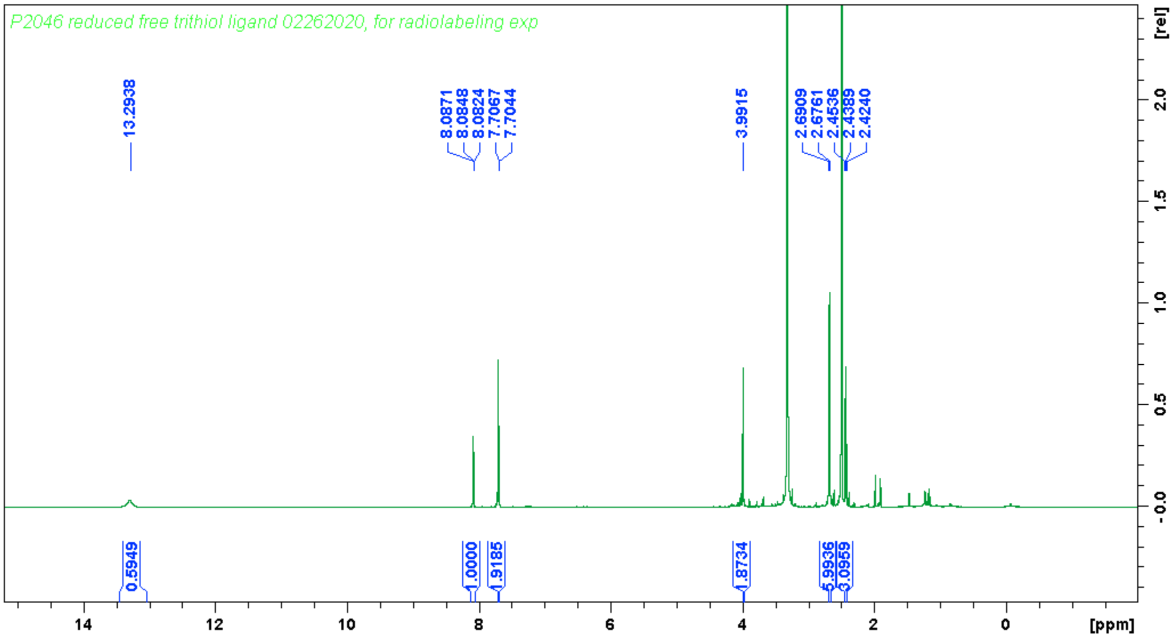

Figure A1: ^{1}H-NMR spectrum of 5-(3-mercapto-2,2-bis(mercaptomethyl)propoxy)isophthalic acid [$C_{13}H_{16}O_5S_3$], deprotected trithiol-diacid, in d$_6$-DMSO.

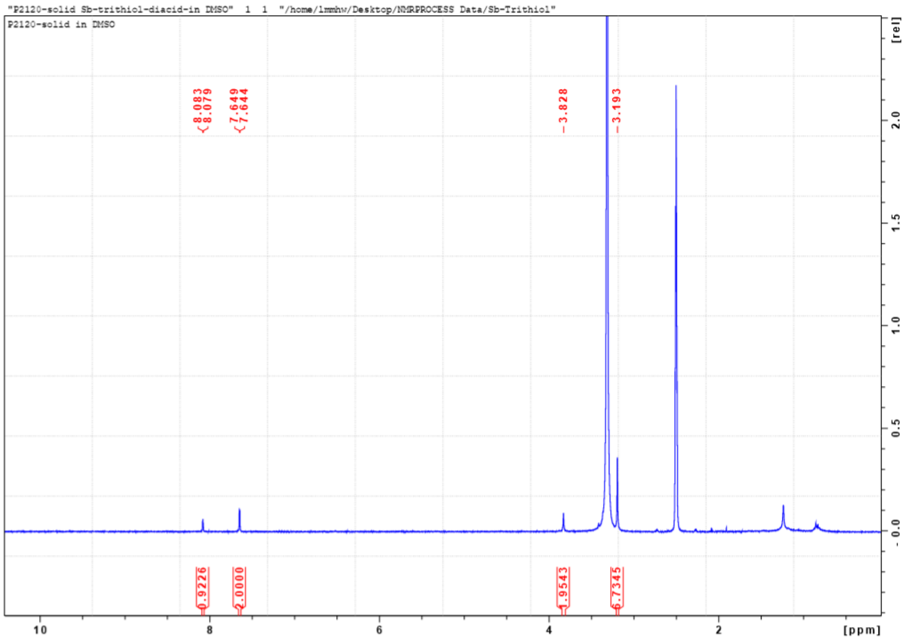

Figure A2: ^{1}H-NMR spectrum of 5-((2,6,7-trithia-1-stibabicyclo[2.2.2]octan-4-yl)methoxy)isothalic acid, Sb-trithiol-diacid, in d$_6$-DMSO

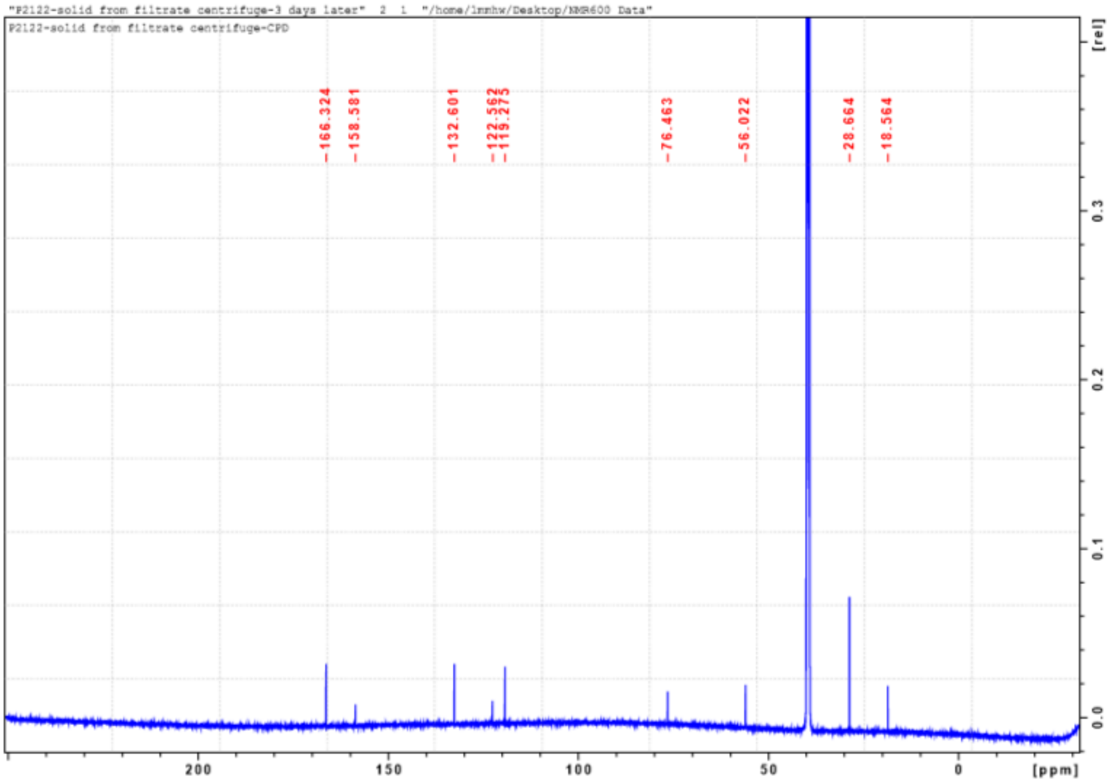

Figure A3: ^{13}C NMR spectrum of Sb-trithiol-diacid in d_6-DMSO

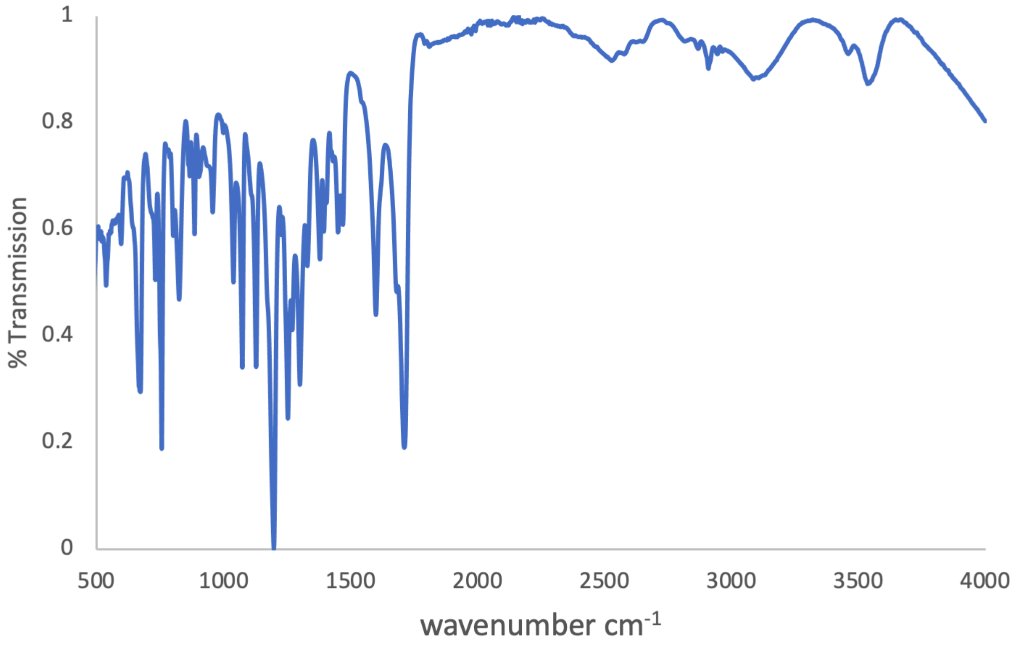

Figure A4: IR spectrum of Sb-trithiol-diacid

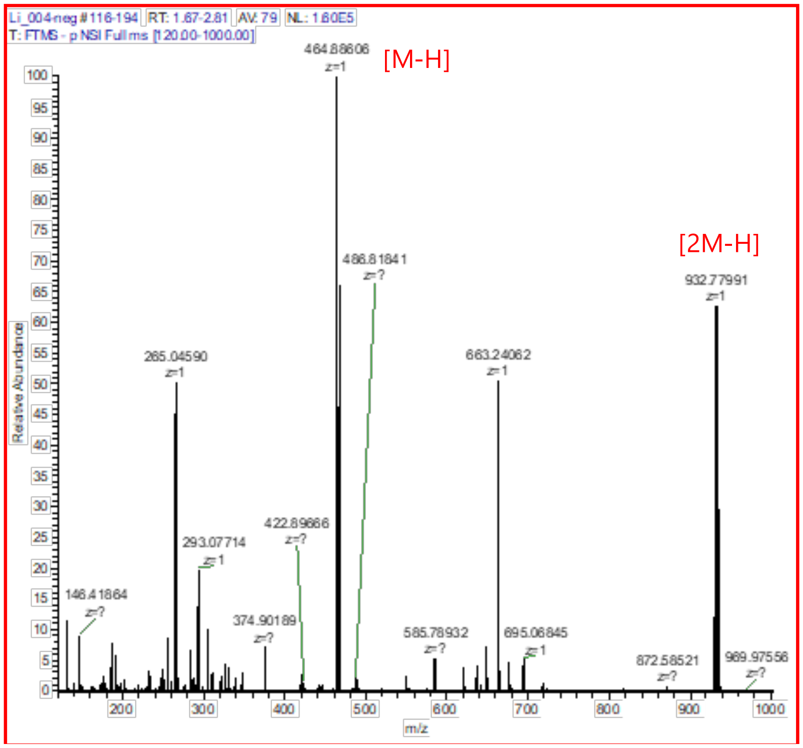

LM04

Negative mode

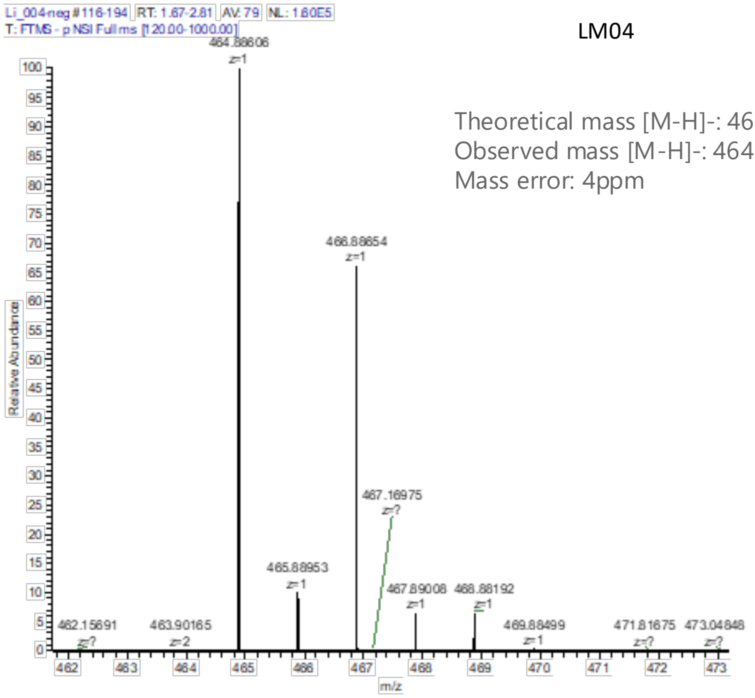

LM04

Theoretical mass [M-H]-: 464.88795 u
Observed mass [M-H]-: 464.88606 u
Mass error: 4ppm

Figure A5: HRMS results for Sb-trithiol-diacid

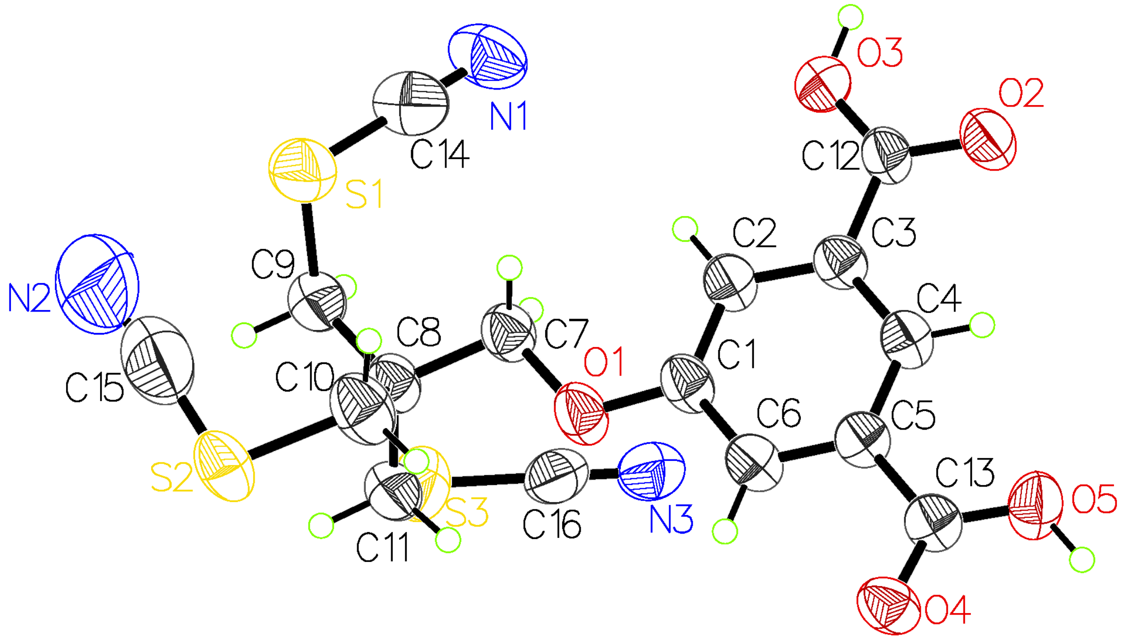

Figure A6: X-Seed representation of **1.** Labeled 50% ellipsoid plot of formula/asymmetric unit (CCDC #2071806)

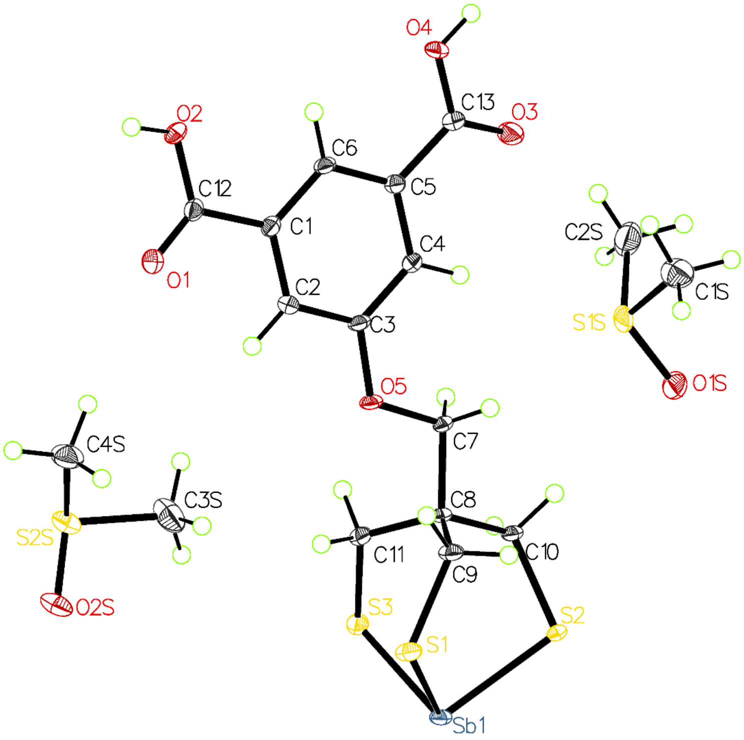

Figure A7: Crystal structure for Sb-trithiol-diacid Labeled 50% probability ellipsoid plot of formula unit. (CCDC #2071807)

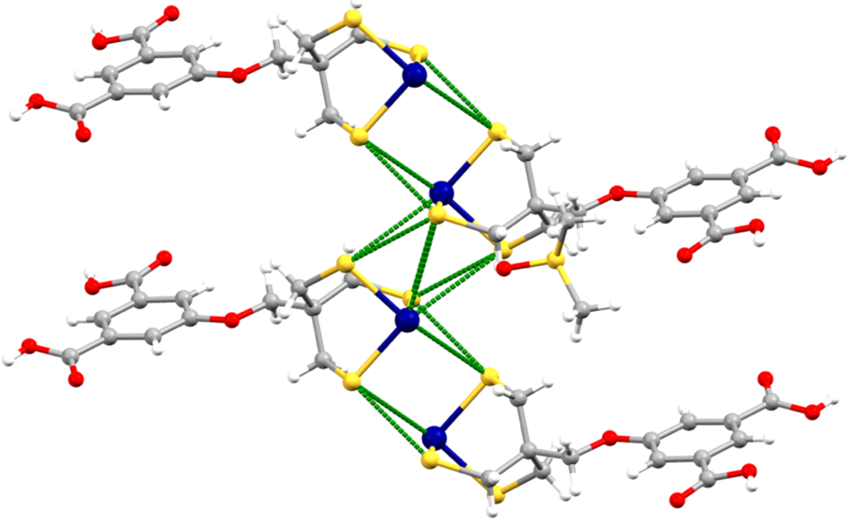

Figure A8: Extended crystal structure of Sb-trithiol-diacid (CCDC #2071807) showing the interactions between molecules in the solid state.

Table A1: Crystal data and structure refinement for compound **3** (CCDC #2071806).

Identification code	s1_sq	
Empirical formula	C19 H17.50 N4.50 O5 S3	
Formula weight	485.05	
Temperature	100.0 K	
Wavelength	1.54178 Å	
Crystal system	Trigonal	
Space group	R -3	
Unit cell dimensions	a = 33.0640(15) Å	☐= 90°.
	b = 33.0640(15) Å	☐= 90°.
	c = 10.4339(7) Å	☐ = 120°.
Volume	9878.4(11) Å^3	
Z	18	
Density (calculated)	1.468 Mg/m^3	
Absorption coefficient	3.449 mm^{-1}	
F(000)	4518	
Crystal size	0.21 x 0.08 x 0.06 mm^3	
Theta range for data collection	2.673 to 72.542°.	
Index ranges	-40<=h<=40, -40<=k<=40, -10<=l<=12	
Reflections collected	72491	
Independent reflections	4315 [R(int) = 0.0956]	
Completeness to theta = 67.679°	99.3 %	
Absorption correction	Semi-empirical from equivalents	
Max. and min. transmission	0.7536 and 0.5495	
Refinement method	Full-matrix least-squares on F^2	
Data / restraints / parameters	4315 / 11 / 252	
Goodness-of-fit on F^2	1.087	
Final R indices [I>2sigma(I)]	R1 = 0.0830, wR2 = 0.2436	
R indices (all data)	R1 = 0.1029, wR2 = 0.2643	
Extinction coefficient	n/a	
Largest diff. peak and hole	0.863 and -0.922 e.Å^{-3}	

Table A2: Bond lengths [Å] and angles [°] for compound **3** (CCDC #2071806).

S(3)-C(16)	1.672(5)
S(3)-C(11)	1.806(5)
S(1)-C(9)	1.836(5)
S(1)-C(14)	1.681(6)
O(3)-C(12)	1.280(5)
O(3)-H(3)	0.90(2)
O(4)-C(13)	1.269(5)
O(1)-C(1)	1.363(5)
O(1)-C(7)	1.426(5)
O(2)-C(12)	1.270(5)
O(5)-C(13)	1.268(5)
O(5)-H(5)	0.90(2)
C(4)-H(4)	0.9500
C(4)-C(3)	1.377(5)
C(4)-C(5)	1.398(5)
N(3)-C(16)	1.171(6)
C(3)-C(12)	1.479(5)
C(3)-C(2)	1.393(5)
C(5)-C(13)	1.488(5)
C(5)-C(6)	1.375(5)
C(6)-H(6)	0.9500
C(6)-C(1)	1.403(6)
C(1)-C(2)	1.400(5)
C(2)-H(2)	0.9500
C(8)-C(7)	1.537(5)
C(8)-C(9)	1.535(6)
C(8)-C(11)	1.524(6)
C(8)-C(10)	1.532(6)
C(7)-H(7A)	0.9900
C(7)-H(7B)	0.9900
N(1)-C(14)	1.172(7)
C(9)-H(9A)	0.9900
C(9)-H(9B)	0.9900
C(11)-H(11A)	0.9900

C(11)-H(11B)	0.9900
C(10)-H(10A)	0.9900
C(10)-H(10B)	0.9900
C(10)-S(2)	1.858(5)
C(15)-N(2)	1.198(12)
C(15)-S(2)	1.538(10)
C(16)-S(3)-C(11)	101.2(2)
C(14)-S(1)-C(9)	100.0(2)
C(12)-O(3)-H(3)	117(5)
C(1)-O(1)-C(7)	116.9(3)
C(13)-O(5)-H(5)	120(7)
C(3)-C(4)-H(4)	120.3
C(3)-C(4)-C(5)	119.4(3)
C(5)-C(4)-H(4)	120.3
C(4)-C(3)-C(12)	119.7(3)
C(4)-C(3)-C(2)	121.1(3)
C(2)-C(3)-C(12)	119.2(3)
C(4)-C(5)-C(13)	119.8(3)
C(6)-C(5)-C(4)	121.0(4)
C(6)-C(5)-C(13)	119.2(3)
O(4)-C(13)-C(5)	118.8(3)
O(5)-C(13)-O(4)	123.8(4)
O(5)-C(13)-C(5)	117.4(3)
C(5)-C(6)-H(6)	120.4
C(5)-C(6)-C(1)	119.1(4)
C(1)-C(6)-H(6)	120.4
O(3)-C(12)-C(3)	118.4(3)
O(2)-C(12)-O(3)	122.9(4)
O(2)-C(12)-C(3)	118.6(3)
O(1)-C(1)-C(6)	115.1(3)
O(1)-C(1)-C(2)	124.4(4)
C(2)-C(1)-C(6)	120.5(3)
C(3)-C(2)-C(1)	118.7(4)
C(3)-C(2)-H(2)	120.6
C(1)-C(2)-H(2)	120.6
C(9)-C(8)-C(7)	107.8(3)

C(11)-C(8)-C(7)	111.4(4)
C(11)-C(8)-C(9)	110.0(3)
C(11)-C(8)-C(10)	107.3(4)
C(10)-C(8)-C(7)	107.3(3)
C(10)-C(8)-C(9)	113.1(4)
O(1)-C(7)-C(8)	107.3(3)
O(1)-C(7)-H(7A)	110.3
O(1)-C(7)-H(7B)	110.3
C(8)-C(7)-H(7A)	110.3
C(8)-C(7)-H(7B)	110.3
H(7A)-C(7)-H(7B)	108.5
N(3)-C(16)-S(3)	176.1(5)
S(1)-C(9)-H(9A)	108.5
S(1)-C(9)-H(9B)	108.5
C(8)-C(9)-S(1)	115.2(3)
C(8)-C(9)-H(9A)	108.5
C(8)-C(9)-H(9B)	108.5
H(9A)-C(9)-H(9B)	107.5
S(3)-C(11)-H(11A)	108.1
S(3)-C(11)-H(11B)	108.1
C(8)-C(11)-S(3)	116.7(3)
C(8)-C(11)-H(11A)	108.1
C(8)-C(11)-H(11B)	108.1
H(11A)-C(11)-H(11B)	107.3
C(8)-C(10)-H(10A)	108.1
C(8)-C(10)-H(10B)	108.1
C(8)-C(10)-S(2)	116.9(3)
H(10A)-C(10)-H(10B)	107.3
S(2)-C(10)-H(10A)	108.1
S(2)-C(10)-H(10B)	108.1
N(1)-C(14)-S(1)	177.6(6)
N(2)-C(15)-S(2)	173.9(8)
C(15)-S(2)-C(10)	98.8(3)

Table A3: Crystal data and structure refinement for compound **5** (CCDC #2071807).

Identification code	s1	
Empirical formula	C17 H25 O7 S5 Sb	
Formula weight	623.42	
Temperature	100.0 K	
Wavelength	1.54178 Å	
Crystal system	Monoclinic	
Space group	P 1 21/c 1	
Unit cell dimensions	a = 7.2465(2) Å	□= 90°.
	b = 20.2943(5) Å	□= 95.6241(9)°.
	c = 16.3506(4) Å	□ = 90°.
Volume	2392.99(11) Å^{3}	
Z	4	
Density (calculated)	1.730 Mg/m^{3}	
Absorption coefficient	13.543 mm^{-1}	
F(000)	1256	
Crystal size	0.7 x 0.11 x 0.09 mm^{3}	
Theta range for data collection	3.481 to 74.174°.	
Index ranges	-8<=h<=7, -25<=k<=25, -20<=l<=20	
Reflections collected	54840	
Independent reflections	4761 [R(int) = 0.0351]	
Completeness to theta = 67.679°	98.5 %	
Absorption correction	Semi-empirical from equivalents	
Max. and min. transmission	0.4257 and 0.1420	
Refinement method	Full-matrix least-squares on F^{2}	
Data / restraints / parameters	4761 / 2 / 281	
Goodness-of-fit on F^{2}	1.106	
Final R indices [I>2sigma(I)]	R1 = 0.0207, wR2 = 0.0537	
R indices (all data)	R1 = 0.0207, wR2 = 0.0538	
Extinction coefficient	n/a	
Largest diff. peak and hole	0.440 and -0.634 e.Å^{-3}	

Table A4: Bond lengths [Å] and angles [°] for Sb-trithiol-diacid (CCDC #2071807).

Sb(1)-S(3)	2.4465(5)
Sb(1)-S(2)	2.4314(5)
Sb(1)-S(1)	2.4416(5)
S(3)-C(11)	1.827(2)
S(2)-C(10)	1.8318(19)
S(2S)-O(2S)	1.5191(16)
S(2S)-C(3S)	1.782(2)
S(2S)-C(4S)	1.790(2)
S(1S)-O(1S)	1.5144(16)
S(1S)-C(1S)	1.781(3)
S(1S)-C(2S)	1.779(3)
S(1)-C(9)	1.8316(19)
O(4)-C(13)	1.329(2)
O(2)-C(12)	1.325(2)
O(3)-C(13)	1.211(3)
O(1)-C(12)	1.210(2)
O(5)-C(3)	1.367(2)
O(5)-C(7)	1.432(2)
C(6)-C(5)	1.390(3)
C(6)-C(1)	1.399(3)
C(3)-C(2)	1.394(3)
C(3)-C(4)	1.387(3)
C(13)-C(5)	1.494(3)
C(11)-C(8)	1.543(3)
C(5)-C(4)	1.400(3)
C(7)-C(8)	1.538(2)
C(1)-C(2)	1.386(3)
C(1)-C(12)	1.496(3)
C(8)-C(10)	1.546(3)
C(8)-C(9)	1.543(3)
S(2)-Sb(1)-S(3)	90.621(16)
S(2)-Sb(1)-S(1)	92.254(16)
S(1)-Sb(1)-S(3)	91.965(16)
C(11)-S(3)-Sb(1)	101.22(7)
C(10)-S(2)-Sb(1)	102.35(6)

O(2S)-S(2S)-C(3S)	105.23(12)
O(2S)-S(2S)-C(4S)	104.07(11)
C(3S)-S(2S)-C(4S)	98.09(12)
O(1S)-S(1S)-C(1S)	107.47(11)
O(1S)-S(1S)-C(2S)	106.75(11)
C(2S)-S(1S)-C(1S)	98.32(12)
C(9)-S(1)-Sb(1)	101.68(7)
C(3)-O(5)-C(7)	117.43(15)
C(5)-C(6)-C(1)	119.14(17)
O(5)-C(3)-C(2)	115.16(17)
O(5)-C(3)-C(4)	124.54(17)
C(4)-C(3)-C(2)	120.30(17)
O(4)-C(13)-C(5)	113.30(17)
O(3)-C(13)-O(4)	123.73(18)
O(3)-C(13)-C(5)	122.96(18)
C(8)-C(11)-S(3)	117.07(13)
C(6)-C(5)-C(13)	121.35(17)
C(6)-C(5)-C(4)	120.81(17)
C(4)-C(5)-C(13)	117.84(17)
O(5)-C(7)-C(8)	107.30(15)
C(6)-C(1)-C(12)	121.53(17)
C(2)-C(1)-C(6)	120.32(17)
C(2)-C(1)-C(12)	118.15(17)
C(1)-C(2)-C(3)	120.09(18)
C(3)-C(4)-C(5)	119.30(17)
C(11)-C(8)-C(10)	112.15(16)
C(11)-C(8)-C(9)	112.15(16)
C(7)-C(8)-C(11)	107.06(15)
C(7)-C(8)-C(10)	104.92(15)
C(7)-C(8)-C(9)	107.01(15)
C(9)-C(8)-C(10)	112.95(16)
O(2)-C(12)-C(1)	112.61(16)
O(1)-C(12)-O(2)	124.22(18)
O(1)-C(12)-C(1)	123.16(17)
C(8)-C(10)-S(2)	116.79(13)
C(8)-C(9)-S(1)	117.06(13)

Appendix B: Chapter 4 Supplemental Information

1. X-ray Crystallography

Collaborators at Oak Ridge National Laboratory performed the following sample preparation (Dr. Md Faizul Islam), data collection, and analysis (Dr. Frankie White).

1.1. Materials and Methods

Using [^{nat}Sb(TREN-CAM)]$^-$ isolated from RP-HPLC, collaborators obtained a single crystal suitable for X-ray diffraction by vapor diffusion of diethyl ether into a dimethylformamide (DMF) complex (~2 mg/mL) solution. The crystal was coated with Type NVH immersion oil and mounted to a Mitegen cryoloop. X-ray diffraction measurements were performed on a Bruker D8 Venture diffractometer equipped with an *I*µs 3.0 molybdenum X-ray source (λ = 0.71073 Å). APEX4 software provided data collection and unit cell determination. SHELXL software within the *OLEX2* graphical user interface determined the structure [181,182]. Hydrogen atoms bound to carbon were geometrically added at calculated positions. Two of the three amide hydrogens of TREN-CAM were located in the Fourier electron density difference map. The third hydrogen atom was added at the geometrically expected position through chemical knowledge. The sodium atom was refined as an ammonium ion, water, chloride, and potassium. The model was best fit as a sodium atom as evidenced by the vastly improved structure model in comparison to the aforementioned.

The structure had B-alerts that relate to the following:

PLAT220_ALERT_2_B Nonsolvent

PLAT242_ALERT_2_B Low ‘MainMol’

PLAT780_ALERT_1_B Coordinates do not form a properly connected set

PLAT973_ALERT_2_B Check Calcd Positive Resid. Density

PLAT978_ALERT_1_B The Flack x is >> 0 Do a BASF/TWIN Refinement

Misassignment of N or O atoms caused the first two alerts, but chemical knowledge of the ligand structure and DMF show the correct assignment of the N and O atoms. These alerts are due to the large thermal parameter of the carbon on one of the outer-sphere DMF molecules. The third alert references the sodium atom. As stated above, refinement of this atom as sodium gave the best model of the structure. The last two B-alerts involve possible twinning. Twining was checked and no twinning or twin laws were observed. The CIF file within this report was archived in the Cambridge Crystallographic Data Centre under CCDC deposition number 2381819. Crystallographic data collection and refinement parameters are collected in **Table B1** below.

1.2. Results and Discussion

A single crystal of $[^{nat}Sb(TREN\text{-}CAM)]^-$ was grown by vapor diffusion and analyzed in the solid state by X-ray diffraction. In the structure (**Figure 46**), TREN-CAM binds to the Sb(V) center via all 6 phenolate donors in a pseudo-octahedral configuration, which is consistent with the structural arrangement inferred by the solution-state NMR and XAS studies. As observed in structures reported previously for other metal complexes of TREN-CAM [211], the amide protons are positioned towards the interior of the cavity, engaged in hydrogen bonding with the *ortho* oxygen donors of the catechol groups. These interactions result in systematically longer $Sb–O_{ortho}$ bond distances (1.992 ± 0.002 Å) in comparison to $Sb–O_{meta}$ bond distances (1.977 ± 0.003 Å). Nonetheless, the Sb–O distances in the crystal structure are similar to the average bond distance calculated from EXAFS measurements. The overall –1 charge of the complex is balanced by a Na^+ ion, which is coordinated by two outer-sphere DMF molecules and three amide carbonyl oxygens from three adjacent TREN-CAM molecules. This bonding arrangement gives rise to a distorted square pyramidal geometry around the Na center (**Figure 46**). The refinement of Na in the crystal structure was somewhat surprising because the Sb–TREN-CAM complex was synthesized using NH_4OH, rather than NaOH, as the base. We speculate, however, that the NH_4^+ countercation could have been exchanged for the ubiquitous Na^+ ion during HPLC purification. Bridging Na^+ ions with similar geometries have also been reported in the structures of DOTA and PCTA complexes of Sb(III) [172,173]. Additional details of the refinement and crystallographic parameters are provided in **Table B1**.

Table B1: X-ray crystallographic data collection and refinement parameters.

Compound	Na[Sb(TREN-CAM)]·2DMF
Empirical formula	$C_{33}H_{38}N_6NaO_{11}Sb$
Formula weight	839.44
a (Å)	9.9803(9)
b (Å)	15.7446(12)
c (Å)	23.032(2)
α (°)	90
β (°)	90
γ (°)	90
V (Å^3)	3619.1(6)
Z	4
Crystal system	Orthorhombic
Space group	$P2_12_12_1$
ρ_{calc} (g/cm^3)	1.541
μ (mm^{-1})	0.842
T (K)	100.6
2θ range (°)	4.382 to 71.744
Independent reflections	9978
R_{int}	0.0474
Number of parameters	481
Max, min peaks (e·Å^{-3})	1.624, 1.588
R1^a/wR2^b (all data)	0.0681/0.1120
R1^a/wR2^b (>2σ)	0.0474/0.1019
Goodness of fit^c	0.98922

^{a} $R_1 = \Sigma||Fo| - |Fc||/\Sigma|Fo|$ for $I > 2\sigma$. ^{b} $wR_2 = \{\Sigma[w(F_o^2 - F_c^2)^2]/\Sigma[w(F_o^2)^2]\}^{1/2}$ for $I > 2\sigma$. ^{c} $GoF = \{\Sigma[w(F_o^2 - F_c^2)^2]/(n - p)\}^{1/2}$, where n is the number of data and p is refined parameters.

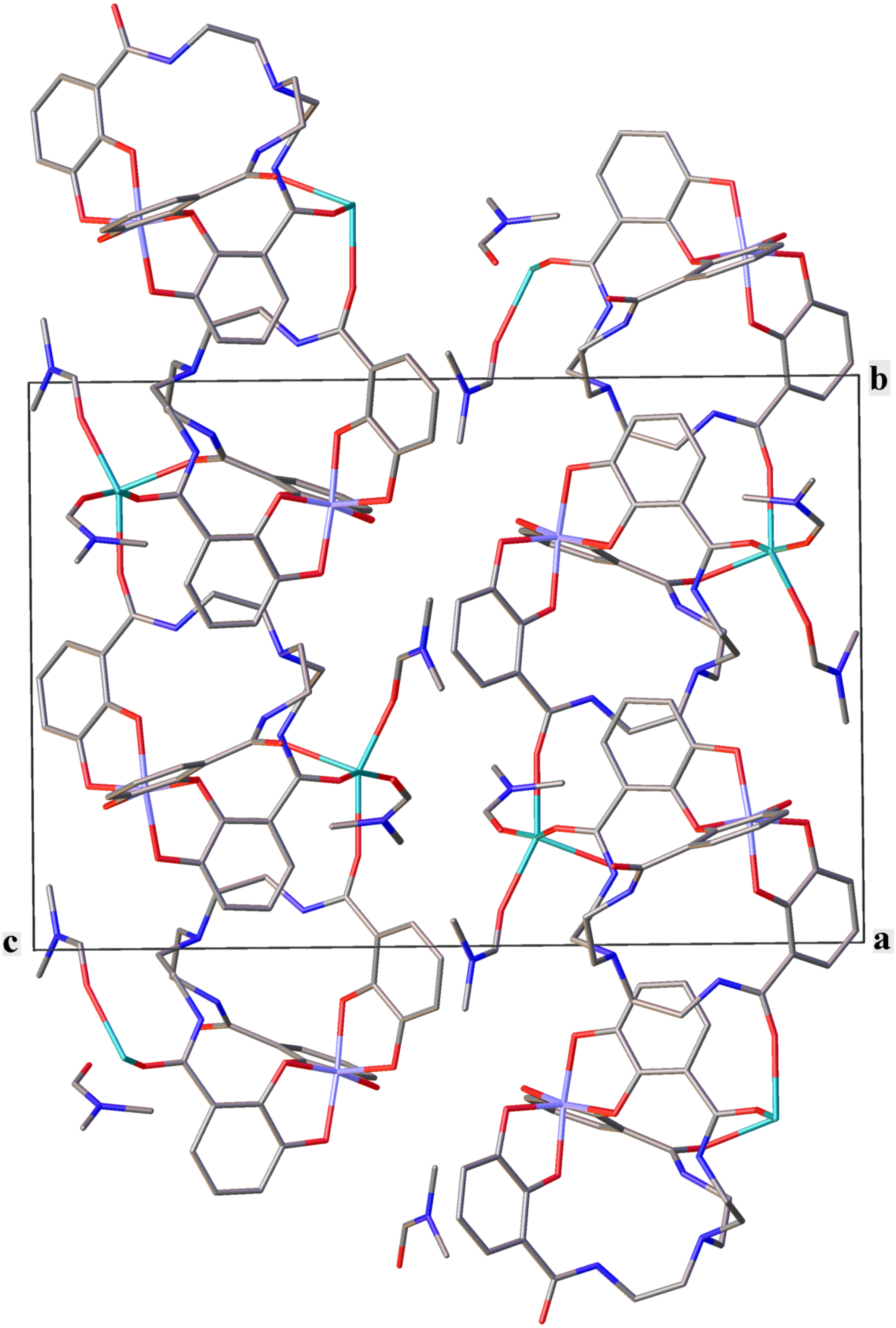

Figure B1: The unit cell packing of Na[Sb(TREN-CAM)]·2DMF. The Na^+ cation charge balances the Sb–TREN-CAM complex and contributes to the packing and crystallinity of the structure by creating an extended framework. Thermal ellipsoids and hydrogen atoms have been omitted for clarity.

2. X-ray Absorption Spectroscopy (XAS)

Collaborators at Oak Ridge National Laboratory performed the following sample preparation (Dr. Briana Schrage), data collection, and analysis (Dr. Alexander Ivanov, Dr. Darren Driscoll).

2.1. Materials and Methods

XAFS samples of Sb(V) in the absence of chelator were prepared as 0.7 mM Sb_2O_5 in 1 M $HClO_4$ (pH 1), 7 mM $KSb(OH)_6$ in pure water (pH 7), 4 mM $KSb(OH)_6$ in 0.01 M NaOH + HCl (pH 9), and 4 mM $KSb(OH)_6$ in 0.01 M NaOH (pH 12). Samples containing Sb(V) (7 mM) and catechol (300 mM) were prepared in water using $KSb(OH)_6$, as described previously by others [139,191]. The pH of the samples was adjusted to 9, 4, and 3, respectively, with NH_4OH. Likewise, a sample containing TREN-CAM (14 mM) and $KSb(OH)_6$ (1 mM) was prepared in water and adjusted to pH 9 with NH_4OH.

Collaborators performed XAS measurements at the Sb K-edge at beamline 8-ID of the National Synchrotron Light Source II (NSLS II). Solid Sb samples (Sb_2O_3 and Sb_2O_5 standards) were prepared as pellets, whereas Sb solution samples were placed in Kapton capillaries (1.8 mm inner diameter, 0.05 mm thickness, Cole-Parmer) and sealed with epoxy. All data were acquired in the fluorescence geometry. The data were energy-calibrated to the first derivative maximum of an Sb foil defined at 30491 eV. Data normalization was performed using the Athena software package [232]. Ejected photoelectrons are defined by their wavenumber (*k)* in relation to the absorption edge energy (E_0) through **Equation B1**:

Eq B0) $$k = \sqrt{2m_e(E - E_0)/\hbar^2}$$

The experimental EXAFS oscillations of each sample, χ(k), are extracted from the normalized XAS data using subtraction of a spline and a cutoff distance (R_{BKG}) of 1.0 Å. For analysis of the EXAFS region, we use the EXAFS relationship given by **Equation B2**:

Eq B1) $$\chi(k) = \sum_i \frac{F_i(k)S_0^2N_i}{kR_i^2} e^{-2k^2\sigma_i^2} e^{\frac{-2R_i}{\lambda(k)}} \sin(2kR_i + \delta_i(k) - \frac{4}{3}k^3C_{3,i})$$

The index, i, is considered the path index and the χ(k) is calculated as the summation over all paths. For fitting of the EXAFS spectra, FEFF6 within the Artemis software package [232] was used with data weighted by k^2. In eq. S2, $F_i(k)$, $\delta_i(k)$, and $\lambda(k)$ represent the effective scattering amplitude, total phase shift, and mean-free-path of the photoelectron and each are derived from FEFF6. The many-body amplitude-reduction factor, S_0^2, is fixed to 0.95. Therefore, the parameters still to be fit include, N_i, the degeneracy of the path (and therefore the coordination number for single scattering paths); R_i, the half-path length; σ^2_i, the Debye-Waller factor; and $C_{3,i}$, the asymmetry of the distribution. Variation of $C_{3,i}$ was found to provide negligible improvements on the single scattering paths and thus was not included in the fitting process. Additionally, a single non-structural parameter for all paths, ΔE_0, is varied to align the k=0 point of the experimental data and theory. All scattering paths were generated utilizing the DFT-optimized Sb–TREN-CAM model structure and included the first and second scatter shells surrounding the Sb atom (O and C paths respectively). Multiple scattering paths (Sb – O – C – Sb & Sb – C – O – Sb) are also included into the fitting procedure and were found to give a slight improvement in the fitting statistics. This approach allowed the number of variables (7) per fit to stay below the number of independent data points (14).

2.2. Results and Discussion

To garner insight into the coordination environment around the Sb center of the TREN-CAM complex in aqueous solution, synchrotron XAS studies were carried out. The sample was prepared in water using $KSb(OH)_6$ (1 mM) and excess TREN-CAM (14 mM), and the solution pH was adjusted to 9 using NH_4OH. K-edge XAS spectra were acquired at room temperature in fluorescence mode at beamline 8-ID of the National Synchrotron Light Source II. To characterize the oxidation state of $[^{nat}Sb(TREN\text{-}CAM)]^-$, its X-ray absorption near-edge structure (XANES) spectrum was acquired and compared with those of $KSb(OH)_6$ (pH 9), Sb_2O_5(s), and Sb_2O_3(s) (Figure 2a). The absorption edge of $[^{nat}Sb(TREN\text{-}CAM)]^-$ (30,501 eV) is consistent with the Sb_2O_5 reference and is shifted to a higher energy relative to the Sb_2O_3 reference. These results confirm that Sb is in the +5 oxidation state and does not undergo reduction upon TREN-CAM complexation in aqueous solution. Additionally, the XANES spectrum of $[^{nat}Sb(TREN\text{-}CAM)]^-$ shows intensities of the white line and post-edge features similar to those of aqueous $KSb(OH)_6$ in the absence of the ligand, indicating a comparable octahedral environment surrounding Sb(V).

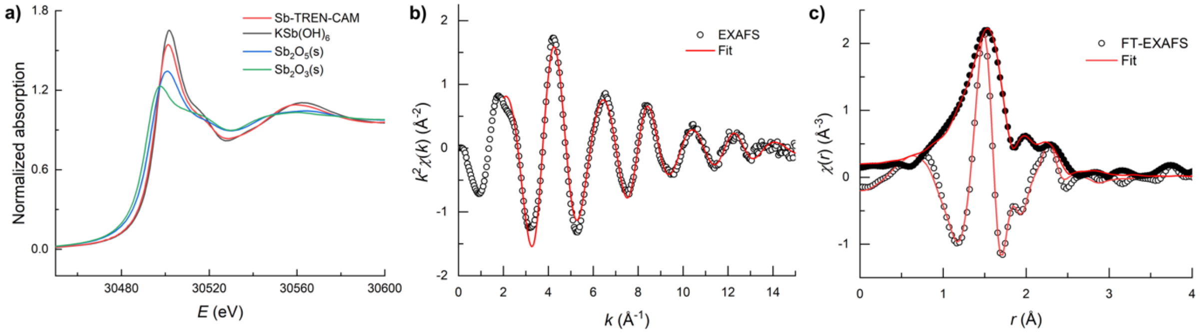

Figure B2: Structural characterization of the ^{nat}Sb–TREN-CAM complex in aqueous solution by X-ray spectroscopy (XAS). (a) Normalized Sb K-edge XANES spectra from aqueous solutions of $[Sb(TREN\text{-}CAM)]^-$ and $KSb(OH)_6$ at pH 9 versus solid Sb_2O_5 and Sb_2O_3 references. (b) K-edge EXAFS spectrum of $[Sb(TREN\text{-}CAM)]^-$ at pH 9. (c) Magnitude of the Fourier transform EXAFS (black circles) and the real component of the FT (empty circles). The fit (red line) represents model scattering paths associated with the $[Sb(TREN\text{-}CAM)]^-$ structure. Spectra are not phase-shift corrected.

Next, we investigated the local coordination of Sb(V) by examining the EXAFS spectrum of the ^{nat}Sb–TREN-CAM complex. A Fourier transform was applied to the EXAFS data in **Figure B2**, generating real-space functions that provide a tangible depiction of the atomic arrangement around the Sb(V) ion. The Fourier transform EXAFS (**Figure B2c**) revealed two intense features at 1.5 Å and 2.3 Å (uncorrected for phase shift), likely originating from the inner-shell Sb–O and nearest-neighbor Sb–C scattering correlations. This interpretation is further supported by good fits of the EXAFS (**Figures B2b,c and Table B2**), which yielded an Sb–O coordination number of 6.7(4) with an average Sb–O bond distance of 1.992(5) Å and an Sb–C coordination number of 4(2) with an average Sb–C distance of 2.79(2) Å. For comparison, EXAFS data of a sample containing catechol (300 mM) and $KSb(OH)_6$ (7 mM) were also acquired at pH 9 and found to be similar to the data obtained with $[Sb(TREN\text{-}CAM)]^-$ and to EXAFS data published previously for the catechol complex (Figure S23, Table S1).[36,37] Notably, for both $[Sb(TREN\text{-}CAM)]^-$ and $[Sb(catechol)_3]^-$, a distinct second shell feature associated with Sb–C scattering paths is observed at approximately 2.3 Å in non-phase corrected real-space FT-EXAFS (**Figure B3, Table B2**), confirming complexation of Sb(V) by these organic ligands. By contrast, sharp second-shell features are absent for $KSb(OH)_6$, reflecting its inorganic coordination environment. Taken together, these results are consistent with hexadentate Sb(V) complexation by the catecholate donors of the TREN-CAM ligand.

Table B2: Structural parameters of Sb(V) coordination environment obtained from fitting Sb K-edge EXAFS spectra.

	$KSb(OH)_6$	$[Sb(TREN\text{-}CAM)]^-$	$[Sb(Catechol)_3]^-$
CN: Sb–O	6.3 ± 0.3	6.7 ± 0.4	6.8 ± 0.4
R: Sb–O (Å)	1.980 ± 0.004	1.992 ± 0.005	1.993 ± 0.005
σ^2: Sb–O (Å^2)	$0.0022 \pm 4 \times 10^{-4}$	$0.0043 \pm 7 \times 10^{-4}$	$0.0040 \pm 6 \times 10^{-4}$
CN: Sb–C	-	4 ± 2	6 ± 3
R: Sb–C (Å)	-	2.79 ± 0.02	2.78 ± 0.02
σ^2: Sb–C (Å^2)	-	0.006 ± 0.005	0.007 ± 0.006

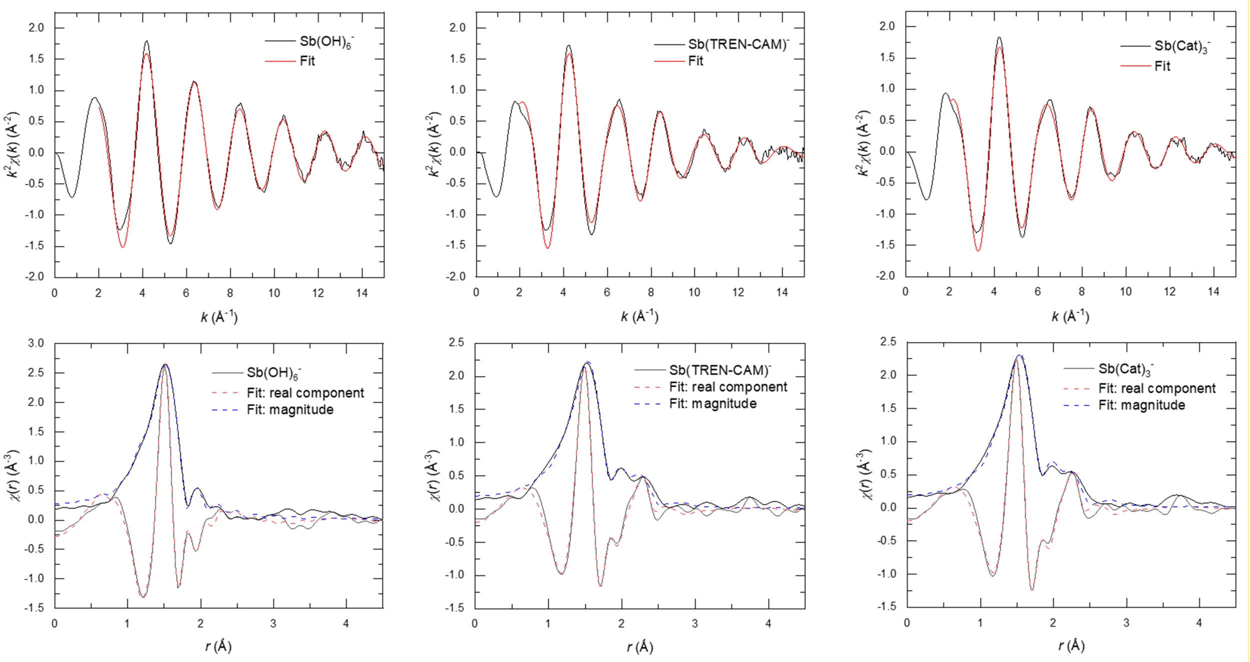

Figure B3: Comparison of K-edge Sb EXAFS data. Top: K-edge EXAFS spectra of $Sb(OH)_6^-$, $[Sb(TREN\text{-}CAM)]^-$, and $[Sb(catechol)_3]^-$ at pH 9. Bottom: Magnitude of the Fourier transform EXAFS and the real component of the FT. The fit (dotted lines) represents model scattering paths associated with the structures. Spectra are not phase-shift corrected.

3. Additional Chapter 4 Data

Collaborators at ORNL (Dr. Nikki Thiele, Dr. Md Faizul Islam) collected NMR spectra.

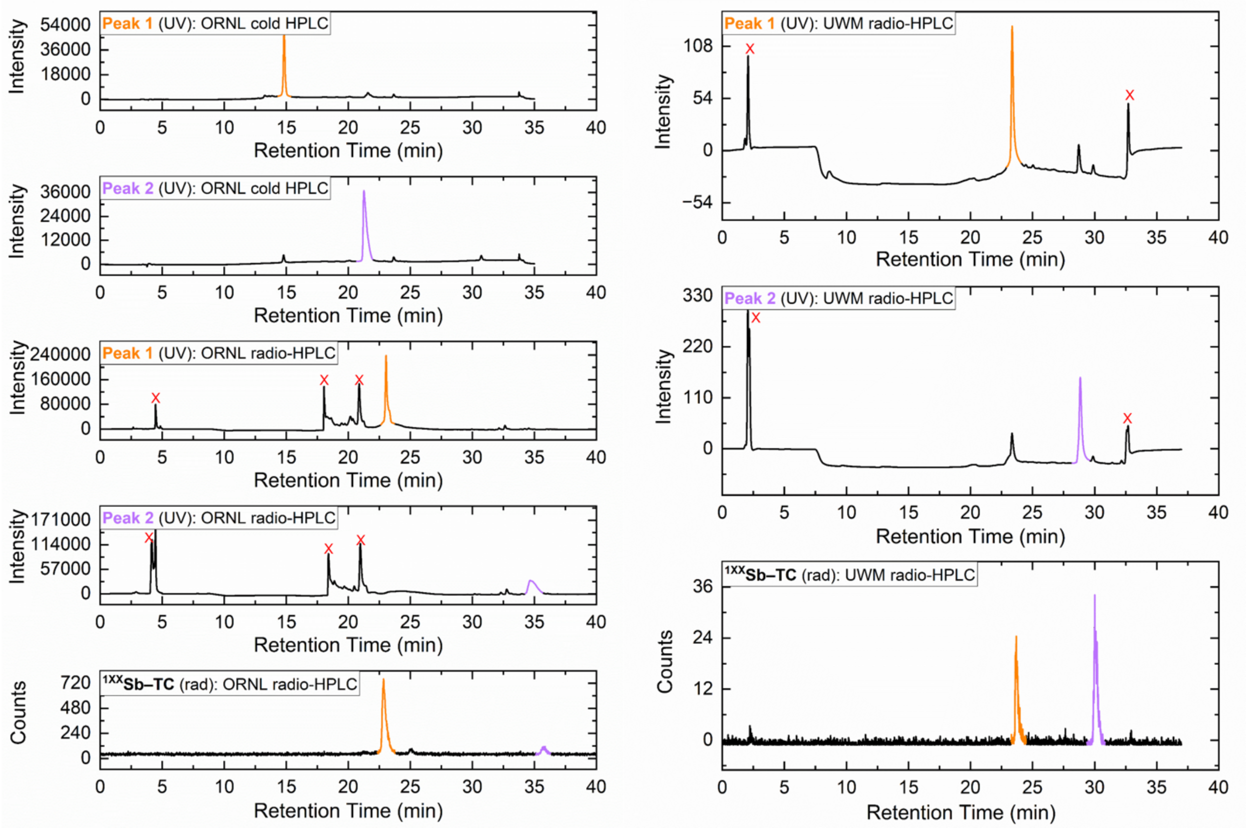

Figure B4: Comparison of retention times of Peak 1 and Peak 2 of $^{nat/1XX}$Sb–TREN-CAM on various HPLC systems across institutions (ORNL, left; UWM, right). For UV chromatograms labeled “Peak 1” and “Peak 2,” fractions were isolated at ORNL, analyzed on ORNL instruments, and then sent to UW-Madison for HPLC analysis. For radio-chromatograms labeled “^{1XX}Sb–TC,” radiolabeled samples were prepared independently at each institution. Peaks marked with an “x” denote background peaks, which were confirmed by running blanks.

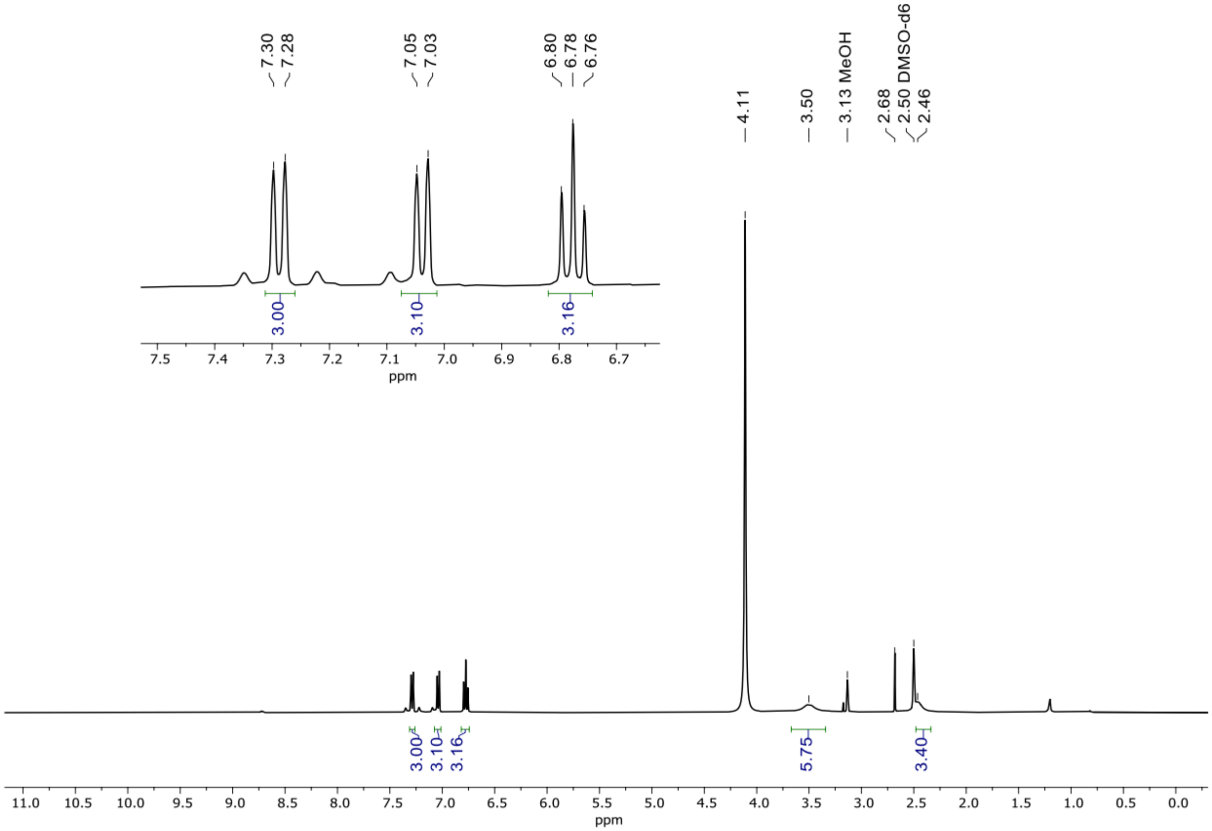

Figure B5: ^{1}H NMR spectrum (400 MHz, DMSO-d_6) of the crude reaction for the synthesis of ^{nat}Sb–TREN-CAM using **method A**. δ 7.29 (d, *J* = 8.1 Hz, 3H), 7.04 (d, *J* = 7.8 Hz, 3H), 6.78 (t, *J* = 7.9 Hz, 3H), 3.50 (br s, 6H), 2.46 (br s). The peak at 2.46 ppm integrates only to slightly greater than 3H, instead of the expected 6H. We attribute this difference to be due to overlap from the residual DMSO peak, preventing the full integration of the –CH$_2$ peak.

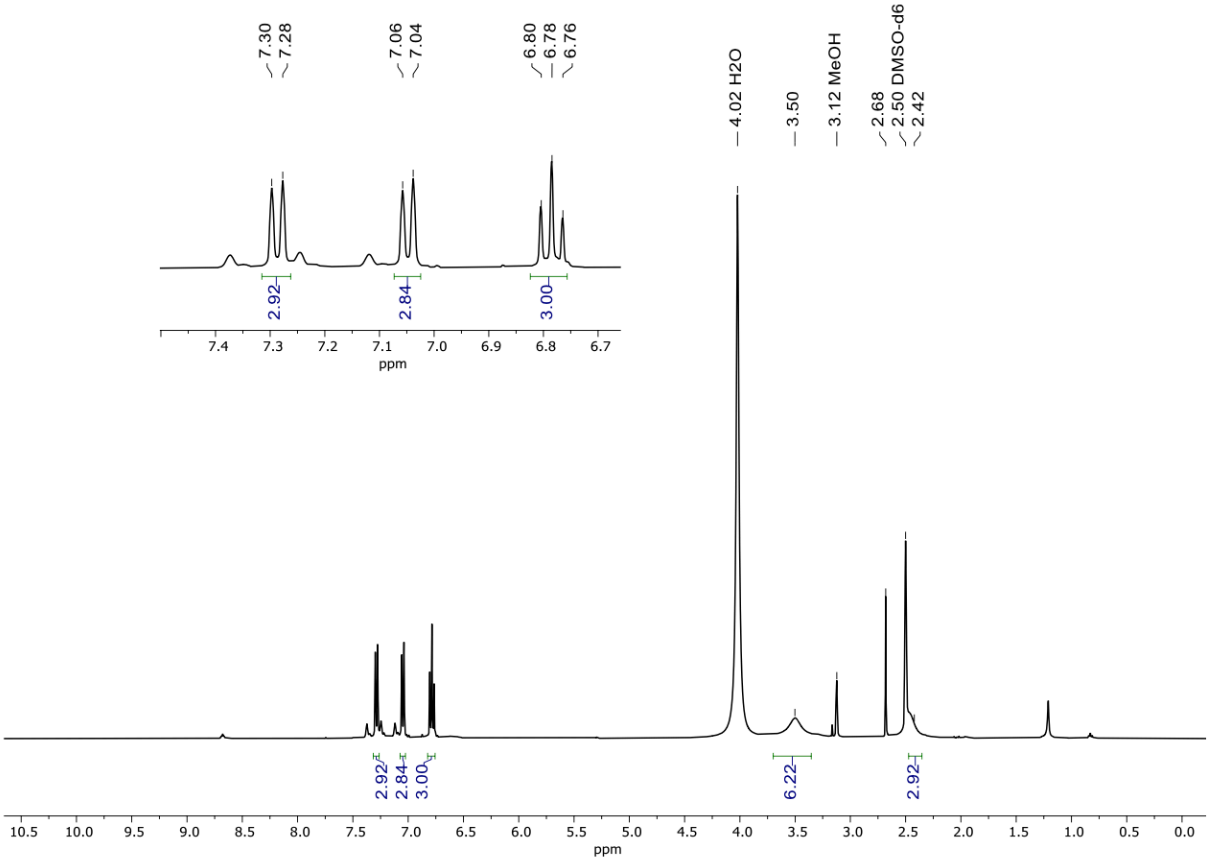

Figure B6: ^{1}H NMR spectrum (400 MHz, DMSO-d_6) of the crude reaction for the synthesis of ^{nat}Sb–TREN-CAM using **method B**. δ 7.29 (d, *J* = 8.1 Hz, 3H), 7.05 (d, *J* = 7.7 Hz, 3H), 6.78 (t, *J* = 7.9 Hz, 3H), 3.50 (br s, 6H), 2.42 (br s). The peak at 2.42 ppm only integrates to 3H, instead of the expected 6H. We attribute this difference to be due to overlap from the residual DMSO peak, preventing the full integration of the –CH_2 peak.

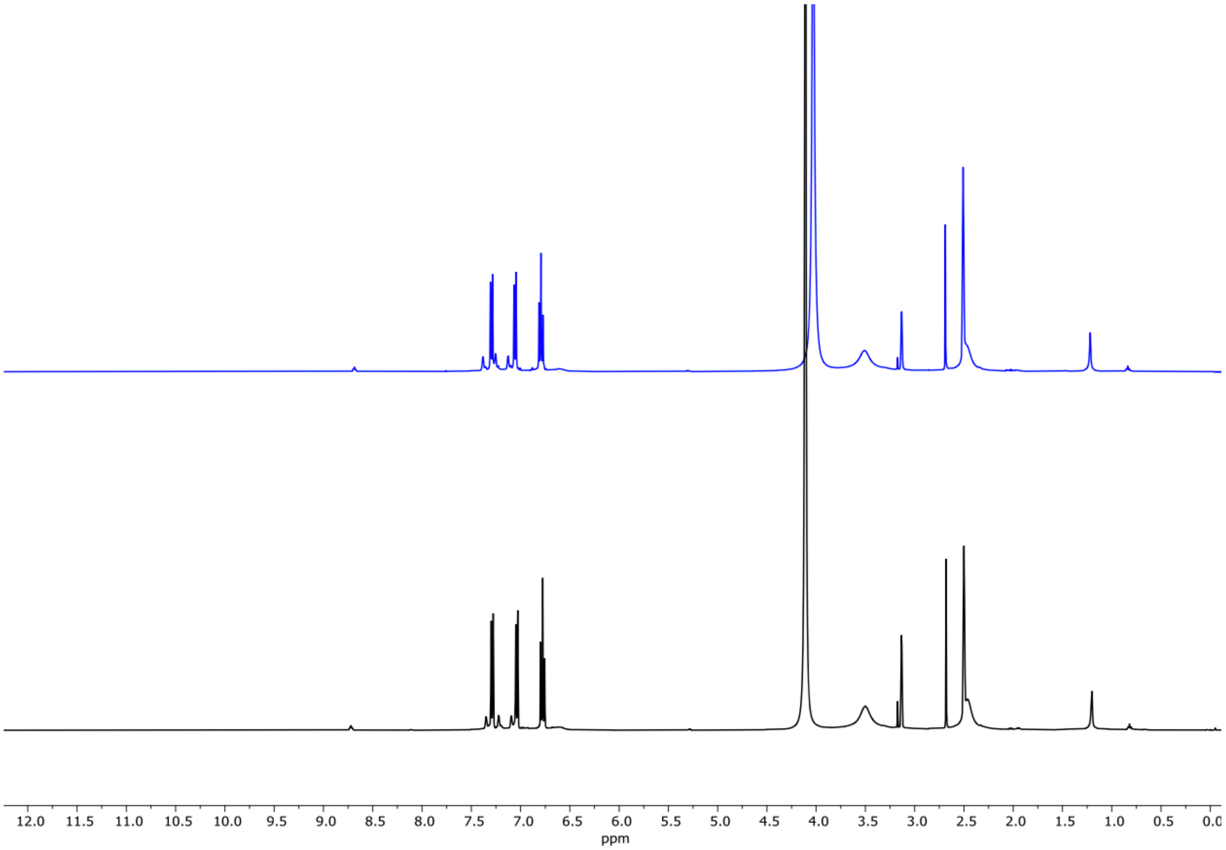

Figure B7: Comparison of the ^{1}H NMR spectra (DMSO-d_6, 400 MHz) of the crude reactions for the synthesis of ^{nat}Sb–TREN-CAM using either **method B** (top) or **method A** (bottom). These spectra show little difference between the two reaction methods, indicating that the same product is obtained whether using $SbCl_5$ or [$SbCl_3$ + H_2O_2] as the source of Sb(V).

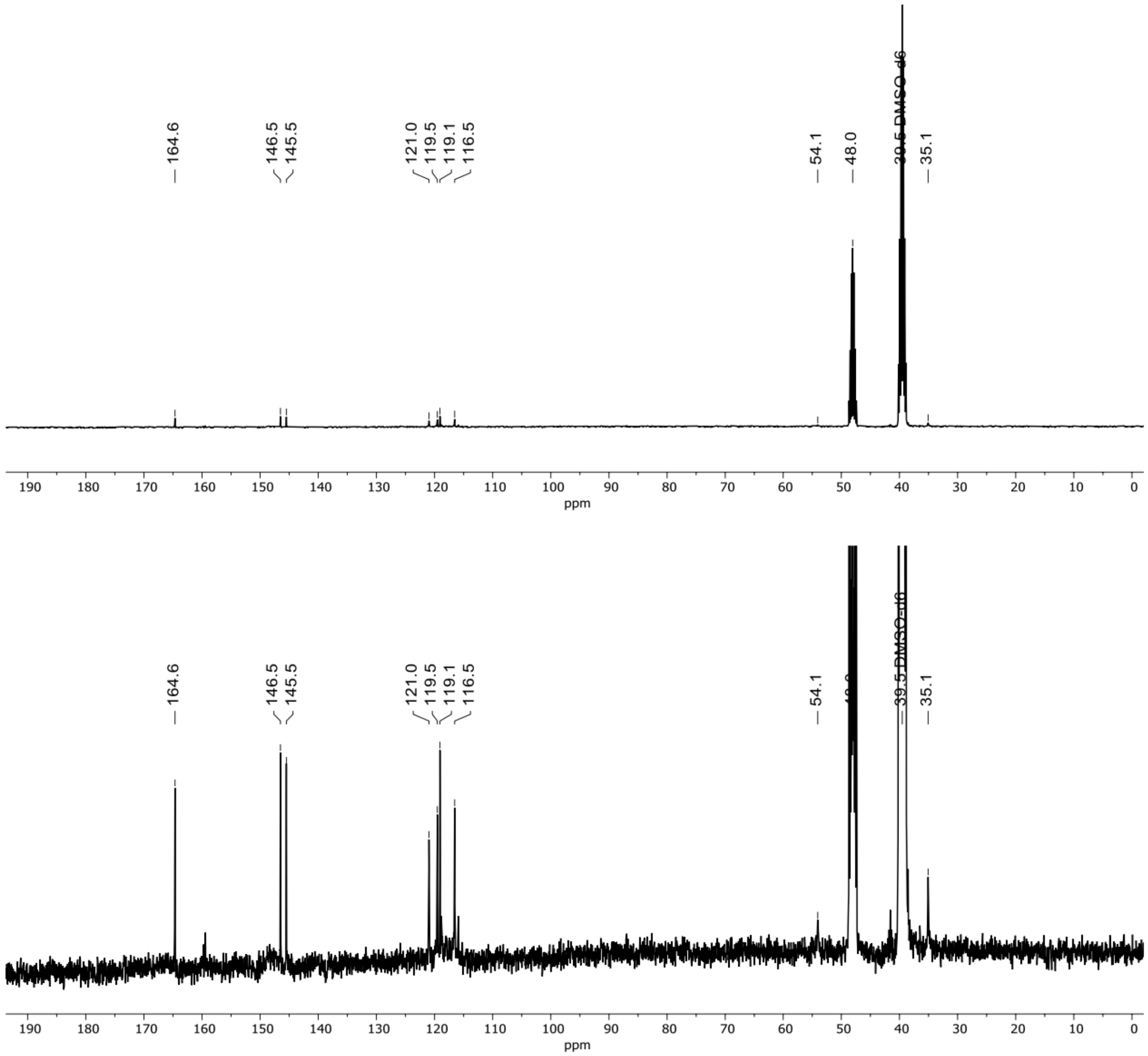

Figure B8: $^{13}C\{^1H\}$ NMR spectrum (400 MHz, DMSO-*d₆*) of the crude reaction for the synthesis of ^{nat}Sb–TREN-CAM using **method A.** Top: full view. Bottom: focused view. δ 164.6, 146.5, 145.5, 121.0, 119.5, 119.1, 116.5, 54.1, 35.1. We postulate that the septet at 48.0 ppm is DMSO coordinated to Sb(V).

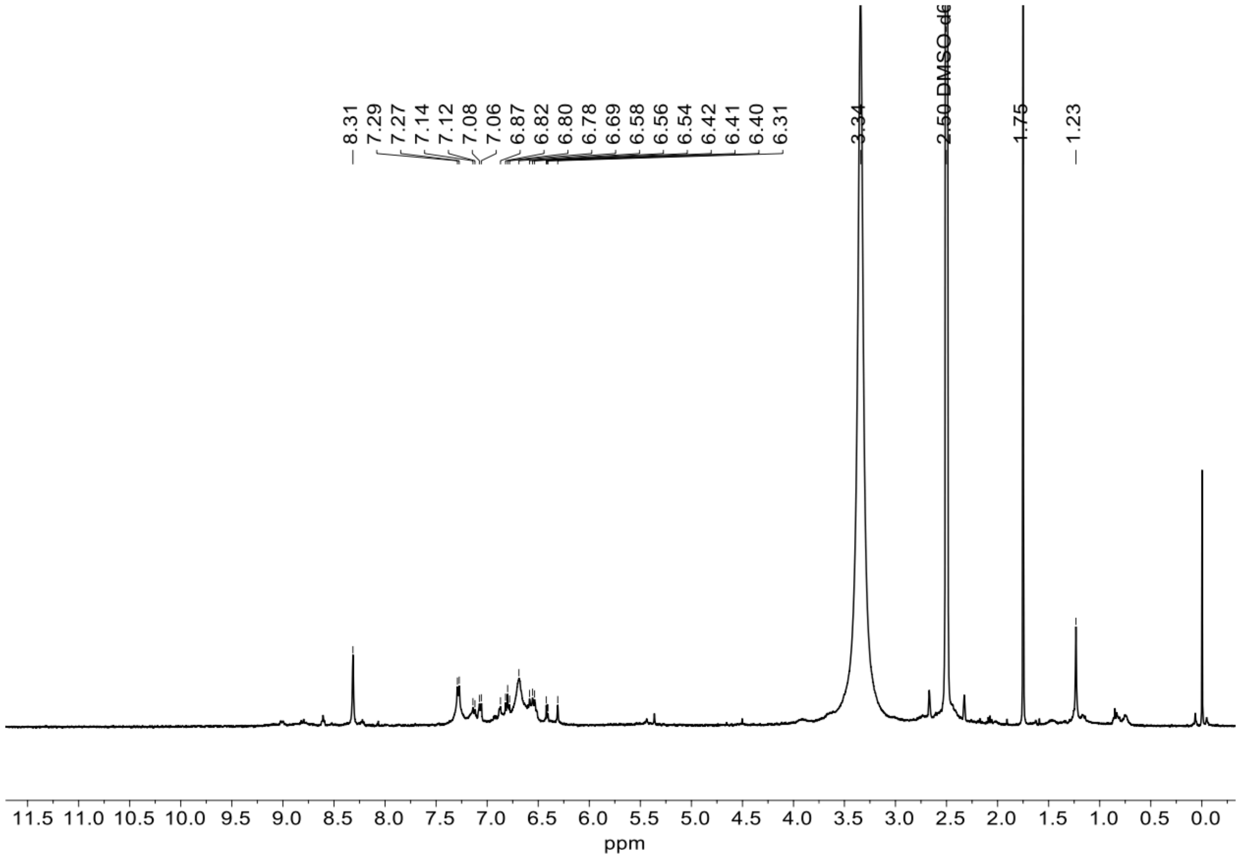

Figure B9: ^{1}H NMR spectrum (DMSO-*d*$_6$, 400 MHz) of **Peak 1** after purification of the ^{nat}Sb–TREN-CAM reaction mixture.

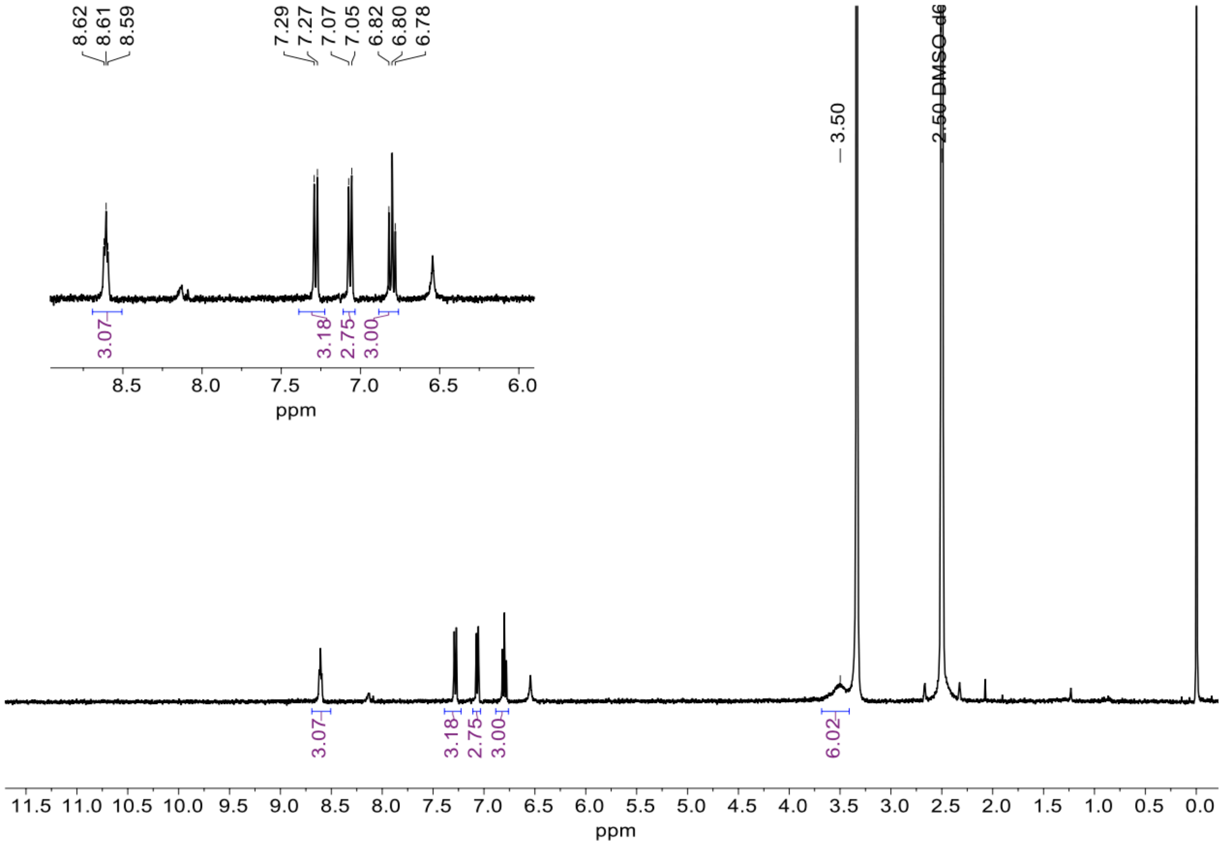

Figure B10: ^{1}H NMR spectrum (DMSO-d_6, 400 MHz) of **Peak 2** after purification of the ^{nat}Sb–TREN-CAM reaction mixture. δ 8.61 (t, J = 4.9 Hz, 3H), 7.28 (d, J = 8.3 Hz, 3H), 7.06 (d, J = 7.9 Hz, 3H), 6.80 (t, J = 8.1 Hz, 3H), 3.50 (br s, 6H). The residual DMSO peak overlaps with the second –CH$_2$ peak, preventing its full integration. Accordingly, a spectrum was obtained in CD$_3$OD to confirm its presence (**Figure B11**)

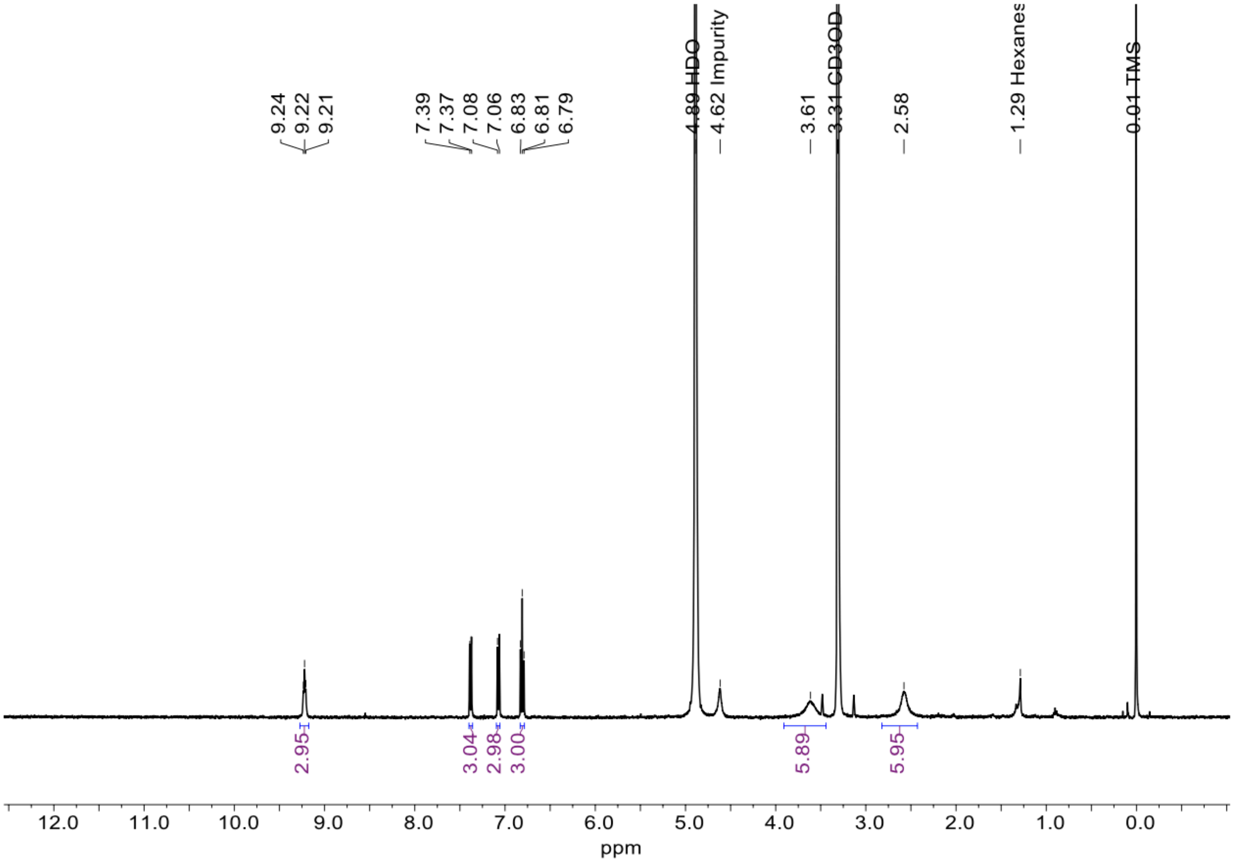

Figure B11: ^{1}H NMR spectrum (CD_3OD, 400 MHz) of **Peak 2** after purification of the ^{nat}Sb–TREN-CAM reaction mixture. Both aliphatic –CH_2 peaks are visible as broad singlets in this deuterated solvent.

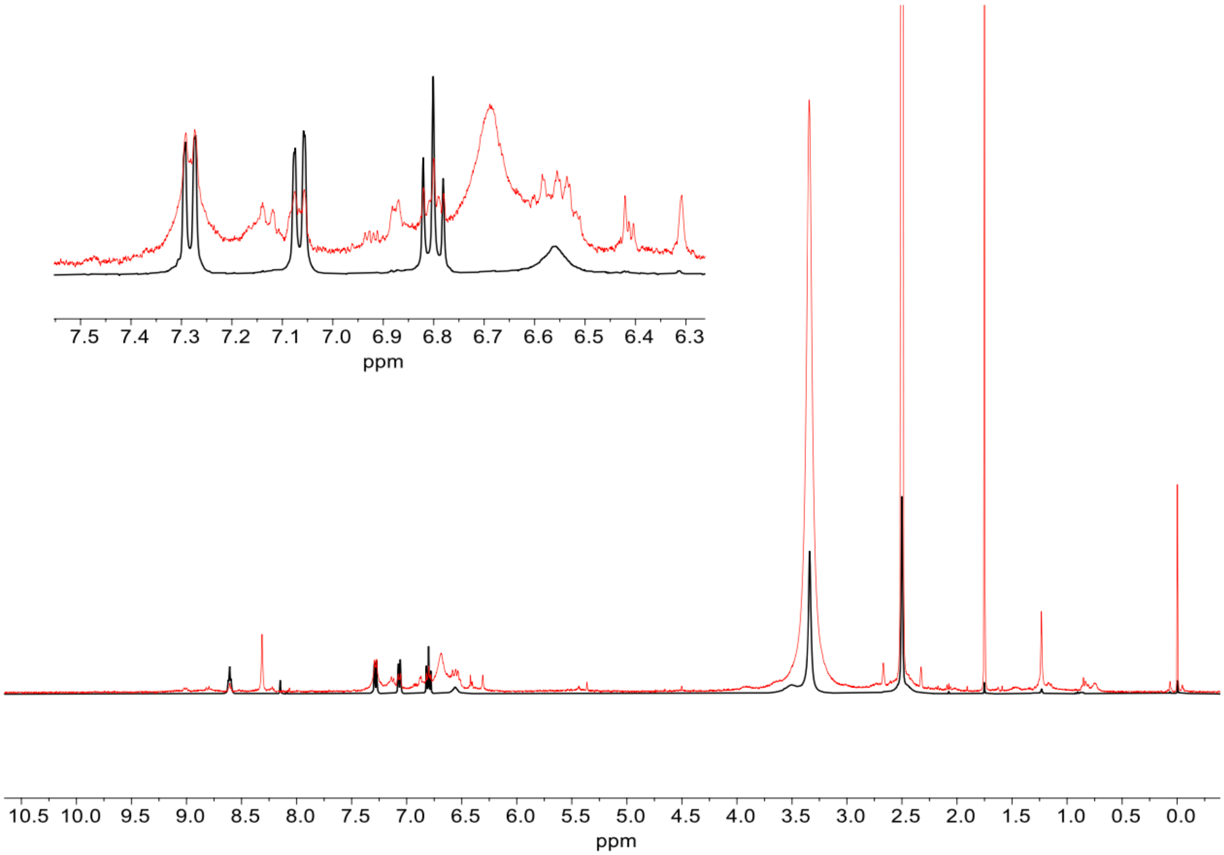

Figure B12: Overlay of the ^{1}H NMR spectra (DMSO-d_6, 400 MHz) of Peak 1 (red) and Peak 2 (black) obtained after isolation by RP-HPLC. The spectrum of Peak 1 could not be fully assigned. The overlay indicates some conversion of the Peak 1 product to [Sb(TREN-CAM)]$^-$ after isolation, lyophilization, and redissolution in the NMR solvent. This observation is consistent with the data obtained from HRMS.

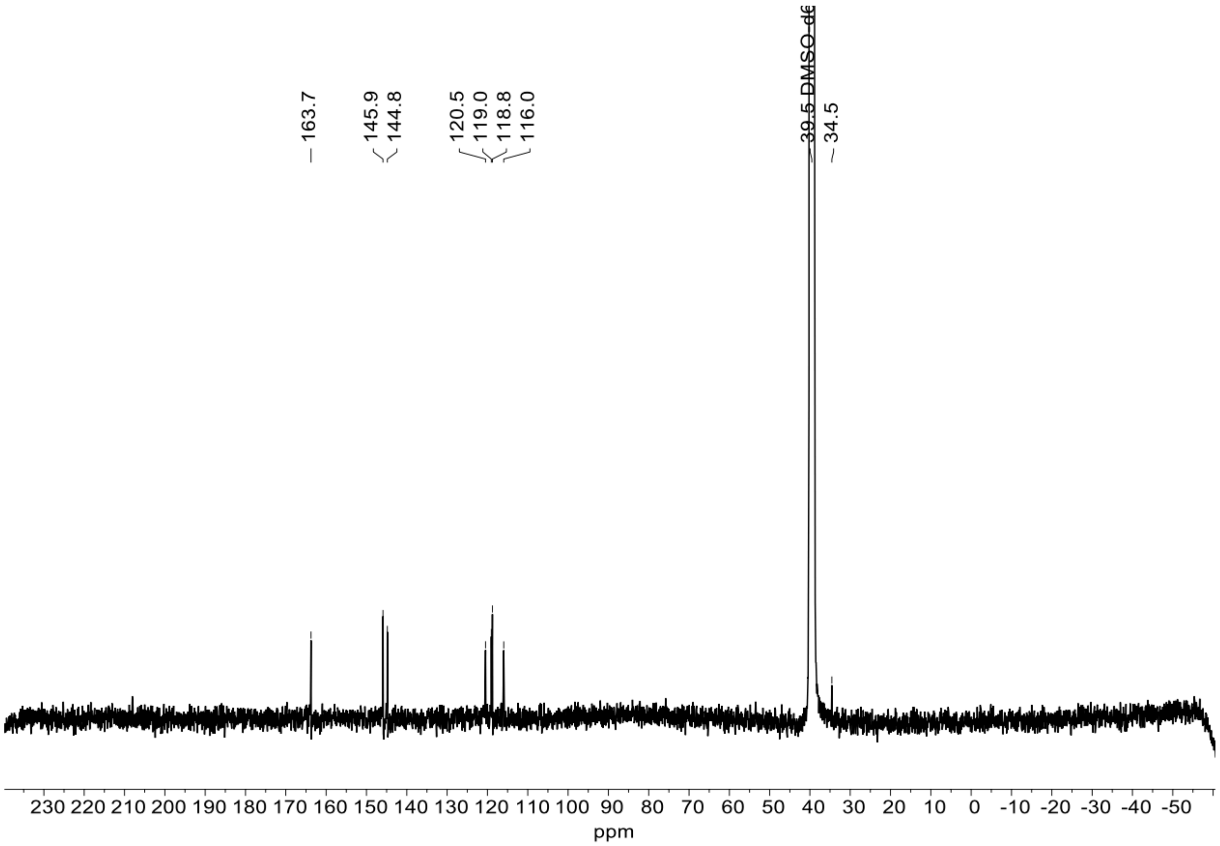

Figure B13: $^{13}C\{^1H\}$ NMR spectrum (DMSO-d_6, 400 MHz) of **Peak 2** after purification of the ^{nat}Sb–TREN-CAM reaction mixture. δ 163.7, 145.9, 144.8, 120.5, 119.0, 118.8, 116.0, 34.6. The resonance at ~54.1 ppm, which was observed in the $^{13}C\{^1H\}$ NMR spectrum of the crude reaction mixture containing mostly Peak 2 (**Figure B8**), is not visible here due to low signal-to-noise ratio.

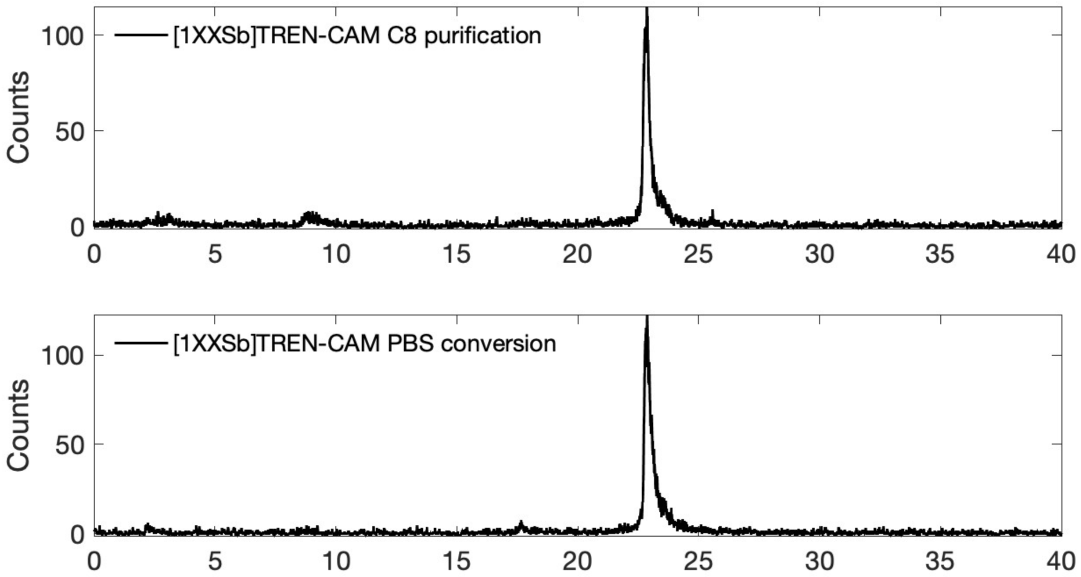

Figure B14: radio-HPLC of [^{1XX}Sb]Sb-TREN-CAM after C8 purification (top) and PBS conversion (bottom) showing complex stability throughout process. Instrument: Agilent 1260 II system (Santa Clara, CA) with Ortec (AMETEK ORTEC, Oak Ridge, TN) detector. Column: 150 mm C18 Jupiter column (Phenomenex, Torrance, CA). Flow rate: 1 mL/min. Solvents: A = 0.1 M ammonium citrate (pH 4.5), B = 0.1% TFA/H_2O, C = 0.1% TFA/MeCN. Method: 0–5 min: 100% A; 5–10 min: 95% B / 5% C; 10–30 min: linear ramp to 5% B / 95% C; 30–35 min: 5% B / 95% C; 35–36 min: linear ramp to 95% B / 5% C; 36–40 min, 100% A.

References

[1] American Cancer Society. Cancer Facts and Figures 2024. American Chemical Society: Atlanta 2024.

[2] Institute, N. C. Advances in Prostate Cancer Research https://www.cancer.gov/types/prostate/research (accessed Mar 26, 2024).

[3] Phillips, C. For Advanced Prostate Cancer, Radiopharmaceutical Improves Survival https://www.cancer.gov/news-events/cancer-currents-blog/2021/prostate-cancer-psma-radiopharmaceutical-vision (accessed Mar 27, 2024).

[4] Pouget, J.-P.; Lozza, C.; Deshayes, E.; Boudousq, V.; Navarro-Teulon, I. Introduction to Radiobiology of Targeted Radionuclide Therapy. *Front Med (Lausanne)* **2015**, *2* (MAR), 12. https://doi.org/10.3389/fmed.2015.00012.

[5] Kratochwil, C.; Bruchertseifer, F.; Giesel, F. L.; Weis, M.; Verburg, F. A.; Mottaghy, F.; Kopka, K.; Apostolidis, C.; Haberkorn, U.; Morgenstern, A. ^{225}Ac-PSMA-617 for PSMA-Targeted -Radiation Therapy of Metastatic Castration-Resistant Prostate Cancer. *Journal of Nuclear Medicine* **2016**, *57* (12), 1941–1944. https://doi.org/10.2967/jnumed.116.178673.

[6] Bodei, L.; Lewis, J. S.; Zeglis, B. M. *Radiopharmaceutical Therapy*; Cham, Switzerland, 2023; Vol. 116. https://doi.org/10.1097/HP.0000000000001000.

[7] Pouget, J. P. Basics of Radiobiology. *Nucl Med Mol Imaging* **2022**, *1–1*, 30–51. https://doi.org/10.1016/B978-0-12-822960-6.00137-X.

[8] Paillas, S.; Ladjohounlou, R.; Lozza, C.; Pichard, A.; Boudousq, V.; Jarlier, M.; Sevestre, S.; Le Blay, M.; Deshayes, E.; Sosabowski, J.; Chardès, T.; Navarro-Teulon, I.; Mairs, R. J.; Pouget, J.-P. Localized Irradiation of Cell Membrane by Auger Electrons Is Cytotoxic

Through Oxidative Stress-Mediated Nontargeted Effects. *Antioxid Redox Signal* **2016**, *25* (8). https://doi.org/10.1089/ars.2015.6309.

[9] Pouget, J. P.; Georgakilas, A. G.; Ravanat, J. L. Targeted and Off-Target (Bystander and Abscopal) Effects of Radiation Therapy: Redox Mechanisms and Risk/Benefit Analysis. *Antioxid Redox Signal* **2018**, *29* (15), 1447–1487. https://doi.org/10.1089/ars.2017.7267.

[10] Howell, R. W.; Rao, D. V.; Narra, V. R.; sast. The Question of Relative Biological Effectiveness and Quality Factor for Auger Emitters Incorporated into Proliferating Mammalian Cells. *Radiat Res* **1991**, *128*, 281–292.

[11] Sage, E.; Shikazono, N. Radiation-Induced Clustered DNA Lesions: Repair and Mutagenesis. *Free Radic Biol Med* **2017**, *107*, 125–135. https://doi.org/10.1016/j.freeradbiomed.2016.12.008.

[12] Pouget, J. P.; Frelon, S.; Ravanat, J. L.; Testard, I.; Odin, F.; Cadet, J. Formation of Modified DNA Bases in Cells Exposed Either to Gamma Radiation or to High-LET Particles. *Radiat Res* **2002**, *157* (5), 589–595. https://doi.org/10.1667/0033-7587(2002)157[0589:FOMDBI]2.0.CO;2.

[13] Kassis, A. I. Therapeutic Radionuclides: Biophysical and Radiobiologic Principles. *Semin Nucl Med* **2008**, *23* (1), 1–7. https://doi.org/10.1038/jid.2014.371.

[14] Pouget, J. P.; Constanzo, J. Revisiting the Radiobiology of Targeted Alpha Therapy. *Front Med (Lausanne)* **2021**, *8* (July), 1–11. https://doi.org/10.3389/fmed.2021.692436.

[15] Howell, R. W.; Bishayee, A. Bystander Effects Caused by Nonuniform Distributions of DNA-Incorporated 125I. *Micron* **2002**, *33* (2), 127–132.

[16] Paillas, S.; Boudousq, V.; Piron, B.; Kersual, N.; Bardiès, M.; Chouin, N.; Bascoul-Mollevi, C.; Arnaud, F. X.; Pèlegrin, A.; Navarro-Teulon, I.; Pouget, J. P. Apoptosis and P53 Are

Not Involved in the Anti-Tumor Efficacy of ^{125}I-Labeled Monoclonal Antibodies Targeting the Cell Membrane. *Nucl Med Biol* **2013**, *40* (4), 471–480. https://doi.org/10.1016/j.nucmedbio.2013.02.001.

[17] Karam, J.; Constanzo, J.; Pichard, A.; Gros, L.; Chopineau, J.; Morille, M.; Pouget, J. P. Rapid Communication: Insights into the Role of Extracellular Vesicles during Auger Radioimmunotherapy. *Int J Radiat Biol* **2023**, *99* (1), 109–118. https://doi.org/10.1080/09553002.2021.1955999.

[18] Kishikawa, H.; Wang, K.; Adelstein, S. J.; Kassis, A. I. Inhibitory and Stimulatory Bystander Effects Are Differentially Induced by Iodine-125 and Iodine-123. *Radiat Res* **2006**, *165* (6), 688–694. https://doi.org/10.1667/RR3567.1.

[19] Xue, L. Y.; Butler, N. J.; Makrigiorgos, G. M.; Adelstein, S. J.; Kassis, A. I. Bystander Effect Produced by Radiolabeled Tumor Cells in Vivo. *Proc Natl Acad Sci U S A* **2002**, *99* (21), 13765–13770. https://doi.org/10.1073/pnas.182209699.

[20] Gaillard, S.; Pusset, D.; de Toledo, S.; Michel, F.; Edouard, A. Propagation Distance of the α-Particle-Induced Bystander Effect: *Radiat Res* **2009**, *171* (5), 513–520. https://doi.org/10.1667/RR1658.1.Propagation.

[21] Bishayee, A.; Hill, H. Z.; Stein, D.; Rao, D. V.; Howell, R. W. Free Radical-Initiated and Gap Junction-Mediated Bystander Effect Due to Nonuniform Distribution of Incorporated Radioactivity in a Three-Dimensional Tissue Culture Model. *Radiat Res* **2001**, *155* (2), 335–344.

[22] Boyd, M.; Sorensen, A.; McCluskey, A. G.; Mairs, R. J. Radiation Quality-Dependent Bystander Effects Elicited by Targeted Radionuclides. *Journal of Pharmacy and Pharmacology* **2010**, *60* (8), 951–958. https://doi.org/10.1211/jpp.60.8.0002.

[23] Chen, S.; Zhao, Y.; Han, W.; Zhao, G.; Zhu, L.; Wang, J.; Bao, L.; Jiang, E.; Xu, A.; Hei, T. K.; Yu, Z.; Wu, L. Mitochondria-Dependent Signalling Pathway Are Involved in the Early Process of Radiation-Induced Bystander Effects. *Br J Cancer* **2008**, *98* (11), 1839–1844. https://doi.org/10.1038/sj.bjc.6604358.

[24] Boyd, M.; Ross, S. C.; Dorrens, J.; Fullerton, N. E.; Ker, W. T.; Zalutsky, M. R.; Mairs, R. J. Radiation-Induced Biologic Bystander Effect Elicited in Vitro by Targeted Radiopharmaceuticals Labeled with α-, β-, and Auger Electron-Emitting Radionuclides. *Journal of Nuclear Medicine* **2006**, *47* (6), 1007–1015.

[25] Gorman, S.; Tosetto, M.; Lyng, F.; Howe, O.; Sheahan, K.; O'Donoghue, D.; Hyland, J.; Mulcahy, H.; O'Sullivan, J. Radiation and Chemotherapy Bystander Effects Induce Early Genomic Instability Events: Telomere Shortening and Bridge Formation Coupled with Mitochondrial Dysfunction. *Mutation Research - Fundamental and Molecular Mechanisms of Mutagenesis* **2009**, *669* (1–2), 131–138. https://doi.org/10.1016/j.mrfmmm.2009.06.003.

[26] Howell, R. W.; Narra, V. R.; Sastry, K. S. R.; Rao, D. V. On the Equivalent Dose for Auger Electron Emitters. *Radiat Res* **1993**, *134* (1), 71–78. https://doi.org/10.1038/jid.2014.371.

[27] Ku, A.; Facca, V. J.; Cai, Z.; Reilly, R. M. Auger Electrons for Cancer Therapy – a Review. *EJNMMI Radiopharm Chem* **2019**, *4* (1). https://doi.org/10.1186/s41181-019-0075-2.

[28] Bernhardt, P.; Forssell-aronsson, E.; Jacobsson, L.; Skarnemark, G. Low-Energy Electron Emitters for Targeted Radiotherapy of Small Tumours. *Acta Oncologica* **2001**, *40* (5), 602-608.

[29] Sastry, K. S. R.; Haydock, C.; Basha, A. M.; Rao, D. V. Electron Dosimetry for Radioimmunotherapy: Optimal Electron Energy. *Radiat Prot Dosimetry* **1985**, *13* (1–4), 249–252.

[30] Marion, J. B. The Effects of Nuclear Radiations. In *Energy in Perspective* **1974**, 140–169. https://doi.org/10.1016/b978-0-12-472275-0.50009-9.

[31] Goddu, S. M.; Howell, R. W.; Rao, D. V. Calculation of Equivalent Dose for Auger Electron Emitting Radionuclides Distributed in Human Organs. *Acta Oncol (Madr)* **1996**, *35* (7), 909–916. https://doi.org/10.3109/02841869609104045.

[32] Howell, R. W.; Narra, V. R.; Hou, D.; Terrone, D. A.; Harapanhalli, R.; Sastry, K. S. R.; Rao, D. V. Relative Biological Effectiveness of Auger Emitters for Cell Inactivation: In Vitro versus in Vivo. *AAPM Symposium Series No. 8* **1992**, 290–318.

[33] Hosono, M.; Ikebuchi, H.; Nakamura, Y.; Nakamura, N.; Yamada, T.; Yanagida, S.; Kitaoka, A.; Kojima, K.; Sugano, H.; Kinuya, S.; Inoue, T.; Hatazawa, J. Manual on the Proper Use of Lutetium-177-Labeled Somatostatin Analogue (Lu-177-DOTA-TATE) Injectable in Radionuclide Therapy (2nd Ed.). *Ann Nucl Med* **2018**, *32* (3), 217–235. https://doi.org/10.1007/s12149-018-1230-7.

[34] Baum, R. P.; Kulkarni, H. R.; Schuchardt, C.; Singh, A.; Wirtz, M.; Wiessalla, S.; Schottelius, M.; Mueller, D.; Klette, I.; Wester, H. J. 177Lu-Labeled Prostate-Specific Membrane Antigen Radioligand Therapy of Metastatic Castration-Resistant Prostate Cancer: Safety and Efficacy. *Journal of Nuclear Medicine* **2016**, *57* (7), 1006–1013. https://doi.org/10.2967/jnumed.115.168443.

[35] Holland, J. P.; Williamson, M. J.; Lewis, J. S. Unconventional Nuclides for Radiopharmaceuticals. **2010**, *9* (1), 1–20. https://doi.org/10.2310/7290.2010.00008.

[36] Elgqvist, J.; Frost, S.; Pouget, J.; Albertsson, P. The Potential and Hurdles of Targeted Alpha Therapy – Clinical Trials and Beyond. **2014**, *3* (January), 1–9. https://doi.org/10.3389/fonc.2013.00324.

[37] Das, T.; Pillai, M. R. A. Options to Meet the Future Global Demand of Radionuclides for Radionuclide Therapy. *Nuclear Medicine and Biology*. 2013. https://doi.org/10.1016/j.nucmedbio.2012.09.007.

[38] Miederer, M.; Benešov, M.; Mamat, C.; Kästner, D.; Pretze, M.; Michler, E.; Brogsitter, C.; Kotzerke, J.; Kopka, K.; Scheinberg, D. A. Alpha-Emitting Radionuclides : Current Status and Future Perspectives. **2024**.

[39] Engle, J. W. The Production of Ac-225. *Curr Radiopharm* **2018**, *11* (3), 173–179. https://doi.org/10.2174/1874471011666180418141357.

[40] Harvey, J. T. NorthStar Perspectives for Actinium-225 Production at Commercial Scale. *Curr Radiopharm* **2018**, *11* (3), 180–191. https://doi.org/10.2174/1874471011666180515123848.

[41] Krane, K. S. *Introductory Nuclear Physics*; John Wiley & Sons, Ltd: New York, 1988.

[42] Kassis, A. I. The Amazing World of Auger Electrons. *Int J Radiat Biol* **2004**, *80* (11–12), 789–803. https://doi.org/10.1080/09553000400017663.

[43] Cornelissen, B.; A Vallis, K. Targeting the Nucleus: An Overview of Auger-Electron Radionuclide Therapy. *Curr Drug Discov Technol* **2010**, *7* (4), 263–279. https://doi.org/10.2174/157016310793360657.

[44] Auger, P. The Auger Effect. *Surf Sci* **1975**, *48* (1), 1–8. https://doi.org/10.1016/0039-6028(75)90306-4.

[45] Duparc, O. H.; Meitner, L.; Ellis, C. D. Pierre Auger – Lise Meitner: Comparative Contributions to the Auger Effect. *International Journal of Materials Research*. **2009**, *100* (9), 1162–1116. https://doi.org/10.3139/146.110163.

[46] Mahnke, H. E. Lise Meitner, β-Decay and Non-Radiative Electromagnetic Transitions. *Notes and Records* **2022**, *76* (1), 107–116. https://doi.org/10.1098/rsnr.2020.0036.

[47] Falzone, N.; Fernández-Varea, J. M.; Flux, G.; Vallis, K. A. Monte Carlo Evaluation of Auger Electron–Emitting Theranostic Radionuclides. *Journal of Nuclear Medicine* **2015**, *56* (9), 1441–1446. https://doi.org/10.2967/jnumed.114.153502.

[48] Thisgaard, H.; Jensen, M. ^{119}Sb - A Potent Auger Emitter for Targeted Radionuclide Therapy. *Med Phys* **2008**, *35* (9), 3839–3846. https://doi.org/10.1118/1.2963993.

[49] Saha, G. B. *Fundamentals of Nuclear Pharmacy*; 2013; Vol. 53. https://doi.org/10.1017/CBO9781107415324.004.

[50] Pouget, J.-P.; Navarro-Teulon, I.; Bardiès, M.; Chouin, N.; Cartron, G.; Pèlegrin, A.; Azria, D. Clinical Radioimmunotherapy-the Role of Radiobiology. *Nat Rev Clin Oncol* **2011**, *8* (12), 720–734. https://doi.org/10.1038/nrclinonc.2011.160.

[51] Chakravarty, N.; Rattan, S. S.; Singh, R. J.; Ramaswami, A. Decay Studies of ^{197}Tl (2.84 H) and ^{197m}Hg (23.8 H). *Radiochim Acta* **1993**, *61* (1), 9–14. https://doi.org/10.1524/ract.1993.61.1.9.

[52] J A O'Donoghue and T E Wheldon. Targeted Radiotherapy Using Auger Electron Emitters. *Phys. Med. Biol.* **1973**, *41* (10). https://doi.org/https://doi-org.proxy.lib.utk.edu/10.1088/0031-9155/41/10/005.

[53] Thisgaard, H.; Jensen, M.; Elema, D. R. Medium to Large Scale Radioisotope Production for Targeted Radiotherapy Using a Small PET Cyclotron. *Applied Radiation and Isotopes* **2011**, *69* (1), 1–7. https://doi.org/10.1016/j.apradiso.2010.07.019.

[54] Filosofov, D.; Kurakina, E.; Radchenko, V. Potent Candidates for Targeted Auger Therapy: Production and Radiochemical Considerations. *Nucl Med Biol* **2021**, *94–95*, 1–19. https://doi.org/10.1016/j.nucmedbio.2020.12.001.

[55] Kassis, A. I.; Adelstein, S. J.; Haydock, C.; Sastry, K. S. R.; McElvany, K. D.; Welch, M. J. Lethality of Auger Electrons from the Decay of Bromine-77 in the DNA of Mammalian Cells. *Radiat Res* **1982**, *90* (2), 362. https://doi.org/10.2307/3575714.

[56] Chan, P. C.; Lisco, E.; Lisco, H.; Adelstein, S. J. The Radiotoxicity of Iodine-125 in Mammalian Cells: II. A Comparative Study on Cell Survival and Cytogenetic Responses to ^{125}IUdR, ^{131}IUdR, and ^{3}HTdR. *Radiat Res* **1976**, *67* (2), 332. https://doi.org/10.2307/3574422.

[57] Narra, V. R.; Howell, R. W.; Harapanhalli, R. S.; Sastry, K. S. R.; Rao, D. V. Radiotoxicity of Some Iodine-123, Iodine-125 and Iodine-131-Labeled Compounds in Mouse Testes: Implications for Radiopharmaceutical Design. *Journal of Nuclear Medicine* **1992**, *33* (12), 2196–2201.

[58] Adelstein, S. J.; Bloomer, W. D.; Kassis, A. I.; Sastry, K. S. R. *Nuclear Medicine in Clinical Oncology*; Springer-Verlag: Berlin, Heidelberg, New York, Tokyo, 1986.

[59] Snelling, L.; Miyamoto, C. T.; Bender, H.; Brady, L. W.; Steplewski, Z.; Class, R.; Emrich, J.; Rackover, M. A. Epidermal Growth Factor Receptor 425 Monoclonal Antibodies Radiolabeled with Iodine-125 in the Adjuvant Treatment of High-Grade Astrocytomas. *Hybridoma* **1995**, *14* (2), 111–114. https://doi.org/10.1089/hyb.1995.14.111.

[60] Aronsson, E. F.; Grétarsdóttir, J.; Jacobsson, L.; Bäck, T.; Hertzman, S.; Lindegren, S.; Karlsson, B.; Lindholm, L.; Holmberg, S.; Hafström, L.; Mattsson, S. Therapy with ^{125}I-Labelled Internalized and Non-Internalized Monoclonal Antibodies in Nude Mice with

Human Colon Carcinoma Xenografts. *Nucl Med Biol* **1993**, *20* (2), 133–144. https://doi.org/10.1016/0969-8051(93)90105-4.

[61] Negret, A.; Singh, B. Nuclear Data Sheets for A = 75. *Nuclear Data Sheets* **2013**, *114* (8–9), 841–1040. https://doi.org/10.1016/j.nds.2013.08.001.

[62] Kassis, A. I.; Adelstein, S. J.; Haydock, C.; Sastry, K. S. R. Radiotoxicity of ^{75}Se and ^{35}S: Theory and Application to a Cellular Model. *Radiat Res* **1980**, *84* (84), 407–425.

[63] Volkert, W. A.; Goeckeler, W. F.; Ehrhardt, G. J.; Ketring, A. R. Therapeutic Radionuclides: Production and Decay Property Considerations. *Journal of Nuclear Medicine* **1991**, *32* (1), 174–185.

[64] Kassis, A. I. Cancer Therapy with Auger Electrons: Are We Almost There? *Journal of Nuclear Medicine* **2003**, *44* (9), 1479–1481.

[65] Kassis, A. A. I.; Fayad, F.; Kinsey, B. M.; Sastry, K. S. R.; Taube, R. A.; Adelstein, S. J. Radiotoxicity of ^{125}I in Mammalian Cells. *Radiat Res* **2015**, *111* (2), 305–318.

[66] Paillas, S.; Ladjohounlou, R.; Lozza, C.; Pichard, A.; Boudousq, V.; Jarlier, M.; Sevestre, S.; Le Blay, M.; Deshayes, E.; Sosabowski, J.; Chardès, T.; Navarro-Teulon, I.; Mairs, R. J.; Pouget, J.-P. Localized Irradiation of Cell Membrane by Auger Electrons Is Cytotoxic Through Oxidative Stress-Mediated Nontargeted Effects. *Antioxid Redox Signal* **2016**. https://doi.org/10.1089/ars.2015.6309.

[67] Pouget, J.-P.; Santoro, L.; Raymond, L.; Chouin, N.; Bardiès, M.; Bascoul-Mollevi, C.; Huguet, H.; Azria, D.; Kotzki, P.-O.; Pèlegrin, M.; Vivès, E.; Pèlegrin, A. Cell Membrane Is a More Sensitive Target than Cytoplasm to Dense Ionization Produced by Auger Electrons. *Radiat Res* **2008**, *170* (2), 192–200. https://doi.org/10.1667/rr1359.1.

[68] Knapp, F. F. (Russ); Dash, A. *Auger Electron-Based Radionuclide Therapy*; Springer: New Delhi, 2016. https://doi.org/10.1007/978-3-319-26236-9_36.

[69] IAEA. Live Chart of Nuclides: nuclear structure and decay data https://nds.iaea.org/relnsd/vcharthtml/VChartHTML.html (accessed Apr 1, 2024).

[70] Eckerman, K. F.; Endo, A. *MIRD: Radionuclide Data and Decay Schemes*, 2nd ed.; Society of Nuclear Medicine, 2008.

[71] Symochko, D. M.; Browne, E.; Tuli, J. K. Nuclear Data Sheets for A = 119. *Nuclear Data Sheets* **2009**, *110* (11), 2945–3105. https://doi.org/10.1016/j.nds.2009.10.003.

[72] Blachot, J. Nuclear Data Sheets for A = 117. *Nuclear Data Sheets* **2002**, *95* (3), 679–836. https://doi.org/10.1006/ndsh.2002.0007.

[73] Kitao, K. Nuclear Data Sheets Update for A = 118. *Nuclear Data Sheets*. 1995, pp 99–198. https://doi.org/10.1006/ndsh.1995.1022.

[74] Kitao, K.; Tendow, Y.; Hashizume, A. Nuclear Data Sheets for A = 120. *Nuclear Data Sheets* **2002**, *96* (2), 241–390. https://doi.org/10.1006/ndsh.2002.0012.

[75] Tamura, T. Nuclear Data Sheets for A = 122. *Nuclear Data Sheets* **2007**, *108* (3), 455–632. https://doi.org/10.1016/j.nds.2007.02.001.

[76] Katakura, J.; Wu, Z. D. Nuclear Data Sheets for A = 124. *Nuclear Data Sheets* **2008**, *109* (7), 1655–1877. https://doi.org/10.1016/j.nds.2008.06.001.

[77] Hsiao, Y. Y.; Hung, T. H.; Tu, S. J.; Tung, C. J. Fast Monte Carlo Simulation of DNA Damage Induction by Auger-Electron Emission. *Int J Radiat Biol* **2014**, *90* (5), 392–400. https://doi.org/10.3109/09553002.2014.892649.

[78] Solnes, L. B.; Werner, R. A.; Jones, K. M.; Sadaghiani, M. S.; Bailey, C. R.; Lapa, C.; Pomper, M. G.; Rowe, S. P. Theranostics: Leveraging Molecular Imaging and Therapy to

Impact Patient Management and Secure the Future of Nuclear Medicine. *J Nucl Med* **2020**, *61* (3), 311–318. https://doi.org/10.2967/jnumed.118.220665.

[79] Basu, S.; Kwee, T. C.; Surti, S.; Akin, E. A.; Yoo, D.; Alavi, A. Fundamentals of PET and PET/CT Imaging. *Ann N Y Acad Sci* **2011**, *1228* (1), 1–18. https://doi.org/10.1111/j.1749-6632.2011.06077.x.

[80] Khalil, M. M. Basic Science of PET Imaging. *Basic Science of PET Imaging* **2016**, 1–619. https://doi.org/10.1007/978-3-319-40070-9.

[81] Cherry, S. R.; Sorenson, J. A.; Phelps, M. E. *Physics of Nuclear Medicine*, 4th ed.; Saunders: Philadelphia, 2012.

[82] Khalil, M. M. *Basic Sciences of Nuclear Medicine: Second Edition*; 2021. https://doi.org/10.1007/978-3-030-65245-6.

[83] Khalil, M. M.; Tremoleda, J. L.; Bayomy, T. B.; Gsell, W. Molecular SPECT Imaging: An Overview. *Int J Mol Imaging* **2011**, *2011*, 1–15. https://doi.org/10.1155/2011/796025.

[84] Pritychenko, B.; Sonzogni, A. Q-value Calculator (QCalc) https://www.nndc.bnl.gov/qcalc/ (accessed Apr 1, 2024).

[85] Chen, J. Nuclear Data Sheets for A=123. *Nuclear Data Sheets* **2021**, *174*, 1–463. https://doi.org/10.1016/j.nds.2021.05.001.

[86] Ohya, S. Nuclear Data Sheets for A = 121. *Nuclear Data Sheets* **2010**, *111* (6), 1619–1806. https://doi.org/10.1016/j.nds.2010.05.002.

[87] Lovchikova, G. N.; Salnikov, O. A.; Simakov, S. P.; Trufanov, A. M.; Kotelnikova, G. V.; Pilz, V.; Streil, T. Investigation of Mechanism of the Reactions 94-Zr(p,n) 94-Nb, 119-Sn(p,n) 119-Sb, 122-Sn(p,n) 122-Sb in the Proton Energy Region 6-9 MeV. *Solviet Journal of Nuclear Physics* **1980**, *31*, 3.

[88] Johnson, C. H.; Kernell, R. L. (P,n) Cross Sections and the Strength Functions for 3- to 5.5-MeV Protons on In and on Sn Isotopes. *Physical Review, Part C, Nuclear Physics* **1970**, *2*, 639.

[89] Johnson, C. H.; Bair, J. K.; Jones, C. M.; Penny, S. K.; Smith, D. W. Wave Size Resonances Observed by the (p,n) Reaction for 2.6- to 7-MeV Protons Incident on Isotopes of Sn. *Physical Review, Part C, Nuclear Physics* **1977**, *15*, 196.

[90] Thisgaard, H.; Jensen, M. Production of the Auger Emitter ^{119}Sb for Targeted Radionuclide Therapy Using a Small PET-Cyclotron. *Applied Radiation and Isotopes* **2009**, *67*, 34–38. https://doi.org/10.1016/j.apradiso.2008.09.003.

[91] Tárkányi, F.; Ditrói, F.; Hermanne, A.; Takács, S.; Király, B.; Baba, M.; Ignatyuk, A. V. Experimental Study of the Excitation Functions of Deuteron Induced Reactions on NatSn up to 40 MeV. *Nucl Instrum Methods Phys Res B* **2011**, *269* (4), 405–416. https://doi.org/10.1016/j.nimb.2010.12.041.

[92] Hermanne, A.; Tárkányi, F.; Ditrói, F.; Takács, S. Extension of the Excitation Functions of Deuteron Induced Reactions on $^{\mathrm{Nat}}$Sn up to 50 MeV. *Nucl Instrum Methods Phys Res B* **2017**, *391*, 1–9. https://doi.org/10.1016/j.nimb.2016.11.005.

[93] Takács, S.; Takács, M. P.; Hermanne, A.; Tárkányi, F.; Adam Rebeles, R. Cross Sections of Proton Induced Reactions on NatSb. *Nucl Instrum Methods Phys Res B* **2013**, *297*, 44–57. https://doi.org/10.1016/j.nimb.2012.12.010.

[94] Mosby, M. A.; Birnbaum, E. R.; Nortier, F. M.; Engle, J. W. Cross Sections for Proton-Induced Reactions On $^{\mathrm{nat}}$Sb up to 68 MeV. *Nucl Instrum Methods Phys Res B* **2017**. https://doi.org/10.1016/j.nimb.2017.08.038.

[95] Lagunas-Solar, M. C.; Carvacho, O. F.; Yang, S. T.; Yano, Y. Cyclotron Production of PET Radionuclides: 118Sb (3.5 Min; B+ 75%; EC 25%) from High-Energy Protons on Natural Sb Targets. *International Journal of Radiation Applications and Instrumentation. Part* **1990**, *41* (6), 521–529. https://doi.org/10.1016/0883-2889(90)90033-D.

[96] Yi, J. H.; Miller, D. A. Cross Sections of ^{Nat}Sb(p,x) Reactions for 30-46 MeV Protons. *International Journal of Radiation Applications and Instrumentation. Part* **1992**, *43* (9), 1103–1106. https://doi.org/10.1016/0883-2889(92)90051-F.

[97] Elbinawi, A.; Al-Abyad, M.; Abd-Elmageed, K. E.; Hassan, K. F.; Ditroi, F. Proton Induced Nuclear Reactions on Natural Antimony up to 17 MeV. *Radiochim Acta* **2016**, *104* (4), 221–226. https://doi.org/10.1515/ract-2015-2483.

[98] Batij, V. G.; Skakun, E. A.; Rastrepin, O. A.; Baskova, K. A.; Makuni, B. M.; Chugaj, T. V.; Shavtvalov, L. Ja. Excitation Functions (p,n) and (a,Xn) Reactions with Formation of Te-119-m,g and Te-121-m,g Isomeric Pairs. In *Conf. 32 Conference on Nuclear Spectral Atomic Nuclear Structure*; 1982; p 134.

[99] Batij, V. G.; Skakun, E. A.; Rastrepin, O. A.; Rakivenko, Ju. N.; Izv, J. Excitation Functions of Sb-121(p,n)Te-121-m,g and Sb-123(p,n)Te-123-m Reactions. *Izvestiya* **1984**, *48* (194).

[100] Ermolaev, S. V; Zhuikov, B. L.; Kokhanyuk, V. M.; Matushko, V. L.; Srivastava, S. C. Cross Sections and Production Yields of ^{117m}Sn and Other Radionuclides Generated in Natural and Enriched Antimony with Protons up to 145 MeV. *Radiochim Acta* **2019**, *108* (5).

[101] Takács, S.; Takács, M. P.; Hermanne, A.; Tárkányi, F.; Adam Rebeles, R. Cross Sections of Deuteron-Induced Reactions on NatSb up to 50 MeV. *Nucl Instrum Methods Phys Res B* **2012**, *278*, 93–105. https://doi.org/10.1016/j.nimb.2012.02.007.

[102] Batij, V. G.; Baskova, K. A.; Kuz'menko, V. A.; Makuni, B. M.; Rastrepin, O. A.; Skakun, E. A.; Chugaj, T. V.; Shavtvalov, L. Ja. Excitation Functions of Sn-116,117 (a,Xn) Reactions in the Energy Range under 30 MeV. In *Conf. 34 Conference on Nuclear Spectral Atomic Nuclear Structure*; 1984; p 355.

[103] Filipescu, D.; Avrigeanu, V.; Glodariu, T.; Mihai, C.; Bucurescu, D.; Ivascu, M.; Cata-Danil, I.; Stroe, L.; Sima, O.; Cata-Danil, G.; Deleanu, D.; Ghita, D. G.; Marginean, N.; Marginean, R.; Negret, A.; Pascu, S.; Sava, T.; Suliman, G.; Zamfir, N. V. Cross Sections for Alpha-Particle Induced Reactions on ^{115,116}Sn around the Coulomb Barrier. *Physical Review, Part C, Nuclear Physics* **2011**, *83*, 64609.

[104] Antropov, A. E.; Khamid, V.; Smirnov, A. V.; Kolozhvari, A. A.; Gusev, V. P.; Zarubin, P. P.; Kordyukevich, V. O.; Giruts, V. L. Analysis of Excitation Function of Alpha-Particle Induced Reactions on ^{116,117,118,120,124}Sn at the Energies of 13-24.4 MeV. In *International Conference on Nuclear Spectroscopy and Nuclear Structure*; 1992; p 288.

[105] Vystoskiy, O. N.; Gaydaenko, S. A.; Gonchar, A. V.; Zaritskiy, V. S.; Kadkin, E. P.; Kondrat'ev, S. N.; Lobach, Yu. N.; Prokopenko, V. S.; Saltykov, L. S.; Sklyarenko, V. D.; Stepanenko, V. A.; Tokarevskiy, V. V. Excitation Functions Sn-Natur(He3,X) Reaction with Formation Radionuclides at He-3 Ions Energy to 95 MeV. In *Conf. 43 Conference on Nuclear Spectoscopy and Nuclear Structure*; 1993; p 257.

[106] IAEA. Medical Isotope Browser (accessed Apr 2, 2024). https://nds.iaea.org/relnsd/isotopia/isotopia.html

[107] Koning, A.; Rochman, D. A.; Sublet, J. C.; Dzysiuk, N. R.; Fleming, M. J.; van der Mark, S. C. TENDL: Complete Nuclear Data Library for Innovative Nuclear Science and Technology. *Nuclear Data Sheets* **2019**, *155*, 1–55.

[108] Sadeghi, M.; Rovais, M. R. A.; Enferadi, M.; Sarabadani, P. Targetry and Radiochemistry for No-Carrier-Added Production of ^{117,118m,119,120m,122}Sb. *Nukleonika* **2011**, *56* (1), 9–15.

[109] Gupta, R. K.; Pramila, G. C.; Srinivasa Raghavan, R. On the Decay of Te-119m and Te-119. *Nuclear Physics* **1962**, *32*, 669–683.

[110] Miller, D. A.; Sun, S.; Smithbauer, S. Separation of Radiotellurium from Proton-Irradiated Antimony Targets. *Radiochim Acta* **1992**, *60* (2–3), 69–74. https://doi.org/10.1524/ract.1993.60.23.69.

[111] Downs, D.; Miller, D. A. Radiochemical Separation of Antimony and Tellurium in Isotope Production and in Radionuclide Generators. *J Radioanal Nucl Chem* **2004**, *262* (1), 241–247. https://doi.org/10.1023/B:JRNC.0000040881.44068.eb.

[112] Bennett, K. T.; Bone, S. E.; Akin, A. C.; Birnbaum, E. R.; Blake, A. V.; Brugh, M.; Daly, S. R.; Engle, J. W.; Fassbender, M. E.; Ferrier, M. G.; Kozimor, S. A.; Lilley, L. M.; Martinez, C. A.; Mocko, V.; Nortier, F. M.; Stein, B. W.; Thiemann, S. L.; Vermeulen, C. Large-Scale Production of ^{119m}Te and ^{119}Sb for Radiopharmaceutical Applications. *ACS Cent Sci* **2019**, *5* (3), 494–505. https://doi.org/10.1021/acscentsci.8b00869.

[113] International Atomic Energy Agency. Cyclotron Master List https://nucleus.iaea.org/sites/accelerators/lists/cyclotron master list/public_cyclotron_db_view.aspx (accessed Sep 1, 2024).

[114] Miller, D. A.; Sun, S.; Yi, J. H. Preparation of A118Te/118Sb Radionuclide Generator. *Journal of Radioanalytical and Nuclear Chemistry Articles* **1992**, *160* (2), 467–476. https://doi.org/10.1007/BF02037122.

[115] Yano, Y.; Lagunas-Solar, M. C. Tellurium-118/Antimony-118 Generator. *Proceedings of the 36th Annual Meeting of the Society of Nuclear Medicine* **1989**.

[116] El-Sadek, A. A.; El-Naggar, M. R.; Mansy, M. S. Purification of Rad-Waste Arising from Irradiated Natural Tin Target towards Tellurium-125m/Antimony-125 Radioisotope Generator Elaboration. *Applied Radiation and Isotopes* **2021**, *172* (March), 109690. https://doi.org/10.1016/j.apradiso.2021.109690.

[117] White, C. E.; Rose, H. J. Separation of Antimony by Solvent Extraction. *Anal Chem* **1953**, *25* (2), 351–353. https://doi.org/10.1021/ac60074a041.

[118] Vibhute, R. G.; Khopkar, S. M. Solvent Extraction of Antimony(III) with 18-Crown-6 from Iodide Media. *Talanta* **1989**, *36* (9), 957–959. https://doi.org/10.1016/0039-9140(89)80038-4.

[119] Sarkar, S. G.; Dhadke, P. M. Solvent Extraction Separation of Antimony (III) and Bismuth (III) with Bis(2,4,4-Trimethylpentyl) Monothiophosphinic Acid (Cyanex 302). *Sep Purif Technol* **1999**, *15* (2), 131–138. https://doi.org/10.1016/S1383-5866(98)00088-4.

[120] Menon, M. P.; Aras, N. K.; Irvine, J. W. Radiochemical Separation of Tin and Antimony by an Initial Phosphate Precipitation Step. *Journal of Inorganic and Nuclear Chemistry* **1965**. https://doi.org/10.1016/0022-1902(65)80436-5.

[121] Kraus, K. A.; Michelson, D. C.; Nelson, F. Adsorption of Negatively Charged Complexes by Cation Exchangers. *J Am Chem Soc* **1959**, *81* (13), 3204–3207. https://doi.org/10.1021/ja01522a011.

[122] Minami, E.; Honda, M.; Sasaki, Y. Ion-Exchange Separation of Fission Products. *Bull Chem Soc Jpn* **1958**, *31* (3), 372–377. https://doi.org/10.1246/bcsj.31.372.

[123] Smith, G. W.; Reynolds, S. A. Anion Exchange Separation of Tin, Antimony and Tellurium. *Analyrica Chimica Acta* **1955**, *12*, 151–153.

[124] Dawson, J.; Magee, R. J. The Anion-Exchange Separation of Tin and Antimony. *Mikrochim Acta* **1958**, *46* (3), 325–329. https://doi.org/10.1007/BF01216027.

[125] Maruyama, Y.; Yamaashi, Y. A Simple Method for the Separation of ^{125}Sb from Neutron-Irradiated Tin. *International Journal of Radiation Applications and Instrumentation*. **1988**, *39* (10), 1079–1080.

[126] Baluev, A. V; Mityakhina, V. S.; Krasnikov, L. V; Galkin, B. Y.; Beznosyuk, V. I. Sb from Neutron-Irradiated Sn. *Radiochemistry* **2003**, *45* (6), 616–619.

[127] Thisgaard, H. Accelerator Based Production of Auger-Electron-Emitting Isotopes for Radionuclide Therapy, Technical University of Denmark, Kongen Lyngby, Denmark, 2008, Vol. Ph.D. Diss.

[128] Randhawa, P.; Olson, A. P.; Chen, S.; Gower-Fry, K. L.; Hoehr, C.; Engle, J. W.; Ramogida, C. F.; Radchenko, V. Meitner-Auger Electron Emitters for Targeted Radionuclide Therapy: Mercury-197m/g and Antimony-119. *Curr Radiopharm* **2021**, *14* (4), 394–419.

[129] Otuka, N.; Takács, S. Definitions of Radioisotope Thick Target Yields. *Radiochim Acta* **2015**, *103* (1), 1–6. https://doi.org/10.1515/ract-2013-2234.

[130] Ellman, G. L. Tissue Sulfhydryl Groups. *Arch Biochem Biophys* **1959**, *82*, 70–77.

[131] Riddles, P. W.; Blakeley, R. L.; Zerner, B. Reassessment of Ellman's Reagent. *Methods Enzymol* **1983**, *91* (C), 49–60. https://doi.org/10.1016/S0076-6879(83)91010-8.

[132] Ellison, P. A.; Olson, A. P.; Barnhart, T. E.; Hoffman, S. L. V.; Reilly, S. W.; Makvandi, M.; Bartels, J. L.; Murali, D.; DeJesus, O. T.; Lapi, S. E.; Bednarz, B.; Nickles, R. J.; Mach, R. H.; Engle, J. W. Improved Production of ^{76}Br, ^{77}Br and ^{80m}Br via CoSe Cyclotron Targets and Vertical Dry Distillation. *Nucl Med Biol* **2020**, *80–81* (xxxx), 32–36. https://doi.org/10.1016/j.nucmedbio.2019.09.001.

[133] Thisgaard, H.; Jensen, M. Production of the Auger Emitter ^{119}Sb for Targeted Radionuclide Therapy Using a Small PET-Cyclotron. *Applied Radiation and Isotopes* **2009**, *67* (1), 34–38. https://doi.org/10.1016/j.apradiso.2008.09.003.

[134] Wojdyr, M. Fityk: A General-Purpose Peak Fitting Program. *J Appl Crystallogr* **2010**, *43* (5 PART 1), 1126–1128. https://doi.org/10.1107/S0021889810030499.

[135] He, A.; Liu, Q.; Ivey, D. G. Electrodeposition of Tin: A Simple Approach. *Journal of Materials Science: Materials in Electronics* **2008**, *19* (6), 553–562. https://doi.org/10.1007/s10854-007-9385-3.

[136] Møller, P.; Nielsen, L. P. *Advanced Surface Technology*, 2nd ed.; 2013.

[137] Bonner, N. A. The Exchange Reaction between Antimony(III) and Antimony (V) in Hydrochloric Acid Solutions. *J Am Chem Soc* **1949**, *71* (12), 3909–3914. https://doi.org/10.1021/ja01180a009.

[138] Özer, U. Y.; Bogucki, R. F. Equilibrium Studies of Antimony(III) Chelates in Aqueous Solution. *Journal of Inorganic and Nuclear Chemistry* **1971**, *33* (12), 4143–4153. https://doi.org/10.1016/0022-1902(71)80514-6.

[139] Tella, M.; Pokrovski, G. S. Stability and Structure of Pentavalent Antimony Complexes with Aqueous Organic Ligands. *Chem Geol* **2012**, *292–293*, 57–68. https://doi.org/10.1016/j.chemgeo.2011.11.004.

[140] Blachot, J. Nuclear Data Sheets for A = 111. *Nuclear Data Sheets* **2009**, *110* (6), 1239–1407. https://doi.org/10.1016/j.nds.2009.04.002.

[141] Olson, A. P.; Ma, L.; Feng, Y.; Najafi Khosroshahi, F.; Kelley, S. P.; Aluicio-Sarduy, E.; Barnhart, T. E.; Hennkens, H. M.; Ellison, P. A.; Jurisson, S. S.; Engle, J. W. A Third Generation Potentially Bifunctional Trithiol Chelate, Its $^{\mathrm{Nat,1XX}}$Sb(III) Complex, and

Selective Chelation of Radioantimony (^{119}Sb) from Its Sn Target. *Inorg Chem* **2021**, *60* (20), 15223–15232. https://doi.org/10.1021/acs.inorgchem.1c01690.

[142] Fischer, R. C. Antimony: Inorganic Chemistry. *Encyclopedia of Inorganic and Bioinorganic Chemistry* **2016**, No. Iii, 1–13. https://doi.org/10.1002/9781119951438.eibc0011.pub2.

[143] Wardell, J. L. Arsenic, Antimony, and Bismuth. In *Comprehensive Organometallic Chemistry II*; Aberdeen, UK, 1995; pp 321–347. https://doi.org/10.1039/9781849732895-00157.

[144] Jones, C. Recent Developments in Low Coordination Organo-Antimony and Bismuth Chemistry. *Coord Chem Rev* **2001**, *215* (1), 151–169. https://doi.org/10.1016/S0010-8545(00)00405-7.

[145] Price, E. W.; Orvig, C. Matching Chelators to Radiometals for Radiopharmaceuticals. *Chem Soc Rev* **2014**, *43* (1), 260–290. https://doi.org/10.1039/c3cs60304k.

[146] Ramogida, C. F.; Orvig, C. Tumour Targeting with Radiometals for Diagnosis and Therapy. *Chemical Communications* **2013**, *49* (42), 4720–4739. https://doi.org/10.1039/c3cc41554f.

[147] House, J. E. *Ch 16: Introduction to Coordination Chemistry*; 2020. https://doi.org/10.1016/b978-0-12-814369-8.00016-9.

[148] Pearson, R. G. Hard and Soft Acids and Bases. **1963**, *85* (22), 3533–3539.

[149] Coughlin, O.; Krämer, T.; Benjamin, S. L. Cationic Triarylchlorostibonium Lewis Acids. *Organometallics* **2023**, *42* (5), 339–346. https://doi.org/10.1021/acs.organomet.2c00426.

[150] Yang, M.; Tofan, D.; Chen, C. H.; Jack, K. M.; Gabbaï, F. P. Digging the Sigma-Hole of Organoantimony Lewis Acids by Oxidation. *Angewandte Chemie - International Edition* **2018**, *57* (42), 13868–13872. https://doi.org/10.1002/anie.201808551.

[151] Scheer, M. The Coordination Chemistry of Group 15 Element Ligand Complexes—a Developing Area. *Journal of the Chemical Society. Dalton Transactions* **2008**, *9226* (33), 4372–4386. https://doi.org/10.1039/b718179p.

[152] Maltz, L. T.; Gabbaï, F. P. Analyzing Fluoride Binding by Group 15 Lewis Acids: Pnictogen Bonding in the Pentavalent State. *Inorg Chem* **2023**. https://doi.org/10.1021/acs.inorgchem.3c01987.

[153] Lothenbach, B.; Ochs, M.; Wanner, H.; Yui, M. Thermodynamic Data for the Speciation and Solubility of Pd, Pb, Sn, Sb, Nb and Bi in Aqueous Solution. *Japan Nuclear Cycle Development Institute* **2004**, 1–356.

[154] Filella, M.; May, P. M. Critical Appraisal of Available Thermodynamic Data for the Complexation of Antimony(III) and Antimony(v) by Low Molecular Mass Organic Ligands. *Journal of Environmental Monitoring* **2005**, *7* (12), 1226–1237. https://doi.org/10.1039/b511453e.

[155] Filella, M.; Belzile, N.; Chen, Y. W. Antimony in the Environment: A Review Focused on Natural Waters II. Relevant Solution Chemistry. *Earth Sci Rev* **2002**, *59* (1–4), 265–285. https://doi.org/10.1016/S0012-8252(02)00089-2.

[156] Quentel, F.; Filella, M.; Elleouet, C.; Madec, C. L. Kinetic Studies on Sb(III) Oxidation by Hydrogen Peroxide in Aqueous Solution. *Environ Sci Technol* **2004**, *38* (10), 2843–2848. https://doi.org/10.1021/es035019r.

[157] Laintz, K. E.; Shieh, G. M.; Wai, C. M. Simultaneous Determination of Arsenic and Antimony Species in Environmental Samples Using Bis(Trifluoroethyl)Dithiocarbamate Chelation and Supercritical Fluid Chromatography. *J Chromatogr Sci* **1992**, *30* (4), 120–123. https://doi.org/10.1093/chromsci/30.4.120.

[158] Varadwaj, A.; Varadwaj, P. R.; Marques, H. M.; Yamashita, K. Definition of the Pnictogen Bond: A Perspective. *Inorganics (Basel)* **2022**, *10* (10), 1–15. https://doi.org/10.3390/inorganics10100149.

[159] de Azevedo Santos, L.; Hamlin, T. A.; Ramalho, T. C.; Bickelhaupt, F. M. The Pnictogen Bond: A Quantitative Molecular Orbital Picture. *Physical Chemistry Chemical Physics* **2021**, *23* (25), 13842–13852. https://doi.org/10.1039/d1cp01571k.

[160] Nicholas, C. Coordination Chemistry of Antimony and Bismuth: Lewis Acidity, Sigma * - Orbitals and Coordination Geometry. *Phosphorus Sulfur Silicon Relat Elem* **1994**, *87* (1–4), 167–176.

[161] Maroulis, G. *Atoms, Molecules and Clusters in Electric Fields*; 2006. https://doi.org/10.1142/p464.

[162] Maroulis, G. Cluster Size Effect on the Electric Polarizability and Hyperpolarizability in Small Antimony Clusters Sbn, n = 1, 2 and 4. *Chem Phys Lett* **2007**, *444* (1–3), 44–47. https://doi.org/10.1016/j.cplett.2007.07.015.

[163] Maroulis, G. *Atomic Static Dipole Polarizabilities*; Imperial College Press: London, England, 2006. https://doi.org/10.1142/p464.

[164] Garje, S. S.; Jain, V. K. Chemistry of Arsenic, Antimony and Bismuth Compounds Derived from Xanthate, Dithiocarbamate and Phosphorus Based Ligands. *Coord Chem Rev* **2003**, *236* (1–2), 35–56. https://doi.org/10.1016/S0010-8545(02)00159-5.

[165] Ozturk, I. I. Novel Antimony(III) Halide Complexes with Some n-Alkyl Thioureas: Synthesis, Characterization and Study of Their Effect upon the Catalytic Oxidation of Linoleic Acid to Hydroperoxylinoleic Acid by Lipoxygenase. *JOTCSA* **2017**, *44* (41), 81–9881. https://doi.org/10.18596/jotcsa.31798.

[166] Hadjikakou, S. K.; Antoniadis, C. D.; Hadjiliadis, N.; Kubicki, M.; Binolis, J.; Karkabounas, S.; Charalabopoulos, K. Synthesis and Characterization of New Water Stable Antimony(III) Complex with Pyrimidine-2-Thione and in Vitro Biological Study. *Inorganica Chim Acta* **2005**, *358* (2861-). https://doi.org/10.1016/j.ica.2004.06.028.

[167] Hadjikakou, S. K.; Ozturk, I. I.; Banti, C. N.; Kourkoumelis, N.; Hadjiliadis, N. Recent Advances on Antimony(III/V) Compounds with Potential Activity against Tumor Cells. *Journal of Inorganic Biochemistry*. 2015. https://doi.org/10.1016/j.jinorgbio.2015.06.006.

[168] Besold, J.; Kumar, N.; Scheinost, A. C.; Lezama Pacheco, J.; Fendorf, S.; Planer-Friedrich, B. Antimonite Complexation with Thiol and Carboxyl/Phenol Groups of Peat Organic Matter. *Environ Sci Technol* **2019**, *53* (9), 5005–5015. https://doi.org/10.1021/acs.est.9b00495.

[169] Clarkson, T. W. Chapter 61 - Inorganic and Organometal Pesticides. *Handbook of Pesticide Toxicology*; 2001; pp 1357–1428.

[170] Thakur, M. L.; Clark, J. C.; Silvester, D. J. The Production of ^{117}Sb-Labelled Potassium Antimonyl Tartrate for Medical Use. *Int. J. AppL Radiat. Isot* **1970**, *21*, 33–36.

[171] Blaurock-Busch, E. Comparison of Chelating Agents DMPS, DMSA and EDTA for the Diagnosis and Treatment of Chronic Metal Exposure. *Br J Med Med Res* **2014**, *4* (9), 1821–1835. https://doi.org/10.9734/bjmmr/2014/6875.

[172] Tóth-Molnár, E.; Lihi, N.; Gál, G. T.; De, S.; Bombicz, P.; Bányai, I.; Szikra, D.; Dénes, E.; Tircsó, G.; Tóth, I.; Kálmán, F. K. Exploring Cyclic Aminopolycarboxylate Ligands for Sb(III) Complexation: PCTA and Its Derivatives as a Promising Solution. *Inorg Chem* **2021**, No. Iii. https://doi.org/10.1021/acs.inorgchem.1c01765.

[173] Chen, C.; Sommer, C.; Thisgaard, H.; McKee, V.; McKenzie, C. J. Facile Transmetallation of [SbIII(DOTA)]_ Renders It Unsuitable for Medical Applications. *RSC Adv* **2022**, *12* (10), 5772–5781. https://doi.org/10.1039/d2ra00642a.

[174] Najafi Khosroshahi, F.; Feng, Y.; Ma, L.; Manring, S.; Rold, T. L.; Gallazzi, F. A.; Kelley, S. P.; Embree, M. F.; Hennkens, H. M.; Hoffman, T. J.; Jurisson, S. S. A New, Second Generation Trithiol Bifunctional Chelate for ^{72,77}As: Trithiol(b)-(Ser)2-RM2. *Bioconjug Chem* **2021**, *32* (7).

[175] Feng, Y.; Jurisson, S. S. Trithiol Compounds—Tricky but Valuable: The Design and Synthesis of Ligands for Stabilizing Radioarsenic for Radiopharmaceutical Development. *Strategies and Tactics in Organic Synthesis* **2019**, *14*, 207–224. https://doi.org/10.1016/B978-0-12-814805-1.00008-9.

[176] Feng, Y.; DeGraffenreid, A. J.; Phipps, M. D.; Rold, T. L.; Okoye, N. C.; Gallazzi, F. A.; Barnes, C. L.; Cutler, C. S.; Ketring, A. R.; Hoffman, T. J.; Jurisson, S. S. A Trithiol Bifunctional Chelate for ^{72,77}As: A Matched Pair Theranostic Complex with High in Vivo Stability. *Nucl Med Biol* **2018**, *61*, 1–10. https://doi.org/10.1016/j.nucmedbio.2018.03.001.

[177] DeGraffenried, A. J.; Feng, Y.; Barnes, C. L.; Ketring, A. R.; Cutler, C. S.; Jurrison, S. S. Trithiols and Their Arsenic Comounds for Potential Use in Diagnostic and Therapeutic Radiopharmaceuticals. *Nucl Med Biol* **2016**, *43* (5), 288–295. https://doi.org/10.1016/j.nucmedbio.2016.01.005.Trithiols.

[178] Apex3, AXScale, and SAINT. Brunker AXS Inc.: Madison, WI 2017.

[179] Sheldrick, G. M. SHELXS. Gottingen, Germany 2017.

[180] Sheldrick, G. M. SHELXS 97, Program for the Solution of Crystal Structure. University of Göttingen: Göttingen, Germany 1990.

[181] Sheldrick, G. M. Crystal Structure Refinement with SHELXL. *Acta Crystallogr C Struct Chem* **2015**, *71* (1), 3–8. https://doi.org/10.1107/S2053229614024218.

[182] Dolomanov, O. V.; Bourhis, L. J.; Gildea, R. J.; Howard, J. A. K.; Puschmann, H. OLEXA2: A Complete Structure Solution, Refinement and Analysis Program. *J Appl Crystallogr* **2009**, *42* (2), 339–341.

[183] Spek, A. L. PLATON SQUEEZE: A Tool for the Calculation of the Disordered Solvent Contribution to the Calculated Structure Factors. *Acta Crystallogr C Struct Chem* **2015**, *71* (1), 9–18.

[184] Ma, L.; Grant, C.; Gallazzi, F.; Watkinson, L. D.; Carmack, T. L.; Embree, M. F.; Smith, C. J.; Medvedev, D.; Cutler, C. S.; Li, Y.; Wilbur, D. S.; Hennkens, H. M.; Jurisson, S. S. Development and Biodistribution Studies of ^{77}As-Labeled Trithiol RM2 Bioconjugates for Prostate Cancer : Comparison of [^{77}As] As-Trithiol-Ser- Ser-RM2 vs . [^{77}As]As-Trithiol-Glu-Ser-RM2. **2022**, *109*, 61–69.

[185] Fu, J.; Turn, S. Q. Oxidation Mechanism of Sulfur-Containing Compounds and Antioxidant Depletion Dynamics: Insights into Interactions. *Fuel* **2025**, *381* (PA), 133341. https://doi.org/10.1016/j.fuel.2024.133341.

[186] Moaven, S.; Watson, B. T.; Thompson, S. B.; Lyons, V. J.; Unruh, D. K.; Casadonte, D. J.; Pappas, D.; Cozzolino, A. F. Self-Assembly of Reversed Bilayer Vesicles through Pnictogen Bonding: Water-Stable Supramolecular Nanocontainers for Organic Solvents. *Chem Sci* **2020**, *11* (17), 4374–4380. https://doi.org/10.1039/d0sc00206b.

[187] Cea-olivares, R.; Mufioz-hern, M.; Hern, S.; Silvestru, C. On the 5-Thia-(Substituted)-1-Oxa-4,6-Dithia-5-Stibocanes. Synthesis and Characterization of $O(CH_2CH_2S)_2$Sb-

$SCH_2CH_2OCH_2CH_2S$-$Sb(SCH_2CH_2)_2O$, a Compound with Two Different Eight-Membered Ring Conformations. *Inorganica Chim Acta* **1995**, *236*, 31–36.

[188] García Y García, P.; Martínez-Salas, P.; Hernández-Ortega, S.; Román-Bravo, P.; López-Cardoso, M.; Del Carmen Pérez-Redondo, M.; Vargas-Pineda, G.; Cotero-Villegas, A. M.; Cea-Olivares, R. Synthesis, Structure and Characterization of New Stibocanes Substituted with Dithiophosphate Ligands. *Polyhedron* **2012**, *37* (1), 48–53. https://doi.org/10.1016/j.poly.2012.02.001.

[189] Harper, C.; Llados, F.; Diamond, G.; Chappell, L. L. Toxicological Profile for Tin and Tin Compounds. *Agency for Toxic Substances and Disease Registry* **2005**, *2*, 1–426.

[190] Greb, L. Lewis Superacids: Classifications, Candidates, and Applications. *Chemistry - A European Journal* **2018**, *24* (68), 17881–17896. https://doi.org/10.1002/chem.201802698.

[191] Tella, M.; Pokrovski, G. S. Antimony(V) Complexing with O-Bearing Organic Ligands in Aqueous Solution: An X-Ray Absorption Fine Structure Spectroscopy and Potentiometric Study. *Mineral Mag* **2008**, *72* (1), 205–209. https://doi.org/10.1180/minmag.2008.072.1.205.

[192] Boelaert, M.; Sundar, S. Manson's Tropical Diseases. *Manson's Tropical Diseases*; 2014; pp 631–651.

[193] Croft, S. T.; Sndar, S.; Fairlamb, A. H. Drug Resistance in Leishmaniasis. *Clinical Microbiology Revews* **2013**, *19* (1), 111–126. https://doi.org/10.1128/CMR.19.1.111.

[194] Tiekink, E. R. T. Antimony and Bismuth Compounds in Oncology. *Crit Rev Oncol Hematol* **2002**, *42* (3), 217–224. https://doi.org/10.1016/S1040-8428(01)00217-7.

[195] Hu, S.-Z.; Fu, Y.-M.; Xu, B.; Tang, W.-D.; Yu, W.-J. Studies of the Antitumor Antimony(III) Triaminocarboxylic Complexonates. Crystal Structures of

NH_4[Sb(Hdtpa)]*H_2O and Na[Sb(Hdtpa)]*4.5H_2O (Dtpa=diethylenetriaminepentaacetic Acid). *Main Group Metal Chemistry* **1997**, *20* (3), 169–180.

[196] Robbins, P. J.; Sodd, V. J.; Scholz, K. L.; Fortman, D. L. Evaluation of Antimony-117 for Tumor Imaging. *Int J Nucl Med Biol* **1976**, *3* (1), 56–57. https://doi.org/10.1016/0047-0740(76)90017-6.

[197] Ando, A.; Hisada, K.; Ando, I. Affinity for a Malignant Tumor and Organs of the Elements in Group V of the Periodic Table. *Radioisotopes (Tokyo)* **1973**, *22* (6), 286–290.

[198] Caboche, J.; Jondreville, C.; Tack, K.; Denys, S.; Rychen, G.; Feidt, C. Tissue Distribution of Antimony (Sb) in Piglets Orally given Graded Levels of Sb (V). *Toxicol Environ Chem* **2009**, *91* (2), 267–278. https://doi.org/10.1080/02772240802175814.

[199] Smith, R. E.; Steele, M.; Eakin, R. E.; Cowie, D. B. The Tissue Distribution of Radioantimony Inhaled as Stibine. **1948**, No. Journal of Laboratory and Clinical Medicine, 635–643.

[200] Kobayashi, A.; Ogra, Y. Metabolism of Tellurium, Antimony and Germanium Simultaneously Administered to Rats. *Journal of Toxicological Sciences* **2009**, *34* (3), 295–303. https://doi.org/10.2131/jts.34.295.

[201] López, S.; Aguilar, L.; Mercado, L.; Bravo, M.; Quiroz, W. Sb(V) Reactivity with Human Blood Components: Redox Effects. *PLoS One* **2015**, *10* (1), 1–12. https://doi.org/10.1371/journal.pone.0114796.

[202] Frézard, F.; Demicheli, C.; Ferreira, C. S.; Costa, M. A. P. Glutathione-Induced Conversion of Pentavalent Antimony to Trivalent Antimony in Meglumine Antimoniate. *Antimicrob Agents Chemother* **2001**, *45* (3), 913–916. https://doi.org/10.1128/AAC.45.3.913-916.2001.

[203] Friedrich, K.; Vieira, F. A.; Porrozzi, R. Disposition of Antimony in Rhesus Monkeys Inected with Leishmania Braziliensis and Treated with Meglumine Antimoniate. *J Toxicol Environ Health* **2012**, *75* (2).

[204] Borborema, S. E. T.; Osso Junior, J. A.; de Andrade Junior, H. F.; do Nascimento, N. Biodistribution of Meglumine Antimoniate in Healthy and Leishmania (Leishmania) Infantum Chagasi-Infected BALB/c Mice. *Mem Inst Oswaldo Cruz* **2013**, *108* (5), 623–630. https://doi.org/10.1590/0074-0276108052013014.

[205] Borborema, S. E. T.; Osso, J. A.; De Andrade, H. F.; Do Nascimento, N. Pharmacokinetics of Neutron-Irradiated Meglumine Antimoniate in Leishmania Amazonensis-Infected BALB/c Mice. *Journal of Venomous Animals and Toxins Including Tropical Diseases* **2019**, *25* (May 2018), 1–9. https://doi.org/10.1590/1678-9199-jvatitd-1446-18.

[206] Coelho, D. R.; Miranda, E. S.; Saint'Pierre, T. D.; Roma Paumgartten, F. J. Tissue Distribution of Residual Antimony in Rats Treated with Multiple Doses of Meglumine Antimoniate. *Mem Inst Oswaldo Cruz* **2014**, *109* (4), 420–427. https://doi.org/10.1590/0074-0276140030.

[207] Gómez, M. A.; Navas, A.; Prieto, M. D.; Giraldo-Parra, L.; Cossio, A.; Alexander, N.; Gore Saravia, N. Immuno-Pharmacokinetics of Meglumine Antimoniate in Patients with Cutaneous Leishmaniasis Caused by Leishmania (Viannia). *Clinical Infectious Diseases* **2021**, *72* (10), E484–E492. https://doi.org/10.1093/cid/ciaa1206.

[208] Hansen, C.; Schmidt, B.; Larsen, E. H.; Gammelgaard, B.; Stürup, S.; Hansen, H. R. Quantitative HPLC-ICP-MS Analysis of Antimony Redox Speciation in Complex Sample Matrices: New Insights into the Sb-Chemistry Causing Poor Chromatographic Recoveries. *Analyst* **2011**, *136* (5), 996–1002. https://doi.org/10.1039/c0an00796j.

[209] Joaqui-Joaqui, M. A.; Pandey, M. K.; Bansal, A.; Raju, M. V. R.; Armstrong-Pavlik, F.; Dundar, A.; Wong, H. L.; Degrado, T. R.; Pierre, V. C. Catechol-Based Functionalizable Ligands for Gallium-68 Positron Emission Tomography Imaging. *Inorg Chem* **2020**, *59* (17), 12025–12038. https://doi.org/10.1021/acs.inorgchem.0c00975.

[210] Accornero, M.; Marini, L.; Lelli, M. The Dissociation Constant of Antimonic Acid at 10-40°C. *J Solution Chem* **2008**, *37* (6), 785–800. https://doi.org/10.1007/s10953-008-9280-4.

[211] Koller, A. J.; Glaser, O.; DeLuca, M. C.; Motz, R. N.; Amason, E. K.; Carbo-Bague, I.; Mixdorf, J. C.; Guzei, I. A.; Aluicio-Sarduy, E.; Śmiłowicz, D.; Barnhart, T. E.; Ramogida, C. F.; Nolan, E. M.; Engle, J. W.; Boros, E. "Off-Label Use" of the Siderophore Enterobactin Enables Targeted Imaging of Cancer with Radioactive Ti(IV). *Angewandte Chemie* **2024**, *136* (18). https://doi.org/10.1002/ange.202319578.

[212] Phipps, M. D.; Cingoranelli, S.; Bhupathiraju, N. V. S. D. K.; Younes, A.; Cao, M.; Sanders, V. A.; Neary, M. C.; Devany, M. H.; Cutler, C. S.; Lopez, G. E.; Saini, S.; Parker, C. C.; Fernandez, S. R.; Lewis, J. S.; Lapi, S. E.; Francesconi, L. C.; Deri, M. A. Sc-HOPO: A Potential Construct for Use in Radioscandium-Based Radiopharmaceuticals. *Inorg Chem* **2023**, *62* (50), 20567–20581. https://doi.org/10.1021/acs.inorgchem.2c03931.

[213] Schweigert, N.; Zehnder, A. J. B.; Eggen, R. I. L. Chemical Properties of Catechols and Their Molecular Modes of Toxic Action in Cells, from Microorganisms to Mammals. *Environ Microbiol* **2001**, *3* (2), 81–91. https://doi.org/10.1046/j.1462-2920.2001.00176.x.

[214] Tella, M.; Pokrovski, G. S. Antimony(III) Complexing with O-Bearing Organic Ligands in Aqueous Solution: An X-Ray Absorption Fine Structure Spectroscopy and Solubility Study. *Geochim Cosmochim Acta* **2009**, *73* (2), 268–290. https://doi.org/10.1016/j.gca.2008.10.014.

[215] Willis, S. B.; Neumann, H. M. Hydrolysis and Nucleophilic Substitution of the Hexachloroantimonate(V) Ion in the PH Range 2-12. *J Am Chem Soc* **1969**, *91* (11), 2924–2928. https://doi.org/10.1021/ja01039a018.

[216] Lehnert, W.; Gregoire, M. C.; Reilhac, A.; Meikle, S. R. Characterisation of Partial Volume Effect and Region-Based Correction in Small Animal Positron Emission Tomography (PET) of the Rat Brain. *Neuroimage* **2012**, *60* (4), 2144–2157. https://doi.org/10.1016/j.neuroimage.2012.02.032.

[217] Soret, M.; Bacharach, S. L.; Buvat, I. Partial-Volume Effect in PET Tumor Imaging. *Journal of Nuclear Medicine* **2007**, *48* (6), 932–945. https://doi.org/10.2967/jnumed.106.035774.

[218] Marquis, H.; Willowson, K. P.; Bailey, D. L. Partial Volume Effect in SPECT & PET Imaging and Impact on Radionuclide Dosimetry Estimates. *Asia Ocean J Nucl Med Biol* **2023**, *11* (1), 44–54. https://doi.org/10.22038/AOJNMB.2022.63827.1448.

[219] (NIST), N. I. of S. and T. PSTAR, ASTAR, ESTAR. *ICRU Report 49, International Commission on Radiation Unites and Measurements* **1993**.

[220] Society, R. C. Periodic Table (accessed Aug 28, 2024).

[221] Kuznetsov, B. V.; Vorobyova, T. N.; Glibin, V. P. A Comparative Study of Tin-Nickel Alloys Obtained by Electroplating and Casting. *Metal Finishing* **2013**, *111* (3), 38–42. https://doi.org/10.1016/S0026-0576(13)70233-2.

[222] Jeon, J. O.; Lee, K. D.; Oh, L. S.; Seo, S. W.; Lee, D. K.; Kim, H.; Jeong, J. H.; Ko, M. J.; Kim, B.; Son, H. J.; Kim, J. Y. Highly Efficient Copper-Zinc-Tin-Selenide (CZTSe) Solar Cells by Electrodeposition. *ChemSusChem* **2014**, *7* (4), 1073–1077. https://doi.org/10.1002/cssc.201301347.

[223] Walsh, F. C.; Low, C. T. J. A Review of Developments in the Electrodeposition of Tin-Copper Alloys. *Surf Coat Technol* **2016**, *304*, 246–262. https://doi.org/10.1016/j.surfcoat.2016.06.065.

[224] Kutyreff, C. J.; Barnhart, T. E.; Lo, Y. H.; Happel, S.; Nickles, R. J.; Ellison, P. A.; Aluicio-Sarduy, E.; Engle, J. W. Intermetallic Cobalt–Gallium Targets for Production of Germanium Radioisotopes. *Applied Radiation and Isotopes* **2022**, *187* (May). https://doi.org/10.1016/j.apradiso.2022.110307.

[225] Fu, Z.; Wang, K.; Tan, T.; Xiong, Y.; He, D.; Wang, Y.; Munir, Z. A. The SPS Process: Characterization and Fundamental Investigations. *Pulse Electric Current Synthesis and Processing of Materials* **2006**, 3–21.

[226] Anselmi-Tamburini, U. Spark Plasma Sintering. *Encyclopedia of Materials: Technical Ceramics and Glasses: Volume 1-3* **2021**, *1*, V1-294-V1-310. https://doi.org/10.1016/B978-0-12-803581-8.11730-8.

[227] Jarvin, M.; Inbanathan, S. S. R.; Rani Rosaline, D.; Josephine Prabha, A.; Martin Britto Dhas, S. A. A Study of the Structural, Morphological, and Optical Properties of Shock Treated SnO_2 Nanoparticles: Removal of Victoria Blue Dye. *Heliyon* **2022**, *8* (6), e09653. https://doi.org/10.1016/j.heliyon.2022.e09653.

[228] Baun, C.; Dam, J. H.; Hildebrandt, M. G.; Ewald, J. D.; Kristensen, B. W.; Gammelsrød, V. S.; Olsen, B. B.; Thisgaard, H. Preclinical Evaluation of [^{58m}Co]Co-DOTA-PSMA-617 for Auger Electron Therapy of Prostate Cancer. *Sci Rep* **2023**, *13* (1), 1–11. https://doi.org/10.1038/s41598-023-43429-8.

[229] International Atomic Energy Agency. Radionnuclidic Purity (accessed Oct 10, 2024).

[230] Abriola, D.; Sonzogni, A. A. Nuclear Data Sheets for A = 72. *Nuclear Data Sheets* **2010**, *111* (1), 1–140. https://doi.org/10.1016/j.nds.2009.12.001.

[231] Singh, B.; Nica, N. Nuclear Data Sheets for A = 77. *Nuclear Data Sheets* **2012**, *113* (5), 1115–1314. https://doi.org/10.1016/j.nds.2012.05.001.

[232] Ravel, B.; Newville, M. ATHENA, ARTEMIS, HEPHAESTUS: Data Analysis for X-Ray Absorption Spectroscopy Using IFEFFIT. *J Synchrotron Radiat* **2005**, *12* (4), 537–541. https://doi.org/10.1107/S0909049505012719.